Electrolysis of Molten Polyphosphate Salts Generates P_4 and O_2: Selectivity, Kinetics and Stability Behind a Promising Alternative to Carbothermal Phosphate Reduction

by

Andrew John Licini

Bachelor of Arts (B.A.)
Princeton University, 2016

Submitted to the Department of Chemistry in Partial Fulfillment of the Requirements of the Degree of

DOCTOR OF PHILOSOPHY IN INORGANIC CHEMISTRY

at the

MASSACHUSETTS INSTITUTE OF TECHNOLOGY

JUNE 2023

Authored by: Andrew John Licini
Department of Chemistry
March 31, 2023

Certified by: Professor Yogesh Surendranath
Department of Chemistry, Thesis Supervisor
Paul M. Cook Career Development Professor

Accepted by: Professor Adam Willard
Department of Chemistry
Associate Professor

This doctoral thesis has been examined by a committee of the
Department of Chemistry as follows:

Professor Christopher C. Cummins……
Thesis Committee Chair
Henry Dreyfus Professor of Chemistry

Professor Yogesh Surendranath……
Thesis Supervisor
Paul M. Cook Career Development Professor, Department of Chemistry

Professor Antoine Allanore……
Thesis Committee Member
Professor of Metallurgy, Department of Materials Science and Engineering

Electrolysis of Molten Polyphosphate Salts Generates P_4 and O_2: The Selectivity, Kinetics and Stability Behind a Promising Alternative to Carbothermal Phosphate Reduction

by

Andrew John Licini

Submitted to the Department of Chemistry on March 31, 2023, in Partial Fulfillment of the Requirements of the Degree of Doctor of Philosophy in Inorganic Chemistry

ABSTRACT

Elemental white phosphorus is a vital feedstock chemical for a vast network of industries, but it is currently produced via a carbothermal reduction rife with environmental and efficiency problems. In this work, we use the molten salt electrolysis of sodium polyphosphates to investigate an alternative means of white phosphorus production. In order to collect robust and meaningful data on these traditionally challenging systems, we introduce a comprehensive toolkit of techniques and design elements, such as a sodium reference electrode and graphite pseudoreference couple, working electrode geometries that prevent gas blockage and inert container and separator materials. Via high-temperature product collection at graphite working electrodes in tandem with electrokinetic analysis, we identify white phosphorus as the major cathodic product with high selectivity and infer a rate-limiting formation of a P^{3+} intermediate involved in its formation. Simultaneously, we find that graphite oxidizes much more efficiently as an anode than the coke used in the industrial thermal process, evolving a mixture of carbon dioxide (96%) and carbon monoxide (4%) instead of exclusively carbon monoxide. When the graphite anode is replaced by a metal anode, we also identify oxygen as the major, and ostensibly only long-term, anodic product. While iridium metal anodes require a higher overpotential for oxygen evolution relative to platinum and gold, they also demonstrate vastly superior corrosion resistance, with corrosion rates as low as 0.93 mm yr^{-1} in Lux-basic melt compositions. Platinum and gold ions released during corrosion also re-reduce in solution to form elemental metal particulates and gaseous oxygen, resulting in roughly 100% oxygen evolution efficiency in all cases and allowing for catalyst material to partially be reclaimed. Finally, we find that the Lux acidity of the melt has a variety of significant effects on the energetics of melt reactions, simultaneously promoting the reduction of phosphates to phosphorus while suppressing the oxidation of graphite or evolution of oxygen and promoting metal anode corrosion. Taken together, these findings indicate that a viable carbon-free electrogeneration of white phosphorus is feasible under appropriate solvent conditions and electrode material choices, and this electrolysis represents an appealing alternative to legacy processes.

Thesis supervisor: Yogesh Surendranath

Title: Paul M. Cook Career Development Professor

Acknowledgments

As I look back my Ph.D. research efforts, I realize that I only arrived at my destination through the aid, guidance and support of many, many wonderful people.

First and foremost, I owe an immeasurable debt of gratitude to my research advisor, Dr. Yogesh ("Yogi") Surendranath, who nurtured this project from its inception into a fruitful body of research. The hands-on style which Yogi took in my mentorship opened my eyes and, I believe, helped me to grow immensely as a researcher and scholar. From helping me to refine my ideas and approaches to actively guiding my professional development, he has modeled a standard of mentorship quality for me that I can only hope to strive for in my desired role as an educator. I also owe a great deal to the other members of my thesis committee as well; Dr. Christopher ("Kit") Cummins's enthusiastic zeal and expertise for phosphorus chemistry almost singlehandedly enabled my product collection and characterization efforts, and he pursued his role as my thesis committee chair with a great degree of responsibility and congeniality. Similarly, Dr. Antoine Allanore's immense knowledge of molten salt chemistry and experimental design was the impetus that drove the inception of our molten salt reactor; without his guidance, my Ph.D. program would have been over before it even began. Additionally, although he was not on my thesis committee, I also want to thank Dr. Donald Sadoway for his guidance; the molten salt focus of the electrochemistry course he presented was invaluable for circumventing unique pitfalls, and his advice regarding sodium-conducting membranes was crucial for the development of a reference electrode that had some measure of reliability under these notoriously harsh and opaque conditions.

Among my colleagues who contributed directly to my research efforts, I owe immense gratitude to Dr. Jonathan ("Jo") Melville, who worked jointly on the phosphate reduction project. During my leave of absence, Jo fearlessly charged forward with the remaining research, generating beautiful data and high yields of phosphorus that acted as the lynchpin in our joint paper. His analysis using the framework of Lux acidity as a lens to interpret the polyphosphate melt composition studies, his ingenious use of thermal decomposition of red phosphorus to measure reversible pinning and his nuanced computational analysis of the opaque cyclic voltammetry also added a great depth to the underlying narrative of the paper, and I feel privileged to have worked with such an inventive, intelligent and resourceful colleague. On top of our joint work, Jo was consistently an encouraging friend who got me through some extremely challenging circumstances prior to my leave, and was always up for sharing a drink or giving me some valuable life advice. I also owe great amount to Sophia Weng, who kindly performed the SEM and XPS characterization on all the many fragile metal coils I gave her. Her expertise and skilled hands resulted in the beautiful images of the oxygen evolution chapter. Additionally, Thejas Wesley was an enormous help for certain thermodynamic calculations regarding the power requirements for a proposed molten salt process based on electrolysis and the input of phosphoric acid, and his keen eye and knowledge of complex heat transfer processes vastly improved the quality of those calculations. Lastly, I want to thank (Dr.) Michael ("Mike") Geeson, an invaluable collaborator through Kit Cummin's group who oriented me in the field of phosphates, provided several key materials and compounds, and provided a high degree of expertise and mentorship in collecting the wonderful ^{31}P NMR spectra to characterize white phosphorus.

A number of MIT staff members have also provided a great deal of support from behind the scenes. Foremost is Andrew Gallant and the other members of the MIT Machine Shop team, who patiently

guided me through many, many iterations of the molten salt cell design and whose skilled hands enabled my research. Along those lines, I also want to thank Liu Gang for his enormous assistance with the wiring of the furnace, especially when the inner coils shorted and needed replacing, and Brian Pretti for advising me on the installation of the furnace and safety enclosure design. I also want to thank the MIT Libraries staff, especially Christine ("Chris") Sherratt, for helping me penetrate through the extremely backdated literature on molten phosphate studies. I also want to thank Harold Fox for his assistance in the patent drafting and assistance process. Additionally, I want to thank Joanne Baldini and the other financial administrators who assisted me in the ins and outs of MIT's research supplies purchasing process. Finally, I want to give a big thanks to Troy van Voorhis, Suraiya Baluch, Jennifer Weisman and the MIT Chemistry Education office for all their valuable advice and for enabling my studies.

I also want to convey special thanks to the National Defense Science and Engineering Graduate Fellowship program, the Office Chèrifien des Phosphates (OCP) Group, and Mohammed VI Polytechnic University (UM6P) for their generous funding. Without their financial contributions, my research would not have been possible, and I feel grateful to have been given this opportunity.

My research was also very much a product of the environment that my friends and coworkers from the Surendranath lab provided. Most helpful were group meetings as well as general office and meal conversations, which all helped to shape the logic of my research and the means I took to address it. I especially want to thank Jaeyune Ryu, who, as my deskmate, was almost always the first person I approached with thoughts, questions and concerns about my research. He is the most intelligent, most humble and hardest-working chemist I can imagine, and it was truly an honor to work with him and call him my friend. I look forward to hearing of his inevitable success in South Korea and beyond. Haixu Wang, my recent deskmate, has also been a great source of support and has always provided an ear when I needed to diagnose the latest problem with the molten salt cell. An Chu has also been a great source of support and advice, and his philosophies on teaching helped to provide a great deal of perspective on my own career direction. His dual efforts in keeping the entire lab running efficiently and in organizing lab group volleyball were both extremely helpful to me. The same is true of Soyoung Kim, Corey Kaminsky, Megan Jackson and Travis Marshall, who formed a core of wise mentorship alongside other veterans of the lab like Anna Wuttig, Youngmin Yoon and Seokjoon Oh. More recent lab members like Kunal Lodaya and Deiaa Harraz have also been wonderful friends and sources of inspiration, and helping them with sodium reference electrodes was a real joy. While these names stand out in particular, everyone in the lab has been a great source of wisdom, advice and support over the years. Outside the lab, I also received support from a great many people, such as Olivia Fiebig, J. Connor Gilhula, Jesse Gordon, Andrea Carney and the entire Sidney-Pacific graduate student community. From Air Force Research Labs and the UNM Advanced Materials Lab, I wish to thank Dr. Thomas Peng and Professor Fernando Garzon for their moral support and career advice at a time when I needed it the most. I also want to give special thanks to my family, especially my parents, for supporting me through difficult times and for the love, support and prayers they gave to me.

Lastly, I want to thank you, the reader, for taking an interest in this science. With some further development, I hope we can look forward to a future together where phosphorus is produced safely, cleanly and in a way that enriches the world to the fullest.

Biographical Notes

Andrew Licini was born in June of 1994 in Allentown, Pennsylvania. He attended Emmaus High School in Emmaus, PA and graduated in 2012. He attended Princeton University for his undergraduate studies beginning in 2012, where he performed surface science research on reversible electrochemical mirror systems under Dr. Steven Bernasek. In 2015 he received an ACS Award in Analytical Chemistry for these research efforts. He received his Bachelor of Arts degree *summa cum laude* in Chemistry from Princeton University in May of 2016 with a certificate in Materials Science and Engineering, as well as the Princeton University Physical Chemistry Prize. His thesis, "Reversible Electrodeposition of Silver Mirror Surfaces from an Ionic Liquid onto a Transparent Conductor," (2016) is available through Princeton University. Additionally, he performed research at the University of New Mexico Advanced Materials Laboratory as an AFRL Space Scholar under Dr. Thomas Peng.

He received a National Defense Science and Engineering Graduate (NDSEG) fellowship in 2016 and matriculated into Massachusetts Institute of Technology (MIT) in Fall of 2016. As a teaching assistant, he helped to inaugurate an electrochemistry lab module in Fall of 2016 (5.37 Module 8) alongside Jaeyune Ryu, and in Spring of 2017 he helped to inaugurate a new version of 5.03 Principles of Inorganic Chemistry I under Dr. Yogesh Surendranath and Dr. Alexander Radosevich, alongside J. Connor Gilhula. For these efforts, he received an MIT Award for Outstanding Teaching in Summer of 2017. He joined the Surendranath Research Group in December of 2016, where he performed research on the electrolysis of molten metaphosphates for application to white phosphorus production and oxygen evolution. A patent on the white phosphorus process was filed jointly with Y. Surendranath (US Patent Application Number 17/275,331 / International Patent Application Number PCT/US2019/052319). The first portion of this research, discussed in Chapter 2 of this work, is published in ACS Central Science ("Electrolytic Synthesis of White Phosphorus Is Promoted in Oxide-Deficient Molten Salts" by J. F. Melville, A. J. Licini and Y. Surendranath, 2023). His work on oxygen evolution on metal catalysts is currently being drafted for publication.

Table of Contents

List of Figures

List of Tables

List of Supplemental Materials and Research Data

All research notes are documented on the MIT Wiki Service under the heading “Andrew Licini’s Lab Notebook.” Notes for Chapter 2 (the reduction of molten metaphosphates) are predominantly featured in Lab Notebook Entries 2016-2017, Lab Notebook Entries 2017-2018, and Lab Notebook Entries 2018-2019. Notes for Chapter 3 (the oxidation of molten metaphosphates) are predominantly featured in Lab Notebook Entries 2020-2021 and Lab Notebook Entries 2021-2022.

Data files are saved on a shared drive #Yogi Lab / Yogi Lab Data / Andrew Licini.

Chapter 1 – Introduction

1.1: ELECTROLYSIS FOR DECARBONIZATION OF THE CARBOTHERMAL REDUCTION OF WHITE PHOSPHORUS

As global production of greenhouse gases continues to expand, the impetus for decarbonizing legacy chemical production processes grows. Since the start of the Industrial Revolution in 1750, the atmospheric carbon dioxide concentration has grown from 280 ppm to 420 ppm, spurred on largely by human activity[1,2]. In particular, chemical and materials industries such as the production of ammonia and methanol[3], steel[4], and aluminum[5] each contribute substantial fractions to carbon dioxide levels. Carbon dioxide contributes to climate change via the absorption of infrared light, so the atmosphere currently absorbs 3.22 more watts of solar energy per square meter relative to 1750[6], and the dissolution of carbon dioxide into global waters has increased the ocean surface's acidity, lowering its pH from 8.21 to 8.10 over the same time period.[1] As a result, global research efforts in recent years have turned towards the decarbonization of legacy chemical processes. The production of white phosphorus, while not in the top five highest CO_2-producing processes, is a particularly compelling innovation challenge because the fundamental nature of its production has remained constant over the past 100 years. White phosphorus currently underpins a number of vital industries and is used to produce food-grade phosphates, acids for processing computer chips, pesticides, flame retardants, PVC piping, lubricants and commercial lithium ion battery electrolytes.[7,8] Since its discovery by Hennig Brand in 1669, elemental phosphorus has derived from a carbothermal reduction process wherein phosphates obtain electrons from carbon oxidation to become elemental phosphorus, generating carbonaceous gases in the process.[9] Since approximately 1928, when the process was patented,[10] industry has carried out the carbothermal phosphorus production process through the reaction of phosphate rock, apatite, with carbonaceous coke and silicon dioxide-based minerals in the following reaction (Equation 1):

$$2\ Ca_3(PO_4)_2 + 10\ C + 2\ SiO_2 \rightarrow P_4 + 10\ CO + 2\ Ca_3OSiO_4 \quad (1)$$

The reaction requires the presence of silicon dioxide because the reduction of phosphates generates more equivalents of oxides than carbon can accept, and thus silicon dioxide acts as a secondary oxide acceptor. Because the reaction at room temperature is highly disfavored (ΔG^0 = +2541 kJ mol^{-1}),[11,12] it

---

[1] Lindsey, R. Climate Change: Atmospheric Carbon Dioxide https://www.climate.gov/news-features/understanding-climate/climate-change-atmospheric-carbon-dioxide (accessed Feb 12, 2023).

[2] Tans, P.; Keeling, R. Trends in Atmospheric Carbon Dioxide https://gml.noaa.gov/ccgg/trends/data.html (accessed Feb 12, 2023).

[3] Sanchez, D. P.; Collina, L.; Levi, P.; Hodgson, D. Chemicals https://www.iea.org/reports/chemicals (accessed Feb 12, 2023).

[4] Kueppers, M.; Hodgson, D.; Levi, P.; Vass, T.; Lechtenbohmer, T. Iron and Steel https://www.iea.org/reports/iron-and-steel (accessed Feb 12, 2023).

[5] Hodgson, D.; Vass, T. Aluminium https://www.iea.org/reports/aluminium (accessed Feb 12, 2023).

[6] Lindsey, R. Climate Change: Annual greenhouse gas index https://www.climate.gov/news-features/understanding-climate/climate-change-annual-greenhouse-gas-index.

[7] Diskowski, H.; Hofmann, T. *Ullmann's Encyclopedia of Industrial Chemistry*; Wiley-VCH: Weinheim, Germany, 2012; Vol. 26, pp 725–746.

[8] Jupp, A. R.; Beijer, S.; Narain, G. C.; Schipper, W.; Slootweg, J. C. *Chem. Soc. Rev.* **2021**, *50* (1), 87–101.

[9] Emsley, J. *The 13th Element: The Sordid Tale of Murder, Fire, and Phosphorus*; Wiley: New York, 2000.

[10] Nigra, G. FR658521A, 1929.

[7] Diskowski, H.; Hofmann, T. *Ullmann's Encyclopedia of Industrial Chemistry*; Wiley-VCH: Weinheim, Germany, 2012; Vol. 26, pp 725–746.

[8] Jupp, A. R.; Beijer, S.; Narain, G. C.; Schipper, W.; Slootweg, J. C. *Chem. Soc. Rev.* **2021**, *50* (1), 87–101.

[11] *CRC Handbook of Chemistry and Physics*, 103rd ed.; Rumble, J. R., Ed.; CRC Press: Ohio, 2023.

[12] Wolery, T. J.; Jove-Colon, C. F. *Qualification of Thermodynamic Data for Geochemical Modeling of Mineral-Water Interactions*

requires extremely high temperatures to proceed, wherein the thermal energy increases the favorability of gas formation from the solid reactants. In industry, an arc reactor generates this heat through the electrical resistance of enormous currents, raising the temperature of the solid reactant mixture to 1500 °C and converting it into a molten slag.[7] The calcium silicate slag flows out of the reactor as molten waste, which leads to staggering thermal losses of approximately 30% of the energy costs of the system, an energy sink of 12,000-14,000 TJ yr^{-1}.[7] Meanwhile, because the highly reducing gaseous phosphorus imposes limitations on oxidation processes, only two of the four valence electrons of the carbon coke are accessible by phosphates in the reaction.[13] Thus, the carbon oxidizes incompletely to carbon monoxide (CO) rather than the thermodynamically preferable carbon dioxide (CO_2). Condensation towers and electrostatic scrubbers separate the white phosphorus from the CO as well as dust and compounds like SiF_4,[7] and the CO is subsequently combusted in an air stream to avoid release of toxic CO into the environment. In addition to being capital-intensive and thermally wasteful, therefore, the thermal process consumes twice as much coke and generates twice as much carbon dioxide as it should require from the standpoint of redox electron economy. Because 0.9 Mt of white phosphorus are produced annually,[14] the process releases 2.3 Mt of CO_2 from a stoichiometric standpoint alone. The plants which produce white phosphorus are also predominantly located in China, Vietnam and Kazakhstan, where electricity generation is predominated by coal and natural gas,[15] so the 12.5-14 kWh kg^{-1} P_4 energy cost also generates substantial additional carbon emissions.[7,8] Finally, because the plants which produce white phosphorus thermally are so capital-intensive due to their immense power requirements, economies of scale currently favor a supply chain where a small number of plants produce a large amount of white phosphorus. Additionally, while China, Vietnam and Kazakhstan are the primary producers of white phosphorus, the top five consumers of white phosphorus are Germany, India, Poland, Japan and Brazil.[16] Thus, the global white phosphorus market requires the compound to be shipped over long distances in enormous tanks, usually by train as a liquid under a layer of water at 55 °C, to the chemical plants which require it.[7] When malfunctions on these railways occur, derailments can lead to the release of massive amounts of highly pyrophoric white phosphorus. These spills kill or injure thousands of bystanders, create massive fires that can devastate local properties, and generate toxic gaseous phosphorus pentoxide that reacts with moisture to form phosphoric acid, rendering the accident zone inhospitable and forcing hundreds of thousands of civilians to evacuate.[17–20] In conclusion, if researchers could find a greener, lower-temperature process for reducing phosphates to white phosphorus, such a development would not only lessen the environmental impact of the process but also allow the production of white phosphorus to be downscaled and decentralized across a greater number of countries.

---

in Dilute Systems; 2004.

[13] Dorn, F. W.; Harnisch, H. *Chemie Ing. Tech.* **1970**, *42* (19), 1209–1215.

[14] Deloitte Sustainability; British Geological Survey; Bureau de Recherches Géologiques et Minières; Netherlands Organisation for Applied Scientific Research. *Study on the Review of the List of Critical Raw Materials: Critical Raw Materials Factsheets*; Brussels, 2017.

[15] British Peroleum. *Bp Statistical Review of World Energy, 71st Ed.*; 2022.

[16] Webeck, E.; Matsubae, K. In *Phosphorus Recovery and Recycling*; Ohtake, H., Tsuneda, S., Eds.; Springer: Singapore, 2019; pp 29–44.

[9] *CRC Handbook of Chemistry and Physics*, 103rd ed.; Rumble, J. R., Ed.; CRC Press: Ohio, 2023.

[17] Ohio History Central. Miamisburg, Ohio, Train Derailment https://ohiohistorycentral.org/w/Miamisburg,_Ohio,_Train_Derailment (accessed Feb 13, 2023).

[18] Scoville, W.; Springer, S.; Crawford, J. *J. Hazard. Mater.* **1989**, *21*, 47–64.

[19] *The Washington Post*. Crofton, KY June 23, 1988.

[20] Train Carrying Phosphorus Leaves Ukraine For Kazakhstan https://www.rferl.org/a/1077823.html (accessed Feb 13, 2023).

In the past, researchers have historically found great success in innovating difficult or inefficient redox processes by means of electrolysis. Spatially separating the two half-reactions of a redox couple through an external electrolysis circuit allows reactions to be run with an electrical driving force instead of a chemical one, and grants independence to the local reaction conditions at each electrode. This principle, for instance, allows for reactions to occur which would never occur spontaneously from a chemical perspective. The chlor-alkali process, for instance, allows an external voltage to drive the uphill reaction of sodium chloride and water to form bleach (sodium hypochlorite), sodium hydroxide and hydrogen gas.[21] Additionally, the spatial separation of electrodes allows for the generation of products which could not typically coexist in the same spatial location. The Hall-Héroult process, for example, allows carbon oxidation to fuel the reduction of alumina to aluminum metal through the physical separation of the media in a molten salt.[22] Finally, the decoupling of the two half-reactions allows for interchangeability of counter reactions if the target reaction is only one half of a redox reaction. Because the reduction of phosphates to phosphorus is fundamentally part of a redox couple, an electrolysis process could ostensibly solve several issues at once: a) the incomplete oxidation of carbon, b) the necessity of extreme temperatures to provide thermodynamic driving force, c) the use of silicon dioxide and the thermally wasteful calcium silicate slag as an oxide acceptor, and d) the need to oxidize carbon as a stoichiometric reagent in the first place.

However, the nature of the phosphate reagent precludes the use of most typical electrolytes, the solution phase media that complete the electrical circuit via ion transfer. To illustrate these practical hurdles, we can consider the hypothetical voltage of the aqueous reduction of phosphoric acid (P^{5+}) to phosphorous acid (P^{3+}), a necessary intermediate to producing white phosphorus (Equation 2):

$$H_3PO_{4(aq)} + 2\ H^+ + 2\ e^- \rightarrow H_3PO_{3(aq)} + H_2O_{(l)} \qquad E^0 = -0.276\ V^{11} \qquad (2)$$

Although this standard reduction potential can be calculated from known thermodynamic values, it has never been observed in aqueous media. This is because, although not thermodynamically prohibited, such a reduction reaction would necessarily compete with the direct reduction of protons (hydronium) in the same aqueous medium (Equation 3):

$$2\ H^+ + 2\ e^- \rightarrow H_{2(g)} \qquad E^0 = 0.000\ V^{11} \qquad (3)$$

Because the standard reduction potential of protons in solution is higher than that of phosphoric acid, the reduction of phosphoric acid can only occur under potentials which are reducing enough to provide a significant overpotential for the evolution of hydrogen. Moreover, hydrogen evolution is a notoriously kinetically facile reaction, requiring researchers who study competing aqueous reactions like carbon dioxide reduction to carefully select catalysts that inhibit hydrogen evolution and even manipulate the reaction kinetics on those surfaces further via specific mesostructures.[23,24] Alternatively, organic solvents

---

[21] Schmittinger, P.; Florkiewicz, T.; Curlin, L. C.; Lüke, B.; Scannell, R.; Navin, T.; Zelfel, E.; Bartsch, R. *Ullmann's Encyclopedia of Industrial Chemistry*; Wiley-VCH: Weinheim, Germany, 2012; Vol. 8, pp 531–622.

[22] Frank, W. B.; Haupin, W. E.; Vogt, H.; Bruno, M.; Thonstad, J.; Dawless, R. K.; Kvande, H.; Taiwo, O. A. *Ullmann's Encyclopedia of Industrial Chemistry*; Wiley-VCH: Weinheim, Germany, 2012; Vol. 2, pp 483–520.

[11] *CRC Handbook of Chemistry and Physics*, 103rd ed.; Rumble, J. R., Ed.; CRC Press: Ohio, 2023.

[23] Hall, A. S.; Yoon, Y.; Wuttig, A.; Surendranath, Y. *J. Am. Chem. Soc.* **2015**, *137* (47), 14834–14837.

[24] Yoon, Y.; Hall, A. S.; Surendranath, Y. *Angew. Chemie - Int. Ed.* **2016**, *55* (49), 15282–15286.

are sometimes utilized as electrolytes to reduce the concentration of protons in solution,[25] but this approach would be particularly problematic for the question of phosphate reduction. Because phosphates are polyanionic (PO_4^{3-}), they exert a stronger electrostatic force on other ions in solution, which scales via the product of charges, relative to monoanions. This ionic bond renders polyanions difficult to solvate in organic media, since solvation requires these bonds to be comparable to or weaker than the bonds between the dissociated ions and the solvent. Researchers can theoretically overcome this solubility issue via ion exchange with bulky organic cations, such as tetrabutylammonium or imidazolium-based cations,[26] but because the reduction reaction requires stoichiometric consumption of the cation-paired phosphates, the consumption volume of specialized cations would be prohibitively costly. Additionally, these cations are mainly effective at solvating anions because of their incredible organic bulk, but that same bulk would introduce severe steric limitations on any reactant which could potentially accept oxides from the phosphate. Elias, Costentin and Nocera, for example, require triaryl borate to act as a Lewis acid to reduce triphenylphosphine oxide (P^{5+}) to triphenylphosphine (P^{3+}) in solvent,[27] but triphenylphosphine oxide is already a neutral species and, therefore, has an exposed oxide. In contrast, even if the cost of bulky reagents were negligible, tetrabutylammonium-solvated phosphates would require a bulky oxide-active acid such as triaryl borate to penetrate through a large mass of closely-associated tetrabutylammonium ions to bind to oxides. As a result, the same factors which inhibit the competing hydrogen evolution reaction in organic media would also prevent the phosphate reduction reaction from proceeding kinetically. Finally, even if elemental phosphorus is produced in either aqueous or organic room-temperature electrolytes, its melting point of 44.1 °C, boiling point of 280.5 °C[11] and negligible solubility in almost all solvents outside of toluene and carbon disulfide[28] would cause the product to act as an insulating solid or oily coating, preventing further passage of current. Thus, the ideal solvent for the reduction of phosphates would be a high-temperature, highly ionic and completely aprotic solvent—in other words, a molten salt.

Molten salts sport several properties which make them the ideal medium for the electrolysis of phosphates. Firstly, molten salts have inherently high conductivity due to their entirely ionic composition as a liquid.[29] As a result, these systems do not require supporting electrolytes, which could potentially interfere with the chemistry of the reduction and oxidation reactions. Secondly, the melt sports strongly localized ionic charges, which makes it ideal for dissolving compounds like phosphates. Additionally, alkali metal cations have notoriously negative reduction potentials even in molten salts,[30] so phosphates would likely be reduced before the cations in a molten salt, unlike the competition protons present for reduction in aqueous media. Because of these collective traits, molten salt electrolytes present a valuable answer to the problems raised by the question of electrochemical phosphate reduction. In fact, industry runs the Hall-Héroult process for aluminum production in molten cryolite (Na_3AlF_6) for this reason; the lack of other chemical species competing for reduction allows for the production of aluminum metal with high selectivity.[22] Molten salts are also being explored for the decarbonization of other media with great

[25] Yoon, Y.; Yan, B.; Surendranath, Y. *J. Am. Chem. Soc.* **2018**, *140* (7), 2397–2400.
[26] Das, P.; Jana, N. R. *ACS Appl. Mater. Interfaces* **2016**, *8* (13), 8710–8720.
[27] Elias, J. S.; Costentin, C.; Nocera, D. G. *J. Am. Chem. Soc.* **2018**, *140* (42), 13711–13718.
[28] Brummer, J. R.; Keely, J. A.; Munday, T. F.; FMC Corporation. *Kirk-Othmer Encyclopedia of Chemical Technology*; John Wiley & Sons, 2005; Vol. 18.
[29] Ubbelohde, A. R. In *Ionic Liquids*; Inman, D., Lovering, D. G., Eds.; Plenum: New York, 1981; pp 1–6.
[30] Scordilis-Kelley, C.; Fuller, J.; Carlin, R. T.; Wilkes, J. S. *J. Electrochem. Soc.* **1992**, *139* (3), 694–699.

success, such as the electrochemical production of iron[31,32] and other metals[33] from molten oxides. In fact, a recent study by Yang and Nohira has attempted to use molten calcium chlorides as a medium for solubilizing and reducing calcium phosphate.[34] Although the authors do not quantify their products, they are able to identify red phosphorus deposits in their cell, and identify a cathode voltage of 2.25 V vs. the chlorine evolution couple Cl_2/Cl^- (as measured via a Ag^+/Ag reference electrode). While this approach is promising, the authors acknowledge that the reaction should generate calcium oxide, the removal of which will constitute a challenge. Additionally, the solubility of calcium phosphates in the calcium chloride melt is low, limiting the operational current density to an unstable maximum of 100 mA cm^{-2}, and this solubility can only be increased by increasing operating temperatures significantly.[35] Finally, the voltage of the reduction is rather high, since the melt does not have an intrinsic oxide acceptor. Thus, such a system offers less room for innovation than other molten salt systems with the potential for phosphate reduction.

In contrast, a class of molten salts, molten polyphosphates (**Figure 1-1**), presents several key benefits over the calcium chloride system. Firstly, because the melt is composed entirely of phosphate-containing cation salts, the concentration of reducible species is very high, which, in theory, should translate to high current densities. Secondly, the melt contains a high concentration of acidic phosphoryl anhydride linkages ([P-O-P] bonds), so called because polyphosphates are derived from the dehydration of sodium phosphoric acids.[36] These bonds are direct analogs to the silicon oxide bonds in the carbothermal reduction process, and should be able to readily accept oxides that are released during the reduction of phosphates. Thirdly, phosphorus and oxides could theoretically be fed into the system through the dehydration of phosphoric acid derived from the wet process. This phosphoric acid derives from the reaction of phosphate rock with sulfuric acid,[37] a readily-available material which is already made on a much larger scale than white phosphorus due to the demand for fertilizer-grade phosphates, and is not sourced from oxidized P_4 like pure but thermally-derived phosphorus pentoxide.[38]

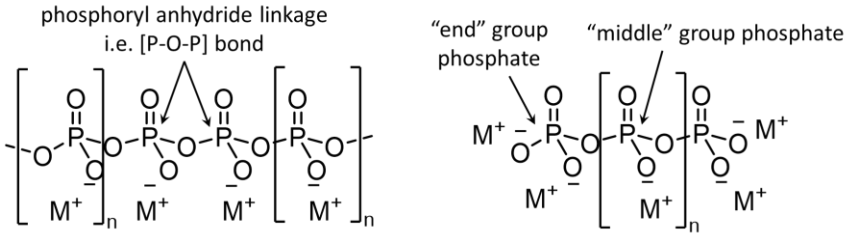

***Figure 1-1**. (left) Diagram of a general polyphosphate chain polyanion paired with alkali metal cations (M+), with a phosphoryl anhydride linkage indicated. (right) Diagram indicating the "middle" and "end" groups of a polyphosphate chain.*

Thus, the net reaction scheme envisioned would proceed as follows (**Figure 1-2**):

[31] Allanore, A. *J. Electrochem. Soc.* **2015**, *162* (1), E13–E22.
[32] Caldwell, A. H.; Lai, E.; Gmitter, A. J.; Allanore, A. *Electrochim. Acta* **2016**, *219*, 178–186.
[33] Martín Treceño, S.; Allanore, A.; Bishop, C. M.; Marshall, A. T.; Watson, M. J. *J. Mater.* **2021**, *73* (6), 1899–1908.
[34] Yang, X.; Nohira, T. *ACS Sustain. Chem. Eng.* **2020**, *8* (36), 13784–13792.
[35] Zhong, Y.; Yang, X. *Metall. Mater. Trans. B Process Metall. Mater. Process. Sci.* **2021**, *52* (5), 3515–3523.
[36] Sorrell, T. N. In *Organic Chemistry*; Castellion, M., Ed.; University Science Books: California, 2006; pp 953–988.
[37] Havelange, S.; Lierde, N.; Germeau, A.; Martins, E.; Theys, T.; Sonveaux, M.; Toussaint, C.; Schrödter, K.; Bettermann, G.; Staffel, T.; Wahl, F.; Klein, T.; Hofmann, T. *Ullmann's Encyclopedia of Industrial Chemistry*; Wiley-VCH, 2022; pp 1–55.
[38] Bettermann, G.; Krause, W.; Riess, G.; Hofmann, T. *Ullmann's Encyclopedia of Industrial Chemistry*; Wiley-VCH, 2012; Vol. 27.

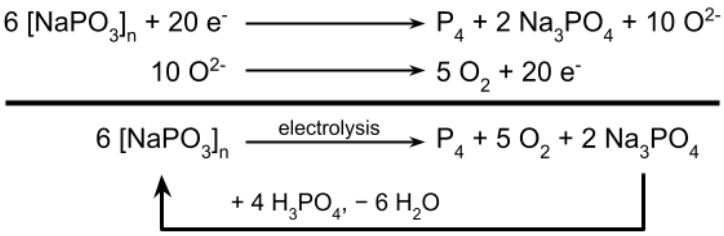

***Figure 1-2**. Overall scheme for a hypothetical electrolysis process of sodium polyphosphate. The top equation indicates the cathodic reduction of polyphosphate to white phosphorus accompanied by the release of oxides, while the second equation indicates the anodic oxidation of oxides in the melt to elemental oxygen. The bottom equation shows the net reaction of the cell, while the connecting arrow indicates how the addition and dehydration of phosphoric acid to the system could restore the melt to its original properties.*

Researchers have, in fact, studied the electrolysis of molten sodium metaphosphate since the early 1930s,[39] proceeding until the late 1970s until the rate of new studies declined substantially. A particularly valuable summary of this body of work can be found in Bard's Encyclopedia of the Elements in Volume X: Electrochemistry of Fused Salt Systems.[40] We attribute the decline in interest in the subject following the 1970s to a combination of factors: 1) the lack of an environmental impetus to decarbonize industrial processes during a period where energy and fuel were comparatively cheaper, 2) the fact that phosphate can be reduced carbothermally, as opposed to processes like aluminum production where chemical means of reduction were unviable, 3) the enormous difficulty of taking delicate and precise electrochemical measurements in a highly hot, highly corrosive system, and 4) the lack of accessibility to the characterization technologies needed to easily identify products. Despite the length of time since the initial discovery, however, the literature of polyphosphate electrolysis remains mired in uncertainty. By taking a fresh look at the field of polyphosphate electrolysis, we have identified fillable knowledge gaps that can best expand our knowledge of the reduction and oxidation reactions, as well as the nature of polyphosphate electrolytes themselves.

1.2: MOLTEN POLYPHOSPHATES: NOMENCLATURE, PROPERTIES, AND KNOWLEDGE GAPS

Although some properties of molten polyphosphate salts are known, the current state of the literature presents a plethora of significant knowledge gaps that leave rich opportunities for further discoveries. Although sodium is the most commonly studied salt of metaphosphate, with a melting point of 629 °C, other salts have been studied, like $LiPO_3$-KPO_3, which has a melting point of 518 °C.[41] Sodium polyphosphates, the most common polyphosphate salts studied in molten form, are very commonly represented in the literature as a ratio of the constituent compounds sodium oxide (Na_2O) and phosphorus pentoxide (P_2O_5).[42] According to this notation, sodium metaphosphates ($(NaPO_3)_n$), which exist as polyphosphate chains of anhydride bonds in rings of varying sizes, would be described as a Na_2O : P_2O_5 ratio of 1. Sodium polyphosphates (linear polyphosphate chains of specific lengths which end in terminating $–O–PO_3^{2-}$ groups), in contrast, result from an increased Na_2O : P_2O_5 ratio which can range anywhere from just over 1 to a value of 1.667, corresponding to the shortest polyphosphate, sodium tripolyphosphate ($Na_5P_3O_{10}$). Increasing the Na_2O : P_2O_5 ratio further would result in the creation of sodium pyrophosphate ($Na_4P_2O_7$) (Na_2O : P_2O_5 = 2) and eventually sodium orthophosphate or tribasic

[39] Centnerzwer, M.; Szper, J. *Bull. Polish Acad. Sci.* **1931**, 364–368.
[40] *Encyclopedia of Electrochemistry of the Elements*; Bard, A. J., Ed.; Marcel Dekker: New York, 1976; Vol. X, pp 373–388.
[41] Caton, R. D.; Freund, H. *Anal. Chem.* **1963**, *35* (13), 2103–2108.
[42] Van Wazer, J. R. In *Phosphorus and its Compounds, Vol. I*; Interscience: New York, 1958; pp 717–800.

sodium phosphate ($Na_2O : P_2O_5 = 3$). **Figure 1-4** shows an example of how changing this ratio affects the composition of "end" and "middle" groups in the melt to produce chains of varying lengths. Although this ratio can be decreased below 1, the result would a class of reactive materials called ultraphosphates (phosphate chains containing branching groups). While physically attainable, these materials are extremely viscous due to their cross-linking, ranging from 70 to 500 poise, and react rapidly with moisture to hydrolyze and form a protic melt.[43] These structures are very reactive within the melt as well, and, as a result, have not been seen as a condensation product from cooled metaphosphate melts.[44]

Likewise, the range of $Na_2O : P_2O_5$ ratios accessible in polyphosphate melts is highly dependent on operating temperature. The melting point of polyphosphate salts increases as chain length decreases,[45] and, as the phase diagram of the $Na_2O : P_2O_5$ compositional space demonstrates (**Figure 1-3**), cooled melts precipitate out either sodium metaphosphate or sodium tripolyphosphate until a eutectic composition is reached.[42,46] The reorganization of polyphosphates at temperature means that the chain length of a given premelted polyphosphate system is not fixed, but, rather, obeys a statistical distribution.[42]

[43] Griffith, E. J.; Callis, C. F. *J. Am. Chem. Soc.* **1959**, *81* (4), 833–836.
[44] Van Wazer, J. R. *J. Am. Chem. Soc.* **1950**, *72* (2), 644–647.
[45] Van Wazer, J. R. In *Phosphorus and its Compounds, Vol. I*; Interscience: New York, 1958; pp 601–678.
[46] Greenfield, S.; Clift, M. *Analytical Chemistry of the Condensed Phosphates*; Pergamon: Oxford, 1975.

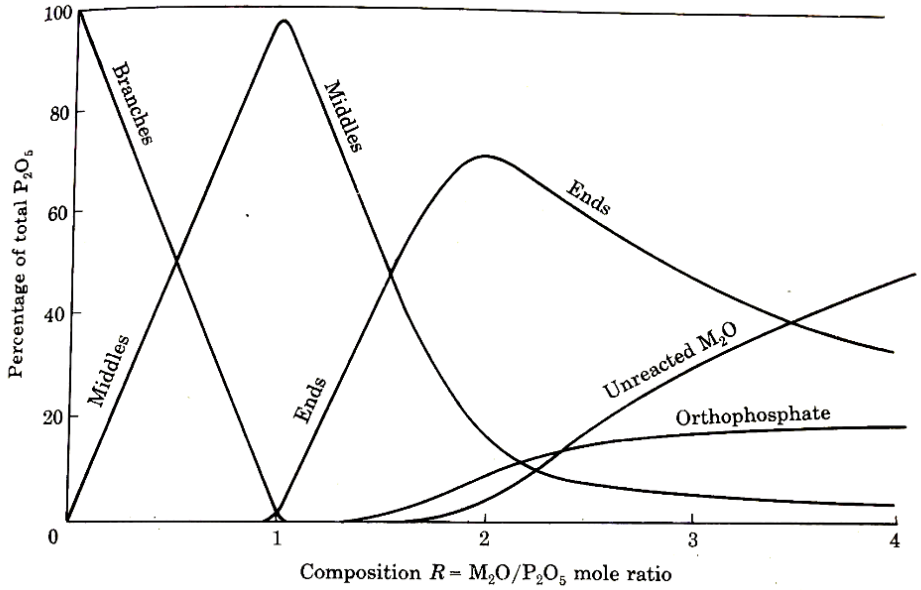

***Figure 1-3**. A hypothetical curve showing relative proportions of branches, middles and orthophosphate and unreacted M_2O as a function of the M_2O/P_2O_5 mole ratio. Reproduced from Van Wazer, J. R. In* Phosphorus and its Compounds, Vol. I*; Interscience: New York, 1958; pp 731.*[42]

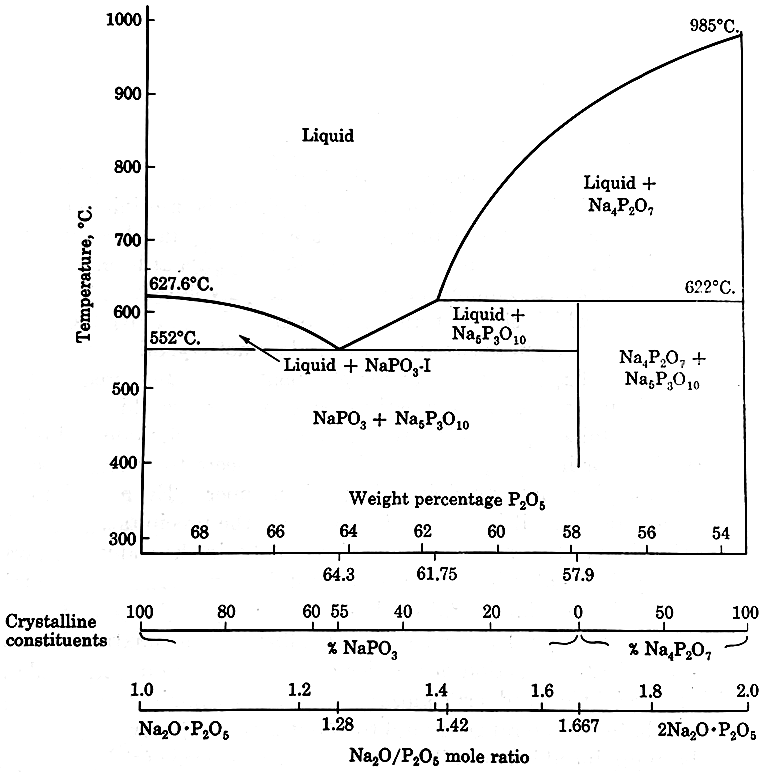

***Figure 1-4**. The sodium phosphate phase diagram between $Na_2O \cdot P_2O_5$ and $2Na_2O \cdot P_2O_5$. Reproduced from Van Wazer, J. R. In* Phosphorus and its Compounds, Vol. I*; Interscience: New York, 1958; pp 604.*[42]

Although authors in the field almost exclusively report their phosphate compositions as $Na_2O : P_2O_5$ ratios, several of these authors have simultaneously criticized the practice of using $Na_2O : P_2O_5$ ratios as nomenclature. The most commonly cited argument against this description is the observation that Na_2O (a strong Lewis base) and P_2O_5 (a strong Lewis acid) react strongly exothermically when combined.[47,48] Additionally, as described above, the cooled products of molten polyphosphate melts have been rigorously characterized via chromatography and spectroscopy, and these products invariably consist of a mixture of meta- and polyphosphates. Taken together, these data do, indeed, heavily imply that Na_2O and P_2O_5 are unlikely to exist in segregated forms in the melt.[42] Such an approach is similar in nature to attempting to describe aqueous solutions as a molar ratio of hydroxide (OH^-) to hydronium (H_3O^+) instead of the far more meaningful and descriptive metric of pH. However, despite the large bearing that melt composition displays on its electrochemical properties and the failure of the current nomenclature to accurately describe the system, no authors have, hitherto, proposed an alternative means of describing polyphosphate composition.

In response to this discourse, we have adopted the practice of describing melts via the concentration of phosphoryl anhydride ([P–O–P]) bonds within the polyphosphate melt. This nomenclature is particularly appealing because it remains descriptive of the system irrespective of the specific chemical composition the melt ultimately takes on. Any starting mixture of meta-, poly-, pyro- and orthophosphates will contain a fixed number of [P–O–P] linkages, and that number will remain constant even if the system composition changes during melting or cooling. This conservation of [P–O–P] bonds exists because, whenever a phosphate group reacts as a base to cleave a [P–O–P] linkage, a new [P–O–P] linkage will result from that reaction. This [P–O–P] composition only changes when chemical species are introduced to the system which cleave or form additional anhydride bonds. Such reactions can be phenomenologically abstracted using the Lux-Flood definition of bases as oxide ion donors and acids as oxide ion acceptors.[49–51] Under this framework, oxide ions in molten salts or other media react with acceptor groups to neutralize them;[52] [P–O–P] linkages, for example, cleave in the presence of oxides and form terminal phosphate groups on both resulting species. Shams El Din and Gerges[53] directly demonstrate this principle via a potentiometric titration of sodium oxide into metaphosphate solvated in potassium nitrate at 350 °C. As the authors add oxide to the buffered molten solution, the potential of a sensory O^{2-}/ O_2 electrode remains stable until the metaphosphate concentration depletes and a precipitous potential drop occurs. Using this method, the authors estimate the equilibrium constant of the acid-base reaction $2\ PO_3^- + O^{2-} = P_2O_7^{4-}$ at an astonishing value of $K = 3.1 \times 10^{15}$, indicating that cleavage of [P–O–P] bonds in this medium is heavily favored.

[42] Van Wazer, J. R. In *Phosphorus and its Compounds, Vol. I*; Interscience: New York, 1958; pp 717–800.
[47] Casey, E. J.; Dubois, A. R. *Can. J. Chem.* **1971**, *49*, 2733–2745.
[48] Andreeva, V. N. *Ukr. Khim. Zh.* **1955**, *21*, 569.
[49] Lux, H. *Zeitschrift für Elektrochemie und Angew. Phys. Chemie* **1949**, *45* (1), 41–43.
[50] Flood, H.; Förland, T. *Acta Chem. Scand.* **1947**, *1* (6), 592–604.
[51] Drago, R. S.; Whitten, K. W. *Inorg. Chem.* **1966**, *5* (4), 677–682.
[52] El Hosary, A. A.; Kerridge, D. H.; Shams El Din, A. M. In *Ionic Liquids*; Inman, D., Lovering, D. G., Eds.; Plenum: New York, 1981; pp 339–362.
[53] Shams El Din, A. M.; Gerges, A. A. A. *Electrochim. Acta* **1964**, *9*, 613–627.

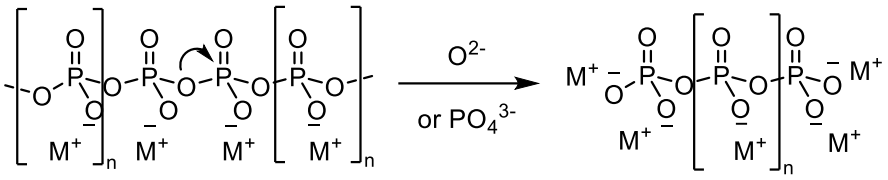

***Figure 1-5**. Depiction of a metaphosphate chain / [P–O–P] bond (a Lux acid) reacting in the molten phase with oxides or orthophosphates (Lux bases) to form shorter-chain polyphosphates.*

Thus, phosphoryl anhydride linkages represent the prevailing Lux acid moieties within the system. A melt with a high concentration of [P–O–P] linkages, such as metaphosphates and long-chain polyphosphates, will react as an acidic medium with oxides. Analogously, melts with low [P–O–P] concentrations will display more basic properties. While we would generally prefer to use a volumetric concentration (molarity), the melt density changes as a function of both temperature and composition, which would result in an entirely new lack of clarity in the literature. Thus, reporting this concentration as a molality (moles [P–O–P] kg^{-1} of melt) supports easier reproducibility. Under this scheme, pure sodium metaphosphate represents a molality of 9.81 mol kg^{-1} [P–O–P], with the extreme of sodium tripolyphosphate manifesting in a molality of 5.43 mol kg^{-1} [P–O–P]. In summary, phosphoryl anhydride molality functions as an intuitive and unambiguous representation of the acidity of a polyphosphate melt while remaining agnostic towards the chemical speciation of that melt.

This metric also preserves the accessibility of previous literature because a) P_2O_5 is simply the reduced empirical formula for phosphorus pentoxide (P_4O_{10}), a compound with six anhydride bonds, and b) Na_2O, as an oxide donor, has the capacity to cleave one anhydride bond. Thus, a researcher in this field can quickly convert any reported Na_2O : P_2O_5 molar ratio r into an anhydride molality using the following formula (Equation 4):

$$m\ (\text{mol [P–O–P] kg}^{-1}) = \frac{3 * (1\ \text{mole P}_2\text{O}_5) - 1 * (r\ \text{moles Na}_2\text{O})}{0.1419445\ \text{kg} * (1\ \text{mole P}_2\text{O}_5) + 0.0619789\ \text{kg} * (r\ \text{moles Na}_2\text{O})}$$

$$= \frac{3-r}{0.0619789r+0.1419445}\ \text{mol [P–O–P] kg}^{-1} \quad (4)$$

Researchers studying molten polyphosphate systems most commonly work in pure metaphosphate (9.81 mol kg^{-1} [P–O–P]) due to its homogeneity and availability. However, several researchers have explored a wider range within the anhydride concentration space. **Table 1-1** shows the interconversion of selected Na_2O : P_2O_5 molar ratios to phosphoryl anhydride molalities, as well as average polyphosphate chain length of these melts and, lastly, the molar percentage of Na_3PO_4 in sodium trimetaphosphate $Na_3(PO_3)_3$ required to experimentally replicate these melt compositions.

$Na_2O : P_2O_5$ ratio	mol kg^{-1} [P–O–P]	Average polyphosphate chain length	% Na_3PO_4 in $Na_3(PO_3)_3$
1	9.81	∞	0
1.15	8.68	13.3	20
1.2	8.32	10	25
1.28	7.77	7.1	33
1.36	7.25	5.6	40
1.5	6.39	4	50
1.667	5.43	3	60

Table 1-1. *Commonly-reported $Na_2O : P_2O_5$ molar ratios, their corresponding phosphoryl anhydride molalities (mol kg^{-1} [P–O–P]), the melt's average polyphosphate chain length, and the experimental percentage of sodium orthophosphate in sodium trimetaphosphate required to make these melts.*

Because of the high temperatures required to melt sodium polyphosphates, *in situ* characterization of polyphosphate melts is extremely difficult and such topics are often the subject of speculation. Although the salt can be cooled and analyzed easily at room temperature via NMR techniques or chromatography,[46] these structures are not necessarily reflective of high-temperature, molten conditions. The evidence that polyphosphates can rapidly restructure from certain compositions into others upon melting and rapid cooling[46] testifies to an environment in which bonds between phosphate tetrahedra are fluid and less rigidly defined. For convenience, many researchers attempting to describe chemical or electrochemical reactions in the melt represent phosphates as orthophosphate, PO_4^{3-}, but heavy debate surrounds the question of whether such phosphate species truly exist in the melt as orthophosphate. While some researchers use the species PO_4^{3-} in electrochemical equations without much comment[41,49,53–55] or refrain from using the nomenclature altogether in favor of descriptors like PO_3^- and O^{2-},[39,56–58] others[59,60] actively argue that orthophosphate is present in substantial quantities in metaphosphates. Indeed, using a comparison between the electrochemistry of phosphates suspended in molten chlorides, one study by Franks and Inman even argues that the concentration of the purportedly spontaneously-forming orthophosphate dictates the rate of the electrochemical reaction at the cathodic solvent window.[60] However, these arguments presuppose that, because a system of phosphate salts dosed into molten chlorides exhibits an onset of electrolysis current at a specific voltage, that same chemical species must also be the origin of a current onset of similar voltage in a different system, pure molten sodium metaphosphate. Firstly, such an argument assumes that the solvation energy of the molten reactants and products in the two media is identical, which is not typically the case when a solvent in an electrochemical

[39] Centnerzwer, M.; Szper, J. *Bull. Polish Acad. Sci.* **1931**, 364–368.
[41] Caton, R. D.; Freund, H. *Anal. Chem.* **1963**, *35* (13), 2103–2108.
[46] Greenfield, S.; Clift, M. *Analytical Chemistry of the Condensed Phosphates*; Pergamon: Oxford, 1975.
[49] Lux, H. *Zeitschrift für Elektrochemie und Angew. Phys. Chemie* **1949**, *45* (1), 41–43.
[54] Gruber, B. A. US2965552A, 1960.
[55] Yocom, P. N. University of Illinois, 1958.
[56] Casey, E. J.; Dubois, A. R.; Gorman, R. W. In *Corrosion*; 1975; Vol. 31, pp 358–363.
[57] Andreeva, V. N.; Delimarskii, Y. K. *Zh. Neorg. Khim.* **1960**, *5* (9), 1008–1011.
[58] Laitinen, H. A.; Lucas, K. R. *J. Electroanal. Chem.* **1966**, *12*, 553–563.
[59] Franks, E.; Inman, D. *J. Electroanal. Chem.* **1970**, *26*, 13–26.
[60] Franks, E.; Inman, D. *J. Appl. Electrochem.* **1971**, *14*, 73–78.

reaction is changed.[30] This argument also assumes that all observed voltage limitations in the system result from the working electrode, but the authors'[59,60] cell design is a two-electrode system where the crucible acts as the counter electrode. Although the surface area of the counter electrode is, indeed, much larger, one would expect the oxidative counter reaction to be vastly different between a chloride melt, where chlorides constitute the most concentrated species, and a polyphosphate melt, where oxides are much more prevalent. Finally, from first principles, polyphosphate chains are more reactive and labile due to their ability to eject stabilized phosphate or polyphosphate groups. Nature uses this behavior to power many uphill cellular processes, such as iron uptake, through the cleavage of the phosphoryl anhydride linkages in adenosine triphosphate (ATP).[61] Since phosphate reduction necessarily requires bond cleavage, one would reasonably expect phosphate groups within metaphosphate chains—which are abundant in the authors' system—to be electrochemically reduced at a substantially lower voltage than a free orthophosphate tetrahedron. Given these important caveats, we do not believe that the authors' specific claim of electrochemically-active orthophosphates forming in the melt is particularly credible. Rather, the reactivity of orthophosphate with metaphosphate to form shorter-chain polyphosphates suggests to us that most phosphate groups in the melt exist as "middle" or "end" groups within polyphosphate chains, and that the concentration of free orthophosphate Na_3PO_4 is either negligible or nonexistent, as will be discussed later in Chapter 2.

Regardless of specific controversies like proper nomenclature and the question of orthophosphate's role in the melt, most researchers in molten metaphosphates agree on several basic principles. Firstly, phosphate-phosphate bonds within polyphosphate melts rapidly break and form, causing the melt to chemically reorganize at temperature.[42] Secondly, molten metaphosphates and polyphosphates are highly viscous,[42,47] requiring elevated temperatures to circumvent electrochemical transport limitations. Thirdly, molten polyphosphates are highly corrosive media, attacking many conventional electrode and container materials under the right conditions.[56] Fourthly, changing the melt's acidity via adjusting the melt's composition or dissolving in metal oxides leads to changes in equilibrium voltage and kinetic current-voltage profiles.[56,57,62,63] And finally, these aforementioned properties of the melt make it difficult to reproducibly extract electrochemical information from polyphosphate systems.[58,60] Unfortunately, given the current state of instrumentation, most conventional spectroscopic techniques cannot glean much information from molten salt systems at temperature due to the corrosive nature of these electrolytes, the damage inflicted by high temperatures or the convolution that thermal noise would present on the collected data. Some high-temperature characterization techniques, such as high-temperature NMR on molten beads, do exist, but these systems are very uncommon and expensive, and present their own challenges for data interpretation.[64] Therefore, until these niche characterization techniques become more accessible, or existing widespread techniques become substantially more

[30] Scordilis-Kelley, C.; Fuller, J.; Carlin, R. T.; Wilkes, J. S. *J. Electrochem. Soc.* **1992**, *139* (3), 694–699.
[42] Van Wazer, J. R. In *Phosphorus and its Compounds, Vol. I*; Interscience: New York, 1958; pp 717–800.
[56] Casey, E. J.; Dubois, A. R.; Gorman, R. W. In *Corrosion*; 1975; Vol. 31, pp 358–363.
[57] Andreeva, V. N.; Delimarskii, Y. K. *Zh. Neorg. Khim.* **1960**, *5* (9), 1008–1011.
[58] Laitinen, H. A.; Lucas, K. R. *J. Electroanal. Chem.* **1966**, *12*, 553–563.
[59] Franks, E.; Inman, D. *J. Electroanal. Chem.* **1970**, *26*, 13–26.
[60] Franks, E.; Inman, D. *J. Appl. Electrochem.* **1971**, *14*, 73–78.
[61] Lippard, S. J.; Berg, J. M. In *Principles of Bioinorganic Chemistry*; University Science Books: Mill Valley, CA, 1994; pp 103–137.
[62] Delimarskii, Y. K.; Andreeva, V. N. *Zh. Neorg. Khim.* **1960**, *5* (5), 540–542.
[63] Delimarskii, Y. K.; Andreeva, V. N. *Zh. Neorg. Khim.* **1960**, *5* (8), 873–876.
[64] Stebbins, J. F. *Chem. Rev.* **1991**, *91* (7), 1353–1373.

robust, electrochemical studies present one of the few means of gaining insight into molten polyphosphate systems.

1.3: ELECTROCHEMICAL REDUCTION OF PHOSPHATES: LITERATURE AND KNOWELDGE GAPS

The cathodic reduction of polyphosphate melts, which would be the lynchpin for an electrolytic production of white phosphorus in these media, has been the focus of studies for roughly 90 years which still leave much unknown to this day. One of the most consistent observations by researchers is the generation of a flammable gas as a major product at the reductive solvent window of molten polyphosphates.[40] This gas has been qualitatively attributed as elemental white phosphorus by researchers as early as 1931.[39] However, the literature presents this claim either without accompanying analytical evidence[54,59,60] or merely by characterizing the solid-phase reaction products between this gas with other media.[55,56,58] For instance, some researchers have analyzed and worked up the combustion products of the produced gas to identify the presence of phosphates,[55] while others have identified red phosphorus deposits which sublime off electrode surfaces at operating temperatures.[47] While these data make a compelling case for white phosphorus as the flammable gas's identity, they fail to completely exclude other potential products such as sodium phosphide, Na_3P, or phosphine gas, PH_3, which trace moisture could generate. Additionally, even if white phosphorus, P_4, is ultimately the gaseous product, it may not necessarily evolve from the cathode surface in that form. At 800 °C, for instance, gaseous P_4 exists in a minor equilibrium with diphosphorus gas, P_2.[7] Thus, one might reasonably envision a mechanism where, at temperature, reduced elemental phosphorus evolves from the counter electrode as diatomic P_2 and then rapidly self-dimerizes to form the more common P_4 tetrahedra. Additionally, questions also remain regarding the existence, if any, of solution-side cathodic products. While some researchers do not report any solution-phase products,[59,60] others report the formation of visible product layers around the electrode surface.[41,47,58] One study found layers of red phosphorus suspended in the melt around a graphite electrode when the system was electrolyzed at high voltages,[55] while others attributed layers formed on platinum or tungsten electrodes to platinum and tungsten phosphides via XRD analysis.[47,58] In brief, researchers have yet to adequately identify the major cathodic product or products, and the identity and distribution of these products may also depend on the voltage conditions and cathode material.

In addition to the reduction reaction's products, deep ambiguities also surround the cathode reaction's electrokinetics and mechanism. The challenges encountered by most electrochemists when investigating this medium are primarily twofold: 1) the lack of a robust, reproducible reference electrode, and 2) the deterioration, passivation or transport limitations experienced by the working electrode surface. As mentioned previously, molten metaphosphates are a particularly corrosive medium due to

---

[7] Diskowski, H.; Hofmann, T. *Ullmann's Encyclopedia of Industrial Chemistry*; Wiley-VCH: Weinheim, Germany, 2012; Vol. 26, pp 725–746.
[39] Centnerzwer, M.; Szper, J. *Bull. Polish Acad. Sci.* **1931**, 364–368.
[40] *Encyclopedia of Electrochemistry of the Elements*; Bard, A. J., Ed.; Marcel Dekker: New York, 1976; Vol. X, pp 373–388.
[41] Caton, R. D.; Freund, H. *Anal. Chem.* **1963**, *35* (13), 2103–2108.
[47] Casey, E. J.; Dubois, A. R. *Can. J. Chem.* **1971**, *49*, 2733–2745.
[54] Gruber, B. A. US2965552A, 1960.
[55] Yocom, P. N. University of Illinois, 1958.
[56] Casey, E. J.; Dubois, A. R.; Gorman, R. W. In *Corrosion*; 1975; Vol. 31, pp 358–363.
[58] Laitinen, H. A.; Lucas, K. R. *J. Electroanal. Chem.* **1966**, *12*, 553–563.
[59] Franks, E.; Inman, D. *J. Electroanal. Chem.* **1970**, *26*, 13–26.
[60] Franks, E.; Inman, D. *J. Appl. Electrochem.* **1971**, *14*, 73–78.

their Lux acid-derived reactivity towards oxides. As a result, the melt rapidly attacks and dissolves porous frits—one of the most common ways electrochemists separate electrolytes of different compositions to create reference electrodes. Molten polyphosphates even corrode some of the most thermodynamically stable ceramics, such as aluminum oxides; aluminum-sodium polyphosphate glasses constitute an entire materials space with enhanced water resistance relative to pure sodium polyphosphate glasses.[42] While some researchers employ fritted reference electrodes, such as Ag(I)/Ag[58,6566] or Pt(II)/Pt,[58] these membranes are only semi-stable at temperatures very close to the melting point of molten polyphosphates, where viscosity-related transport limitations confound electrochemical data. As a result, most researchers opt to either a) perform electrochemical measurements in a two-electrode cell, relying on the smaller surface area of the working electrode to dominate reactions,[55,59,60] or b) attempt to pin a platinum electrode to a O_2/O^{2-} couple by flowing oxygen through a platinum needle[57,62,63] or polarizing an auxiliary electrode at a fixed anodic current.[47,56] However, under such setups, the relative electrode sizes, geometries and configuration should all theoretically influence the observed voltages, which may partly explain the literature's reproducibility issues. Reference electrodes underpin all assumptions regarding the energy of the working electrode reaction, so a reproducible and robust reference electrode system would constitute a major breakthrough in the study of molten metaphosphates.

However, even within the context of individual studies which feature a consistent electrochemical reference scheme, many authors report reproducibility issues in molten polyphosphates associated with electrode surface instability. Laitinen and Lucas, for instance, report that polarization curves of sodium trimetaphosphate dissolved in a chloride eutectic suffer from poor reproducibility on platinum electrodes.[58] The authors report the formation of grey films on their platinum cathodes, which, through XRD, they attribute to platinum phosphide (PtP_x). Similarly, Casey and Dubois, who operate in pure molten sodium metaphosphate, appear to lack much control over the reduction reaction on metal substrates.[47] Their operating temperatures of 650 °C is close to the melting point of metaphosphate, so mass transport limitations are expectedly significant. However, they also report the formation of films on their platinum cathodes that limit charge passage—even the highest current densities they report for the reduction reaction are 10 mA cm^{-2}, whereas industry runs the comparable molten salt electrolysis of alumina at current densities of 1 A cm^{-2}.[66] The authors observe the formation of this grey film visually and examine it under XRD, and, like Laitinen and Lucas, they attribute the observed signals to platinum phosphides PtP_x. Instead of traditional steady-state analysis of the reaction, therefore, the authors are forced to interrogate the reaction through low-current density potential drift experiments, potential decay experiments and reverse-polarization charge recovery. Interestingly, although the authors do not identify the presence of sodium metal via spectroscopy, they attribute the charging process in the cathodic

[42] Van Wazer, J. R. In *Phosphorus and its Compounds, Vol. I*; Interscience: New York, 1958; pp 717–800.
[47] Casey, E. J.; Dubois, A. R. *Can. J. Chem.* **1971**, *49*, 2733–2745.
[56] Casey, E. J.; Dubois, A. R.; Gorman, R. W. In *Corrosion*; 1975; Vol. 31, pp 358–363.
[57] Andreeva, V. N.; Delimarskii, Y. K. *Zh. Neorg. Khim.* **1960**, *5* (9), 1008–1011.
[58] Laitinen, H. A.; Lucas, K. R. *J. Electroanal. Chem.* **1966**, *12*, 553–563.
[59] Franks, E.; Inman, D. *J. Electroanal. Chem.* **1970**, *26*, 13–26.
[60] Franks, E.; Inman, D. *J. Appl. Electrochem.* **1971**, *14*, 73–78.
[62] Delimarskii, Y. K.; Andreeva, V. N. *Zh. Neorg. Khim.* **1960**, *5* (5), 540–542.
[63] Delimarskii, Y. K.; Andreeva, V. N. *Zh. Neorg. Khim.* **1960**, *5* (8), 873–876.
[65] Caton, R. D.; Wolfe, C. R. *Anal. Chem.* **1971**, *43* (6), 660–662.
[66]. Prasad, S. *J. Braz. Chem. Soc.* **2000**, *11* (3), 245–251.

polarization to the reduction of sodium ions reducing and forming an amalgam with the platinum electrode.

The question of whether the electrochemical reduction of phosphates passes through metallic sodium as an intermediate has been debated heavily in the literature. Regarding Casey and Dubois's claims, the reduction of sodium ions to sodium metals seems unlikely given the reduction reaction onsets at a mere 0.8 V from the oxygen evolution reference the authors use to pin currents. Although solvation environments change the reduction potentials of various species, the overwhelming gap between oxygen's reduction potential at 1.23 V and sodium's reduction potential at −2.71 V seems difficult to explain by solvation effects alone. Among the literature, Yocom seems to address the question of sodium generation most directly by investigating the possible absorption of reduced radioactive Na^{22} from molten radioactive sodium metaphosphate electrolyte into a lead pool molten cathode.[55] Even after passing enough charge to electrolyze 20% of the metaphosphate in the sample, the authors observe a negligible difference of 1 radiation count per minute between the electrolyzed lead pool and a control where no current was passed. By comparison, the radioactive sodium metaphosphate samples generated 10,000 counts per minute. These results suggest that sodium metal is not a significant product in the cathodic reduction. Thus, one might reasonably deduce that the polarizations Casey and Dubois attribute to sodium metal derive instead from the formation of reversible phosphide layers that insulate and limit current passage. Even Franks and Inman, who can operate at a higher temperature of 700 °C due to the lack of a reference electrode, are limited by observed transport effects.[59,60] At currents somewhere between 3 mA and 20 mA (42 to 283 mA cm^{-2} geometric area, assuming a perfectly flat surface), the potential of the 3 mm-diameter graphite disc begins to oscillate by a large margin, around 0.2 to 0.3 V. These variations force the authors to average most of their reported potentials. They report that increasing the melt's temperature from 660 to 810 °C increases the limiting current from 10 to 40 mA. However, since the 1-mm diameter tungsten wire is sheathed in alumina and silica glass, which is soluble in the metaphosphate, it is unlikely that the electrode remains perfectly sheathed by the sealant in the melt. Thus, assigning the electrode an area of 0.007 cm^2 and describing these currents as "1273 to 5092 mA cm^{-2}" would be a highly dubious aspersion. These potential fluctuations could be attributed to the evolution of gas bubbles,[67] which could make sense given that the electrodes employed in this study are sheathed. In fact, gas blockages are common industrial complications which raise operating voltages and intensify wear on electrodes, especially in systems where graphite is employed as a sacrificial anode; these processes are collectively referred to as "anode effects."[68] Thus, innovations in electrode identity and geometry may drastically increase the amount of information researchers can glean from the electrochemical reduction process.

[55] Yocom, P. N. University of Illinois, 1958.
[59] Franks, E.; Inman, D. *J. Electroanal. Chem.* **1970**, *26*, 13–26.
[60] Franks, E.; Inman, D. *J. Appl. Electrochem.* **1971**, *14*, 73–78.
[67] Wilson, S. D. R.; Hulme, A. *Proc. R. Soc. London, Ser. A Math. Phys. Sci.* **1983**, *387* (1792), 133–146.
[68] Tabereaux, A. T.; Peterson, R. D. In *Treatise on Process Metallurgy*; Elsevier: Oxford, 2014; Vol. 3, pp 839–917.

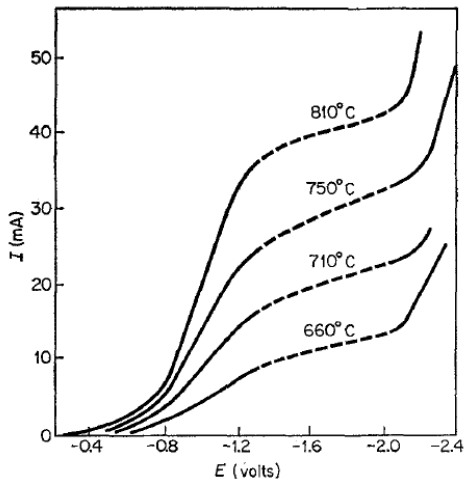

Figure 1-6. *Polarography of a 1-mm diameter tungsten wire in molten metaphosphate as a function of temperature. Voltages reported as a 2-electrode polarization between the wire and a graphite crucible counter electrode. Reproduced from Franks, E.; Inman, D. J. Appl. Electrochem. 1971, 14, 73–78.*[60]

Generally, electrokinetic information on a molten salt system is obtained through current-voltage analysis. For instance, cyclic voltammetry is commonly used to survey the approximate working electrode potentials at which reactions occur, as well as how these values deviate from predicted thermodynamic values.[69] This analysis is often coupled with steady-state electrokinetic analysis, where the relationship between current and voltage under mixed-control kinetics is observed to easily infer information about the ease of electron transfer and the nature of the rate-limiting state. However, when this electrochemical measurement process is convolved with reference electrode stability issues or orthogonal transport limitation issues, as is the case for polyphosphate electrolysis systems, researchers will find meaningful data collection to be nearly impossible.

Despite these challenges, researchers have historically employed several resourceful techniques with limited technology to attempt to interrogate the metaphosphate reduction process. Among these methods, one of the most intriguing is the use of current decay techniques to work around the absence of reliable current-voltage steady-state data. Both Laitinen and Lucas[58] and Franks and Inman[59,60] perform analysis around the transients observed in the cathode potentials after abruptly polarizing to diffusion-limited voltages. Under diffusion-limited conditions, the current density becomes almost entirely divorced from potential and is instead related to fundamental mass transport constants of the system. Thus, one can glean certain information about an electrochemical reaction, even if a reference electrode is unavailable or unreliable, by observing the transition time required for the current to stabilize to a fixed value (i.e. where the surface concentration of the reagent at the electrode first reaches zero). This value is related to the current through certain fundamental mass transport constants of the system via the Sand equation, an offshoot of the Cottrell equation.[70] The current density and transition time obeys the following relationship (Equation 5), where $j(\tau)$ is current density, n is the number of electrons involved in

[58] Laitinen, H. A.; Lucas, K. R. *J. Electroanal. Chem.* **1966**, *12*, 553–563.
[59] Franks, E.; Inman, D. *J. Electroanal. Chem.* **1970**, *26*, 13–26.
[60] Franks, E.; Inman, D. *J. Appl. Electrochem.* **1971**, *14*, 73–78.
[69] Bard, A. J.; Faulkner, L. R. *Electrochemical Methods: Fundamentals and Applications*, 2nd ed.; Wiley: New York, 2000.
[70] Stolz, L.; Homann, G.; Winter, M.; Kasnatscheew, J. *Mater. Today* **2021**, *44* (April), 9–14.

the rate-limiting reduction step, *F* is Faraday's constant, *D* is the diffusion constant of the electroactive species, and τ is the transition time between initial polarization and reaching steady-state current:

$$j(\tau) = \frac{1}{2}\pi^{\frac{1}{2}}nFD^{\frac{1}{2}}C\tau^{-\frac{1}{2}} \quad \text{or} \quad j\tau^{\frac{1}{2}} = \frac{1}{2}\pi^{\frac{1}{2}}nFD^{\frac{1}{2}}C \tag{5}$$

By analyzing these decay transients, Laitinen and Lucas are able to derive a value for the product $nD^{½}C$. Additionally, because the concentration of metaphosphate in their molten chloride system is known (~ 9 mM), Laitinen and Lucas further simplify this value to $nD^{½}$. However extrapolating information from this value, roughly 0.019, requires Laitinen and Lucas to assume a value for either *n* or *D*. The authors choose the former, and in a separate experiment they fully electrolyze the electroactive metaphosphate in a chloride melt to conclude that a total of *n* = 2.67 electrons were passed per metaphosphate ion. Using this value, they arrive at a diffusion constant of D = 4.09 x 10^{-5} cm^2 sec^{-1} for the metaphosphate, which they remark would be atypically high for such a melt at these temperatures. However, this finding led the authors to analyze the melt composition, and, in the process, they found that the metaphosphates were decomposing over time in the melt as their anhydride bonds were lysed by chloride ions. An increase in active species concentration would help to explain their findings, and this result instead serves as a testament to the acidity of phosphoryl anhydrides; even ions as relatively inert as chlorides can react with such linkages to cleave them. Meanwhile, Franks and Inman apply Sand analysis on a pure metaphosphate melt to infer data about the electroactive species under pure conditions.[59,60] However, since the authors impute orthophosphate (PO_4^{3-}) to be the active species during reduction, as has been discussed above, the assumptions used to dissect the derived $nD^{½}C$ are rather unconventional. Firstly, Franks and Inman use Sand analysis on separate solutions of orthophosphate dissolved in molten chlorides and arrive at a value of *n* = 2 for that diffusion-limited reduction reaction. From there, they use arguments regarding two-electrode voltage matching, which have been dissected at length above (see "1.2: MOLTEN POLYPHOSPHATES: NOMENCLATURE, PROPERTIES, AND KNOWLEDGE GAPS"), to claim that these orthophosphates must be the electroactive species at the cathode in pure metaphosphates as well. After this, they assume that *n* must = 2 for the reduction process in metaphosphates. Simultaneously, they argue that since the diffusion coefficient of Cu^{2+} drops by a factor of 8 in molten metaphosphates relative to molten chlorides, the diffusion coefficient of phosphate will fall by a similar value. The authors subsequently use this scaling factor to derive a diffusion coefficient of the putative PO_4^{3-} species in metaphosphates. Finally, using these assumptions for *n* and *D*, the authors solve for the putative PO_4^{3-} concentration *C*. By this methodology, Franks and Inman conclude that the putative PO_4^{3-} concentration is not only temperature-dependent, but that sodium metaphosphate self-dissociates at temperatures of 780 °C to generate putative PO_4^{3-} concentrations as alarmingly high as 4.95 M. However, given that the high viscosity of molten salts decreases with temperature,[71] a more skeptical reader might instead infer that the authors' observed increase in $nD^{½}C$ with temperature results from an increased diffusion coefficient at higher temperatures. While the data may imply a simpler explanation than the existence of free PO_4^{3-} ions, the author's experiments are valuable insofar as they indicate that the electroreductively active species in the melt is present in high concentrations; the derived value of C is far too high to be a trace species in the melt even if the *D* and *n* values are lowered drastically. In the cases of both Franks and Inman and Laitinen and Lucas, therefore, diffusion-limited data analysis has led to incidental insights

[59] Franks, E.; Inman, D. *J. Electroanal. Chem.* **1970**, *26*, 13–26.
[60] Franks, E.; Inman, D. *J. Appl. Electrochem.* **1971**, *14*, 73–78.
[71] Liu, T. L.; Liu, W. R.; Xu, X. H. *IOP Conf. Ser. Earth Environ. Sci.* **2017**, *93* (1).

regarding the nature of the reduction process despite the uncertainty which the underlying assumptions introduce.

In lieu of the difficulty of obtaining quantitative electrokinetic information about the reduction reaction in molten polyphosphate systems, researchers have produced a compelling slew of more general observations. Laitinen and Lucas, for instance, combine the diffusion-limited analysis on platinum electrodes above with reverse-pulse analysis to find that the intermediate reduction product of metaphosphates in chlorides quickly converts into an oxidatively inert species, since almost no re-oxidation is observed to occur.[58] This observation points to a disproportionation reaction—for example, a P^{3+} species rapidly undergoing self-disproportionation into the more stable P^{5+} and P^{0} states could explain this phenomenon. They also note an overpotential of metaphosphate reduction on gold relative to platinum and graphite, suggesting that the overall reduction may involve an inner-sphere process. Meanwhile, Casey and Dubois observe radically different behavior in pure metaphosphate, noting that the reductive film formation on platinum, while limiting the overall current density, is reversible, and nearly 100% of the reductive charge can be reclaimed during depolarization under certain conditions.[47] When taken together, these results suggest that the surrounding melt acidity and solvent environment may play a significant role in the mechanism of metaphosphate reduction on platinum surfaces and in the stability of the reaction's intermediates.

In summary, the topic of metaphosphates electroreduction is filled with understanding gaps regarding product characterization, mechanistic understanding and the role that solvent conditions play in its thermodynamics and kinetics. Past studies have left behind tantalizing clues regarding the nature of the reaction that modern technologies and improved materials understanding can potentially address. Given the creation of a proper electrochemical reference system in conjunction with the proper electrode material to avoid cathodic material deterioration, the field of molten salt electrochemistry can make major leaps and bounds in our understanding of metaphosphate reduction and whether it can serve as a viable alternative to the carbothermal process for white phosphorus production.

1.4: ELECTROCHEMICAL OXIDATION OF PHOSPHATES: STATE OF THE FIELD AND KNOWLEDGE GAPS

While the nature of the cathodic reaction is shrouded in uncertainty, researchers have comparatively a better understanding of the anodic reaction. This statement is particularly true of platinum, since among the anode material candidates, platinum is by far the most widely-utilized in the literature.[47,56,57,62,63] The literature also mentions gold as a stable anode, but little electrochemical data on gold as an anode seems to exist.[47] Aside from precious metals like these and the seemingly anodically inert zirconium and zircalloy-2,[56] the corrosive nature of the salt precludes most metals from acting as anodes. Silver,[56,65] copper,[47] nickel,[47,56] iron,[47,72] titanium[56] and calcium[47] all reportedly oxidize and corrode readily into molten metaphosphates.

---

[47] Casey, E. J.; Dubois, A. R. *Can. J. Chem.* **1971**, *49*, 2733–2745.
[53] Caton, R. D.; Wolfe, C. R. *Anal. Chem.* **1971**, *43* (6), 660–662.
[56] Casey, E. J.; Dubois, A. R.; Gorman, R. W. In *Corrosion*; 1975; Vol. 31, pp 358–363.
[57] Andreeva, V. N.; Delimarskii, Y. K. *Zh. Neorg. Khim.* **1960**, *5* (9), 1008–1011.
[58] Laitinen, H. A.; Lucas, K. R. *J. Electroanal. Chem.* **1966**, *12*, 553–563.
[62] Delimarskii, Y. K.; Andreeva, V. N. *Zh. Neorg. Khim.* **1960**, *5* (5), 540–542.
[63] Delimarskii, Y. K.; Andreeva, V. N. *Zh. Neorg. Khim.* **1960**, *5* (8), 873–876.
[65] Caton, R. D.; Wolfe, C. R. *Anal. Chem.* **1971**, *43* (6), 660–662.
[72] Pryor, M. J.; Cohen, M. *J. Electrochem. Soc.* **1951**, *98* (7), 263.

While researchers are confident that the evolved gas at stable anodes is oxygen, this confidence seems similar in nature to the literature's self-assuredness that phosphorus gas is the cathodic product. These assertions mostly appear to come from the observation that the reaction involves the evolution of gas at the anode.[41] Unlike the cathodic reaction, however, there are admittedly few to no alternative gas candidates which could evolve anodically from the melt given the infeasible difficulty of oxidizing P^{5+} or Na^{+}, so this assertion is somewhat justified. Yocom also isolates roughly 2% to 3% oxygen gas from the exhaust stream of his graphite anodes using his solvent trap system, but observes that this oxygen could result from leaks or incomplete purging.[55] To date, however, no studies seem to rigorously report the faradaic efficiency of gaseous oxygen generation, especially on metal anodes.

Although reference systems in molten metaphosphates are temperamental, the ease of oxygen evolution in these systems relative to the convoluted cathodic reaction has permitted some sparse electromechanistic studies. Foremost among these in quality is the polarography which Casey and Dubois perform on a platinum electrode in molten metaphosphate at 650 °C.[47] Although their choice of reference electrode—a second platinum electrode polarized at a current density of 10 μA cm^2—is somewhat controversial, it has some foundation in the established principle of pinning the potential of platinum to the oxygen / oxide couple in metaphosphates.[57,62,63] Using this method, they report steady-state polarization data on the working electrode characterized by several linear regions on a log current – voltage plot (**Figure 1-7**): 1) an initial rise with a slope of 70 mV $decade^{-1}$ at low current densities, followed by a sharp transition to 2) a linear region of 360 mV $decade^{-1}$ at higher current densities and overpotential, followed by 3) a return wave with a slope of 200 mV $decade^{-1}$.

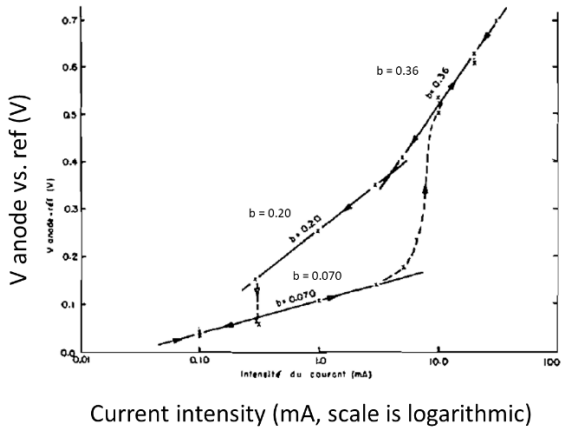

Current intensity (mA, scale is logarithmic)

Figure 1-7. *Galvanostatic steady-state measurements of a platinum anode in molten sodium metaphosphate, reproduced from Casey, E. J.; Dubois, A. R. Can. J. Chem. 1971, 49, 2733–2745.*[47] *with captions and slope values relabeled in V* dec^{-1}.

[41] Caton, R. D.; Freund, H. *Anal. Chem.* **1963**, *35* (13), 2103–2108.
[47] Casey, E. J.; Dubois, A. R. *Can. J. Chem.* **1971**, *49*, 2733–2745.
[57] Andreeva, V. N.; Delimarskii, Y. K. *Zh. Neorg. Khim.* **1960**, *5* (9), 1008–1011.
[62] Delimarskii, Y. K.; Andreeva, V. N. *Zh. Neorg. Khim.* **1960**, *5* (5), 540–542.
[63] Delimarskii, Y. K.; Andreeva, V. N. *Zh. Neorg. Khim.* **1960**, *5* (8), 873–876.

Under a mixed-control state where the reverse reaction rate does not contribute significantly to observed current, electrochemical systems become subject to a linear relationship between applied overpotential η and the logarithm of the current density i via the Tafel equation,[69]

$$\eta = \frac{2.303RT}{\alpha zF}\log\left(\frac{i}{i_0}\right)$$

where R is the ideal gas constant, T is temperature in K, z is the number of electrons transferred, F is Faraday's constant, i_0 is the exchange current density, and α is a mechanism-dependent experimental value. For a single rate-limiting electron transfer, α is approximately 0.5, but this value can vary by integer or half-integer values depending on the number of electrons transferred before the rate-limiting step.[73] Thus, the slopes that Casey and Dubois obtain through polarography have implications for the nature of the mechanism of oxygen evolution on platinum. The value of $2.303RT/F$ at 650 °C is 183 mV decade^{-1}, so the three slopes of 70, 360 and 200 mV decade^{-1} would correspond to experimental α of 2.6, 0.5, and 0.9, respectively. Because the first region occurs at low current densities, it likely occurs within the activation-controlled region of OER and, thus, Tafel conditions do not apply. However, the 360 mV decade^{-1} region (α = 0.5) would suggest that the oxidation reaction is governed by a single rate-limiting electron transfer, and the 200 mV decade^{-1} region (α = 0.9) would, likewise, correspond most closely to a redox-neutral chemical rate-limiting step that follows a reversible single-electron transfer. The authors propose that the rate limiting step in the first case is the 1-electron oxidation of oxygen anions bound to the metaphosphate, and that the rate-limiting step in the second case is the release of the polyphosphate chain from the bound, oxidized oxide species. However, while the first claim seems reasonable, the second claim is somewhat suspect within its context. Higher current densities should lead to a depletion of polyphosphate-bound oxides, or, conversely, an increase in the concentration of Lux-acidic phosphoryl anhydride linkages that bind tightly to surface oxides. Thus, if the proposed release of metaphosphate chains does not limit the reaction rate more than charge transfer does at higher current densities in the 360 mV decade^{-1} region, where the metaphosphate linkage concentration should be enriched and oxide concentration depleted, then such a condition dictating reaction rates at low current densities under a lower driving force for charge transfer would be highly unusual in the 200 mV decade^{-1} region. The slope in this region might be better explained by the convolution of oxide oxidation with a second oxidation process, such as the oxidation of platinum phosphides. Many authors have reported the formation of platinum phosphides on platinum electrodes, even under aerobic conditions,[47,58,74] and the oxidation of these phosphides could explain the large outward voltage shift that occurs upon initial polarization. If platinum phosphides continue to manifest under these conditions at low current densities between polarizations, for instance, their oxidation would increase the apparent current density at the same voltage and, as a result, lower the apparent Tafel slope.

In another study, Higgins[75] also reports on the anodic polarization of platinum in molten sodium pyrophosphate ($Na_4P_2O_7$) as part of a larger survey of oxygen evolution in molten glasses. The methodology is similar to Sand transition time analysis[58] insofar as its focus lies on the period between

[47] Casey, E. J.; Dubois, A. R. *Can. J. Chem.* **1971**, *49*, 2733–2745.
[58] Laitinen, H. A.; Lucas, K. R. *J. Electroanal. Chem.* **1966**, *12*, 553–563.
[69] Bard, A. J.; Faulkner, L. R. *Electrochemical Methods: Fundamentals and Applications*, 2nd ed.; Wiley: New York, 2000.
[73] Taylor, R. J.; Humffray, A. A. *J. Electroanal. Chem.* **1975**, *64*, 63–84.
[74] Fischer, B. *Platin. Met. Rev.* **1992**, *36* (1), 14–25.
[75] Higgins, J. K. *J. Electrochem. Soc.* **1993**, *140* (12), 3436–3448.

polarization and the stabilization of oxygen evolution current. However, Higgins instead focuses on the charge passed during this interval and subsequently correlates it to the charging of an oxide layer. Unlike platinum's behavior in other molten glasses, he claims that the pyrophosphate melt does not produce an observable oxide layer charging at any temperature from 600 to 1350 °C. According to this theory, oxygen evolution onsets immediately while accompanied by the oxidation of the platinum metal into the solution, and this oxidation process is reversed upon reverse-polarization. Unfortunately, the experimental system is 2-electrode, and, therefore, the energies of these processes cannot be easily interrogated. Nevertheless, even the presence of interpretable electrokinetic data for oxygen evolution is a vast improvement over the state of the literature for the cathodic reaction in molten polyphosphates.

The literature, in addition to exploring the electrokinetics of the polyphosphate oxidation reaction, also documents a clear dependence of the anode energetics on the Lux acidity of the melt. This principle is most comprehensively illustrated by Andreeva and Delimarskii,[57,62,63] who observe the impact of dissolving oxides into a metaphosphate melt in contact with platinum tube electrode sparging oxygen at a fixed rate. As oxides dissolve into the melt, the potential of the working electrode becomes more negative. This phenomenon suggests that a reversible equilibrium redox couple exists between oxygen gas and oxide in the melt, analogously to the relationship between pH and the potential of oxygen evolution. The negative shift in the working electrode potential is logical because as the basicity of the melt increases, the chemical activity of oxides in the melt increases and pushes the equilibrium in favor of oxygen evolution, shifting the equilibrium to more negative potentials at constant oxygen concentration. In fact, this potential shift is sensitive enough for Andreeva and Delimarskii to use it to quantify the solubility of a variety of metal oxides, including bismuth oxides, nickel oxides, antimony oxides,[57,62] and lead oxide,[63] in the melt.

Building on knowledge of the thermodynamic role Lux basicity plays in oxygen evolution, Casey and Dubois provide insights into the kinetic impact of Lux basicity through a second study on platinum electrodes.[56] By studying three melts with Lux acidities of 9.81 mol kg^{-1} [P−O−P], 8.68 mol kg^{-1} [P−O−P] and 8.32 mol kg^{-1} [P−O−P], the authors observe that the potential gap between the polarizations of the most acidic and least acidic melts widens dramatically at high current densities relative to the thermodynamic potential differences. Although the authors do not comment on this voltage gap, the large gap (as high as 500 mV at the highest current densities) seems difficult to explain purely by a change in the concentration of the active species. Interestingly, the kinetic behavior of the intermediate acidity (8.68 mol kg^{-1}) seems to straddle the voltage profile of the basic condition (8.32 mol kg^{-1}) at low current densities, but then then swings outward to that of the acidic condition (9.81 mol kg^{-1}) at high current densities. A change in the oxidized phosphate species, from "end groups" at low current densities to more plentiful "middle groups" at high current densities after the more basic phosphates are depleted, could potentially explain this behavior, similarly to the ability of both hydronium (H_3O^+) and water to act as proton donors in mildly acidic aqueous media. Regardless of the explanation, these data collectively serve as evidence that the Lux basicity of the melt plays a vital role in dictating the thermodynamic and kinetic conditions of the oxidation reaction.

[56] Casey, E. J.; Dubois, A. R.; Gorman, R. W. In *Corrosion*; 1975; Vol. 31, pp 358–363.
[57] Andreeva, V. N.; Delimarskii, Y. K. *Zh. Neorg. Khim.* **1960**, *5* (9), 1008–1011.
[62] Delimarskii, Y. K.; Andreeva, V. N. *Zh. Neorg. Khim.* **1960**, *5* (5), 540–542.
[63] Delimarskii, Y. K.; Andreeva, V. N. *Zh. Neorg. Khim.* **1960**, *5* (8), 873–876.

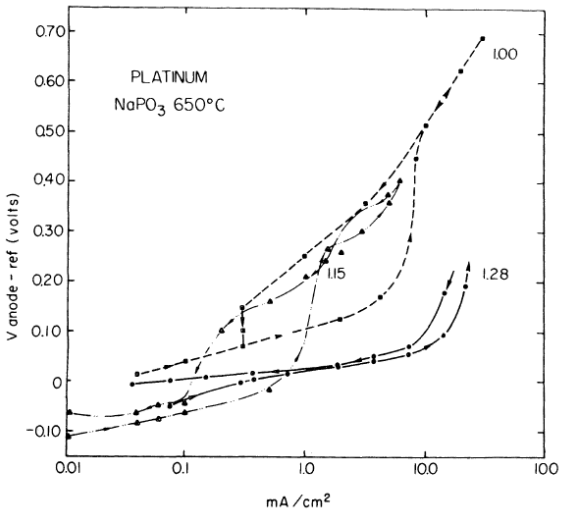

Figure 1-8. *Steady-state current-voltage profiles of platinum electrodes in melts with phosphoryl anhydride molalities of 9.81 mol kg^{-1} (Na_2O:P_2O_5 = 1), 8.68 mol kg^{-1} (Na_2O:P_2O_5 = 1.15), and 8.32 mol kg^{-1} (Na_2O:P_2O_5 = 1.28). Current presented in logarithmic scale. Reproduced from Casey, E. J.; Dubois, A. R.; Gorman, R. W. In* Corrosion*; 1975; Vol. 31, pp 358–363.*[56]

However, while the anodic decomposition of metaphosphates has been studied from a mechanistic perspective, the corrosion of such anodes is a matter which is poorly understood and characterized. Any commercial anode, especially a precious metal anode, must not only demonstrate high selectivity and efficiency for the desired reaction, but also high stability and corrosion resistance under operating conditions. While Casey and Dubois comment on the corrosion stability of platinum, they assert that the platinum electrode is only stable to anodic corrosion in melts which are rigorously free of moisture, a condition which would prove challenging for industrial operation. Additionally, while Casey and Dubois claim that corrosion becomes generally more severe as the basicity of the melt increases, the lack of quantitation renders these assertions difficult to substantiate, and this claim is complicated by the observation that decreasing the acidity even further to 7.25 mol kg^{-1} [P–O–P] (Na_2O:P_2O_5 = 1.36) causes the corrosion rate to decline. In general, very little care has been taken in the literature to quantify corrosion of anodes in molten polyphosphates. While researchers have performed sophisticated electrochemical corrosion studies in structural analogs of molten polyphosphates, like molten metavanadates,[76] the rates and mechanisms of these corrosion processes will not necessarily translate into analogous properties in molten polyphosphates.

While quantification of electrochemical corrosion in molten polyphosphates is practically nonexistent, one study quantifies the open-circuit potential aerobic corrosion of platinum in a molten metaphosphate mixture meant to mimic the composition of commercial phosphate glass.[74] The mixture contained exclusively non-alkali metal cations, namely 60% $Al(PO_3)_3$, 15% $Zn(PO_3)_2$, 15% $Mg(PO_3)_2$ and 10% BPO_4, and, as a result, the operating temperature of the melt was higher than sodium salt melts would require,

[56] Casey, E. J.; Dubois, A. R.; Gorman, R. W. In *Corrosion*; 1975; Vol. 31, pp 358–363.
[74] Fischer, B. *Platin. Met. Rev.* **1992**, *36* (1), 14–25.
[76] Sotelo-Mazón, O.; Cuevas-Arteaga, C.; Porcayo-Calderón, J.; Salinas Bravo, V. M.; Izquierdo-Montalvo, G. *Adv. Mater. Sci. Eng.* **2014**, *2014*.

around 1370 °C. Platinum wire deterioration was measured via tensile strength. Although the experiment was performed under air, a highly oxidizing environment, the primary deterioration mechanism of platinum was correlated to the formation of intergranular layers of Pt_5P_2 within the macrostructure of the polycrystalline platinum, widening and weakening grain boundaries. This phenomenon purportedly only occurs during the melting process of the melt rather than over a prolonged period. While these findings do not provide much clarity to platinum's stability as an anode, they do further contextualize the observations reported by several authors regarding the decomposition of platinum as a cathode.[47,56,58] Additionally, the issue of platinum phosphide formation may be critical for preventing corrosion in the anodic oxidation reaction.

Finally, the corrosion of platinum under anodic polarization is well-documented, but platinum ions also appear to spontaneously react in polyphosphate melts to reform platinum metal. When platinum(IV) chloride reacts with alkali polyphosphate melts of various compositions, the characteristic yellow coloration of the glass solution from platinum ions quickly becomes an opaque grey as platinum metal crystalizes as particulates out of the solution.[77] This phenomenon suggests that platinum ions cannot remain in molten metaphosphates for prolonged periods, so if platinum corrodes oxidatively into the melt, the oxidation products should be short-lived. This behavior is more nuanced than a unilateral principle, however, since the authors report that, under certain circumstances, addition of more platinum(IV) chloride to reach a specific concentration window of 0.01 to 0.1% re-oxidizes the platinum to platinum ions to reform a clear yellow glass solution. Anodic platinum corrosion should theoretically release platinum ions, so this concentration effect could potentially lead to unusual effects where the enriched local concentration of platinum ions at the electrode surface permits dissolution but leads to formation of platinum particles in the bulk as the platinum ion concentration decreases.

In short, the literature surrounding the electrochemical oxidation of molten polyphosphates is not lacking overmuch in product characterization or basic electrokinetic information around the oxygen evolution reaction. Rather, the primary intellectual obstacle for a functional oxygen-evolving anode lies in the necessity of understanding the interplay between the voltage requirements, oxygen evolution selectivity and corrosion dynamics that are specific to individual metals. Additionally, the role of Lux acidity and corrosion must be elucidated to choose optimal solvent conditions for electrolysis cell longevity.

[47] Casey, E. J.; Dubois, A. R. *Can. J. Chem.* **1971**, *49*, 2733–2745.
[56] Casey, E. J.; Dubois, A. R.; Gorman, R. W. In *Corrosion*; 1975; Vol. 31, pp 358–363.
[58] Laitinen, H. A.; Lucas, K. R. *J. Electroanal. Chem.* **1966**, *12*, 553–563.
[77] Rindone, G. E.; Rhoads, J. L. *J. Am. Ceram. Soc.* **1956**, *39* (5), 173–180.

1.5: THIS WORK

In light of the state of the literature, we set out to contribute new insights the electrolysis of molten polyphosphate salts by developing better reference systems, innovating on working electrode design to prevent transport effects, and couple electrochemistry with detailed product collection and characterization.

In Chapter 2, we address the design of a robust molten salt electrochemical reactor and use it to interrogate the cathodic reaction in molten polyphosphate electrolytes. Some of this work has been published in the form of a patent[78] and a paper which reports joint results between the author and Jonathan Melville.[79] By coupling graphite psuedoreferences with a sodium-based reference electrode, we develop a system of characterizing the energy of working electrodes in a 3-electrode system. This system enables us to interrogate the kinetics of the reductive reaction and gain insight into its mechanism. Through product collection and characterization, we identify the cathodic product as white phosphorus as well as the major product of the reaction. Oxide-dependence studies further elucidate the role of Lux acidity in determining the energetics of the reaction and its mechanistic pathway. Finally, using thermodynamic analysis on our results, we estimate the energy requirements for an industrial process using this method.

In Chapter 3, we address the question of anodic oxygen evolution in the melt by surveying three candidate metals: platinum, gold and iridium. We take advantage of the separated nature of our cell to record the first oxygen evolution reaction efficiencies on these electrodes. By varying the acidity of our melts, we interrogate the extent to which melt composition impacts the energetics of oxygen evolution. Finally, by characterizing our electrodes through weighing and imaging techniques, we quantitate the anodic corrosion of these metals under industrially relevant current densities. The presence of acid accelerates this corrosion, suggesting that the electrode material and melt composition are both vital design elements for a robust oxygen evolution anode.

Through these two sets of studies, we demonstrate the overall feasibility of carbon-free production of white phosphorus via molten salt electrolysis (**Figure 1-9**). We also lay the groundwork for electrochemists to interrogate these particularly challenging electrochemical systems through tested electrode potential control methods and gaseous separation and collection techniques.

[78] Licini, A.; Surendranath, Y. WO2020061551A1, 2019.
[79] Melville, J. F.; Licini, A. J.; Surendranath, Y. *ACS Cent. Sci.* **2023**, *9* (3), 373-380.

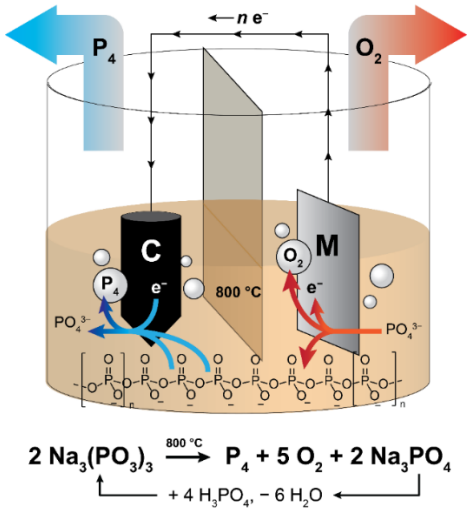

Figure 1-9. *Overall proposed scheme of molten metaphosphate electrolysis, resulting in the generation of white phosphorus and oxygen. Lux base equivalents are generated at the cathode, while Lux acid equivalents are generated at the anode, with polyphosphate chains acting as the electrolyte.*

1.6: REFERENCES

(1) Lindsey, R. Climate Change: Atmospheric Carbon Dioxide https://www.climate.gov/news-features/understanding-climate/climate-change-atmospheric-carbon-dioxide (accessed Feb 12, 2023).

(2) Tans, P.; Keeling, R. Trends in Atmospheric Carbon Dioxide https://gml.noaa.gov/ccgg/trends/data.html (accessed Feb 12, 2023).

(3) Sanchez, D. P.; Collina, L.; Levi, P.; Hodgson, D. Chemicals https://www.iea.org/reports/chemicals (accessed Feb 12, 2023).

(4) Kueppers, M.; Hodgson, D.; Levi, P.; Vass, T.; Lechtenbohmer, T. Iron and Steel https://www.iea.org/reports/iron-and-steel (accessed Feb 12, 2023).

(5) Hodgson, D.; Vass, T. Aluminium https://www.iea.org/reports/aluminium (accessed Feb 12, 2023).

(6) Lindsey, R. Climate Change: Annual greenhouse gas index https://www.climate.gov/news-features/understanding-climate/climate-change-annual-greenhouse-gas-index.

(7) Diskowski, H.; Hofmann, T. *Ullmann's Encyclopedia of Industrial Chemistry*; Wiley-VCH: Weinheim, Germany, 2012; Vol. 26, pp 725–746.

(8) Jupp, A. R.; Beijer, S.; Narain, G. C.; Schipper, W.; Slootweg, J. C. *Chem. Soc. Rev.* **2021**, *50* (1), 87–101.

(9) Emsley, J. *The 13th Element: The Sordid Tale of Murder, Fire, and Phosphorus*; Wiley: New York, 2000.

(10) Nigra, G. FR658521A, 1929.

(11) *CRC Handbook of Chemistry and Physics*, 103rd ed.; Rumble, J. R., Ed.; CRC Press: Ohio, 2023.

(12) Wolery, T. J.; Jove-Colon, C. F. *Qualification of Thermodynamic Data for Geochemical Modeling of Mineral-Water Interactions in Dilute Systems*; 2004.

(13) Dorn, F. W.; Harnisch, H. *Chemie Ing. Tech.* **1970**, *42* (19), 1209–1215.

(14) Deloitte Sustainability; British Geological Survey; Bureau de Recherches Géologiques et Minières; Netherlands Organisation for Applied Scientific Research. *Study on the Review of the List of Critical Raw Materials: Critical Raw Materials Factsheets*; Brussels, 2017.

(15) British Peroleum. *Bp Statistical Review of World Energy, 71st Ed.*; 2022.

(16) Webeck, E.; Matsubae, K. In *Phosphorus Recovery and Recycling*; Ohtake, H., Tsuneda, S., Eds.; Springer: Singapore, 2019; pp 29–44.

(17) Ohio History Central. Miamisburg, Ohio, Train Derailment https://ohiohistorycentral.org/w/Miamisburg,_Ohio,_Train_Derailment (accessed Feb 13, 2023).

(18) Scoville, W.; Springer, S.; Crawford, J. *J. Hazard. Mater.* **1989**, *21*, 47–64.

(19) *The Washington Post*. Crofton, KY June 23, 1988.

(20) Train Carrying Phosphorus Leaves Ukraine For Kazakhstan https://www.rferl.org/a/1077823.html (accessed Feb 13, 2023).

(21) Schmittinger, P.; Florkiewicz, T.; Curlin, L. C.; Lüke, B.; Scannell, R.; Navin, T.; Zelfel, E.; Bartsch, R. *Ullmann's Encyclopedia of Industrial Chemistry*; Wiley-VCH: Weinheim, Germany, 2012; Vol. 8, pp 531–622.

(22) Frank, W. B.; Haupin, W. E.; Vogt, H.; Bruno, M.; Thonstad, J.; Dawless, R. K.; Kvande, H.; Taiwo, O. A. *Ullmann's Encyclopedia of Industrial Chemistry*; Wiley-VCH: Weinheim, Germany, 2012; Vol. 2, pp 483–520.

(23) Hall, A. S.; Yoon, Y.; Wuttig, A.; Surendranath, Y. *J. Am. Chem. Soc.* **2015**, *137* (47), 14834–14837.

(24) Yoon, Y.; Hall, A. S.; Surendranath, Y. *Angew. Chemie - Int. Ed.* **2016**, *55* (49), 15282–15286.

(25) Yoon, Y.; Yan, B.; Surendranath, Y. *J. Am. Chem. Soc.* **2018**, *140* (7), 2397–2400.

(26) Das, P.; Jana, N. R. *ACS Appl. Mater. Interfaces* **2016**, *8* (13), 8710–8720.

(27) Elias, J. S.; Costentin, C.; Nocera, D. G. *J. Am. Chem. Soc.* **2018**, *140* (42), 13711–13718.

(28) Brummer, J. R.; Keely, J. A.; Munday, T. F.; FMC Corporation. *Kirk-Othmer Encyclopedia of Chemical Technology*; John Wiley & Sons, 2005; Vol. 18.

(29) Ubbelohde, A. R. In *Ionic Liquids*; Inman, D., Lovering, D. G., Eds.; Plenum: New York, 1981; pp 1–6.

(30) Scordilis-Kelley, C.; Fuller, J.; Carlin, R. T.; Wilkes, J. S. *J. Electrochem. Soc.* **1992**, *139* (3), 694–699.

(31) Allanore, A. *J. Electrochem. Soc.* **2015**, *162* (1), E13–E22.

(32) Caldwell, A. H.; Lai, E.; Gmitter, A. J.; Allanore, A. *Electrochim. Acta* **2016**, *219*, 178–186.

(33) Martín Treceño, S.; Allanore, A.; Bishop, C. M.; Marshall, A. T.; Watson, M. J. *J. Mater.* **2021**, *73* (6), 1899–1908.

(34) Yang, X.; Nohira, T. *ACS Sustain. Chem. Eng.* **2020**, *8* (36), 13784–13792.

(35) Zhong, Y.; Yang, X. *Metall. Mater. Trans. B Process Metall. Mater. Process. Sci.* **2021**, *52* (5), 3515–3523.

(36) Sorrell, T. N. In *Organic Chemistry*; Castellion, M., Ed.; University Science Books: California, 2006; pp 953–988.

(37) Havelange, S.; Lierde, N.; Germeau, A.; Martins, E.; Theys, T.; Sonveaux, M.; Toussaint, C.; Schrödter, K.; Bettermann, G.; Staffel, T.; Wahl, F.; Klein, T.; Hofmann, T. *Ullmann's Encyclopedia of Industrial Chemistry*; Wiley-VCH, 2022; pp 1–55.

(38) Bettermann, G.; Krause, W.; Riess, G.; Hofmann, T. *Ullmann's Encyclopedia of Industrial Chemistry*; Wiley-VCH, 2012; Vol. 27.

(39) Centnerzwer, M.; Szper, J. *Bull. Polish Acad. Sci.* **1931**, 364–368.

(40) In *Encyclopedia of Electrochemistry of the Elements*; Bard, A. J., Ed.; Marcel Dekker: New York, 1976; Vol. X, pp 373–388.

(41) Caton, R. D.; Freund, H. *Anal. Chem.* **1963**, *35* (13), 2103–2108.

(42) Van Wazer, J. R. In *Phosphorus and its Compounds, Vol. I*; Interscience: New York, 1958; pp 717–800.

(43) Griffith, E. J.; Callis, C. F. *J. Am. Chem. Soc.* **1959**, *81* (4), 833–836.

(44) Van Wazer, J. R. *J. Am. Chem. Soc.* **1950**, *72* (2), 644–647.

(45) Van Wazer, J. R. In *Phosphorus and its Compounds, Vol. I*; Interscience: New York, 1958; pp 601–678.

(46) Greenfield, S.; Clift, M. *Analytical Chemistry of the Condensed Phosphates*; Pergamon: Oxford, 1975.

(47) Casey, E. J.; Dubois, A. R. *Can. J. Chem.* **1971**, *49*, 2733–2745.

(48) Andreeva, V. N. *Ukr. Khim. Zh.* **1955**, *21*, 569.

(49) Lux, H. *Zeitschrift für Elektrochemie und Angew. Phys. Chemie* **1949**, *45* (1), 41–43.

(50) Flood, H.; Förland, T. *Acta Chem. Scand.* **1947**, *1* (6), 592–604.

(51) Drago, R. S.; Whitten, K. W. *Inorg. Chem.* **1966**, *5* (4), 677–682.

(52) El Hosary, A. A.; Kerridge, D. H.; Shams El Din, A. M. In *Ionic Liquids*; Inman, D., Lovering, D. G., Eds.; Plenum: New York, 1981; pp 339–362.

(53) Shams El Din, A. M.; Gerges, A. A. A. *Electrochim. Acta* **1964**, *9*, 613–627.

(54) Gruber, B. A. US2965552A, 1960.

(55) Yocom, P. N. University of Illinois, 1958.

(56) Casey, E. J.; Dubois, A. R.; Gorman, R. W. In *Corrosion*; 1975; Vol. 31, pp 358–363.

(57) Andreeva, V. N.; Delimarskii, Y. K. *Zh. Neorg. Khim.* **1960**, *5* (9), 1008–1011.

(58) Laitinen, H. A.; Lucas, K. R. *J. Electroanal. Chem.* **1966**, *12*, 553–563.

(59) Franks, E.; Inman, D. *J. Electroanal. Chem.* **1970**, *26*, 13–26.

(60) Franks, E.; Inman, D. *J. Appl. Electrochem.* **1971**, *14*, 73–78.

(61) Lippard, S. J.; Berg, J. M. In *Principles of Bioinorganic Chemistry*; University Science Books: Mill Valley, CA, 1994; pp 103–137.

(62) Delimarskii, Y. K.; Andreeva, V. N. *Zh. Neorg. Khim.* **1960**, *5* (5), 540–542.

(63) Delimarskii, Y. K.; Andreeva, V. N. *Zh. Neorg. Khim.* **1960**, *5* (8), 873–876.

(64) Stebbins, J. F. *Chem. Rev.* **1991**, *91* (7), 1353–1373.

(65) Caton, R. D.; Wolfe, C. R. *Anal. Chem.* **1971**, *43* (6), 660–662.

(66) Prasad, S. *J. Braz. Chem. Soc.* **2000**, *11* (3), 245–251.

(67) Wilson, S. D. R.; Hulme, A. *Proc. R. Soc. London, Ser. A Math. Phys. Sci.* **1983**, *387* (1792), 133–146.

(68) Tabereaux, A. T.; Peterson, R. D. In *Treatise on Process Metallurgy*; Elsevier: Oxford, 2014; Vol. 3, pp 839–917.

(69) Bard, A. J.; Faulkner, L. R. *Electrochemical Methods: Fundamentals and Applications*, 2nd ed.; Wiley: New York, 2000.

(70) Stolz, L.; Homann, G.; Winter, M.; Kasnatscheew, J. *Mater. Today* **2021**, *44* (April), 9–14.

(71) Liu, T. L.; Liu, W. R.; Xu, X. H. *IOP Conf. Ser. Earth Environ. Sci.* **2017**, *93* (1).

(72) Pryor, M. J.; Cohen, M. *J. Electrochem. Soc.* **1951**, *98* (7), 263.

(73) Taylor, R. J.; Humffray, A. A. *J. Electroanal. Chem.* **1975**, *64*, 63–84.

(74) Fischer, B. *Platin. Met. Rev.* **1992**, *36* (1), 14–25.

(75) Higgins, J. K. *J. Electrochem. Soc.* **1993**, *140* (12), 3436–3448.

(76) Sotelo-Mazón, O.; Cuevas-Arteaga, C.; Porcayo-Calderón, J.; Salinas Bravo, V. M.; Izquierdo-Montalvo, G. *Adv. Mater. Sci. Eng.* **2014**, *2014*.

(77) Rindone, G. E.; Rhoads, J. L. *J. Am. Ceram. Soc.* **1956**, *39* (5), 173–180.

(78) Licini, A.; Surendranath, Y. WO2020061551A1, 2019.

(79) Melville, J. F.; Licini, A. J.; Surendranath, Y. *ACS Cent. Sci.* **2023**, *9* (3), 373-380.

Chapter 2 – Cathodic Reduction of Sodium Polyphosphates to White Phosphorus

This chapter, and the corresponding Appendix A, contains work that was obtained collaboratively with another researcher at the Massachusetts Institute of Technology (Jonathan F. Melville). Specifically, the following contributions are noted:

The CVs and chronopotentiometry data in **Figure 2-7** were collected by Jo Melville as replications of data previously collected by the author. Jo Melville conceived of, designed and executed in its entirety the linear sweep voltammetry experiments depicted in **Figure 2-8**. Based on preliminary findings from the author on oxide dependencies measured in alumina crucibles (**Figure 2-4**) and on alumina dissolution (**Figure 2-5**), Jo Melville selected the conditions for, collected and analyzed the Lux acidity dependence CVs / chronopotentiometry experiments depicted in **Figure 2-9**. Pseudo-Tafel data collection in pure metaphosphate (9.8 mol kg) and its corresponding analysis were performed by the author, although these results were reproduced by Jo Melville for the purposes of **Figure 2-9**.

This joint work is accessible as an *ACS Central Science* article through the following "ACS Articles on Request" link: https://pubs.acs.org/articlesonrequest/AOR-JRRB6NQ6WRSNGIMBZAFN

2.1: PREFACE

As discussed in Chapter 1, the production of white phosphorus is a critical chemical industry which generates a considerable amount of carbon dioxide and negative environmental impacts.[1–3] Although alternative processes are emerging to circumvent P_4 as an intermediate,[4,5] the phosphorus chemical value chain relies upon the "thermal process" (Equation 1), which employs extremely forcing conditions to drive the reduction of phosphate to P_4 by carbon coke.

$$2\ Ca_3(PO_4)_2 + 6\ SiO_2 + 10\ C \rightarrow 6\ CaSiO_3 + 10\ CO + P_4 \quad (1)$$

This process occurs at temperatures of 1500 °C to generate white phosphorus, calcium silicate slag and carbon monoxide,[3] but while these particular reaction conditions have been fixed for many decades, this process may be abstracted through the lens of Lux-Flood acid-base theory, with orthophosphate acting as a 'Lux basic' oxide donor and silica acting as a 'Lux acidic' oxide acceptor.[6–8] If the reduction reaction can be performed through an external circuit in the rich chemistry of molten metaphosphates and an alternative Lux acid to accept oxides, the result will be a drastically milder, more environmentally friendly electrolysis process (Scheme 2-1).

[1] Schipper, W. *Eur. J. Inorg. Chem.* **2014**, No. 10, 1567–1571.
[2] Emsley, J. *The 13th Element: The Sordid Tale of Murder, Fire, and Phosphorus*; Wiley: New York, 2000.
[3] Diskowski, H.; Hofmann, T. *Ullmann's Encyclopedia of Industrial Chemistry*; Wiley-VCH: Weinheim, Germany, 2012; Vol. 26, pp 725–746.
[4] Geeson, M. B.; Cummins, C. C. *Science (80-.).* **2018**, *359*, 1383–1385.
[5] Geeson, M. B.; Cummins, C. C. *ACS Cent. Sci.* **2020**, *6* (6), 848–860.
[6] Lux, H. *Zeitschrift für Elektrochemie und Angew. Phys. Chemie* **1949**, *45* (1), 41–43.
[7] Flood, H.; Förland, T. *Acta Chem. Scand.* **1947**, *1* (6), 592–604.
[8] Drago, R. S.; Whitten, K. W. *Inorg. Chem.* **1966**, *5* (4), 677–682.

Scheme 2-1. Half-reaction and overall electrolysis scheme for metaphosphate electrolysis and regeneration.

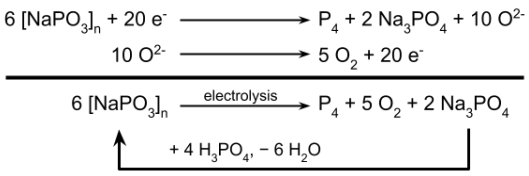

Condensed phosphates represent a broad reaction space, enabling transverse studies across a continuum of electrolytes to directly interrogate the role of Lux acidic moieties in promoting electrochemical P—O activation. This complexity poses its own challenges, as, despite a plethora of studies which examine the electrolysis of molten polyphosphate salts,[6,9–15] many unknowns still remain regarding the reduction process, what chemical species it generates and what chemical factors influence its generation. Adding new insights to this field necessitates applying principles of rational design to this multifaceted electrolyte canvas to develop heretofore-nonexistent electroanalytical methodologies to enable product identities, kinetics and solvent conditions to be interrogated. To this end, we present a toolbox of techniques for quantifying reaction overpotential, selectivity, and efficiency across a range of electrolyte compositions, and employ these tools to elucidate the governing attributes which underpin the promotion of P_4 electrosynthesis by phosphoryl anhydride linkages.

2.2: RESULTS AND DISCUSSION

We began by constructing a robust system for quantitative high-temperature electroanalysis and mechanistic investigation of molten salt electrolysis. Because we wanted to maximize our electrochemical options and capabilities, the first generation molten salt reactor was a large cell with multiple chambers which we designed to fit the full internal radius of our top-loading furnace (**Figure 2-1**, left). We based the overall design on a model used by the Sadoway and Allanore groups and scaled to a larger 5-inch outer radius. We did this in part to accommodate an interior chamber comprised of a 2-inch outer diameter closed-end alumina tube. We chose this design with the intention that the tube would serve as a locus for small-scale studies, with the melt enclosed in the bottom, and that in the long-term, small holes could be drilled in the bottom of the closed-end tube. The reactor placed a focus on airtight seals, sporting copper cooling coils towards the top of the cell to protect the rubber gasket between the top and bottom of the cell. We also installed sheets of steel baffle plates onto the tops of both cell caps, which acted as further insulation to protect the seals. Using this design, we performed survey experiments on a variety of different molten salt media, initially attempting to solvate phosphates in molten chloride salts before

[9] Centnerzwer, M.; Szper, J. *Bull. Polish Acad. Sci.* **1931**, 364–368.
[10] Caton, R. D.; Freund, H. *Anal. Chem.* **1963**, *35* (13), 2103–2108.
[11] Laitinen, H. A.; Lucas, K. R. *J. Electroanal. Chem.* **1966**, *12*, 553–563.
[12] Franks, E.; Inman, D. *J. Electroanal. Chem.* **1970**, *26*, 13–26.
[13] Franks, E.; Inman, D. *J. Appl. Electrochem.* **1971**, *14*, 73–78.
[14] Casey, E. J.; Dubois, A. R. *Can. J. Chem.* **1971**, *49*, 2733–2745.
[15] Casey, E. J.; Dubois, A. R.; Gorman, R. W. In *Corrosion*; 1975; Vol. 31, pp 358–363.

switching to molten sodium polyphosphate. Doing so, we were able to identify a clear solvent window for molten metaphosphate on graphite, perform rudimentary electrolysis studies, refine the geometry of the working electrodes from sheathed, flat designs to sharpened points and observe the generation of red phosphorus on the baffle plates of the cell.

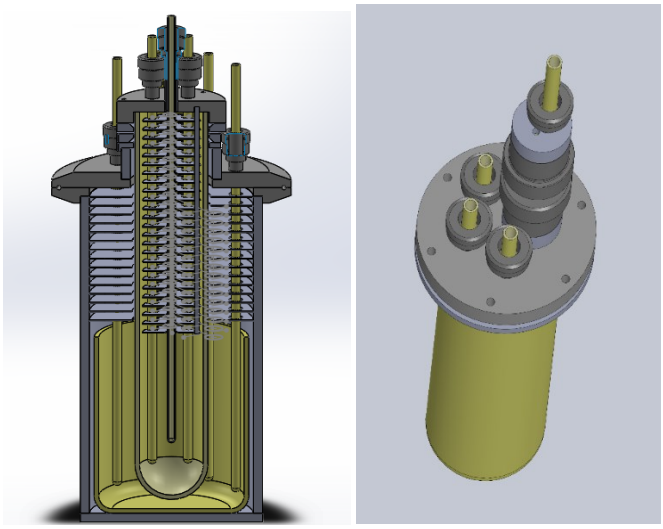

Figure 2-1. *(left) Cutaway diagram of the first-generation molten salt reactor. Alumina components are indicated in yellow, while steel components are indicated in gray. (right) Diagram of the redesigned top cap for the first-generation electrochemical cell to allow for gas separation.*

In practice, however, this design came with several critical drawbacks. Most significantly, the baffle plates and cooling coils of the first-generation cell protected the rubber seals at the cost of an inability to collect or quantify gaseous products—due to the high boiling point of white phosphorus, product would condense on the baffle plates rather than exiting as exhaust. Additionally, the large size of the outer crucible made separated-cell experiments infeasible from a solvent volume perspective, while the smaller chamber precluded separation of the headspaces around the cathode and anode. As a result, we redesigned the cap to the inner alumina tube so the counter electrode could be contained by an external alumina separator. This modification allowed the inner tube to be operated as a gas-separated cell, sporting temperature-resistant Kalrez® O-rings to allow for higher-temperature seals and permit product collection. While this redesign allowed for cathodic product characterization, it nevertheless introduced complications because the molten salt was eventually discovered to react with aluminum oxide and dissolve it, convolving electrochemical measurements due to aluminum ion contamination and variable Lux basicity.

While the cell's design was being refined, we performed some exploratory chemistry in the field. Hoping to operate at lower temperatures, we initially attempted to perform our phosphate reductions in a molten KCl-LiCl eutectic of 59.5% LiCl and 40.5% KCl by moles, which we selected using a database of molten salt eutectics data.[16] By investigation with differential scanning calorimetry (DSC), we found that the mixture melted at around 353 °C, with a heat of fusion of approximately 242 J per gram of eutectic. Despite attempting to solvate phosphates in the melt at 400 °C, we found the solubility to be less than 32

[16] Centre for Research in Computational Thermochemistry. FTsalt - FACT Salt Phase Diagrams https://www.crct.polymtl.ca/fact/documentation/FTsalt/FTsalt_Figs.htm (accessed Feb 18, 2023).

mmol K_3PO_4 kg^{-1} eutectic as evaluated by visible solid in the bottom of a 1-g eutectic melt liquid. As a result, we transitioned our electrochemical studies to higher temperature mixtures. Using the same method, however, we evaluated a lower estimate on solubilities of various carbonate salts in the KCl-LiCl eutectic at 400 °C, which may prove useful for topics such as moderate-temperature carbon dioxide reduction studies (**Table 2-1**).

Carbonate Salt	Solubility in 400 °C KCl-LiCl (mM)
Li_2CO_3	1610
Na_2CO_3	221
K_2CO_3	925
$BaCO_3$	616

***Table 2-1**. Solubilities of some carbonate salts in a 400 C eutectic of 59.5% LiCl and 40.5% KCl.*

At higher operation temperatures (~710 °C), we found that chloride salts evaporated out of the melt and condensed on top of the cell baffles, which rendered the chloride eutectic impractical for the electrolysis of phosphates. Computational studies on related KCl-NaCl salts in the literature, in fact, posit that both KCl and NaCl salts have appreciable vapor pressures above 600 °C, and those vapors consist of both the monomer and dimer.[17] Cyclic voltammetry studies on the melt at these temperatures also showed relatively no difference between a blank eutectic and a eutectic with phosphate salt added, suggesting that solubility issues of orthophosphate were persistent even at higher temperature. Given that these operating temperatures were close to the melting point of sodium metaphosphate,[18] we opted to transition to pure molten sodium metaphosphate.

When we performed cyclic voltammetry on molten metaphosphate with graphite electrodes, we were able to observe unambiguous reduction features. However, while we observed electrochemical reduction features (**Figure 2-2** right, red trace), these features were very broad, and attempts to perform steady-state electrolysis resulted in vacillating, unstable currents. Through a series of experiments involving raising and lowering the electrode, these oscillations were eventually attributed to the formation of gas bubbles on the surface of the electrode. In practice, the sheath and flat surface of the original electrode geometry trapped bubbles in the highly viscous melt. By switching from sheathed, flat electrodes to sharpened graphite electrodes of lower surface area (**Figure 2-2** right, black trace), we were able to obtain both much sharper, higher resolution on electrochemical features via cyclic voltammetry under the same currents. The steady-state currents also stabilized significantly, allowing much higher current densities. We initially sharpened these electrodes by hand via whittling with a shard of alumina, but we switched to a traditional steel-blade pencil sharpener after the use of a metal blade was determined to have no obvious effect on the catalysis of the cathode.

[17] Wang, L. L.; Wallace, T. C. *Metall. Mater. Trans. B* **1996**, *27* (1), 141–146.
[18] Van Wazer, J. R. In *Phosphorus and its Compounds, Vol. I*; Interscience: New York, 1958; pp 717–800.

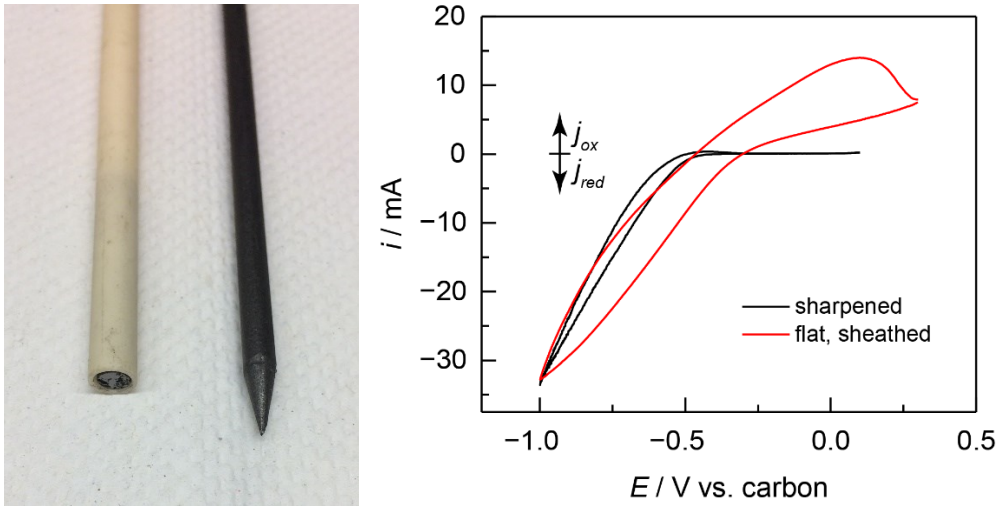

Figure 2-2. *(*left*) Photographs of a sheathed graphite rod electrode and a sharpened graphite cone electrode in molten sodium trimetaphosphate contained in an alumina tube vessel. (*right*) Cyclic voltammetry of a sheathed, flat graphite electrode (red) vs. a sharpened graphite electrode (*black*) at scan rates of 50 mV s^{-1}.*

Using this electrode geometry allowed us to collect high-resolution data on electrochemical features in alumina-housed melts of sodium trimetaphosphate. Under these conditions, we identified a solvent window of roughly 0.7 V from -0.1 to 0.6 V vs. a graphite psuedoreference (**Figure 2-3**, left). We also observed reproducible pseudo-Tafel behavior, with a slope of roughly 116 mV $decade^{-1}$ at 800 °C from two identical trials which each consisted of four polarization sets, as well as a noisy region with a slope of 38 mV $decade^{-1}$ that levels off (**Figure 2-3**, right). We attributed this second region to a charge transfer onset due to its extremely low slope for 800 °C. We attributed the first reduction process at lower current densities, with a slope of 116 mV $decade^{-1}$, to a rate-limiting chemical step following two prior electron transfers due to the experimental alpha of ~1.8 (see Appendix PPPPPPPPPPPPPPPPA-1.5e – Methodology for Tafel Analysis).

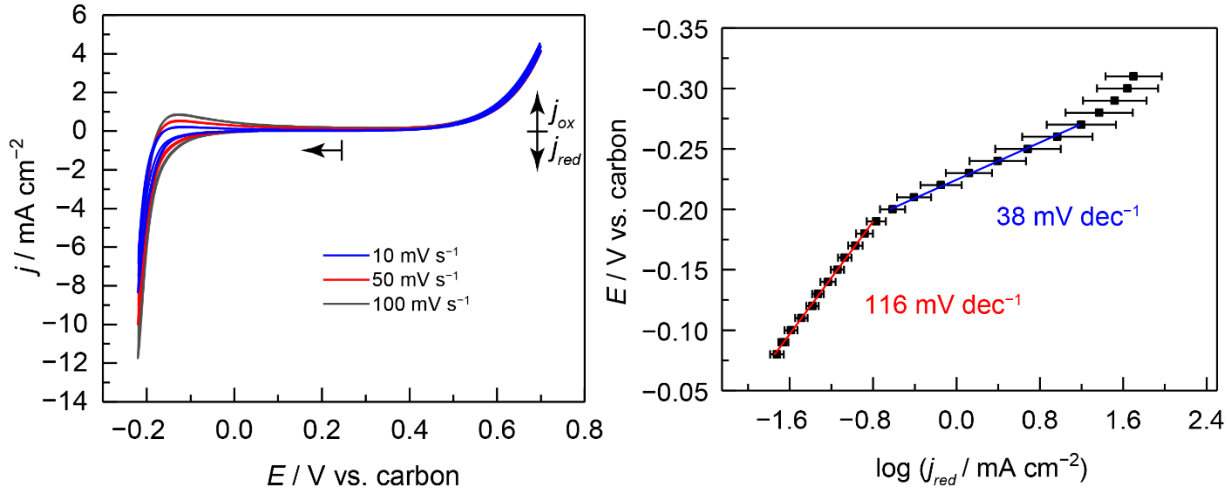

Figure 2-3. *(left) Cyclic voltammetry of a sharpened graphite working electrode in alumina-housed molten sodium metaphosphate at 800 C, at several scan rates. (right) Steady-state chronoamperometry profiles for sharpened graphite working electrodes in same melt composition at 800 °C. Error bars reported for two distinct electrodes with four identical steady-state chronoamperometry sequences.*

In addition to these studies, we also began product collection trials. After redesigning the cap to remove the baffles and cooling coils, the cell accommodated higher temperatures for product collection, but even under these modifications, additional heating was necessary. Themal profile studies were collected and it was found that as furnace temperatures varied from 500-900 °C, the portion of the alumina tube protruding from the cell only varied from 170-270 °C and the steel cap ranged from 95-145 °C, and, as a result, red phosphorus continued to condense in the cell. Additional heating was needed, which was accomplished via heating coils accompanied by careful monitoring of thermocouples to ensure that the temperature remained within the window of 280 °C, the boiling point of phosphorus, and 320 °C, the decomposition point of the Kalrez seals. Using these methods, we were able to isolate and identify white phosphorus via ^{31}P NMR (see section A-1.3a – ^{31P} NMR Identification of P4).

Because the reduction of phosphates would involve the release of oxides, we anticipated that added oxide equivalents would affect the energies of the phosphate reduction reaction (PRR). To investigate this hypothesis, we began dosing in oxide-donating equivalents (Na_2CO_3 and, later, Na_3PO_4, which we found preferable due to eliminating the bubbling generated by Na_2CO_3). These results were compiled and compared relative to the graphite pseudoreference (**Figure 2-4**). As more base was dosed into the metaphosphates contained in the alumina tube, the onsets of both the phosphate reduction and carbon oxidation were found to shift to more negative potentials (**Figure 2-4**, left). This behavior was also mirrored in steady-state chronoamperometry, where the voltages were found qualitatively to shift to much more negative potentials by about 400 mV over a 1 mol kg^{-1} change in theoretical concentration (**Figure 2-4**, right). However, this shift was much larger than expected purely based on the amount of base added, and results were found to vary depending on how long the melt was allowed to sit in molten state before experimentation. These findings first led us to consider the possibility of compositional changes induced by the aluminum oxide container. As an aside: it was ultimately found in a separate study that the potential of the graphite pseudoreference should vary with Lux acidity with a similar dependence to the reductive onsets,[19] so the reason why this shift is observable under these conditions is puzzling. The two most likely explanations are as follows: a) because these experiments were performed without a gas-phase separator tube, much of the white phosphorus is immediately consumed in the gas phase and, therefore, the pseudoreference may not pin to the phosphate/P_4 couple as strongly, and b) the presence aluminum ions in solution may potentially introduce new redox couples or redox-active chemical environments which the reference electrode senses but which do not affect the working electrode at higher current densities.

[19] Melville, J. F.; Licini, A. J.; Surendranath, Y. *ACS Cent. Sci.* **2023**, *9* (3), 373-380.

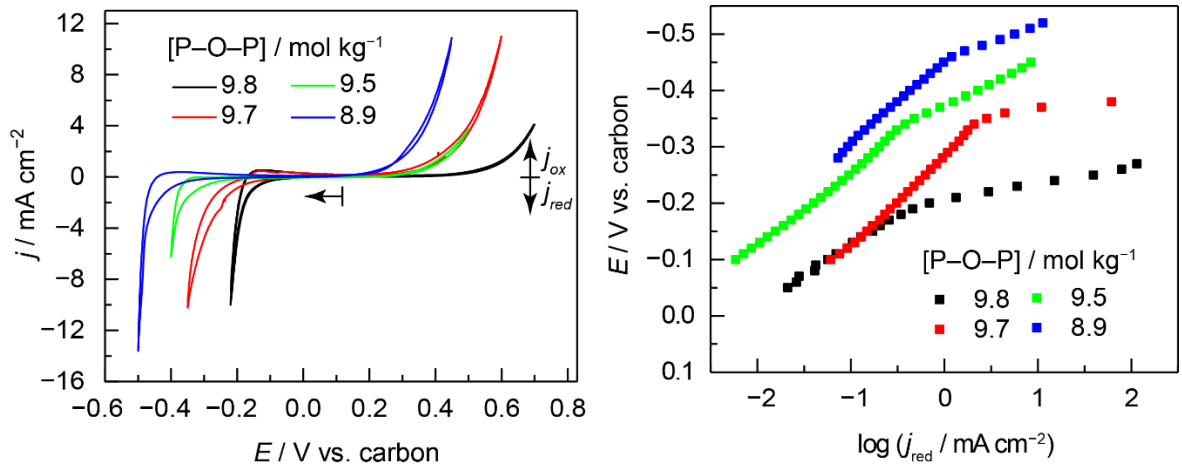

Figure 2-4. (left) *Cyclic voltammetry of metaphosphate housed in an alumina container and dosed with oxide-donating bases to theoretically produce melts of varying anhydride concentrations, as indicated.* (right) *Steady-state chronoamperometry of the same systems housed in an alumina container. The alumina crucible likely also cleaved additional anhydride bonds in all cases.*

The shattering of alumina crucibles under certain cooling conditions also catalyzed the discovery of alumina leaching. Early on, several alumina tubes would break on cooldown, spilling their contents of sodium metaphosphate into the furnace body. We analyzed this phenomenon, and we found that holding the melt as a liquid for longer durations prevented the alumina tube from shattering, even when all samples were cooled at the same rate. This high-temperature stabilization was accompanied by the production of a glassy melt, whereas melts which we heated, analyzed, and cooled immediately subsequently froze into white crystals while causing the alumina to shatter. After transitioning to glassy carbon crucibles, we found that pure metaphosphate crystallized as a solid rather than forming an amorphous glass. The volume change associated with this freezing process causes crucibles with rough surfaces, like alumina or improperly polished glassy carbon, to shatter.

Spurred on by these discoveries, we investigated the composition of glasses as a function of added base via NMR spectroscopy (**Figure 2-5**). We collected these samples by dosing in oxide equivalents of sodium carbonate as a mol % in sodium metaphosphate ($NaPO_3$) and allowing the crucibles to sit at 770 °C overnight in a box furnace. The surface of these glasses were then soaked for an hour with 1 mL aliquots of deuterium oxide containing a small amount of dissolved phosphonoacetic acid as an internal standard (0.0179 g in 5 mL solution, $\delta \approx +17$ ppm). We found that more anhydride was cleaved in all cases than the acid-base chemistry should have predicted. As observed via 31P NMR, metaphosphate, which should be comprised entirely of "middle" polyphosphate chain groups ($\delta \approx -21$ ppm), also displays a substantial number of "end" or terminal polyphosphate groups in alumina crucibles ($\delta \approx -10$ ppm).[20] The integration of the "end" vs. "middle" groups was 0.45 : 1, suggesting that after overnight leaching of alumina, roughly 30% of the water-soluble components of the glass were cleaved in actuality to form end groups (anhydride concentration = 7.19 mol kg^{-1} [P–O–P]). This ratio kept increasing until the solubility of the glass in the solution became negligible (10-15 mol % oxide in $NaPO_3$), and eventually only pyrophosphate and orthophosphate ($\delta \approx 0$ ppm) were observable soluble products. These findings suggest that aluminum

[20] Greenfield, S.; Clift, M. *Analytical Chemistry of the Condensed Phosphates*; Pergamon: Oxford, 1975.

oxide changes the composition of metaphosphate substantially. We later confirmed the dissolution of alumina by dosing molten metaphosphate salt at 800 °C directly with alumina powder, which dissolved visibly up to concentrations as high as 2 M. As a result, the cell was redesigned to accommodate a glassy carbon crucible, which was found to have negligible mass loss while containing metaphosphate at temperature.

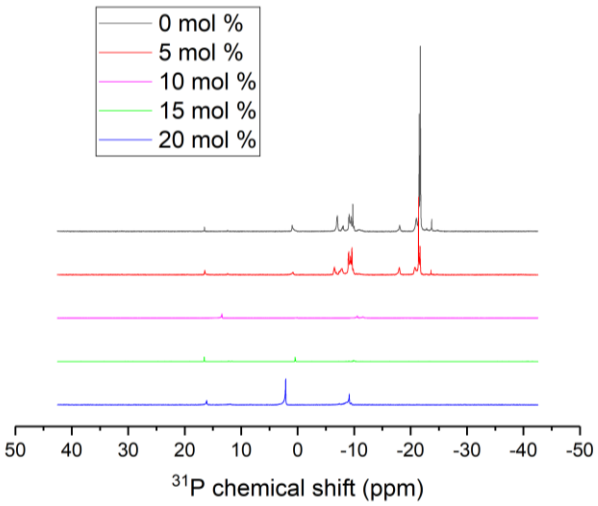

***Figure 2-5**. 31P NMR spectra of metaphosphate samples contained in alumina crucibles which were dosed with sodium carbonate (reported in mol % in $NaPO_3$) and heated overnight at 770 °C. Phosphonoacetic acid was added as an internal standard (δ ≈ +17 ppm).*

We made several attempts to produce high-temperature porous frits by mixing yttria-stabilized zirconia cement with ZrO_2 fibers and sintering the mixture in the end of alumina tubes. After sintering, the frits allowed water to flow through slowly, but the frit quickly disintegrated in the melt. The two main failure modes were a) loss of cohesion of the frits with the alumina tube sides and b) dissolution of the frit in the melt. As a result, we opted to use commercially-produced sodium reference electrodes (see below and section A-1.1g – Liquid Sodium Electrode), which could not remain in the melt for extended periods but were found to measure stable potentials.

After another significant redesign following these findings, the molten salt electrolysis cell was finalized (**Figure 2-6** and **Figure A-1** to **Figure A-4**). Our cell included separated anodic and cathodic chambers with independent N_2 flow streams, a Na/Na^+ electrode for use as a fixed-potential reference, and a cold trap for product characterization and quantification. Graphite rods were used for all electrodes in a standard 3-electrode analytical setup (working, counter, and reference). Whereas many transition metals readily form metal phosphide alloys,[21,22] carbon is highly immiscible with phosphorus;[23,24] accordingly, we found graphite to be stable under cathodic conditions, displaying no significant changes in mass nor surface area under any conditions examined in this study. By comparison, the β-alumina membrane of the Na/Na^+ reference electrode was subject to corrosion upon prolonged exposure to the melt; as a result, it was instead used to calibrate a graphite pseudoreference electrode, the two comprising

[21] Carenco, S.; Hu, Y.; Florea, I.; Ersen, O.; Boissière, C.; Mézailles, N.; Sanchez, C. *Chem. Mater.* **2012**, *24*, 4134–4145.
[22] Carenco, S.; Portehault, D.; Boissière, C.; Mézailles, N.; Sanchez, C. *Adv. Mater.* **2014**, *26* (3), 371–390.
[23] Guan, J.; Liu, D.; Zhu, Z.; Tománek, D. *Nano Lett.* **2016**, *16*, 3247–3252.
[24] Ma, X.; Zhou, J.; Yang, T.; Li, D.; Feng, Y. P. *Phys. Rev. Mater.* **2021**, *5*, 024005.

a quasireference electrode pair (**Figure A-6**).[25] Since these studies focus on the promotion of the cathodic half-reaction, our setup employed a sacrificial graphite counter electrode which underwent oxidation principally to CO_2, as determined by GC analysis. Robust experimental design is essential for reproducible electrochemistry at high temperatures, and as such we provide in Appendix A full specifications and part numbers for construction of the molten salt electrolysis system employed in these studies.

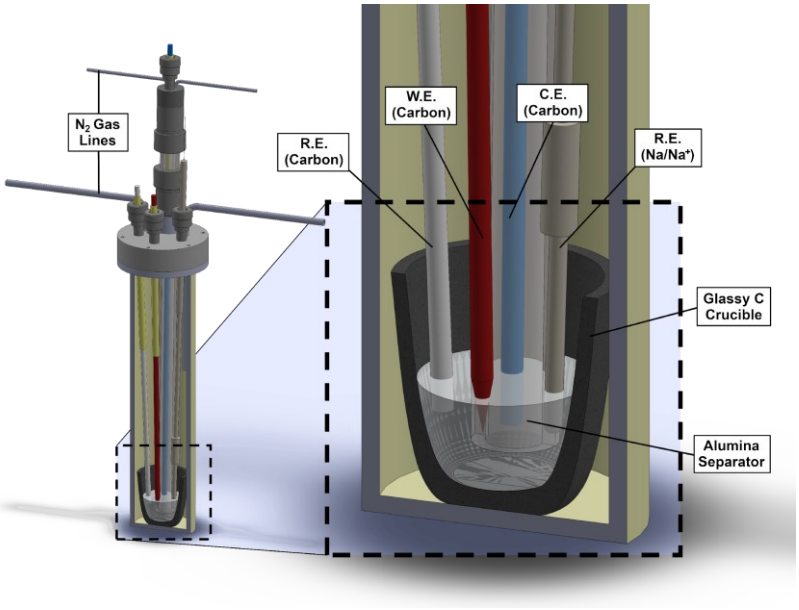

Figure 2-6. *Cutaway schematic of high-temperature electrochemical cell featuring separated working and counter chambers and a Na/Na⁺ reference electrode. W.E. = working electrode; R.E. = reference electrode; C.E. = counter electrode.*

Using this molten salt electroanalytical setup, we investigated the electrochemical behavior of molten sodium trimetaphosphate using cyclic voltammetry (CV), as seen in **Figure 2-7**. To mitigate the effects of bubble formation and associated occlusion of the electrode surface area, we employed a graphite working electrode with a conical tip (**Figure 2-6**, red and **Figure A-4b**). Voltammetric data reveal the onset of substantial reductive current at approximately +2.4 V against a Na/Na^+ reference electrode. As our electrolyte is itself our reactant, this cathodic wave does not peak; rather, we observe an exponentially rising reductive feature of the type associated with solvent reduction in conventional electrolytes. However, unlike a typical catalytic wave, this cathodic process displays a square-root dependence on scan rate, implying the participation of a diffusion-limited species. Upon reversal of the potential sweep, we observe the immediate appearance of a broad oxidative wave, which we ascribe to a reverse redox process. The peak potential and current magnitude in this anodic wave are also scan rate-dependent; a prominent oxidative feature is observed at 100 $mV \cdot s^{-1}$, whereas it is almost nonexistent at 10 $mV \cdot s^{-1}$. These data are characteristic of the formation and build-up of a transient reduced species at the electrode interface. To further probe the reductive voltammetry, computational CV were performed in a separate study,[19] which indicated that the voltammetric shape and scan rate dependence could result from diffusion-limited back-oxidation of partially reduced intermediates in a reversible redox process. Finally, at

[25] Inzelt, G. In *Handbook of Reference Electrodes*; Inzelt, G., Lewenstam, A., Scholz, F., Eds.; Springer: Berlin, 2013; pp 331–332.

+3.0 V vs. Na/Na^+ we observe an irreversible anodic feature with minimal scan rate dependence, which we assign to the oxidation of our graphite electrode; prolonged electrolysis at this potential will result in visible corrosion of the otherwise-inert graphite.

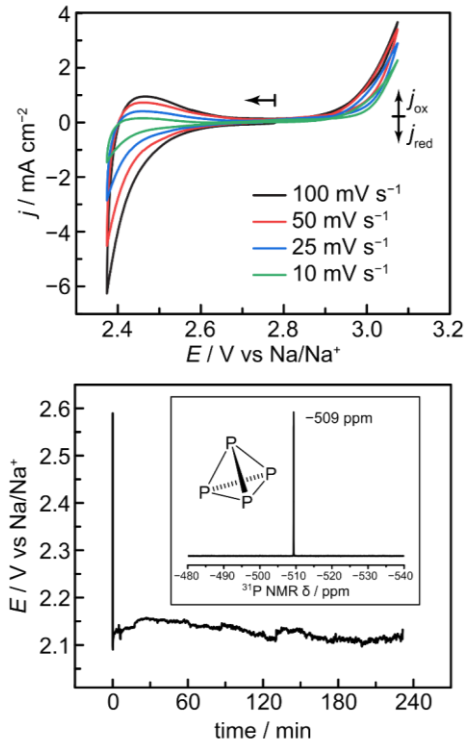

***Figure 2-7**. (top) Cyclic voltammograms of a graphite electrode in molten sodium trimetaphosphate at 800 °C. Arrow indicates point of initiation and direction of scan. (bottom) Chronopotentiometry trace of molten sodium trimetaphosphate electrolysis at a current density of 48 mA·cm^{-2}. (bottom, inset) proton-coupled ^{31}P NMR spectrum of electrogenerated P_4 dissolved in CS_2.*

Steady-state electrolysis was used to determine the product of electroreduction and the faradaic efficiency of its formation. Bulk electrolysis at a fixed current density of 48 mA·cm^{-2} results in a steady potential of +2.1 V vs. Na/Na^+ (**Figure 2-7**, bottom) over a time scale of hours (see A-2.4 – Longer-Term Electrolysis for additional details). Electrolysis in this potential region with sustained flow of N_2 gas through the cathode chamber results in the formation of pyrophoric yellow-white crystals (**Figure A-7a**) in the cold trap. ^{31}P NMR analysis of these waxy crystals in carbon disulfide (**Figure 2-7**, bottom inset), reveals a single peak at a chemical shift of −509.4 ppm vs an 85% H_3PO_4 reference, which is highly characteristic of white phosphorus.[26] If the glass trap is not lined with aluminum foil, these crystals will slowly decay over the course of several hours into a reddish-brown coating (**Figure A-7b**), consistent with the photoconversion of molecular white phosphorus to polymeric red phosphorus. Additional accumulations of red phosphorus accrete on tubing and surfaces near the reactor head (**Figure 1-8**). These products are generated exclusively upon the passage of current, as collection experiments performed at open circuit over the course of 12 hours yielded no condensate on the reactor head nor observable products in the bleach or cold traps. Following electrolysis, red and white phosphorous residues in the trap and associated transfer lines were oxidized with bleach for quantification by integration of proton-coupled ^{31}P NMR against an

[26] Seitz, A. E.; Hippauf, F.; Kremer, W.; Kaskel, S.; Scheer, M. *Nat. Commun.* **2018**, *9* (1), 2–7.

internal standard (see section A-1.3b – Quantitative ^{31P} NMR and **Figure A-9 to Figure A-10**). While the isolated yield of volatilized phosphorus products is highly dependent on the integrity of the O-ring reactor seals at temperature, we observe under optimal conditions a peak isolated yield of elemental phosphorus of 64.5% relative to the charge passed, for the four-hour galvanostatic electrolysis pictured in **Figure 2-7**. Accounting for the 68% reactor gas-flow retention rate (thereby accounting for P_4 losses from gas leakage), this isolated yield corresponds to a faradaic yield of for P_4 evolution. We note that this gas leakage is attributed to the poor thermal stability of the perfluoroelastomer O-ring seals employed in our laboratory-scale electrochemical setup; incumbent electrochemical devices (such as solid-oxide electrolyzers) utilize metal, ceramic, and/or glass based seals that are stable to higher temperatures and pressures than those demanded in this process,[27] and thus, we envision that increased gas collection efficiency can be realized with improved engineering of a larger scale reactor. In line with this high estimated FE for P_4 production, post-electrolysis analysis of the electrode surface by XPS and the electrolyte by ^{31}P NMR shows no accumulation of P(III) species (see sections A-1.3b – Quantitative ^{31P} NMR and A-2.6 – XPS of Graphite Cathode Tips). In contrast to legacy and contemporaneous studies of phosphate electrolysis that omit quantitative product analysis,[6,9–15] our spectroscopic and faradaic efficiency data provide the first numerical evidence that P_4 is the predominant cathodic product of metaphosphate electrolysis.

As little thermochemical reference data on condensed phosphate melts exists, a theoretical energetic efficiency for this process cannot be readily calculated and must instead be measured empirically. In particular, the excess energy or overpotential, η, required to drive PRR in this system relative to the thermodynamic minimum is necessary. Calculating η requires knowledge of the thermodynamic equilibrium reduction potential E_{eq} for the P^V to $P^{(0)}$ redox couple under the conditions of our electrolysis, as the former is defined in terms of the latter: $E = E_{eq} + \eta$. Obtaining this information requires a direct probe of this minimum potential at which the reverse oxidation of $P^{(0)}$ to P^V can occur; however, the cathodic product, white phosphorus, rapidly escapes from the electrode interface due to its gaseous nature at the temperature of reaction. This challenge of increasing residency time of the $P^{(0)}$ product, was ultimately addressed in a separate study[19] by employing a graphite cathode with a concave depression capable of trapping a P_4 bubble, with the aim of establishing a $PO_3^- \rightleftharpoons P_4$ equilibrium at the graphite-metaphosphate-phosphorus triple-phase boundary. As was discovered, a graphite electrode can catalyze both anodic and cathodic half-reactions, the open-circuit potential (OCP) recorded in the presence of reactant, polyphosphate, and the product, white phosphorus gas, provides an estimate of the equilibrium potential E_{eq} for the reaction.[28]

[27] Mahapatra, M. K.; Lu, K. *Mater. Sci. Eng. R Reports* **2010**, *67* (5–6), 65–85.

[28] Bard, A. J.; Faulkner, L. R. *Electrochemical Methods: Fundamentals and Applications*, 2nd ed.; Wiley: New York, 2000.
Need melville

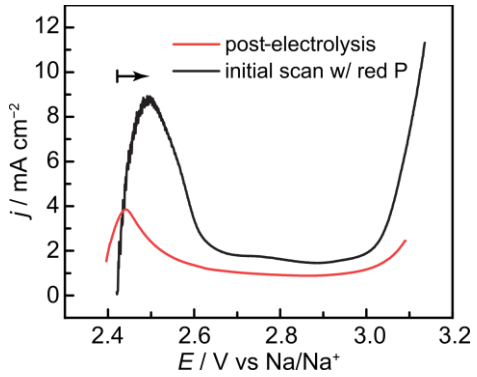

***Figure 2-8**. Linear-sweep voltammograms scanning oxidatively from OCP at 100 mV·s^{-1} with hollowed graphite electrodes containing electrosynthesized (red) and chemically generated (black) P_4. Reproduced from Melville, J. F.; Licini, A. J.; Surendranath, Y. ACS Cent. Sci. 2023.*[19]

Using the electrochemical setup, the PRR equilibrium potential, E_{eq}, was estimated in a separate study to be +2.45 V vs. Na/Na$^+$ by observation of the oxidation of electrostatically-generated white phosphorus.[19] The other peak of the redox couple $PO_3^- \rightleftharpoons P_4$ was separately confirmed via chemical generation of white phosphorus through packing of the cone electrode with red phosphorus, followed by a thermal decomposition in the melt before an oxidative sweep that demonstrated a peak at 2.38 V vs. Na/Na$^+$.[19] The confluence of these two findings suggests that a reversible equilibrium exists between the $PO_3^- \rightleftharpoons P_4$ equilibrium which sits at approximately 2.4 V vs. Na/Na$^+$ in a metaphosphate melt. Furthermore, comparing these values to the onset potentials observed in **Figure 2-7** highlight that P_4 electrogeneration occurs near the thermodynamic limit under these conditions. This product-dosing methodology allowed for steady-state voltages to be reported as true overpotentials η (**Figure 2-9**).

As previously mentioned, the reduction of PO_3^- to P_4 generates Lux basic oxide equivalents, which are consumed in this system via cleavage of Lux acidic phosphoryl anhydride linkages in the electrolyte (**Figure A-13**). To assess the kinetic role of these linkages in facilitating PRR, we performed an initial survey of Lux acidity conditions via the dissolution of aluminum oxide powder or sodium orthophosphate to generate several melts with anhydride concentrations ranging from 9.02 mol·kg^{-1} (2% orthophosphate in metaphosphate) to 9.8 mol·kg^{-1}. We observed a general trend wherein the more basic melts demonstrated steady-state reduction currents at more negative voltages than those in the more acidic pure metaphosphate. This principle was later interrogated in a more robust and rigorous fashion in a separate study[19] through the study of a series of melts of varying anhydride concentration, ranging from 5.4 mol·kg^{-1} to 9.8 mol·kg^{-1}, via cyclic voltammetry (CV) and potentiometry. The concentrations were chosen to correspond to the anhydride concentrations of pure sodium tripolyphosphate, tetrapolyphosphate, decapolyphosphate, and metaphosphate (**Table A-2**). This study also investigated the potential dependence of the graphite psuedoreference, which was found to vary linearly with anhydride molality (**Figure 2-9,** top inset). CV data of across those electrolytes are reproduced below (**Figure 2-9, top**), plotted on a common Na/Na$^+$ reference scale (**Figure 2-9 top**).

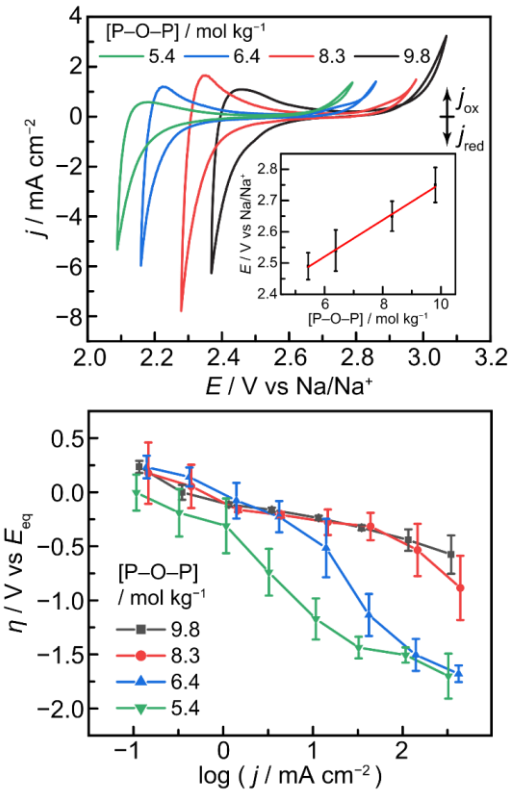

Figure 2-9. *(top) Cyclic voltammograms (scan rate = 100 mV·s^{-1}) of condensed sodium phosphate melts, reproduced from Melville, J. F.; Licini, A. J.; Surendranath, Y. ACS Cent. Sci. 2023.[19] [P—O—P] denotes the molal concentration of phosphoryl anhydride linkages in the melt, corresponding in decreasing order to the anhydride concentrations of pure sodium metaphosphate, decapolyphosphate, tetrapolyphos-phate, and tripolyphosphate melts. (top, inset) Plot of graphite pseudoreference open-circuit potentials against an Na/Na$^+$ reference electrode as a function of phosphoryl anhydride linkage concentration. Error bars represent 95% confidence intervals as collected from three independent experimental setups. (bottom) Plot of phosphate reduction overpotential as a function of chronopotentiometric current density in sodium trimetaphosphate, decapolyphosphate, tetrapolyphosphate, and tripolyphosphate melts. Error bars represent 95% confidence intervals of a set of three independent experimental setups, each setup itself being performed in triplicate, for a total of nine data points.*

These data reveal a positive shift in the PRR wave by ~250 mV as the anhydride concentration increases from 5.4 mol·kg^{-1} to 9.8 mol·kg^{-1}. In effect, as the Lux acidity of the medium increases with rising anhydride fraction, PRR becomes increasingly favorable – comparable to the potential shift observed for proton-coupled electrochemical reactions in water as the pH decreases. These data highlight that phosphate electroreduction is highly sensitive to the Lux acidity of the melt, providing a valuable handle that can be tuned to optimize the efficiency and durability of P_4 electrosynthesis. In accordance with **Scheme 2-1**, we find that addition of phosphoric acid to an anhydride-depleted melt restores the Lux acidity of the medium and regenerates the electrochemical features of a freshly-prepared trimetaphosphate melt (see section A-2.1 – Replenishment of Anhydride-Depleted Melt with Phosphoric Acid and **Figure A-15** to **Figure A-16**). We also found that varying the Lux acidity also serves to modulate the solubility of spectator ions such as Ca^{2+} (see A-2.3 – Solubility of Calcium in Condensed Phosphate Melts). Modulating the Lux acidity

of alternative fluxes such as $CaCl_2$ could additionally serve to promote P_4 electrosynthesis across a wide range of reaction media.[29]

Insights into the mechanism of PRR may be gleaned by analyzing the steady-state current-overpotential (Tafel) behavior of the system. In anhydride-rich pure trimetaphosphate melts, which we analyzed in triplicate in data that was later incorporated into the acidity dependence study (**Figure 2-9** bottom, black trace), we observe a roughly log-linear scaling in current and overpotential across a range of 3.5 orders of magnitude in current density, with current densities in excess of −300 $mA \cdot cm^{-2}$ accessible at modest overpotentials of −500 mV. In the pure metaphosphate melt we observe a Tafel slope of 150 $mV \cdot dec^{-1}$, corresponding to an empirical transfer coefficient of $b \approx 1.4$. This accords with an ideal transfer coefficient of 1.5, for a mechanism involving a reversible one-electron transfer followed by a rate-limiting one-electron transfer step.[30,31] In the context of phosphate reduction, a mechanistic sequence involving quasi-equilibrium P^V to P^{IV} reduction, followed by rate-limiting P^{IV} to P^{III} reduction, would be consistent with the observed Tafel behavior. This electrogenerated P^{III} species may then proceed to $P^{(0)}$ via rapid electroreduction or disproportionation.[32]

The observed Tafel behavior also demonstrates the importance of the Lux acidity in this system. Within error, the Tafel plots overlay at low overpotential, but a progressive deviation from linearity is observed at higher overpotentials and current densities as the Lux acidity of the melt decreases (black to red to blue to green in **Figure 2-9**, bottom). For the melts with the lowest anhydride population, the Tafel plots recoalesce at a −1.5 V overpotential. In line with literature reports and thermochemical reference data, this data was imputed to a high overpotential region to the reduction of orthophosphate generated at the electrode surface.[12,13,33–39] Thus, we attribute this transition in the Tafel behavior to the local consumption of anhydrides near the electrode surface, a phenomenon that occurs at lower current densities for melts with lower bulk Lux acidities. We note that while a high anhydride population permits P_4 production at reduced overpotentials, any anode reaction must regenerate these anhydride linkages, potentially introducing a countervailing overpotential penalty on the anode. However, just as the kinetics of aqueous half reactions such as hydrogen evolution display complex non-monotonic trends with pH,[40] we too find that graphite oxidation is less sensitive to changes in Lux acidity (see section A-2.5 – Steady-State Kinetics of Graphite Rod Oxidation and **Figure A-20**) than PRR. Notwithstanding, for the PRR, the anhydride

[29] Yang, X.; Nohira, T. *ACS Sustain. Chem. Eng.* **2020**, *8* (36), 13784–13792.
[30] Bockris, J. O.; Nagy, Z. *J. Chem. Educ.* **1973**, *50* (12), 839–843.
[31] Taylor, R. J.; Humffray, A. A. *J. Electroanal. Chem.* **1975**, *64*, 63–84.
[32] Liu, D.; Li, X.; Wei, L.; Zhang, T.; Wang, A.; Liu, C.; Prins, R. *Dalt. Trans.* **2017**, *46* (19), 6366–6378.
[33] Guan, J.; Liu, D.; Zhu, Z.; Tománek, D. Two-Dimensional Phosphorus Carbide: Competition between sp^2 and sp^3 Bonding. *Nano Lett.* **2016**, *16*, 3247–3252.
[34] Ma, X.; Zhou, J.; Yang, T.; Li, D.; Feng, Y. P. Phase diagram and superlattice structures of monolayer phosphorus carbide $P_xC_{(1-x)}$. *Phys. Rev. Mater.* **2021**, *5*, 024005.
[35] Inzelt, G. Pseudo-reference electrodes. In *Handbook of Reference Electrodes*; Inzelt, G.; Lewenstam, A.; Scholz, F., Eds.; Springer: Berlin, **2013**; pp 331–332.
[36] Seitz, A. E.; Hippauf, F.; Kremer, W.; Kaskel, S.; Scheer, M. Facile storage and release of white phosphorus and yellow arsenic. *Nat. Commun.* **2018**, *9*, 2–7.
[37] Mahapatra, M. K.; Lu, K. Glass-based seals for solid oxide fuel and electrolyzer cells – A review. *Materials Science and Engineering: R: Reports*. **2010**, *67*, 65–85.
[38] Bard, A. J.; Faulkner, L. R. 11.8 Stripping Analysis. In *Electrochemical Methods: Fundamentals and Applications*, 2nd ed.; Wiley: New York, **2000**; pp 458–464.
[39] Morey, G. W. The system sodium metaphosphate—calcium metaphosphate. *J. Am. Chem. Soc.* **1952**, *74*, 5783-5784.
[40] Jung, O.; Jackson, M. N.; Bisbey, R. P.; Kogan, N. E.; Surendranath, Y. *Joule* **2022**, *6* (2), 476–493.

linkages in these melts play a key promoting role by functioning as preassociated Lewis acids, promoting P—O cleavage and dramatically reducing the overpotential for P_4 synthesis by nearly a full volt, by direct analogy to prior reports of Lewis acid-promoted reduction of organophosphine oxides.[41] Together, these factors pay off in an overall voltage that, factoring in the thermodynamics of the proposed reagents and products (section A-2.7 – Estimation of Power Efficiency), compares favorably with the thermal process.

2.3: CONCLUSIONS

This work establishes a foundation for investigating phosphate electroreduction in molten salts. We present a set of electroanalytical methodologies capable of quantifying the overpotential, selectivity, and efficiency of phosphate reduction, and use these tools to compare reactivity across a continuum of electrolyte compositions with varying Lux acidity. These studies reveal that Lux acidic phosphoryl anhydride moieties are powerful activators of P—O bonds, enabling the reversible 20-electron reduction of phosphate to white phosphorus and the sustained production of P_4 at high faradaic efficiency and low overpotentials.

The versatility of the condensed phosphate electrolyte system opens the door to numerous future studies towards decarbonization of the phosphorus industry. The fundamental insights presented here about the role of Lux acidity in phosphate electroreduction suggest that phosphoryl anhydride moieties may serve to promote phosphate reduction across a wide array of electrolyte compositions.[12,13,29,42,43] Complementarily, the full decarbonization of P_4 electrosynthesis (like many industrial electrolyses, including the Hall process) requires the development of stable and efficient oxygen-evolving anodes. Analogous to the promotion of oxygen evolution in alkaline aqueous electrolytes,[44,45] oxygen evolution in molten salts may be promoted by modulating the Lux basicity of the electrolyte,[15] providing a powerful handle for balancing anode and cathode efficiency, selectivity, and durability. Cation studies present an orthogonal avenue of inquiry; the melt cation composition may be varied to tune half-reaction selectivity, while eutectic cation mixtures could serve to further reduce the operating temperature of phosphorus electrosynthesis and enable combined solar-thermal routes to low-carbon P_4 synthesis.[10,46,47] Given the imperative to decarbonize all sectors of the chemical industry, continued fundamental study of electrolytic phosphorus synthesis may one day enable replacement of the thermal process altogether.

2.4: ABBREVIATIONS

PRR, phosphate reduction reaction; W.E., working electrode; R.E., reference electrode; C.E., counter electrode; GC, gas chromatography; CV, cyclic voltammetry; NMR, nuclear magnetic resonance; OCP, open-circuit potential; LSV, linear sweep voltammetry.

---

[41] Elias, J. S.; Costentin, C.; Nocera, D. G. *J. Am. Chem. Soc.* **2018**, *140* (42), 13711–13718.
[42] Morey, G. W. *J. Am. Chem. Soc.* **1952**, *74* (22), 5783–5784.
[43] Voskresenskaya, N. K.; Sokolova, I. D. *Russ. Chem. Rev.* **1969**, *38*, 862−872.
[44] Gerken, J. B.; McAlpin, J. G.; Chen, J. Y. C.; Rigsby, M. L.; Casey, W. H.; Britt, R. D.; Stahl, S. S. *J. Am. Chem. Soc.* **2011**, *133*, 14431−14442.
[45] Bediako, D. K.; Surendranath, Y.; Nocera, D. G. *J. Am. Chem. Soc.* **2013**, *135* (9), 3662–3674.
[46] Vignarooban, K.; Xu, X.; Arvay, A.; Hsu, K.; Kannan, A. M. *Appl. Energy.* **2015**, *146*, 383−396.
[47] Licht, S.; Wu, H. *J. Phys. Chem. C* **2011**, *115*, 25138−25147.

2.5: REFERENCES

(1) Schipper, W. *Eur. J. Inorg. Chem.* **2014**, No. 10, 1567–1571.

(2) Emsley, J. *The 13th Element: The Sordid Tale of Murder, Fire, and Phosphorus*; Wiley: New York, 2000.

(3) Diskowski, H.; Hofmann, T. *Ullmann's Encyclopedia of Industrial Chemistry*; Wiley-VCH: Weinheim, Germany, 2012; Vol. 26, pp 725–746.

(4) Geeson, M. B.; Cummins, C. C. *Science (80-.).* **2018**, *359*, 1383–1385.

(5) Geeson, M. B.; Cummins, C. C. *ACS Cent. Sci.* **2020**, *6* (6), 848–860.

(6) Lux, H. *Zeitschrift für Elektrochemie und Angew. Phys. Chemie* **1949**, *45* (1), 41–43.

(7) Flood, H.; Förland, T. *Acta Chem. Scand.* **1947**, *1* (6), 592–604.

(8) Drago, R. S.; Whitten, K. W. *Inorg. Chem.* **1966**, *5* (4), 677–682.

(9) Centnerzwer, M.; Szper, J. *Bull. Polish Acad. Sci.* **1931**, 364–368.

(10) Caton, R. D.; Freund, H. *Anal. Chem.* **1963**, *35* (13), 2103–2108.

(11) Laitinen, H. A.; Lucas, K. R. *J. Electroanal. Chem.* **1966**, *12*, 553–563.

(12) Franks, E.; Inman, D. *J. Electroanal. Chem.* **1970**, *26*, 13–26.

(13) Franks, E.; Inman, D. *J. Appl. Electrochem.* **1971**, *14*, 73–78.

(14) Casey, E. J.; Dubois, A. R. *Can. J. Chem.* **1971**, *49*, 2733–2745.

(15) Casey, E. J.; Dubois, A. R.; Gorman, R. W. In *Corrosion*; 1975; Vol. 31, pp 358–363.

(16) Centre for Research in Computational Thermochemistry. FTsalt - FACT Salt Phase Diagrams https://www.crct.polymtl.ca/fact/documentation/FTsalt/FTsalt_Figs.htm (accessed Feb 18, 2023).

(17) Wang, L. L.; Wallace, T. C. *Metall. Mater. Trans. B* **1996**, *27* (1), 141–146.

(18) Van Wazer, J. R. In *Phosphorus and its Compounds, Vol. I*; Interscience: New York, 1958; pp 717–800.

(19) Melville, J. F.; Licini, A. J.; Surendranath, Y. *ACS Cent. Sci.* **2023**, *9* (3), 373-380.

(20) Greenfield, S.; Clift, M. *Analytical Chemistry of the Condensed Phosphates*; Pergamon: Oxford, 1975.

(21) Carenco, S.; Hu, Y.; Florea, I.; Ersen, O.; Boissière, C.; Mézailles, N.; Sanchez, C. *Chem. Mater.* **2012**, *24*, 4134–4145.

(22) Carenco, S.; Portehault, D.; Boissière, C.; Mézailles, N.; Sanchez, C. *Adv. Mater.* **2014**, *26* (3), 371–390.

(23) Guan, J.; Liu, D.; Zhu, Z.; Tománek, D. *Nano Lett.* **2016**, *16*, 3247–3252.

(24) Ma, X.; Zhou, J.; Yang, T.; Li, D.; Feng, Y. P. *Phys. Rev. Mater.* **2021**, *5*, 024005.

(25) Inzelt, G. In *Handbook of Reference Electrodes*; Inzelt, G., Lewenstam, A., Scholz, F., Eds.; Springer: Berlin, 2013; pp 331–332.

(26) Seitz, A. E.; Hippauf, F.; Kremer, W.; Kaskel, S.; Scheer, M. *Nat. Commun.* **2018**, *9* (1), 2–7.

(27) Mahapatra, M. K.; Lu, K. *Mater. Sci. Eng. R Reports* **2010**, *67* (5–6), 65–85.

(28) Bard, A. J.; Faulkner, L. R. *Electrochemical Methods: Fundamentals and Applications*, 2nd ed.; Wiley: New York, 2000.

(29) Yang, X.; Nohira, T. *ACS Sustain. Chem. Eng.* **2020**, *8* (36), 13784–13792.

(30) Bockris, J. O.; Nagy, Z. *J. Chem. Educ.* **1973**, *50* (12), 839–843.

(31) Taylor, R. J.; Humffray, A. A. *J. Electroanal. Chem.* **1975**, *64*, 63–84.

(32) Liu, D.; Li, X.; Wei, L.; Zhang, T.; Wang, A.; Liu, C.; Prins, R. *Dalt. Trans.* **2017**, *46* (19), 6366–6378.

(33) Stephenson, C. C.; Potter, R. L.; Maple, T. G.; Morrow, J. C. *J. Chem. Thermodyn.* **1969**, *1*, 59–76.

(34) Chase, M. *J. Phys. Chem. Ref. Data Monogr.* **1998**, 1948–1951.

(35) Cox, J. D.; Wagman, D. D.; Medvedev, V. A. *CODATA Key Values for Thermodynamics, 1984*; 1984.

(36) Irving, R. J.; McKerrell, H. *Trans. Faraday Soc.* **1967**, *63*, 2913–2916.

(37) Ashcroft, S. J.; Keen, E.; Mortimer, C. T. *Trans. Faraday Soc.* **1969**, *65*, 2851−2855.

(38) Rard, J. A.; Wolery, T. J. *J. Solut. Chem.* **2007**, *36*, 1585−1599.

(39) Vieillard, P.; Tardy, Y. In *Phosphate Minerals*; Nriagu, J. O., Moore, P. B., Eds.; Springer: Berlin, 1984; pp 171–198.

(40) Jung, O.; Jackson, M. N.; Bisbey, R. P.; Kogan, N. E.; Surendranath, Y. *Joule* **2022**, *6* (2), 476–493.

(41) Elias, J. S.; Costentin, C.; Nocera, D. G. *J. Am. Chem. Soc.* **2018**, *140* (42), 13711–13718.

(42) Morey, G. W. *J. Am. Chem. Soc.* **1952**, *74* (22), 5783–5784.

(43) Voskresenskaya, N. K.; Sokolova, I. D. *Russ. Chem. Rev.* **1969**, *38*, 862−872.

(44) Gerken, J. B.; McAlpin, J. G.; Chen, J. Y. C.; Rigsby, M. L.; Casey, W. H.; Britt, R. D.; Stahl, S. S. *J. Am. Chem. Soc.* **2011**, *133*, 14431−14442.

(45) Bediako, D. K.; Surendranath, Y.; Nocera, D. G. *J. Am. Chem. Soc.* **2013**, *135* (9), 3662–3674.

(46) Vignarooban, K.; Xu, X.; Arvay, A.; Hsu, K.; Kannan, A. M. *Appl. Energy.* **2015**, *146*, 383−396.

(47) Licht, S.; Wu, H. *J. Phys. Chem. C* **2011**, *115*, 25138−25147.

Chapter 3 – Anodic Oxidation of Sodium Polyphosphates to Oxygen

This chapter contains work that was obtained collaboratively with another researcher at the Massachusetts Institute of Technology (Sophia Weng). Specifically, the following contributions are noted:

The SEM images presented in **Figure 3-4**, **Figure 3-5**, and **Figure 3-6** were collected by Sophia Weng, accompanied in some cases by EDX analysis. Sophia Weng also performed XPS analysis on certain samples.

3.1: PREFACE

As discussed in Chapter 1, the production of white phosphorus is a critical chemical industry which generates a considerable amount of carbon dioxide and negative environmental impacts.[1–3] Although alternative processes are emerging to circumvent P_4 as an intermediate,[4,5] the phosphorus chemical value chain relies upon the "thermal process" (Equation 1), which employs extremely forcing conditions to drive the reduction of phosphate to P_4 by carbon coke.

$$2\ Ca_3(PO_4)_2 + 6\ SiO_2 + 10\ C \rightarrow 6\ CaSiO_3 + 10\ CO + P_4 \quad (1)$$

This process occurs at temperatures of 1500 °C to generate white phosphorus, calcium silicate slag and carbon monoxide,[3] but while these particular reaction conditions have been fixed for many decades, this process may be abstracted through the lens of Lux-Flood acid-base theory, with orthophosphate acting as a 'Lux basic' oxide donor and silica acting as a 'Lux acidic' oxide acceptor.[6–8] If the reduction reaction can be performed through an external circuit in the rich chemistry of molten metaphosphates and an alternative Lux acid to accept oxides, the result will be a drastically milder, more environmentally friendly electrolysis process (Scheme 3-1).

Scheme 3-1. Half-reaction and overall electrolysis scheme for metaphosphate electrolysis and regeneration.

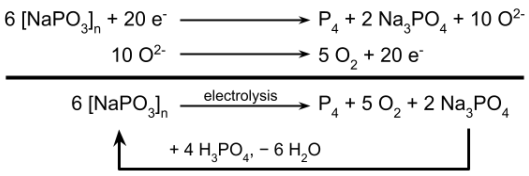

[1] Schipper, W. *Eur. J. Inorg. Chem.* **2014**, No. 10, 1567–1571.
[2] Emsley, J. *The 13th Element: The Sordid Tale of Murder, Fire, and Phosphorus*; Wiley: New York, 2000.
[3] Diskowski, H.; Hofmann, T. *Ullmann's Encyclopedia of Industrial Chemistry*; Wiley-VCH: Weinheim, Germany, 2012; Vol. 26, pp 725–746.
[4] Geeson, M. B.; Cummins, C. C. *Science (80-.).* **2018**, *359*, 1383–1385.
[5] Geeson, M. B.; Cummins, C. C. *ACS Cent. Sci.* **2020**, *6* (6), 848–860.
[6] Lux, H. *Zeitschrift für Elektrochemie und Angew. Phys. Chemie* **1949**, *45* (1), 41–43.
[7] Flood, H.; Förland, T. *Acta Chem. Scand.* **1947**, *1* (6), 592–604.
[8] Drago, R. S.; Whitten, K. W. *Inorg. Chem.* **1966**, *5* (4), 677–682.

Previously in Chapter 2 and in a separate companion study,[9] the cathodic reaction was identified as the evolution of white phosphorus and analyzed under a variety of solvent conditions. The reaction was found to be promoted by the presence of Lux acid, which served to remove oxide ions from the reducing phosphate species. However, this reaction must be paired with an anodic reaction, and hitherto this reaction was graphite oxidation. In order to produce a carbon-free process, a robust oxygen evolution anode must be identified. The literature has previously characterized the kinetics of the oxygen evolution reaction on platinum,[10–12] and the oxide dependence of the O_2/O^{2-} couple's open circuit potential on platinum is well-characterized,[13–15] but corrosion data under polarization is scarce and merely qualitative, while corrosion studies at open circuit potentials are not reflective of industrially relevant conditions.[10,11,16] Thus, robust pairing of product collection, electrochemical measurements and corrosion quantification are required to analyze the factors at work in oxygen evolution and the related anodic corrosion of the anode. To this end, we present a toolbox of techniques for quantifying anodic corrosion, selectivity, and efficiency across a range of electrolyte compositions, and employ these tools to examine the governing attributes which underpin the oxygen evolution reaction (OER) and anodic corrosion on three candidate metals—platinum (Pt), gold (Au) and iridium (Ir).

3.2: RESULTS AND DISCUSSION

In order to accurately monitor oxygen evolution current density and corrosion, we first developed methods to gauge and control electrode surface area. Molten salts are generally viscous and display low gas solubility,[17–19] and among molten salts, molten polyphosphates are especially viscous due to the presence of extended polyphosphate chains.[20,21] We previously utilized this principle in the separated reactor design to inhibit the crossover of gases between the working and counter electrodes, permitting oxygen and phosphorus to evolve without reacting. However, these gas-exclusionary characteristics render traditional flat, sheathed electrode geometries ineffective for investigating gas-evolving electrochemical reactions in this medium. As bubbles form on a downward-facing electrode surface, they spread out and block the surface of the electrode through processes commonly termed "anode effects."[22,23] This physical blockage results in decreased transportation of reactant to the surface and

[9] Melville, J. F.; Licini, A. J.; Surendranath, Y. *ACS Cent. Sci.* **2023**, *9* (3), 373-380.
[10] Casey, E. J.; Dubois, A. R. *Can. J. Chem.* **1971**, *49*, 2733–2745.
[11] Casey, E. J.; Dubois, A. R.; Gorman, R. W. In *Corrosion*; 1975; Vol. 31, pp 358–363.
[12] Higgins, J. K. *J. Electrochem. Soc.* **1993**, *140* (12), 3436–3448.
[13] Delimarskii, Y. K.; Andreeva, V. N. *Zh. Neorg. Khim.* **1960**, *5* (5), 540–542.
[14] Andreeva, V. N.; Delimarskii, Y. K. *Zh. Neorg. Khim.* **1960**, *5* (9), 1008–1011.
[15] Delimarskii, Y. K.; Andreeva, V. N. *Zh. Neorg. Khim.* **1960**, *5* (8), 873–876.
[16] Fischer, B. *Platin. Met. Rev.* **1992**, *36* (1), 14–25.
[17] Ubbelohde, A. R. In *Ionic Liquids*; Inman, D., Lovering, D. G., Eds.; Plenum: New York, 1981; pp 1–6.
[18] International Union of Pure and Applied Chemistry. In *Solubility Data Series*; Lorimer, J. W., Clever, H. L., Young, C. L., Eds.; Pergamon: Oxford, 1991; Vol. 45.
[19] Liu, T. L.; Liu, W. R.; Xu, X. H. *IOP Conf. Ser. Earth Environ. Sci.* **2017**, *93* (1).
[20] Griffith, E. J.; Callis, C. F. *J. Am. Chem. Soc.* **1959**, *81* (4), 833–836.
[21] Van Wazer, J. R. In *Phosphorus and its Compounds, Vol. I*; Interscience: New York, 1958; pp 717–800.
[22] Frank, W. B.; Haupin, W. E.; Vogt, H.; Bruno, M.; Thonstad, J.; Dawless, R. K.; Kvande, H.; Taiwo, O. A. *Ullmann's Encyclopedia of Industrial Chemistry*; Wiley-VCH: Weinheim, Germany, 2012; Vol. 2, pp 483–520.
[23] Tabereaux, A. T.; Peterson, R. D. In *Treatise on Process Metallurgy*; Elsevier: Oxford, 2014; Vol. 3, pp 839–917.

increased electrical fields around the edges of the bubble, leading to increased operating voltages, flattened electrochemical features and irreproducibility. We previously minimized these gas blockages with a conical electrode design.[9] However, metal films electrochemically deposited on graphite electrodes were unstable at temperature, and crafting solid cones of precious metal would have been prohibitively costly. To work around these limitations, we instead crafted anodes by bending one end of commercially available precious metal wires (Pt, Au, Ir) into coils with 3-8 turns that were roughly 3 mm in diameter (section B-1.2b –Metal Coil Working Electrode Preparation). This coiled geometry came with tradeoffs, since, for instance, the overlapping diffusion gradients on the coil precluded traditional steady-state current analysis methods (e.g. Tafel plots, etc.).[24] However, this design enabled us to minimize depth-related variations in the wire's submerged surface area (B-1.2a –Metal Anode Working Electrode Design) without trapping evolved gases. This design choice provided the additional benefit of amplifying corrosion-based mass losses, rendering corrosion quantitation more sensitive. We initially attempted to estimate the submerged surface area via capacitance in the melt, but the pinning of metal open circuit potentials to electrochemical reactions in the polyphosphate melt precluded such analysis. Therefore, we estimated the anode surface area by evaluating the electrochemical capacitance of each coil ahead of time in an aqueous 0.1 M $NaClO_4$ solution (see section B-1.5b – Calculation of Electrochemical Surface Area).[25–27] Thus, through coil-based working electrode design choice, we were able to control electrode surface area while avoiding the transport limitations and anode effects which previously plagued literature on polyphosphate anodic reactions.

After preparing and weighing our metal anode coils, we collected electrochemical measurements in a molten salt electrochemical cell optimized for gaseous product collection (see section B-1.1 – Molten Salt Electroanalytical Reactor). We employed a sharpened graphite rod as the cathodic counter electrode for all electrochemical measurements. Our electrochemical reference electrode was a graphite pseudoreference, which we calibrated using an auxiliary Na/Na^+ electrode that we immersed at the beginning and end of each experiment (see section B-1.2e – Liquid Sodium Reference Electrode). We used a glassy carbon crucible to contain the electrolyte powder, which was either pure sodium trimetaphosphate ($Na_3(PO_3)_3$), ([P–O–P] molality = 9.8 mol kg^{-1}) or an equimolar mixture of $Na_3(PO_3)_3$ and tribasic sodium orthophosphate (Na_3PO_4) ([P–O–P] molality = 6.4 mol kg^{-1}). The cell was assembled, purged thoroughly with nitrogen and subsequently raised at 800 °C for all experiments (see section B-1.3 – Cell Assembly and High-Temperature Operation).

When we performed cyclic voltammetry on Pt, Au and Ir wires in molten polyphosphates at 100 mA cm^{-2}, we found distinct differences between the metals' individual oxidative features (**Figure 3-1**). In a phosphoryl anhydride ([P–O–P]) concentration of 6.4 mol kg^{-1}, all three of these metals demonstrate a sharp anodic feature consistent with a catalytic onset of gas evolution (**Figure 3-1a**), but the specific onset potentials varied depending on catalyst metal identity. Pt, for instance, demonstrated the most negative onset voltage, around 3.2 V vs. Na/Na^+. Because the Lux basicity of the melt was the same for all three metals, this also indicates the lowest onset potential for the catalytic reaction. The onset of catalysis for Au was comparable to that of Pt, around 3.25 V vs. Na/Na^+. Ir, however, demonstrated drastically different behavior; around the catalytic onset potential of Pt and Au, Ir instead shows a small oxidative

[24] Bard, A. J.; Faulkner, L. R. *Electrochemical Methods: Fundamentals and Applications*, 2nd ed.; Wiley: New York, 2000.
[25] Hall, A. S.; Yoon, Y.; Wuttig, A.; Surendranath, Y. *J. Am. Chem. Soc.* **2015**, *137* (47), 14834–14837.
[26] Yoon, Y.; Hall, A. S.; Surendranath, Y. *Angew. Chemie - Int. Ed.* **2016**, *55* (49), 15282–15286.
[27] Yoon, Y.; Yan, B.; Surendranath, Y. *J. Am. Chem. Soc.* **2018**, *140* (7), 2397–2400.

feature with peaks at 3.25 and 3.35 V which converge to the same potential at slower scan rates. Scan rate dependence analysis on this feature region indicates that the second peak has a higher barrier to electron transfer than the second, and that these peaks and the reductive peak observed on the return sweep are coupled, diffusion-based processes that form a redox couple (see section B-2.1 - Cyclic Voltammetry: Scan Rate Analysis of Iridium Anodic Features and **Figure B-10**). Based on these findings, we ascribe these oxidative peaks to the formation of IrO_x layer and the back-reduction peak to the reduction of IrO_x back to Ir metal. Since IrO_x is known to be a potent oxygen evolution catalyst which can exist in multiple layers, we will refer to IrO_x instead of Ir when discussing matters of oxygen evolution catalysis.[28–31] The catalytic onset of oxygen evolution on IrO_x lies at drastically more positive potentials, around 3.4 V vs. Na/Na^+. In order to confirm that the products generated in our cell were indicative of the processes observed in these catalytic onsets, we also interrogated the cyclic voltammetry behavior of these metals at higher current densities under iR compensation (**Figure 3-1b**). While Au and IrO_x showed no further peaks at more anodic poentials, Pt produced a substantial peak couched within the catalytic onset observed, a peak which is likely coupled to Pt's reductive return rate. Because the catalytic onset and observed peak coexist in the same potential range, we cannot differentiate the chemical species associated with the two processes using product collection. However, because Pt possessed the most aggressive electrochemical corrosion rates of the three metals while still predominantly generating oxygen (**Figure 3-2**), we attribute this oxidative peak to the corrosion of Pt to Pt^{2+} and the reverse peak to the re-reduction of Pt^{2+} ions in solution.

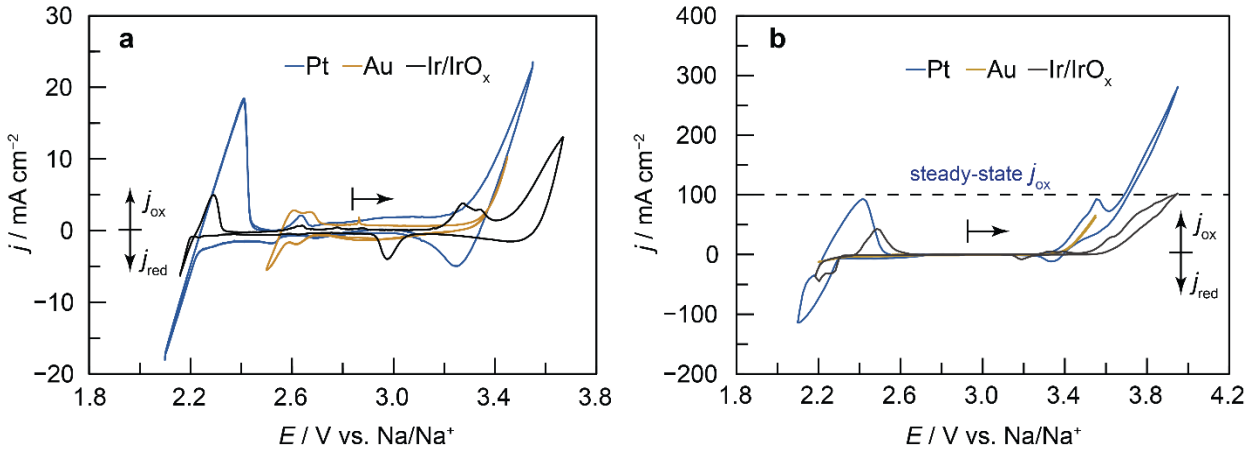

***Figure 3-1**. a) Cyclic voltammograms of Pt, Au and Ir/IrO_x metal coil anodes in molten sodium polyphosphate with a phosphoryl anhydride molality of 6.4 mol kg^{-1}, corresponding to tetrapolyphosphate. All measurements collected at a 100 mA cm^{-2} scan rate. Voltages referenced to a Na^+/Na reference electrode after calibration of graphite psuedoreference. B) same cyclic voltammetry conditions at higher current densities, with iR compensation.*

After cyclic voltammetry measurements, we performed bulk electrolyses at current densities of 100 mA cm^{-2} on these metals to characterize the products and selectivity of the anodic reaction. We performed this characterization through the use of binary gas analysis (BGA) on oxygen (the primary gas)

[28] Nunes, D. In *Metal Oxide Nanostructures: Synthesis, Properties and Applications*; Elsevier: Amsterdam, 2019; pp 103–147.
[29] Scarpelli, F.; Godbert, N.; Crispini, A.; Aiello, I. *Inorganics* **2022**, *10* (8).
[30] Altowyan, A. S.; Shaban, M.; Abdelkarem, K.; El Sayed, A. M. *Nanomaterials* **2022**, *12* (19), 1–13.
[31] Shchetkovskiy, A.; McKechnie, Timothy Sadoway, Donald R. Paramore, J.; Melendez, O.; Curreri, P. A. In *Earth and Space 2010: Engineering, Science, Construction, and Operations in Challenging Environments*; American Society of Civil Engineers: Honolulu, 2010.

within the nitrogen carrier gas stream (the secondary gas) exiting the working electrode chamber's headspace as exhaust (see section B-1.6 – Binary Gas Analysis of Gas Outflow Streams). For these trials, we studied both the Lux-acidic melt composition ([P–O–P] molality = 9.8 mol kg^{-1}) and the Lux-basic melt composition ([P–O–P] molality = 6.4 mol kg^{-1}). Regardless of metal identity or phosphoryl anhydride concentration in the melt, oxygen was incontrovertibly the dominant product of the anodic reaction at these current densities (**Figure 3-2**), with faradaic efficiencies approaching 100% in almost all cases (see section B-1.6 – Binary Gas Analysis of Gas Outflow Streams for calculation details). Within the margin of trial-to-trial variability, we find no clear trend was between the Lux basicity of the melt and the faradaic efficiency of oxygen evolution. Since the current densities in these experiments are comparable to the catalytic onsets observed via cyclic voltammetry (**Figure 3-1**), we feel confident in ascribing these onsets to the oxygen evolution reaction (OER) within the melt.

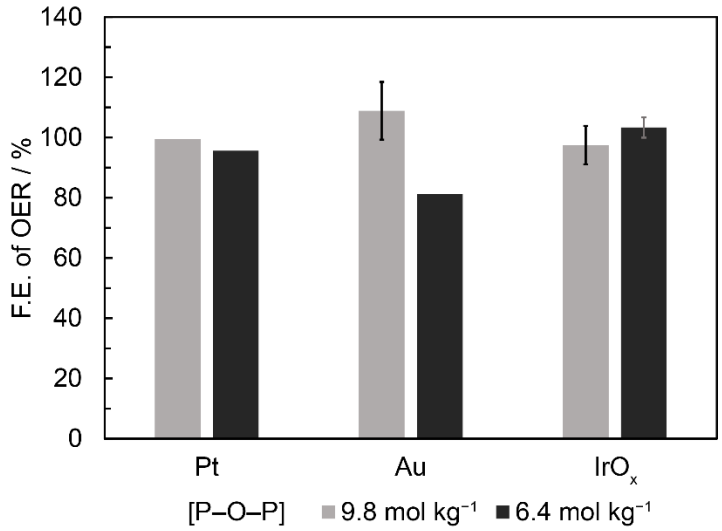

Figure 3-2. *Bar graph plotting faradaic efficiency, as a percentage of current passed, of the oxygen evolution reaction (OER) on Pt, Au and IrO_x catalysts, as measured by binary gas analysis (BGA). All current densities fixed at 100 mA cm^{-2}. (black) OER F.E. at phosphoryl anhydride concentration of molality of 9.8 mol kg^{-1}. (blue) OER F.E. at phosphoryl anhydride concentration of molality of 6.4 mol kg^{-1}. Error bars indicate 95% confidence level between two identical trials on two separate precious metal anodes.*

Following the discovery of OER's high selectivity on Pt, Au and IrO_x anodes in the melt, we subsequently used cyclic voltammetry to interrogate the potential role of Lux basicity[6–8] on the OER onset potentials. Because the melt is entirely comprised of sodium polyphosphates, the anodically active oxide reactants (O^{2-}) must be sourced from polyphosphates and subject to the acidity of the melt. Thus, we anticipated that the concentration of phosphoryl anhydride linkages ([P–O–P]) in the solution could alter the energetics of OER. To investigate this hypothesis, we collected cyclic voltammograms on Pt, Au and IrO_x under both the 9.8 mol kg^{-1} and 6.4 mol kg^{-1} [P–O–P] melt compositions (**Figure 3-3**). Indeed, as referenced to the Na/Na^+ couple, a sizeable positive shift of 100-300 mV is observed for the onset of catalytic anodic current for all three metals as the melt composition increases in acidity from 6.4 mol kg^{-1} to 9.8 mol kg^{-1} [P–O–P]. This shift indicates that the energetics of the reaction, whether thermodynamic or kinetic, are, indeed, hampered by the presence of more Lux acid, i.e. phosphoryl anhydride linkages. This observation would be consistent with two separate hypotheses. Firstly, if "end groups" within polyphosphate chains are the primary electrochemically active species for oxidation, increasing Lux acidity

would suppress oxidation by reducing their concentration in the melt. Secondly, if the rate-limiting step involves the formation of a P-O bond, increased Lux acidity would suppress oxidation by increasing the concentration of a chemical product. These two interpretations are not mutually exclusive, and our prior studies on the steady-state behavior of the anodic reaction suggest that both "end" and "middle" groups can participate in these reactions.[9] The coiled geometry of our electrodes precludes conventional steady-state current-voltage analysis which could reduce the ambiguity between these interpretations, but the anodic behaviors we observe compare favorably with those documented by Casey and Dubois on platinum in three molten polyphosphate solutions varying in composition from 9.8 to 7.7 mol kg^{-1} [P–O–P] (**Table 1-1**).[11] Interestingly, the steady-state data of their intermediate anhydride concentration (8.68 mol kg^{-1}) seems to transition from aligning with the basic voltage profile at low current densities to that of the acidic, higher-overpotential profile at high current densities. This behavior mimics a similar transition behavior we observed previously in the cathodic reaction[9] and was attributed to local generation of phosphates at the electrode surface, so the same could hold true of local ultraphosphate generation, although the unstable and hygroscopic nature of such species renders thermodynamic data difficult to collect.[20,32] If such a relationship exists for the anodic reaction as well, then increasing Lux acidity would reduce the concentration of the more easily oxidizable "end groups" and force a transition to oxidizing the more stable "middle groups" at more positive potentials. Regardless of the specific means by which Lux acidity suppresses the oxidation reaction, however, these data demonstrate that the phenomenon is not exclusive to the surface chemistry of platinum but, rather, indicative of a broader solution-phase trend in OER favorability.

[32] Van Wazer, J. R. *J. Am. Chem. Soc.* **1950**, *72* (2), 644–647.

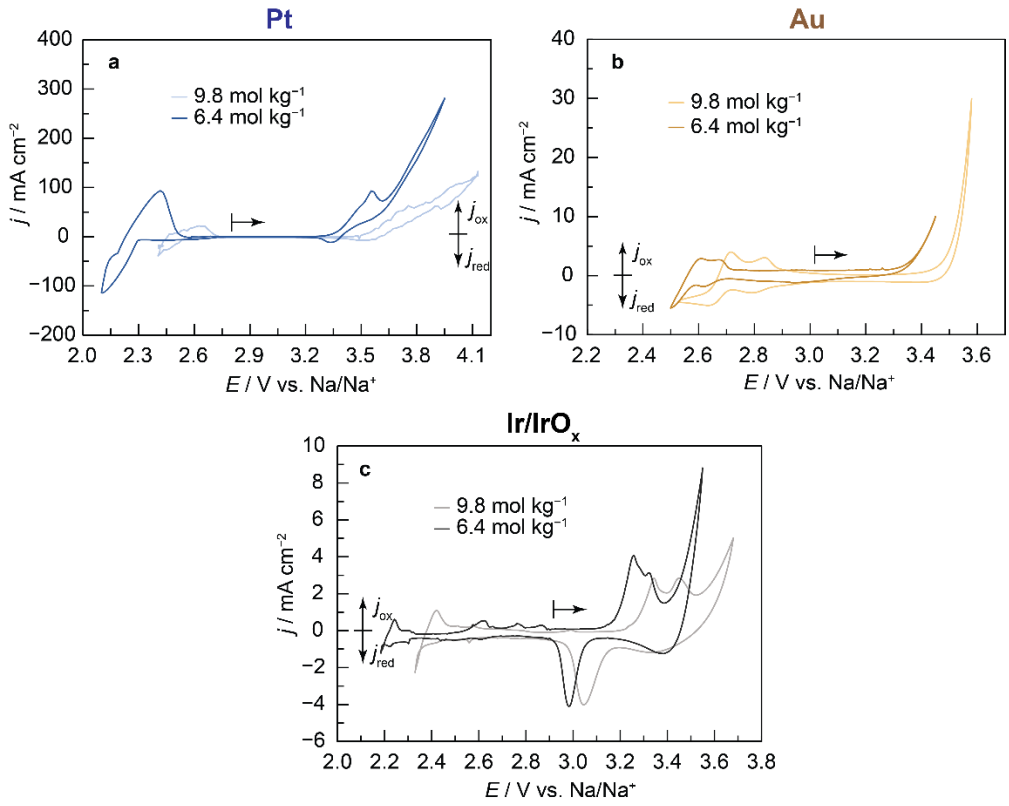

***Figure 3-3**. Cyclic voltammograms of (a) Pt, (b) Au and (c) Ir/IrO$_x$ in molten sodium polyphosphates with phosphoryl anhydride molalities of 9.8 and 6.4 mol kg^{-1}, corresponding to metaphosphate and tetrapolyphosphate, respectively. Voltages referenced to a Na$^+$/Na reference electrode.*

In parallel with the characterization of OER, we also investigated the question of anode corrosion through a combination of mass loss and imaging techniques. Mass loss, measured by massing coils before and after electrolysis, was our primary quantitative metric of corrosion (see section B-1.7a – Mass-Based Quantification of Metal Anode Corrosion). After electrolysis, we also performed secondary electron microscopy (SEM) on select metal coil samples to search for evidence of corrosion, such as pitting, flaking or dendrites. In a preliminary survey, we varied anodic current density on various gold coils under variable current densities and melt compositions to verify that corrosion was electrochemical in nature (B-2.2 – Survey of Gold Corrosion Varying Current Density and Melt Acidity and **Figure B-11**). In doing so, we found strong correlations in corrosion rate to both the anodic current density and the Lux acidity of the melt. Moreover, this dependence of corrosion on Lux acidity increased as the magnitude of the current density increased, suggesting that the factors of electrochemical oxidation and acid act in tandem phenomenologically within the confines of the primary corrosion mechanism. Bolstered by this finding, we proceeded to systematically evaluate the long-term acid-dependent corrosion of Pt, Au and Ir wires at a fixed current density of 100 mA cm^{-2}, using both a Lux-basic polyphosphate melt (9.8 mol kg^{-1} [P-O-P]) and a Lux-acidic polyphosphate melt (6.4 mol kg^{-1}).

For all three metals (**Figure 3-4** to **Figure 3-6**), we found a strong increase in corrosion rate at 100 mA cm^{-2} under the acidic condition relative to that of the basic condition. This increase in corrosion was

demonstrated both in mass loss-based corrosion quantification (**Figure 3-4** to **Figure 3-6, c**) as well as SEM images of the metal coils corroded at 6.4 mol kg^{-1} (**Figure 3-4** to **Figure 3-6, a,b**) and 9.8 mol kg^{-1} (**Figure 3-4** to **Figure 3-6, d,e**). Platinum shows the highest overall corrosion rates on average (**Figure 3-4c**), to the point that under the acidic melt conditions, only the most stable of three platinum wire samples could be accurately massed, while the other two metal coils disintegrated into fragments. Even under the basic 6.4 mol kg^{-1} condition, Pt displays an average corrosion rate of 110 mm yr^{-1}, which renders platinum prohibitively expensive to use as an industrial oxygen-evolving anode. Both the basic and acidic Pt coils show signs of pitting and corrosion under SEM imaging (**Figure 3-4a,b, d,e**), but the corrosion in the 9.8 mol kg^{-1} is substantially more severe than that of the 6.4 mol kg^{-1} sample despite being polarized for a shorter time span (3200 s vs. 4540 s in the 6.4 mol kg^{-1} melt). From a faradaic perspective, the mass loss of the electrode would account for a value ranging from 5-10% of the total current passed. This value, however, is at odds with the fact that the OER faradaic efficiency we observe is roughly 95-100% in all cases, which would indicate that nearly all the electrons pulled oxidatively from the electrolyte around the anode eventually manifest as elemental oxygen (O_2). Additionally, the SEM images of both platinum wires indicate the presence of frond-like formations which seem more like the product of dendritic growth than corrosion and pitting. We posit that these observations originate from the release of oxidized Pt^{2+} ions from the corroding electrode surface into the melt under highly oxidizing conditions, followed by the subsequent back-reduction of those ions to platinum metal by oxides in the bulk (Equations 2 and 3):

$$Pt_{(s)} \rightarrow Pt^{2+}_{(\text{in melt})} + 2\ e^{-} \quad (2)$$

$$2\ Pt^{2+}_{(\text{in melt})} + 2\ O^{2-}_{(\text{in melt})} \rightarrow 2\ Pt_{(s)} + O_{2(g)} \quad (3)$$

Such a reaction would result in the net generation of gaseous oxygen while also contributing to the observed mass loss of the platinum electrodes. The observed generation of a dark grey powdered suspension within the working electrode chamber of the cell, which we presume to be platinum particulates akin to those observed by Rhindone and Rhoads formed when platinum ions re-reduce in molten metaphosphates,[33] would also support this hypothesis. If so, these collective observations suggest that, instead of a thermodynamic process driven by the favorability of platinum oxidation, the corrosion of platinum is primarily a kinetically-driven process that results from the applied overpotentials.

[33] Rindone, G. E.; Rhoads, J. L. *J. Am. Ceram. Soc.* **1956**, *39* (5), 173–180.

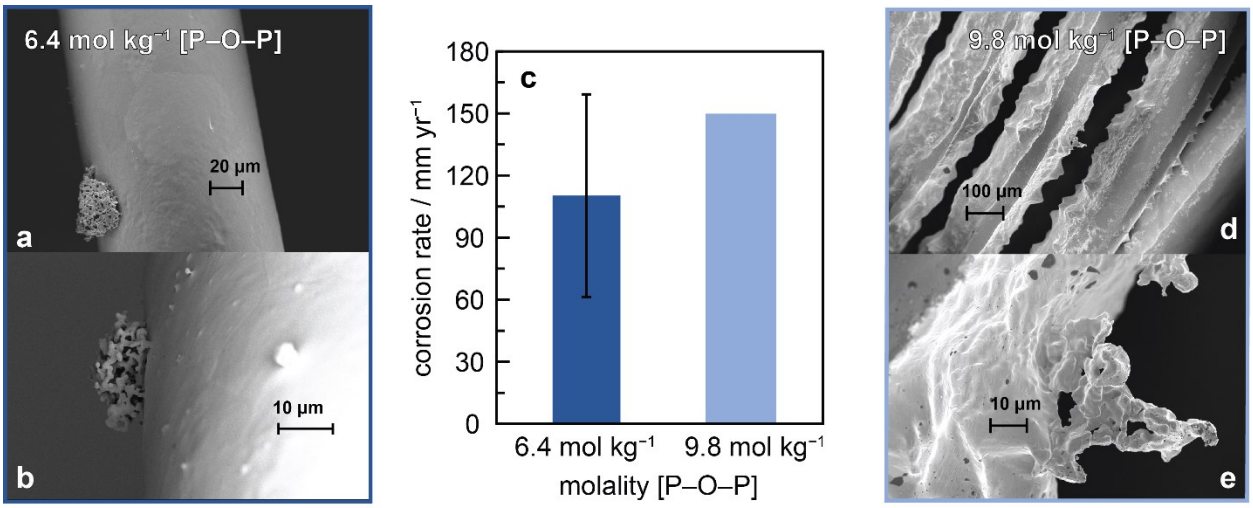

Figure 3-4. *a,b) SEM images of a platinum coil anode, with scale bars, after a prolonged anodic current of 100 mA cm^{-2} in molten sodium polyphosphate with an anhydride molality of 6.4 mol kg^{-1}. c) Indicated corrosion rate of Pt in mm yr–1 at Lux acidities of 6.4 and 9.8 mol kg^{-1} [P-O-P] with error bars indicating 95% confidence levels. Two additional trials for the 9.8 mol kg^{-1} condition were attempted, but in both cases the coil disintegrated into fragments and mass loss could not be accurately gauged. d,e) SEM images of a platinum coil anode, with scale bars, after a prolonged anodic current of 100 mA cm^{-2} in molten sodium metaphosphate with an anhydride molality of 9.8 mol kg^{-1}.*

As in the case of platinum, we find that the corrosion data collected for gold anodes (**Figure 3-5**) illustrates the kinetic control of anode control even more visibly. Gold wires tended to be more stable to long-term oxidation than platinum, so mass loss values were more accurate and, thus, the effect of acidity on corrosion is more evident. While corrosion rates for gold electrodes in basic media (6.4 mol kg^{-1} [P-O-P]) were roughly 53 mm yr^{-1} , this value quadrupled to 222 mm yr^{-1} in pure sodium metaphosphate (9.8 mol kg^{-1} [P-O-P]) (**Figure 3-5c**). While gold and iridium are both precious metal catalysts, this corrosion rate is much more tolerable than that of platinum, especially under basic conditions. Au SEM imaging not only reveals substantially less pitting and deformation of the gold electrode under basic conditions (**Figure 3-5a,b**), but also more clearly illustrates the phenomenon where the corroding electrode under acidic conditions develops frond-like dendrites. Gold from the electrode also agglomerated and welded together into highly visible macroscopic flakes which we collected and weighed. Although the reclaimable mass was variable, the amount of gold retrieved ranged from around 30-60% of the mass lost by the electrode. Similarly to platinum, the "faradaic efficiency" of this corrosion as evaluated by mass loss surpasses the margin of error observed in the faradaic efficiency of oxygen evolution, which approached 100%. Considering these finding, we posit a similar reaction scheme for the re-reduction of gold ions in solution (Equations 4 and 5):

$$Au_{(s)} \rightarrow Au^{3+}_{(\text{in melt})} + 3\ e^- \quad (4)$$

$$4\ Au^{3+}_{(\text{in melt})} + 6\ O^{2-}_{(\text{in melt})} \rightarrow 4\ Au_{(s)} + 3\ O_{2(g)} \quad (5)$$

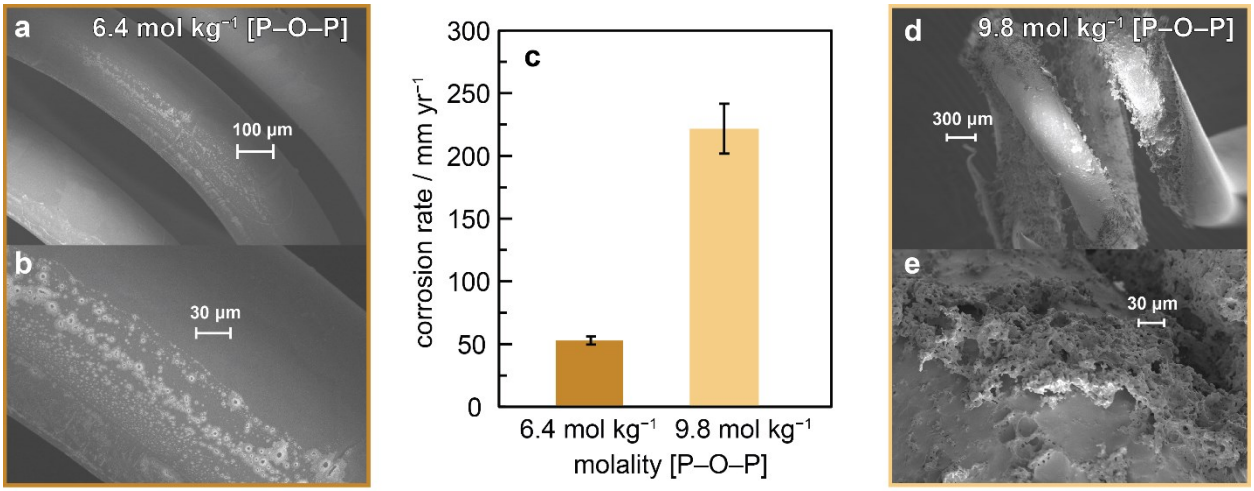

Figure 3-5. *a,b) SEM images of a gold coil anode, with scale bars, after a prolonged anodic current of 100 mA cm^{-2} in molten sodium polyphosphate with an anhydride molality of 6.4 mol kg^{-1}. c) indicated corrosion rate of Au in mm yr^{-1} at Lux acidities of 6.4 and 9.8 mol kg^{-1} [P-O-P] with error bars indicating 95% confidence levels. d,e) SEM images of a gold coil anode, with scale bars, after a prolonged anodic current of 100 mA cm^{-2} in molten sodium metaphosphate with an anhydride molality of 9.8 mol kg^{-1}.*

While both platinum and gold demonstrated very costly rates of corrosion, iridium metal (**Figure 3-6**) and its corresponding oxide IrO_x proved to be extremely resilient under current densities of 100 mA cm^{-2}. The lowest observed rate thus far was 55 mm yr^{-1} for Au in basic media, but Ir consistently showed corrosion rates of less than 2.5 mm yr^{-1} even under the most acidic conditions (9.8 mol kg^{-1} [P-O-P]), and corrosion rates reached an average as low as 0.94 mm yr^{-1} under basic conditions (6.4 mol kg^{-1} [P-O-P]) (**Figure 3-6c**). SEM imaging of the Ir coils showed little to no visible damage, to the point that under basic conditions (**Figure 3-6a,b**), we found no clear difference between the electroactive surface area and the portion of the wire that had remained above the electrolyte surface. Even under acidic conditions, the evidence of corrosion appears to be fairly superficial, consisting of sub-micrometer-thin small cracks or grooves in the surface visible only at extremely high resolutions (**Figure 3-6d,e**). This finding is especially interesting because at standard state, the aqueous standard reduction potential of IrO_x to Ir is 0.73 V vs. the standard reduction potential of oxygen, 1.23 V.[24] Thus, oxidation of iridium should theoretically be much more thermodynamically favorable than oxidation of oxides, even if the high temperatures of the melt provide an entropic driving force for the evolution of gases like oxygen. Additionally, from the cyclic voltammetry behavior, oxygen evolution appears to first require the formation of an IrO_x catalytic layer on the iridium surface, and, therefore, oxygen evolution seems to only occur on IrO_x under a significant additional overpotential (roughly 0.2 to 0.3 V) relative to gold and platinum, so the driving force for iridium oxidation should be even more extreme under these conditions. The melt is also notoriously corrosive towards oxides, even having the capability to break strong aluminum oxide bonds.[21] Additionally, iridium oxide is known to be subject to slow acid corrosion in aqueous media, and is faster for electrochemically-formed IrO_x relative to thermal IrO_x below OER potentials.[34] However, polarization at OER is reported to change the corrosion mechanism such that the predominant oxidation state of the iridium oxide changes from IrO_2 to Ir_2O_3 under polarization, increasing the iridium oxide layer's resistance to specific corrosion

[34] Jovanovič, P.; Hodnik, N.; Ruiz-Zepeda, F.; Arčon, I.; Jozinović, B.; Zorko, M.; Bele, M.; Šala, M.; Šelih, V. S.; Hočevar, S.; Gaberšček, M. *J. Am. Chem. Soc.* **2017**, *139* (36), 12837–12846.

pathways.[34] Considering the use of iridium as a corrosion-stable anode material in other molten salt systems,[31,35] this property may not be unique to aqueous media, and could result in the corrosion resistance we observe here. Thus, these collective observations suggest that, while Ir/IrO_x incurs overpotentials as an OER anode in molten metaphosphates relative to Pt and Au, its incredible stability to corrosion at high current densities renders it easily the most promising metal candidate thus far for a high-performance, corrosion-resistant oxygen evolution anode material in metaphosphates.

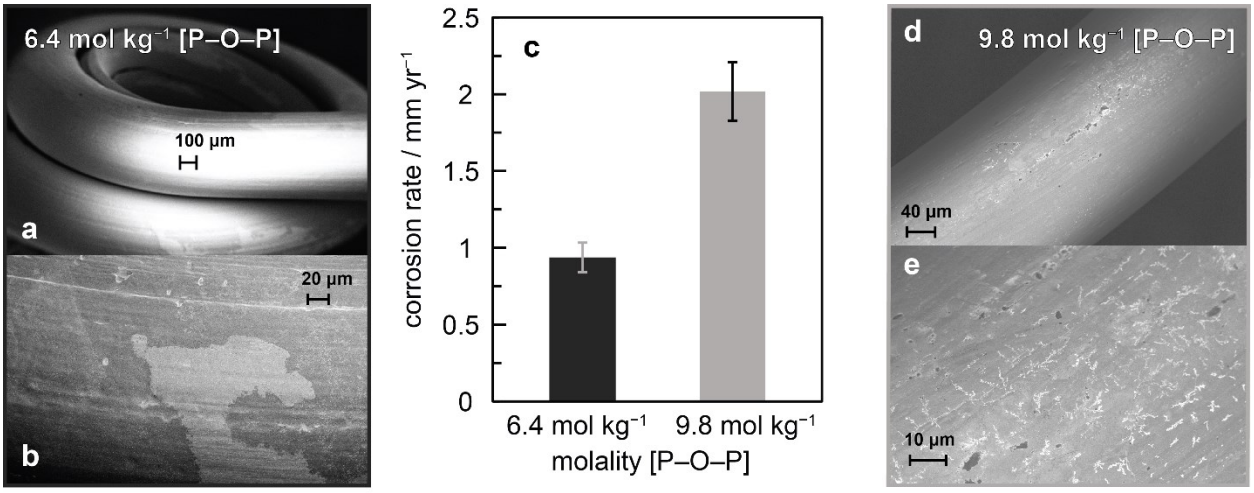

Figure 3-6. *a) SEM images of an iridium coil anode, with scale bars, after a prolonged anodic current of 100 mA cm^{-2} in molten sodium polyphosphate with an anhydride molality of 6.4 mol kg^{-1}. c) indicated corrosion rate of Ir in mm yr^{-1} at Lux acidities of 6.4 and 9.8 mol kg^{-1} [P-O-P] with error bars indicating 95% confidence levels. d,e) SEM images of an iridium coil anode, with scale bars, after a prolonged anodic current of 100 mA cm^{-2} in molten sodium metaphosphate with an anhydride molality of 9.8 mol kg^{-1}.*

3.3: CONCLUSIONS

Thanks to careful gaseous product collection in conjunction with electrochemical analysis, platinum, gold and iridium oxide were all found to perform OER with extremely high faradaic efficiencies. Increasing the Lux basicitiy of the melt was found to not only promote OER on all metal anodes but also suppress the corrosion of said metal anodes. Ir/IrO_x demonstrated substantially lower corrosion rates than Au and Pt under similar current densities, but Au and Pt seem to corrode via a kinetically-driven process that results in metal ions which rapidly back-react to form their constituent metals and oxygen gas. If industry develops careful metal recollection techniques under these molten salt conditions, some of the costs incurred by anode corrosion could potentially be averted. As things stand, however, IrO_x appears to be the most promising OER anode candidate in these media, and opens up interesting avenues for further study regarding the interplay between metal oxide bond strength, oxygen evolution catalysis and corrosion resistance. Iridium is currently a popular oxygen evolution catalyst in other media, including

[35] Shchetkovskiy, A.; McKechnie, Timothy Sadoway, Donald R. Paramore, J.; Melendez, O.; Curreri, P. A. In *Earth and Space 2010: Engineering, Science, Construction, and Operations in Challenging Environments*; American Society of Civil Engineers: Honolulu, 2010.

[36] Herrmann, S. D.; Tripathy, P. K.; Frank, S. M.; King, J. A. *J. Appl. Electrochem.* **2019**, *49* (4), 379–388.

molten salts,[31,35] and advances in the nanostructuring of iridium oxide nanowire catalysts could allow for better utilization of the catalyst relative to our macroscopic wire coil.[29] Additionally, Au, Pt and Ir/IrO_x represent a very small subset of potential anode materials, and other metals, or even alloys of the same metals, may demonstrate superior properties than their elements. Composite materials which combine conductivity with strong metal-oxygen bonds, such as cermets,[36,37] may also prove valuable anode candidates. The question of anode corrosion in acidic molten salt media not only affects the electrolysis of molten polyphosphates but also the Hall-Héroult process of electrolytic aluminum production,[22,23,38] so iridium's incredible stability to corrosion may apply in the presence of molten cryolite as well. While numerous additional questions must first be answered regarding the oxygen evolution process in molten polyphosphates before industrialization, this initial survey of catalyst metals and the fundamental insights presented by this work suggest that a future where the generation of white phosphorus is carbon-free may be much closer than originally anticipated.

3.4: ABBREVIATIONS

OER, oxygen evolution reaction; W.E., working electrode; R.E., reference electrode; C.E., counter electrode; GC, gas chromatography; CV, cyclic voltammetry; NMR, nuclear magnetic resonance; OCP, open-circuit potential; BGA, binary gas analysis.

3.5: REFERENCES

(1) Schipper, W. *Eur. J. Inorg. Chem.* **2014**, No. 10, 1567–1571.

(2) Emsley, J. *The 13th Element: The Sordid Tale of Murder, Fire, and Phosphorus*; Wiley: New York, 2000.

(3) Diskowski, H.; Hofmann, T. *Ullmann's Encyclopedia of Industrial Chemistry*; Wiley-VCH: Weinheim, Germany, 2012; Vol. 26, pp 725–746.

(4) Geeson, M. B.; Cummins, C. C. *Science (80-.).* **2018**, *359*, 1383–1385.

(5) Geeson, M. B.; Cummins, C. C. *ACS Cent. Sci.* **2020**, *6* (6), 848–860.

(6) Lux, H. *Zeitschrift für Elektrochemie und Angew. Phys. Chemie* **1949**, *45* (1), 41–43.

(7) Flood, H.; Förland, T. *Acta Chem. Scand.* **1947**, *1* (6), 592–604.

(8) Drago, R. S.; Whitten, K. W. *Inorg. Chem.* **1966**, *5* (4), 677–682.

(9) Melville, J. F.; Licini, A. J.; Surendranath, Y. *ACS Cent. Sci.* **2023**, *9* (3), 373-380.

(10) Casey, E. J.; Dubois, A. R. *Can. J. Chem.* **1971**, *49*, 2733–2745.

(11) Casey, E. J.; Dubois, A. R.; Gorman, R. W. In *Corrosion*; 1975; Vol. 31, pp 358–363.

[37] Li, T.; Parbey, J. In *Intermediate Temperature Solid Oxide Fuel Cells: Electrolytes, Electrodes and Interconnects*; 2020; pp 165–194.

[38] Wang, Y.; He, H. B. *Mater. Sci. Forum* **2018**, *921 MSF*, 119–127.

(12) Higgins, J. K. *J. Electrochem. Soc.* **1993**, *140* (12), 3436–3448.

(13) Delimarskii, Y. K.; Andreeva, V. N. *Zh. Neorg. Khim.* **1960**, *5* (5), 540–542.

(14) Andreeva, V. N.; Delimarskii, Y. K. *Zh. Neorg. Khim.* **1960**, *5* (9), 1008–1011.

(15) Delimarskii, Y. K.; Andreeva, V. N. *Zh. Neorg. Khim.* **1960**, *5* (8), 873–876.

(16) Fischer, B. *Platin. Met. Rev.* **1992**, *36* (1), 14–25.

(17) Ubbelohde, A. R. In *Ionic Liquids*; Inman, D., Lovering, D. G., Eds.; Plenum: New York, 1981; pp 1–6.

(18) International Union of Pure and Applied Chemistry. In *Solubility Data Series*; Lorimer, J. W., Clever, H. L., Young, C. L., Eds.; Pergamon: Oxford, 1991; Vol. 45.

(19) Liu, T. L.; Liu, W. R.; Xu, X. H. *IOP Conf. Ser. Earth Environ. Sci.* **2017**, *93* (1).

(20) Griffith, E. J.; Callis, C. F. *J. Am. Chem. Soc.* **1959**, *81* (4), 833–836.

(21) Van Wazer, J. R. In *Phosphorus and its Compounds, Vol. I*; Interscience: New York, 1958; pp 717–800.

(22) Frank, W. B.; Haupin, W. E.; Vogt, H.; Bruno, M.; Thonstad, J.; Dawless, R. K.; Kvande, H.; Taiwo, O. A. *Ullmann's Encyclopedia of Industrial Chemistry*; Wiley-VCH: Weinheim, Germany, 2012; Vol. 2, pp 483–520.

(23) Tabereaux, A. T.; Peterson, R. D. In *Treatise on Process Metallurgy*; Elsevier: Oxford, 2014; Vol. 3, pp 839–917.

(24) Bard, A. J.; Faulkner, L. R. *Electrochemical Methods: Fundamentals and Applications*, 2nd ed.; Wiley: New York, 2000.

(25) Hall, A. S.; Yoon, Y.; Wuttig, A.; Surendranath, Y. *J. Am. Chem. Soc.* **2015**, *137* (47), 14834–14837.

(26) Yoon, Y.; Hall, A. S.; Surendranath, Y. *Angew. Chemie - Int. Ed.* **2016**, *55* (49), 15282–15286.

(27) Yoon, Y.; Yan, B.; Surendranath, Y. *J. Am. Chem. Soc.* **2018**, *140* (7), 2397–2400.

(28) Nunes, D. In *Metal Oxide Nanostructures: Synthesis, Properties and Applications*; Elsevier: Amsterdam, 2019; pp 103–147.

(29) Scarpelli, F.; Godbert, N.; Crispini, A.; Aiello, I. *Inorganics* **2022**, *10* (8).

(30) Altowyan, A. S.; Shaban, M.; Abdelkarem, K.; El Sayed, A. M. *Nanomaterials* **2022**, *12* (19), 1–13.

(31) Shchetkovskiy, A.; McKechnie, Timothy Sadoway, Donald R. Paramore, J.; Melendez, O.; Curreri, P. A. In *Earth and Space 2010: Engineering, Science, Construction, and Operations in Challenging Environments*; American Society of Civil Engineers: Honolulu, 2010.

(32) Van Wazer, J. R. *J. Am. Chem. Soc.* **1950**, *72* (2), 644–647.

(33) Rindone, G. E.; Rhoads, J. L. *J. Am. Ceram. Soc.* **1956**, *39* (5), 173–180.

(34) Jovanovič, P.; Hodnik, N.; Ruiz-Zepeda, F.; Arčon, I.; Jozinović, B.; Zorko, M.; Bele, M.; Šala, M.; Šelih, V. S.; Hočevar, S.; Gaberšček, M. *J. Am. Chem. Soc.* **2017**, *139* (36), 12837–12846.

(35) Herrmann, S. D.; Tripathy, P. K.; Frank, S. M.; King, J. A. *J. Appl. Electrochem.* **2019**, *49* (4), 379–388.

(36) Li, T.; Parbey, J. In *Intermediate Temperature Solid Oxide Fuel Cells: Electrolytes, Electrodes and Interconnects*; 2020; pp 165–194.

(37) Wang, Y.; He, H. B. *Mater. Sci. Forum* **2018**, *921 MSF*, 119–127.

(38) Prasad, S. *J. Braz. Chem. Soc.* **2000**, *11* (3), 245–251.

Conclusions

Through the course of this work, we have demonstrated an alternative process to the environmentally harmful carbothermal reduction of white phosphorus. Through development of robust characterization techniques in this corrosive medium, we have enabled major breakthroughs in the understanding of the underlying processes involved in molten salt electrolysis. Our analysis of the electrochemical reduction process of metaphosphate to white phosphorus indicates that white phosphorus can be produced on graphite cathodes with high selectivity in a mechanism which travels through a P^{3+} intermediate, and that the presence of Lux acid contributes to promotion of the phosphate reduction process. On the other hand, Lux acid was found to suppress oxygen evolution and promote corrosion on oxygen-evolving metal anodes. While iridum / IrO_x anodes showed the lowest corrosion, an energy tradeoff is made for the sluggish OER kinetics on it, and design of an overall metaphosphate electrolysis system in an industrial setting will require a delicate balancing act of solvent conditions and material cost decisions. Nevertheless, these results suggest that the carbothermal process of P_4 production has the potential to be reasonably circumvented through a molten metaphosphate electrolysis which can be downscaled, operated under milder conditions and evolve much less or no carbon dioxide. The findings of this paper will also undoubtedly pave the way for other discoveries not only in the context of molten metaphosphate studies, but in molten salts in general

Bibliography

Sources listed in order of appearance throughout the complete document.

I. Lindsey, R. Climate Change: Atmospheric Carbon Dioxide https://www.climate.gov/news-features/understanding-climate/climate-change-atmospheric-carbon-dioxide (accessed Feb 12, 2023).

II. Tans, P.; Keeling, R. Trends in Atmospheric Carbon Dioxide https://gml.noaa.gov/ccgg/trends/data.html (accessed Feb 12, 2023).

III. Sanchez, D. P.; Collina, L.; Levi, P.; Hodgson, D. Chemicals https://www.iea.org/reports/chemicals (accessed Feb 12, 2023).

IV. Kueppers, M.; Hodgson, D.; Levi, P.; Vass, T.; Lechtenbohmer, T. Iron and Steel https://www.iea.org/reports/iron-and-steel (accessed Feb 12, 2023).

V. Hodgson, D.; Vass, T. Aluminium https://www.iea.org/reports/aluminium (accessed Feb 12, 2023).

VI. Lindsey, R. Climate Change: Annual greenhouse gas index https://www.climate.gov/news-features/understanding-climate/climate-change-annual-greenhouse-gas-index.

VII. Diskowski, H.; Hofmann, T. *Ullmann's Encyclopedia of Industrial Chemistry*; Wiley-VCH: Weinheim, Germany, 2012; Vol. 26, pp 725–746.

VIII. Jupp, A. R.; Beijer, S.; Narain, G. C.; Schipper, W.; Slootweg, J. C. *Chem. Soc. Rev.* **2021**, *50* (1), 87–101.

IX. Emsley, J. *The 13th Element: The Sordid Tale of Murder, Fire, and Phosphorus*; Wiley: New York, 2000.

X. Nigra, G. FR658521A, 1929.

XI. *CRC Handbook of Chemistry and Physics*, 103rd ed.; Rumble, J. R., Ed.; CRC Press: Ohio, 2023.

XII. Wolery, T. J.; Jove-Colon, C. F. *Qualification of Thermodynamic Data for Geochemical Modeling of Mineral-Water Interactions in Dilute Systems*; 2004.

XIII. Dorn, F. W.; Harnisch, H. *Chemie Ing. Tech.* **1970**, *42* (19), 1209–1215.

XIV. Deloitte Sustainability; British Geological Survey; Bureau de Recherches Géologiques et Minières; Netherlands Organisation for Applied Scientific Research. *Study on the Review of the List of Critical Raw Materials: Critical Raw Materials Factsheets*; Brussels, 2017.

XV. British Peroleum. *Bp Statistical Review of World Energy, 71st Ed.*; 2022.

XVI. Webeck, E.; Matsubae, K. In *Phosphorus Recovery and Recycling*; Ohtake, H., Tsuneda, S., Eds.; Springer: Singapore, 2019; pp 29–44.

XVII. Ohio History Central. Miamisburg, Ohio, Train Derailment https://ohiohistorycentral.org/w/Miamisburg,_Ohio,_Train_Derailment (accessed Feb 13, 2023).

XVIII. Scoville, W.; Springer, S.; Crawford, J. *J. Hazard. Mater.* **1989**, *21*, 47–64.

XIX. *The Washington Post*. Crofton, KY June 23, 1988.

XX. Train Carrying Phosphorus Leaves Ukraine For Kazakhstan https://www.rferl.org/a/1077823.html

XXI. Schmittinger, P.; Florkiewicz, T.; Curlin, L. C.; Lüke, B.; Scannell, R.; Navin, T.; Zelfel, E.; Bartsch, R. *Ullmann's Encyclopedia of Industrial Chemistry*; Wiley-VCH: Weinheim, Germany, 2012; Vol. 8, pp 531–622.

XXII. Frank, W. B.; Haupin, W. E.; Vogt, H.; Bruno, M.; Thonstad, J.; Dawless, R. K.; Kvande, H.; Taiwo, O. A. *Ullmann's Encyclopedia of Industrial Chemistry*; Wiley-VCH: Weinheim, Germany, 2012; Vol. 2, pp 483–520.

XXIII. Hall, A. S.; Yoon, Y.; Wuttig, A.; Surendranath, Y. *J. Am. Chem. Soc.* **2015**, *137* (47), 14834–14837.

XXIV. Yoon, Y.; Hall, A. S.; Surendranath, Y. *Angew. Chemie - Int. Ed.* **2016**, *55* (49), 15282–15286.
XXV. Yoon, Y.; Yan, B.; Surendranath, Y. *J. Am. Chem. Soc.* **2018**, *140* (7), 2397–2400.
XXVI. Das, P.; Jana, N. R. *ACS Appl. Mater. Interfaces* **2016**, *8* (13), 8710–8720.
XXVII. Elias, J. S.; Costentin, C.; Nocera, D. G. *J. Am. Chem. Soc.* **2018**, *140* (42), 13711–13718.
XXVIII. Brummer, J. R.; Keely, J. A.; Munday, T. F.; FMC Corporation. *Kirk-Othmer Encyclopedia of Chemical Technology*; John Wiley & Sons, 2005; Vol. 18.
XXIX. Ubbelohde, A. R. In *Ionic Liquids*; Inman, D., Lovering, D. G., Eds.; Plenum: New York, 1981; pp 1–6.
XXX. Scordilis-Kelley, C.; Fuller, J.; Carlin, R. T.; Wilkes, J. S. *J. Electrochem. Soc.* **1992**, *139* (3), 694–699.
XXXI. Allanore, A. *J. Electrochem. Soc.* **2015**, *162* (1), E13–E22.
XXXII. Caldwell, A. H.; Lai, E.; Gmitter, A. J.; Allanore, A. *Electrochim. Acta* **2016**, *219*, 178–186.
XXXIII. Martín Treceño, S.; Allanore, A.; Bishop, C. M.; Marshall, A. T.; Watson, M. J. *J. Mater.* **2021**, *73* (6), 1899–1908.
XXXIV. Yang, X.; Nohira, T. *ACS Sustain. Chem. Eng.* **2020**, *8* (36), 13784–13792.
XXXV. Zhong, Y.; Yang, X. *Metall. Mater. Trans. B Process Metall. Mater. Process. Sci.* **2021**, *52* (5), 3515–3523.
XXXVI. Sorrell, T. N. In *Organic Chemistry*; Castellion, M., Ed.; University Science Books: California, 2006; pp 953–988.
XXXVII. Havelange, S.; Lierde, N.; Germeau, A.; Martins, E.; Theys, T.; Sonveaux, M.; Toussaint, C.; Schrödter, K.; Bettermann, G.; Staffel, T.; Wahl, F.; Klein, T.; Hofmann, T. *Ullmann's Encyclopedia of Industrial Chemistry*; Wiley-VCH, 2022; pp 1–55.
XXXVIII. Bettermann, G.; Krause, W.; Riess, G.; Hofmann, T. *Ullmann's Encyclopedia of Industrial Chemistry*; Wiley-VCH, 2012; Vol. 27.
XXXIX. Centnerzwer, M.; Szper, J. *Bull. Polish Acad. Sci.* **1931**, 364–368.
XL. In *Encyclopedia of Electrochemistry of the Elements*; Bard, A. J., Ed.; Marcel Dekker: New York, 1976; Vol. X, pp 373–388.
XLI. Caton, R. D.; Freund, H. *Anal. Chem.* **1963**, *35* (13), 2103–2108.
XLII. Van Wazer, J. R. In *Phosphorus and its Compounds, Vol. I*; Interscience: New York, 1958; pp 717–800.
XLIII. Griffith, E. J.; Callis, C. F. *J. Am. Chem. Soc.* **1959**, *81* (4), 833–836.
XLIV. Van Wazer, J. R. *J. Am. Chem. Soc.* **1950**, *72* (2), 644–647.
XLV. Van Wazer, J. R. In *Phosphorus and its Compounds, Vol. I*; Interscience: New York, 1958; pp 601–678.
XLVI. Greenfield, S.; Clift, M. *Analytical Chemistry of the Condensed Phosphates*; Pergamon: Oxford, 1975.
XLVII. Casey, E. J.; Dubois, A. R. *Can. J. Chem.* **1971**, *49*, 2733–2745.
XLVIII. Andreeva, V. N. *Ukr. Khim. Zh.* **1955**, *21*, 569.
XLIX. Lux, H. *Zeitschrift für Elektrochemie und Angew. Phys. Chemie* **1949**, *45* (1), 41–43.
L. Flood, H.; Förland, T. *Acta Chem. Scand.* **1947**, *1* (6), 592–604.
LI. Drago, R. S.; Whitten, K. W. *Inorg. Chem.* **1966**, *5* (4), 677–682.
LII. El Hosary, A. A.; Kerridge, D. H.; Shams El Din, A. M. In *Ionic Liquids*; Inman, D., Lovering, D. G., Eds.; Plenum: New York, 1981; pp 339–362.
LIII. Shams El Din, A. M.; Gerges, A. A. A. *Electrochim. Acta* **1964**, *9*, 613–627.
LIV. Gruber, B. A. US2965552A, 1960.
LV. Yocom, P. N. University of Illinois, 1958.
LVI. Casey, E. J.; Dubois, A. R.; Gorman, R. W. In *Corrosion*; 1975; Vol. 31, pp 358–363.

LVII. Andreeva, V. N.; Delimarskii, Y. K. *Zh. Neorg. Khim.* **1960**, *5* (9), 1008–1011.
LVIII. Laitinen, H. A.; Lucas, K. R. *J. Electroanal. Chem.* **1966**, *12*, 553–563.
LIX. Franks, E.; Inman, D. *J. Electroanal. Chem.* **1970**, *26*, 13–26.
LX. Franks, E.; Inman, D. *J. Appl. Electrochem.* **1971**, *14*, 73–78.
LXI. Lippard, S. J.; Berg, J. M. In *Principles of Bioinorganic Chemistry*; University Science Books: Mill Valley, CA, 1994; pp 103–137.
LXII. Delimarskii, Y. K.; Andreeva, V. N. *Zh. Neorg. Khim.* **1960**, *5* (5), 540–542.
LXIII. Delimarskii, Y. K.; Andreeva, V. N. *Zh. Neorg. Khim.* **1960**, *5* (8), 873–876.
LXIV. Stebbins, J. F. *Chem. Rev.* **1991**, *91* (7), 1353–1373.
LXV. Caton, R. D.; Wolfe, C. R. *Anal. Chem.* **1971**, *43* (6), 660–662.
LXVI. Prasad, S. *J. Braz. Chem. Soc.* **2000**, *11* (3), 245–251.
LXVII. Wilson, S. D. R.; Hulme, A. *Proc. R. Soc. London, Ser. A Math. Phys. Sci.* **1983**, *387* (1792), 133–146.
LXVIII. Tabereaux, A. T.; Peterson, R. D. In *Treatise on Process Metallurgy*; Elsevier: Oxford, 2014; Vol. 3, pp 839–917.
LXIX. Bard, A. J.; Faulkner, L. R. *Electrochemical Methods: Fundamentals and Applications*, 2nd ed.; Wiley: New York, 2000.
LXX. Stolz, L.; Homann, G.; Winter, M.; Kasnatscheew, J. *Mater. Today* **2021**, *44* (April), 9–14.
LXXI. Liu, T. L.; Liu, W. R.; Xu, X. H. *IOP Conf. Ser. Earth Environ. Sci.* **2017**, *93* (1).
LXXII. Pryor, M. J.; Cohen, M. *J. Electrochem. Soc.* **1951**, *98* (7), 263.
LXXIII. Taylor, R. J.; Humffray, A. A. *J. Electroanal. Chem.* **1975**, *64*, 63–84.
LXXIV. Fischer, B. *Platin. Met. Rev.* **1992**, *36* (1), 14–25.
LXXV. Higgins, J. K. *J. Electrochem. Soc.* **1993**, *140* (12), 3436–3448.
LXXVI. Sotelo-Mazón, O.; Cuevas-Arteaga, C.; Porcayo-Calderón, J.; Salinas Bravo, V. M.; Izquierdo-Montalvo, G. *Adv. Mater. Sci. Eng.* **2014**, *2014*.
LXXVII. Rindone, G. E.; Rhoads, J. L. *J. Am. Ceram. Soc.* **1956**, *39* (5), 173–180.
LXXVIII. Licini, A.; Surendranath, Y. WO2020061551A1, 2019.
LXXIX. Melville, J. F.; Licini, A. J.; Surendranath, Y. *ACS Cent. Sci.* **2023**, *9* (3), 373-380.
LXXX. Schipper, W. *Eur. J. Inorg. Chem.* **2014**, No. 10, 1567–1571.
LXXXI. Geeson, M. B.; Cummins, C. C. *Science (80-.).* **2018**, *359*, 1383–1385.
LXXXII. Geeson, M. B.; Cummins, C. C. *ACS Cent. Sci.* **2020**, *6* (6), 848–860.
LXXXIII. Centre for Research in Computational Thermochemistry. FTsalt - FACT Salt Phase Diagrams https://www.crct.polymtl.ca/fact/documentation/FTsalt/FTsalt_Figs.htm (accessed Feb 18, 2023).
LXXXIV. Wang, L. L.; Wallace, T. C. *Metall. Mater. Trans. B* **1996**, *27* (1), 141–146.
LXXXV. Carenco, S.; Hu, Y.; Florea, I.; Ersen, O.; Boissière, C.; Mézailles, N.; Sanchez, C. *Chem. Mater.* **2012**, *24*, 4134–4145.
LXXXVI. Carenco, S.; Portehault, D.; Boissière, C.; Mézailles, N.; Sanchez, C. *Adv. Mater.* **2014**, *26* (3), 371–390.
LXXXVII. Guan, J.; Liu, D.; Zhu, Z.; Tománek, D. *Nano Lett.* **2016**, *16*, 3247–3252.
LXXXVIII. Ma, X.; Zhou, J.; Yang, T.; Li, D.; Feng, Y. P. *Phys. Rev. Mater.* **2021**, *5*, 024005.
LXXXIX. Inzelt, G. In *Handbook of Reference Electrodes*; Inzelt, G., Lewenstam, A., Scholz, F., Eds.; Springer: Berlin, 2013; pp 331–332.
XC. Seitz, A. E.; Hippauf, F.; Kremer, W.; Kaskel, S.; Scheer, M. *Nat. Commun.* **2018**, *9* (1), 2–7.
XCI. Mahapatra, M. K.; Lu, K. *Mater. Sci. Eng. R Reports* **2010**, *67* (5–6), 65–85.
XCII. Bockris, J. O.; Nagy, Z. *J. Chem. Educ.* **1973**, *50* (12), 839–843.
XCIII. Liu, D.; Li, X.; Wei, L.; Zhang, T.; Wang, A.; Liu, C.; Prins, R. *Dalt. Trans.* **2017**, *46* (19), 6366–6378.

XCIV. Stephenson, C. C.; Potter, R. L.; Maple, T. G.; Morrow, J. C. *J. Chem. Thermodyn.* **1969**, *1*, 59–76.
XCV. Chase, M. *J. Phys. Chem. Ref. Data Monogr.* **1998**, 1948–1951.
XCVI. Cox, J. D.; Wagman, D. D.; Medvedev, V. A. *CODATA Key Values for Thermodynamics, 1984*; 1984.
XCVII. Irving, R. J.; McKerrell, H. *Trans. Faraday Soc.* **1967**, *63*, 2913–2916.
XCVIII. Ashcroft, S. J.; Keen, E.; Mortimer, C. T. *Trans. Faraday Soc.* **1969**, *65*, 2851−2855.
XCIX. Rard, J. A.; Wolery, T. J. *J. Solut. Chem.* **2007**, *36*, 1585−1599.
C. Vieillard, P.; Tardy, Y. In *Phosphate Minerals*; Nriagu, J. O., Moore, P. B., Eds.; Springer: Berlin, 1984; pp 171–198.
CI. Jung, O.; Jackson, M. N.; Bisbey, R. P.; Kogan, N. E.; Surendranath, Y. *Joule* **2022**, *6* (2), 476–493.
CII. Morey, G. W. *J. Am. Chem. Soc.* **1952**, *74* (22), 5783–5784.
CIII. Voskresenskaya, N. K.; Sokolova, I. D. *Russ. Chem. Rev.* **1969**, *38*, 862−872.
CIV. Gerken, J. B.; McAlpin, J. G.; Chen, J. Y. C.; Rigsby, M. L.; Casey, W. H.; Britt, R. D.; Stahl, S. S. *J. Am. Chem. Soc.* **2011**, *133*, 14431−14442.
CV. Bediako, D. K.; Surendranath, Y.; Nocera, D. G. *J. Am. Chem. Soc.* **2013**, *135* (9), 3662–3674.
CVI. Vignarooban, K.; Xu, X.; Arvay, A.; Hsu, K.; Kannan, A. M. *Appl. Energy.* **2015**, *146*, 383−396.
CVII. Licht, S.; Wu, H. *J. Phys. Chem. C* **2011**, *115*, 25138−25147.
CVIII. International Union of Pure and Applied Chemistry. In *Solubility Data Series*; Lorimer, J. W., Clever, H. L., Young, C. L., Eds.; Pergamon: Oxford, 1991; Vol. 45.
CIX. Nunes, D. In *Metal Oxide Nanostructures: Synthesis, Properties and Applications*; Elsevier: Amsterdam, 2019; pp 103–147.
CX. Scarpelli, F.; Godbert, N.; Crispini, A.; Aiello, I. *Inorganics* **2022**, *10* (8).
CXI. Altowyan, A. S.; Shaban, M.; Abdelkarem, K.; El Sayed, A. M. *Nanomaterials* **2022**, *12* (19), 1–13.
CXII. Shchetkovskiy, A.; McKechnie, Timothy Sadoway, Donald R. Paramore, J.; Melendez, O.; Curreri, P. A. In *Earth and Space 2010: Engineering, Science, Construction, and Operations in Challenging Environments*; American Society of Civil Engineers: Honolulu, 2010.
CXIII. Jovanovič, P.; Hodnik, N.; Ruiz-Zepeda, F.; Arčon, I.; Jozinović, B.; Zorko, M.; Bele, M.; Šala, M.; Šelih, V. S.; Hočevar, S.; Gaberšček, M. *J. Am. Chem. Soc.* **2017**, *139* (36), 12837–12846.
CXIV. Herrmann, S. D.; Tripathy, P. K.; Frank, S. M.; King, J. A. *J. Appl. Electrochem.* **2019**, *49* (4), 379–388.
CXV. Li, T.; Parbey, J. In *Intermediate Temperature Solid Oxide Fuel Cells: Electrolytes, Electrodes and Interconnects*; 2020; pp 165–194.
CXVI. Wang, Y.; He, H. B. *Mater. Sci. Forum* **2018**, *921 MSF*, 119–127.
CXVII. Campbell, F. H. *Trans. Faraday Soc.* **1907**, *3*, 103–113.
CXVIII. Cherevko, S.; Topalov, A. A.; Zeradjanin, A. R.; Katsounaros, I.; Mayrhofer, K. J. J. *RSC Adv.* **2013**, *3* (37), 16516–16527.
CXIX. Korzeniewski, C.; Conway, B. E. In *Proceedings of the Symposium on the Electrochemical Double Layer*; The Electrochemical Society, 1997; Vol. 97, pp 349–350.
CXX. Chen, P.; Zhang, H.-B.; Lin, G.-D.; Hong, Q.; Tsai, K. R. *Carbon N. Y.* **1997**, *35* (10–11), 1495–1501.
CXXI. Wiberg, E.; Holleman, A. F.; Wiberg, N. In *Inorganic Chemistry*; San Diego, 2001; pp 810–811.
CXXII. Basu, P. In *Biomass Gasification, Pyrolysis and Torrefaction*; Basu, P., Ed.; Academic Press, 2018; pp 211–262.
CXXIII. Feki, M.; Ayedi, H. F. *Sep. Sci. Technol* **2008**, *33*, 2609–2622.
CXXIV. Engel, T.; Reid, P. In *Thermodynamics, Statistical Thermodynamics, & Kinetics: Pearson New International Edition*; Pearson: Harlow, 2013; p 546.
CXXV. Williams, M. In *The Merck Index: An Encyclopedia of Chemicals, Drugs, and Biologicals*; Neil, M. J., Ed.; Royal Society of Chemistry: Cambridge, UK, 2013; Vol. 74, p 1266.

CXXVI. Southard, J. C.; Nelson, R. A. *J. Am. Chem. Soc.* **1937**, *59*, 911–916.
CXXVII. Butland, A. T. D.; Maddison, R. J. *J. Nucl. Mater.* **1973**, *49*, 45–56.
CXXVIII. Speight, J. G. *Environmental Organic Chemistry for Engineers*; Butterworth-Heinemann, 2016.
CXXIX. Egan, E. P.; Luff, B. B. *J. Phys. Chem.* **1961**, *65*, 523–526.
CXXX. Walsh, M. E.; Collins, C. M.; Racine, C. H. *Environ. Toxicol. Chem.* **1996**, *15*, 846–855.
CXXXI. McCabe, W.; Smith, J.; Harriott, P. In *Unit Operations of Chemical Engineering*; McGraw-Hill Education: Boston, 2004; p 454.

Appendix A – Supplemental Information for Chapter 2

A-1: MATERIALS AND METHODS

A-1.1 – High-Temperature Electroanalytical Reactor Design

An electrochemical reactor (**Figure 2-6**, **Figure A-1 to Figure A-3**) was designed from the ground up to accommodate the electroanalysis of a molten-salt system while maintaining separation of cathodic and anodic gas flow streams. The main reactor body consisted of a closed-end alumina tube (designated "Alumina tube, one-end-closed, OD60.33mm*ID52mm*L279.4mm (OD+/-4%, ID+3/-0)" by AdValue Technologies), to which a custom-machined stainless-steel cap with four Swagelok™ Ultra-Torr® fittings could be attached. These fittings, as well as the junction between the reactor head and body, were sealed with DuPont™ Kalrez® perfluoroelastomer O-rings (temperature rated to 325 °C). Of the four fittings, three (of 1/4" diameter) held alumina-sheathed electrodes, while the fourth (of 3/4" diameter) held the isolated counter compartment and electrode. Careful management of the temperature of these O-rings, accomplished by glass insulation wool and Variac-controlled heating tape, is essential to reconcile the thermal rating of these O-rings with the temperatures of reaction; at low temperatures, P_4 will collect on the reactor head and interior instead of venting through the cold trap, while at high temperatures the O-rings will melt, eventually compromising the reactor seal. The furnace itself was designed to fit a CF56622C Lindberg/Blue M™ top-loading Crucible Furnace (now discontinued) as controlled by a CC58114C-1 Lindberg/Blue M™ Furnace Controller.

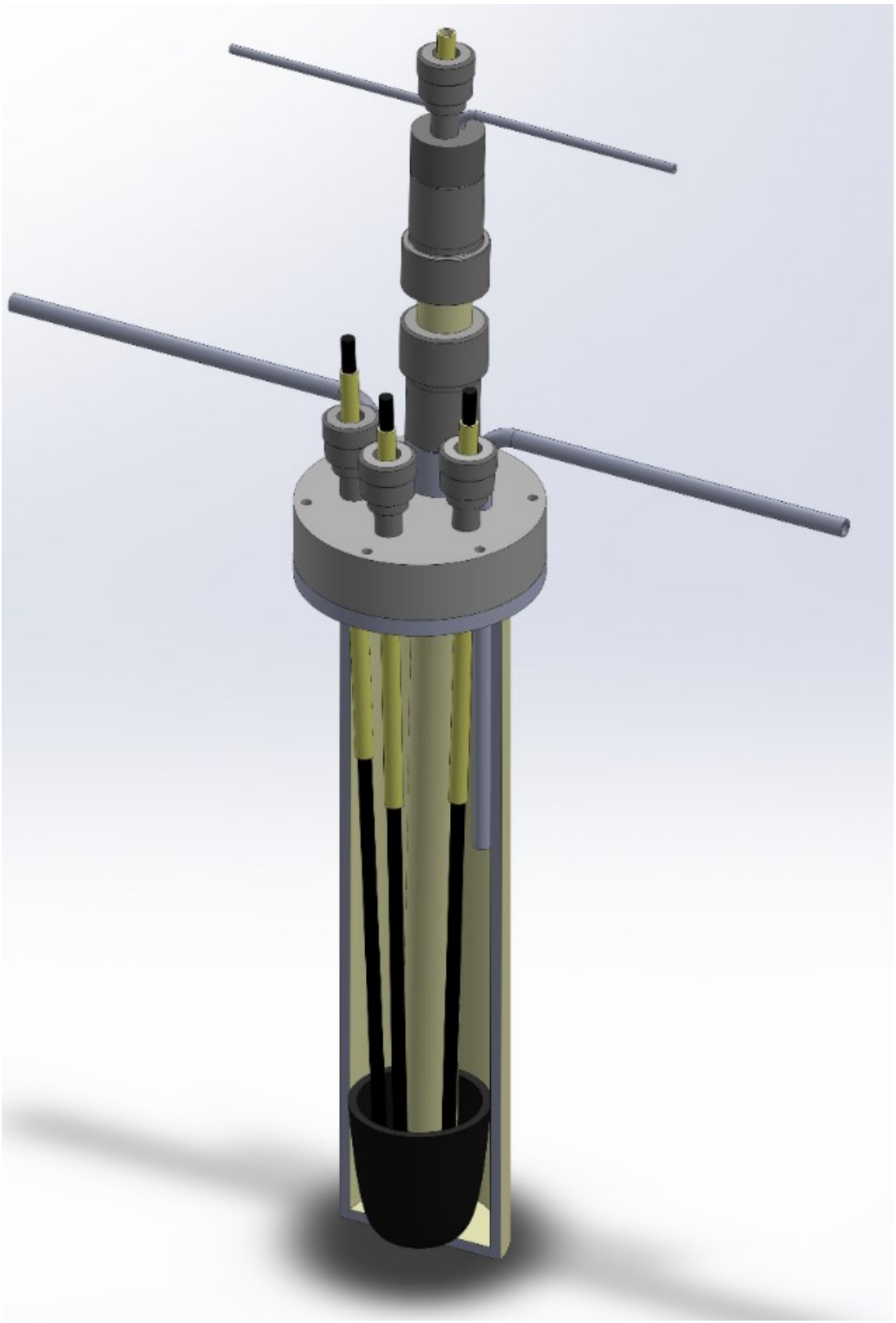

Figure A-1. *Cutaway render of assembled high-temperature electrochemical reactor.*

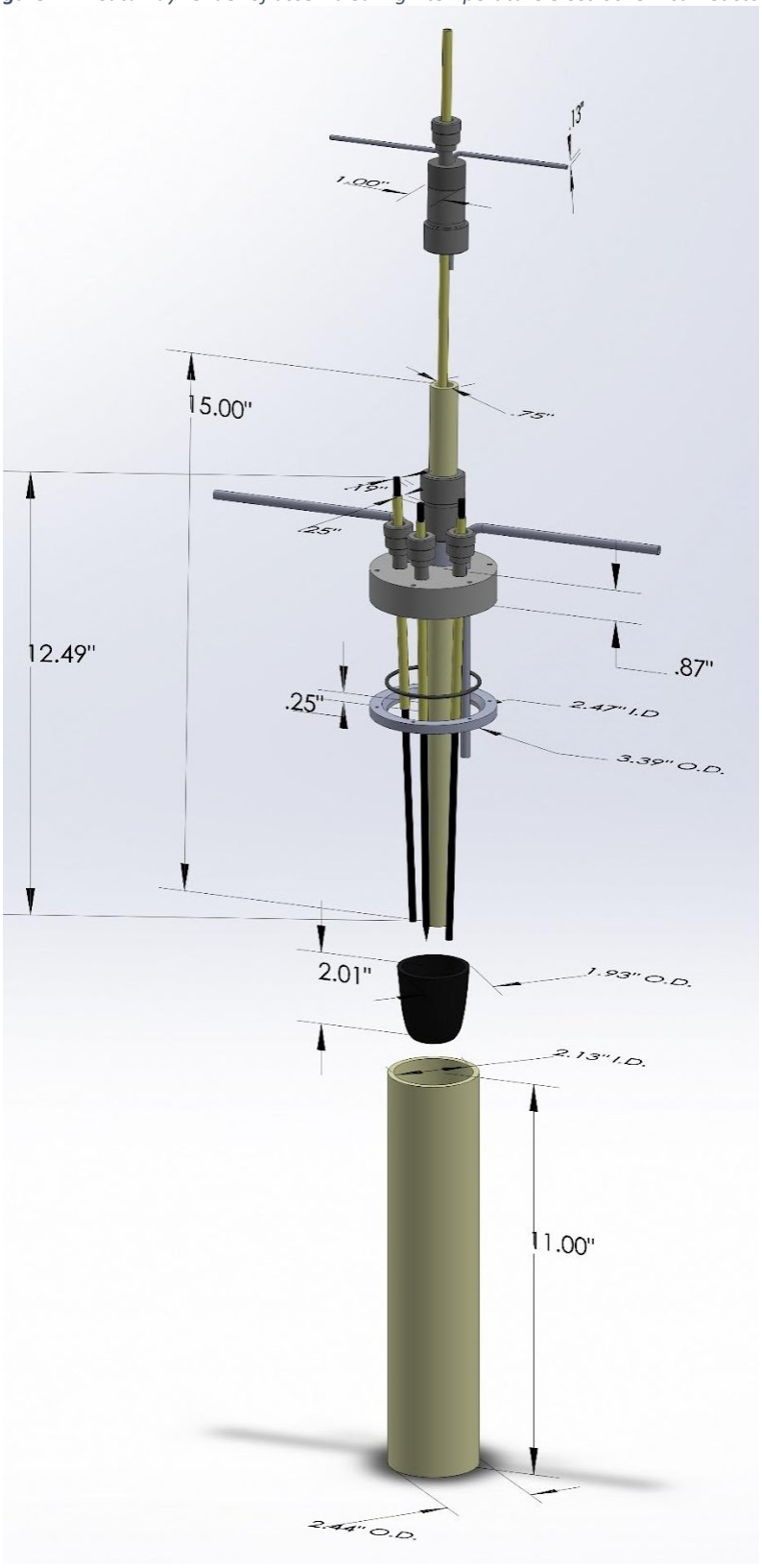

Figure A-2. *Exploded render of high-temperature reactor, including component dimensions.*

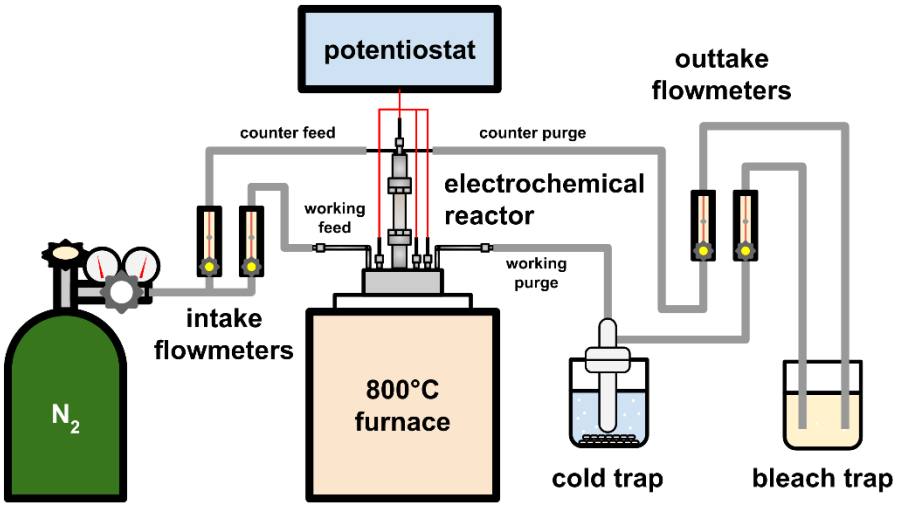

Figure A-3. *Diagram of molten-salt electrolysis setup configured for P_4 capture and quantitation, including separated cathodic and anodic N_2 gas flow streams.*

A-1.1a – Crucible Selection

The bottom of the electrochemical reactor contained a conical glassy carbon crucible (60 mL, 52 mm outer diameter (OD), part #39006KT from Alfa Aesar), so chosen for its inertness to the metaphosphate melt and the temperatures of reaction while under inert atmosphere. Between experiments, the crucible was polished with 800 grit sandpaper and an alumina slurry (1 micron deagglomerated hexagonal alumina powder, part #PSI-5601-5 by Precision Surfaces International, Inc.), then rinsed with reagent grade water (Millipore Type 1, 18.2 MΩ·cm resistivity). This polishing procedure was necessary to ensure that the fused melts could be easily separated from the crucible upon cooling following a reaction run.

A-1.1b – Counter Compartment

For all experiments conducted in this study, the counter compartment consisted of a single-bore alumina tube (3/4" OD, 1/2" inner diameter (ID), 18" overall length, part #AL-T-N3/4-N1/2-18 by AdValue Technologies). Following the conclusion of these experiments, it was discovered that a clear fused quartz tube (19 mm OD, 15 mm ID, 1219 mm length, part #FQ-T-19-15-4 by AdValue Technologies, subsequently cut into 16"-long segments) was better suited to isolate the counter compartment. Quartz displayed enhanced resistance to corrosion in the presence of the molten metaphosphate electrolyte and its transparency allowed for visual inspection of the electrical contact made to the counter electrode.

A-1.1c – Working Electrode

Unless indicated otherwise, the working electrode for all experiments was a graphite rod (Spectro-Grade: total impurity level < 2 ppm, individual element impurity levels < 1 ppm, 3/16 ” diameter, 12” length, part # 70231 by Electron Microscopy Sciences) with the end sharpened to a point in a pencil sharpener (**Figure A-4**, center) and subsequently polished clean by rubbing with a Kimwipe™ to exfoliate potential trace metal impurities. In experiments which utilized a hollowed-electrode morphology, the end of a graphite rod (Spectro-Grade, 3/16 ” diameter, 12” length, part # 70231 by Electron Microscopy Sciences) was carved into a conical hollow using the corner of a razor blade (**Figure A-4**, right), and subsequently polished clean by rubbing with a Kimwipe to exfoliate trace metal impurities. To prevent shorting of the electrode against the conductive reactor head, a single-bore alumina tube (1/4” OD, 3/16” ID, part #AL-T-N1/4-N3/16-12 by AdValue Technologies, cut to a length of approximately 4 inches) was used as an electrode sheath. Graphite electrodes were flame-sealed to the electrode sheath by using a propane blowtorch to melt a pea-sized volume of sodium metaphosphate salt, which was then dabbed onto the junction of the alumina sheath and the graphite electrode, adhering the two together.

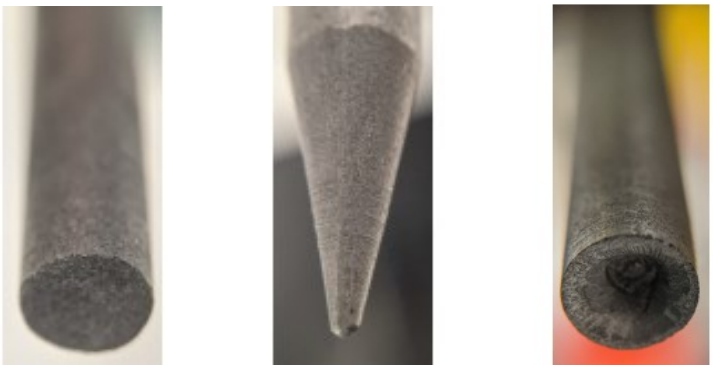

Figure A-4. *Graphite working-electrode morphologies employed in the study: (a) an unaltered rod (b) a sharpened rod to facilitate release of electrogenerated gas bubbles, and (c) a rod modified with a concave depression to trap P_4 bubbles.*

A-1.1d – Counter Electrode

Unless indicated otherwise, the counter electrode for all experiments was a graphite rod (Spectro-Grade, 1/4" diameter, 12" length, part #70230 by Electron Microscopy Sciences™), the end polished by rubbing against a Kimwipe™ to exfoliate potential impurities. As this work focuses primarily on investigating the cathodic reduction of phosphate to elemental phosphorus, graphite was chosen as a sacrificial anode for these studies. The development of corrosion-resistant oxygen evolving anodes for high-temperature molten salt electrolysis is the subject of active ongoing investigations.[1–5][1][2][3][4][5]

A-1.1e – Reference Electrodes

All electrolytic experiments were performed using a graphite pseudoreference electrode. We found that this pseudoreference maintains a stable potential in a quiescent melt over long timescales, but the precise value of its potential was found to vary both within an experiment (due to local variations in melt composition induced by electrochemical action) and between experiments (due to alterations in the bulk composition of the melt). Thus, the graphite pseudoreference electrode was calibrated before and after each experiment against a liquid-sodium Na/Na^+ absolute reference electrode (S4 Na/Al by Ionotec Ltd.). The solid-electrolyte junction of the sodium reference electrode was subject to slow corrosion in the metaphosphate electrolyte precluding its direct use as a full-time reference electrode. This calibration procedure minimized exposure of the Na/Na+ reference to the corrosive medium, but still allowed for comparison of the potentials across a variety of melt compositions. Further experimental details about the graphite pseudoreference and the Na/Na^+ reference are provided below.[66][6]

[1] Frank, W. B.; Haupin, W. E.; Vogt, H.; Bruno, M.; Thonstad, J.; Dawless, R. K.; Kvande, H.; Taiwo, O. A. *Ullmann's Encyclopedia of Industrial Chemistry*; Wiley-VCH: Weinheim, Germany, 2012; Vol. 2, pp 483–520.

[2] Prasad, S. *J. Braz. Chem. Soc.* **2000**, *11* (3), 245–251.

[3] Tabereaux, A. T.; Peterson, R. D. In *Treatise on Process Metallurgy*; Elsevier: Oxford, 2014; Vol. 3, pp 839–917.

[4] Campbell, F. H. *Trans. Faraday Soc.* **1907**, *3*, 103–113.

[5] Cherevko, S.; Topalov, A. A.; Zeradjanin, A. R.; Katsounaros, I.; Mayrhofer, K. J. J. *RSC Adv.* **2013**, *3* (37), 16516–16527.

[6] Inzelt, G. In *Handbook of Reference Electrodes*; Inzelt, G., Lewenstam, A., Scholz, F., Eds.; Springer: Berlin, 2013; pp 331–332.

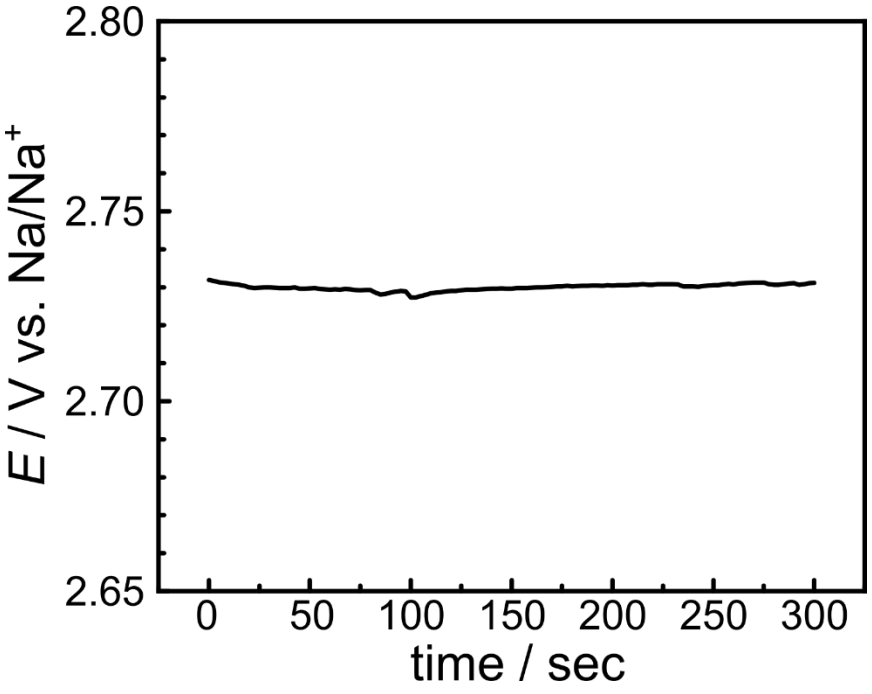

Figure A-5. *5-minute open-circuit potential trace of graphite pseudoreference electrode against a Na/Na^+ reference electrode.*

A-1.1f – Graphite Pseudoreference

Unless indicated otherwise, the reference electrode for all experiments was a graphite rod (Spectro-Grade, 3/16" diameter, 12" length, part #70231 by Electron Microscopy Sciences™), the end polished clean by a Kimwipe™ to exfoliate potential impurities. To prevent shorting of the electrode against the conductive reactor head, a single-bore alumina tube (1/4" OD, 3/16" ID, part #AL-T-N1/4-N3/16-12 by AdValue Technologies, cut to a length of approximately 4 inches) was used as an electrode sheath. The graphite electrode was flame-sealed to the electrode sheath by using a propane blowtorch to melt a pea-sized volume of sodium metaphosphate salt, which was then dabbed onto the junction of the alumina sheath and the graphite electrode, adhering the two together.

A-1.1g – Liquid Sodium Electrode

The liquid sodium reference electrode was custom-ordered from Ionotec Ltd. under the product designation "S4 Na/Al: Na beta-alumina reference electrode, 4.0 mm ID x 70 mm length x 0.6 mm wall thickness" and used as received. The potential pinned by the reference is the equilibrium between the sodium metal and the sodium ions within the membrane, as depicted by **Figure A-6**.

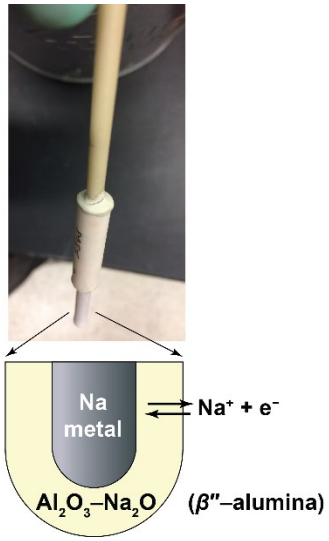

Figure A-6. *Photograph of Na/Na⁺ reference electrode, with blowup indicating the structure of the electrochemically active sodium metal tip encased in a sodium ion-selective β"-alumina ceramic membrane.*

A-1.2 – Product Detection and Quantitation

A-1.2a – Gas Flowthrough Setup

In order to account for potential gas flow losses due to loss of O-ring seal integrity at temperature, a gas flowthrough setup (**Figure A-3**) was constructed to enable quantitation of N_2 gas flow into and out of the electrochemical reactor, utilizing acrylic valved bead flowmeters (part #PB-3246040 by Cole-Parmer Scientific™) leading into and out of both the working and counter electrode compartments. Working compartment flowmeters were rated for between 40 to 500 standard cubic centimetres per minute

(sccm), while counter compartment flowmeters were rated for between 10 and 50 sccm. At typical flowrates of 40 sccm through the counter compartment and 400 sccm through the working compartment, temperature effects due to volumetric expansion were found to be within the error of the system. In quantitating P_4 yield for calculating Faradaic efficiency (FE%), observed yield was normalized by working compartment gas outflow as a fraction of working compartment gas inflow. In order to verify that all nitrogen flow loss occurred after the nitrogen gas entered the cell headspace chambers rather than in the feed line junctions, an experiment was conducted where the cell was bypassed and the feed lines were connected directly to the exhaust lines via Swaglok seals. No nitrogen leaks were observed as judged by identical upstream and downstream volumetric flow rates and manual inspection via application of soapy solution to seal junctions. For analysis of counter electrode outflow streams, gas chromatography (GC) analysis was performed by injection into a Multi-Gas Analyzer (#3; SRI Instruments) equipped with a thermal conductivity detector, methanizer, and flame ionization detector in series after Molsieve 13x and Hayesep D Columns.

We note that gas losses between the inlet and outlet of the cell result principally from advective gas flow small but macroscopic gaps between the rough alumina cell components and the Kalrez rubber-based O-rings used in the Ultra-Torr fittings. The leaks are especially pronounced through the 2.37-inch-diameter O-ring that seals the outer wall of the cell. We also note that Kalrez O-rings also have limited stability at the very high temperatures of our cell, contributing to these macroscopic leaks. The advection is induced by the positive pressure differential at which the cell is maintained relative to the outside environment to minimize the ingress of air into the electrochemical cell. Maintaining a positive pressure differential is key to the safe operation of the cell due to the pyrophoric nature of P_4. Although N_2 and P_4 have distinct diffusivities, advective transport is not dependent on the molecular mass of the gas and so, we expect P_4 losses to be in direct proportion to the overall gas losses in the cell.

A-1.2b – Product Capture

Evolved phosphorus was collected from three primary locations: the cold trap, the bleach trap, and the reactor head. The cold trap, immersed in a dry ice/acetone bath at -78 °C, was the primary method of capture and the only method by which molecular P_4 could be collected. To mitigate photoconversion of P_4 to polymeric red phosphorus (**Figure A-7**), the cold trap was wrapped in aluminum foil; following an experiment, the valves were sealed and the cold trap was pumped into a N_2 glovebox, within which P_4 samples for ^{31}P NMR could be prepared. The terminal bleach trap sometimes accumulated measurable quantities of phosphorus in the form of oxidized polyphosphate species, presumably formed by the oxidation of residual P_4 that exited the cold trap. Finally, polymeric red phosphorus deposits on the reactor interior (**Figure A-8**), formed when the reactor head cooled below the 280.5 °C boiling point of P_4, were collected for quantification by oxidation and dissolution with bleach. As a control experiment, the reactor was brought to temperature and its graphite electrodes were submerged and held at open circuit potential for 12 hours. Under these conditions, no gaseous products were observed, as supported by the lack of condensate on the reactor head and the absence of observable products in the bleach or cold traps. This finding establishes that faradaic current is required for the generation of white phosphorus and that white phosphorus does not occur carbothermally under our conditions.

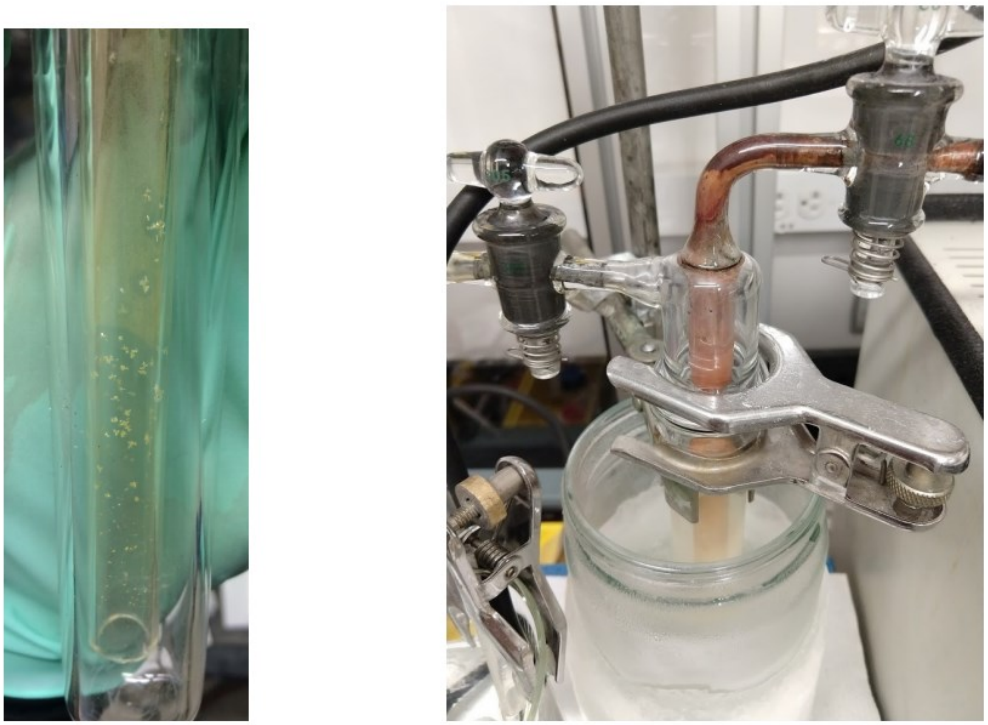

Figure A-7. *(a) Yellow-white crystals of white phosphorus are observed to form in the cold trap upon sustained electrolysis. (b) Upon exposure to light, electrogenerated white phosphorus will photoconvert to polymeric red phosphorus.*

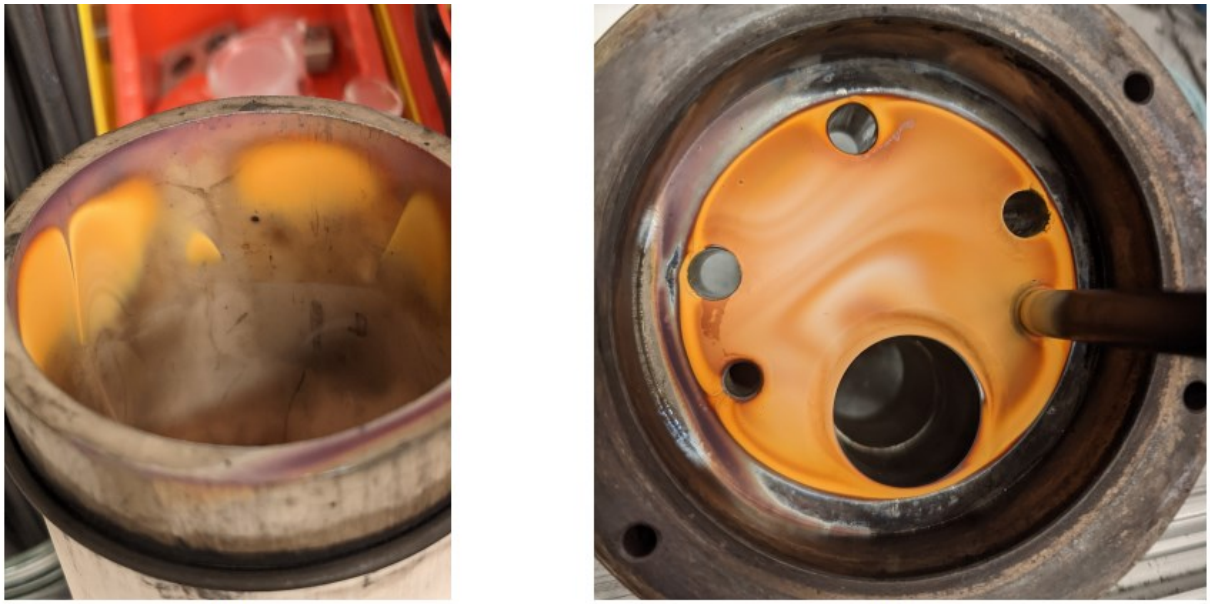

***Figure A-8**. Post-electrolysis accumulation of red phosphorus on reactor body (a) and head (b) interiors.*

A-1.3 – ^{31}P NMR Analysis and Quantitation

^{31}P NMR spectra were recorded with either Bruker AVANCE-400 or Bruker AVANCENeo-500 spectrometers and processed using MestReNova software. In order to allow for accurate integration of phosphate peaks for quantification, all ^{31}P NMR spectra were recorded without proton or deuterium decoupling pulses. ^{31}P shifts are given in ppm with respect to externally referenced triphenylphosphine (TPP) (δ = −6.0 ppm) or phosphonoacetic acid (δ = −17.0 ppm). Coupling constants are reported as J-values in Hz.

A-1.3a – ^{31}P NMR Identification of P_4

For the collection of ^{31}P NMR spectra of molecular P_4, such as that seen in **Figure 2-7**, the reactor cold trap (wrapped in aluminum foil) was sealed following a bulk electrolysis (typically around 50 mA·cm^{-2} for several hours). The cold trap was then pumped into a N_2 glovebox, where the contents of the trap were dissolved with approximately 2 mL carbon disulfide (CS_2) along with a known quantity of triphenylphosphine (as an internal standard) as well as approximately 25 mg (0.072 mmol) of chromium(III) acetylacetonate as a paramagnetic relaxation agent. The sample was then transferred to a J. Young tube for ^{31}P NMR analysis. To ensure full spin relaxation for quantitation, a delay time of 10.0 s was used.

A-1.3b – Quantitative ^{31}P NMR

Quantitative ^{31}P NMR techniques were applied for the calculation of total reduced phosphorus yield. Phosphorus residues were collected from four primary locations: the cold trap, the bleach trap, surfaces within the reactor head, and the internal surfaces of the transfer lines. As we had already established the formation of P_4 with the preceding NMR in CS_2, for these experiments, we dissolve all products in a 7.4 % w/w aqueous solution of sodium hypochlorite to facilitate the quantitation of all phosphorus emanating from the reactor. This bleach solution was used to oxidize elemental red phosphorus deposits (**Figure A-8**) to soluble ortho- and polyphosphate species. These products were then quantified by aqueous ^{31}P NMR against an internal standard of phosphonoacetic acid, again using a delay time of 10.0 s to ensure full spin relaxation for quantitation. For quantitation of phosphorus in the bleach trap, an aliquot was taken and analyzed against a phosphonoacetic acid internal standard to determine the concentration of phosphorus in the bleach trap, which was then multiplied by the volume of liquid in the bleach trap. The total phosphorus content in the bleach trap, cold trap, reactor head, and transfer lines were summed to determine the overall phosphorus yield, N_P.

A similar analysis process was applied to the cooled melt compacts, where the melt compacts at the bottom of the crucible were powdered and dissolved in D_2O milli-Q water. The subsequent solutions were then analyzed via aqueous ^{31}P NMR. Following both Tafel and bulk electrolysis trials, ^{31}P NMR of the electrolyte displays peaks in the −20 to 0 ppm range corresponding to P(V) species—specifically polyphosphate ‘middle’ groups, ‘end’ groups and orthophosphate. However, we do not observe any peaks at more positive chemical shifts in the P(III) region of the spectrum, suggesting the absence of any detectable accumulation of partially reduced phosphorus species.

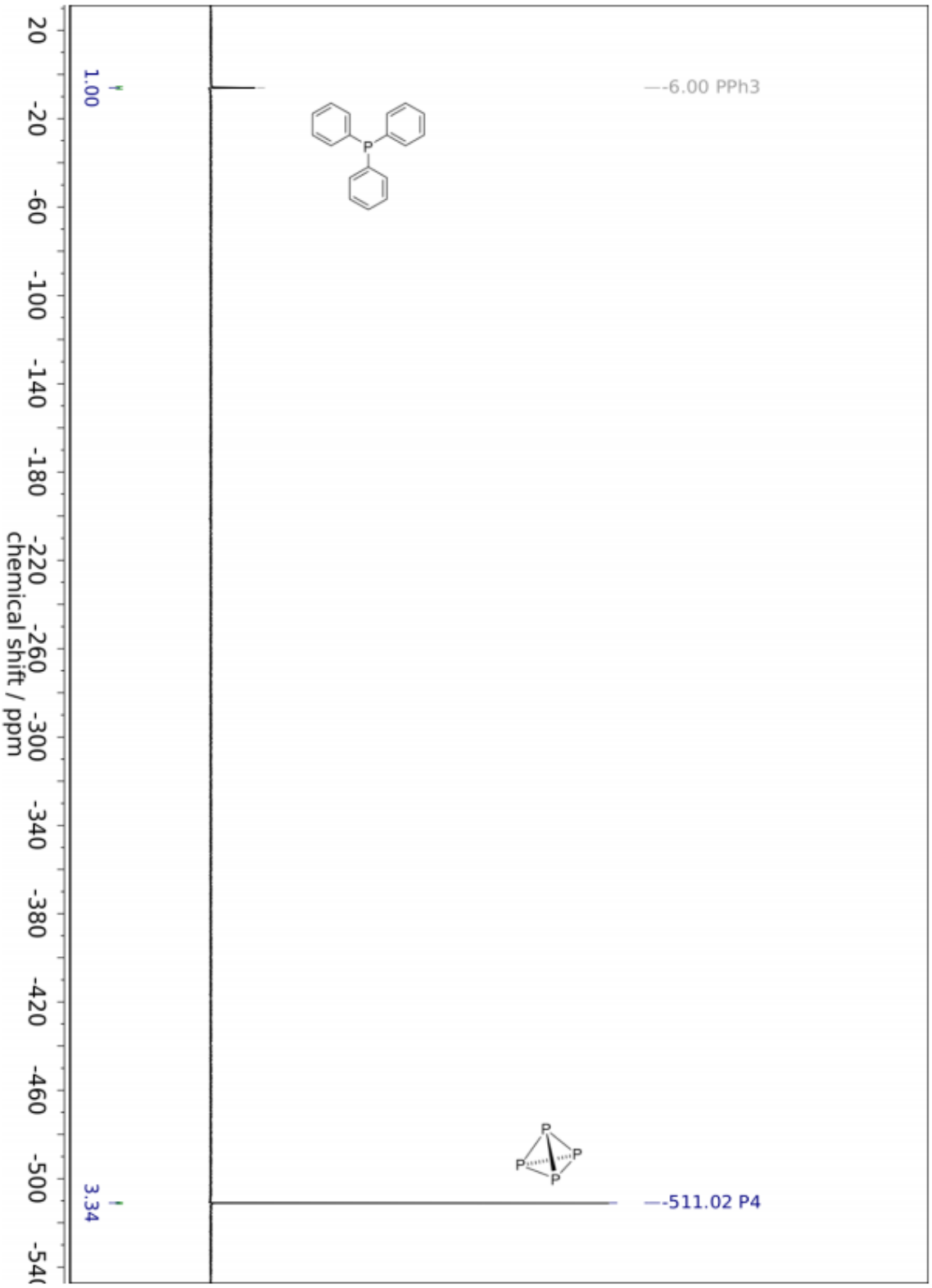

Figure A-9. *^{31}P NMR spectrum of electrogenerated P_4 collected from cold trap, dissolved in CS_2 against a triphenylphosphine internal standard.*

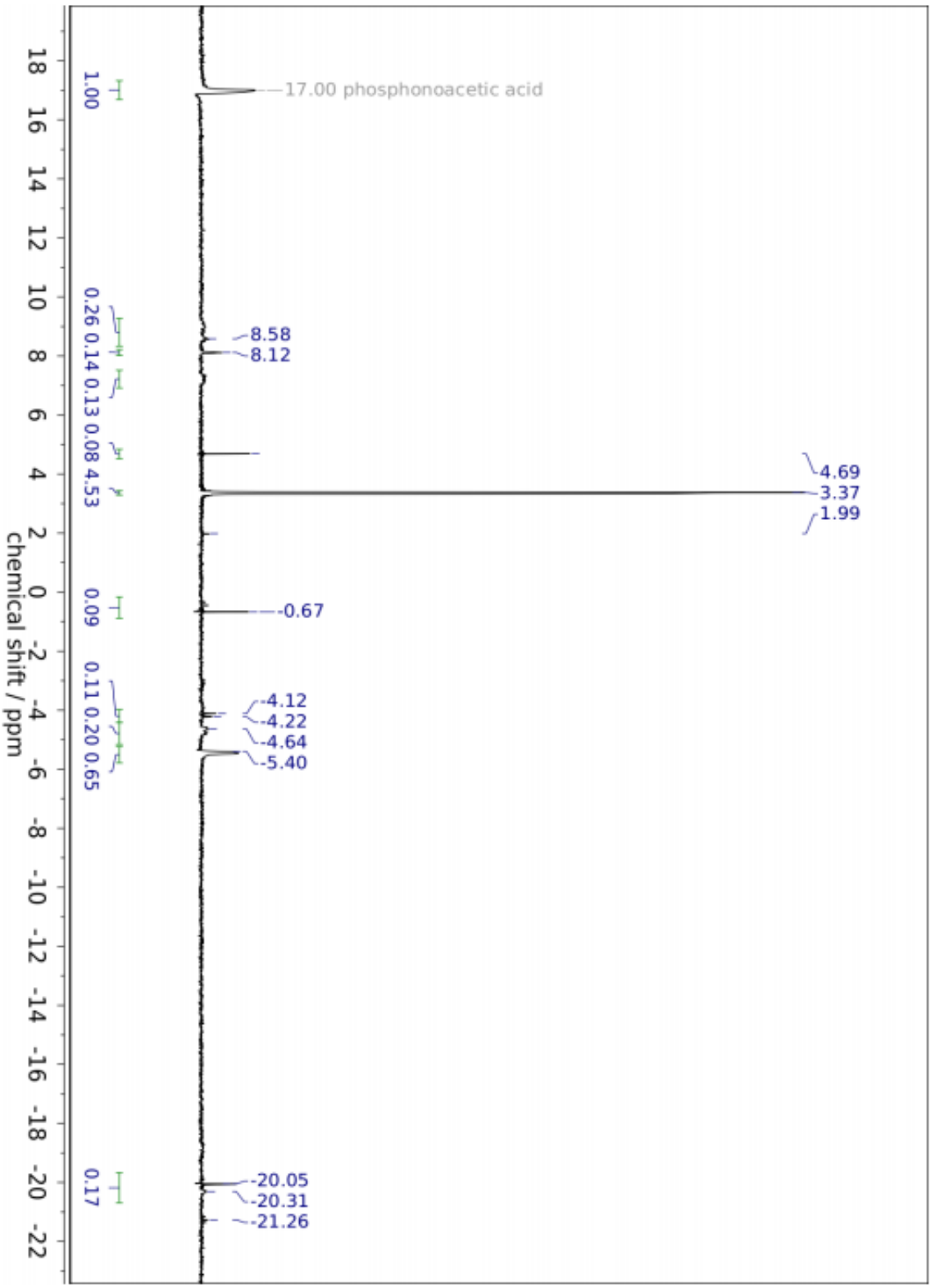

Figure A-10. *Representative quantitative ^{31}P NMR spectrum of bleach trap post-electrolysis. Integrals are normalized to phosphonoacetic acid internal standard at +17 ppm.*

A-1.3c – Calculation of Faradaic Efficiency

The Faradaic efficiency (FE%) of a process, also known as the current efficiency, is defined as the fraction of the total charge passed that proceeds towards a desired reaction product. We assess Q_{PRR} in coulombs for phosphate reduction from the total molar quantity of phosphorus N_P collected in the cold trap, bleach trap, reactor head, and transfer lines:

$$Q_{\mathrm{PRR}} = N_{\mathrm{P}} \times \frac{5\,\mathrm{mol\ e^-}}{1\,\mathrm{mol\ P}} \times 96\,485\,\mathrm{C{\cdot}mol^{-1}}.$$

We then normalize this observed value by the gas flow fraction m_{out}:m_{in} (as measured by the flow meters described above) to account for product losses from O-ring leakage, all of which occurs within the cell's working compartment. Meanwhile, Q_{total} is determined from the current integral $\int_0^t i_{total}dt$, which for a galvanostatic experiment is merely $i_{applied}t$. Putting these values together, we have:

$$\mathrm{FE\%} = \frac{N_{\mathrm{P}} \times \frac{5\,\mathrm{mol\ e^-}}{1\,\mathrm{mol\ P}} \times 96\,485\,\mathrm{C{\cdot}mol^{-1}}}{i_{\mathrm{applied}}t \times \frac{m_{\mathrm{out}}}{m_{\mathrm{in}}}},$$

which for the NMR spectrum depicted in **Figure A1.12** and its associated galvanostatic bulk electrolysis in **Figure 2.3** gives us

$$\begin{aligned}\mathrm{FE\%} &= \frac{1.40\,\mathrm{mmol\ P} \times \frac{5\,\mathrm{mol\ e^-}}{1\,\mathrm{mol\ P}} \times 96\,485\,\mathrm{C{\cdot}mol^{-1}}}{75\,\mathrm{mA} \times 13\,878\,\mathrm{s} \times \frac{170\,\mathrm{cm^3{\cdot}min^{-1}}}{250\,\mathrm{cm^3{\cdot}min^{-1}}}} \\ &= 94.9\%.\end{aligned}$$

This value of 94.9% represents a peak observed value for flowthrough-normalized Faradaic efficiency. Preceding attempts at flowthrough-normalized FE% assessment recorded values of 51% (22.3% observed FE out of 45% gas flowthrough) and 76% (41.5% observed FE out of 55% gas flowthrough). We attribute this variability to the ingress of oxygen into the system due to O-ring seal failure at temperature, resulting in the pre-capture oxidation of evolved P_4. Next-generation molten-salt electrolysis reactors may seek to mitigate this factor by incorporating more temperature-resistant gaskets instead of the Kalrez O-rings used in this work.

A-1.4 – Experimental Electrochemical Studies

Unless specified otherwise, all electrochemical experiments were conducted with the furnace set to a temperature of 800 °C, which we found to correlate well to the internal equilibrated reactor temperature as measured by an internal thermocouple. Electrochemical data were collected using a Biologic VSP potentiostat using IR compensation values of no more than 20% for noncapacitive voltammetric studies, as higher values were found to induce IR overcompensation at modest current densities. Except where specified otherwise, a graphite electrode was employed as a pseudoreference electrode for all experiments, the potential of which was retroactively corrected for against a Na/Na^+ reference that was briefly (15 seconds – 2 minutes) dipped into the melt before and after each experiment (see above). Uncompensated resistance (R_u) values were measured by the current-interrupt (CI) method; typical R_u values for the melt ranged from 1-10 Ω for all the electrolyte conditions, with higher-melting salts displaying greater solution resistances.

A-1.4a – Calculation of Electrochemical Surface Area

Observed currents i were normalized to areal current densities j using electrochemical surface areas (ECSAs) assessed following adapted literature methodologies.[7–9][7–9] For bare graphite electrodes, specific capacitance values in aqueous solution were found to be approximately 20 $\mu F \cdot cm^{-2}$ relative to the geometric surface area, well in line with literature reports.[10][10] Within the melt, specific capacitances of approximately 100 $\mu F \cdot cm^{-2}$ for graphite were determined empirically from geometric surface area. Having determined these values, the ECSAs of an electrode could be determined in terms of the double-layer capacitances (DLCs) of the electrode, both in the melt preceding and following every experiment, as well as within the melt to assess the depth of electrode immersion and ensure the absence of a short between an electrode and the glassy carbon crucible. DLC values were assessed by CV scans spanning ±50 mV around the measured OCP, with three cycles each at scan rates of 10 $mV \cdot s^{-1}$, 20 $mV \cdot s^{-1}$, 30 $mV \cdot s^{-1}$, 40 $mV \cdot s^{-1}$ and 50 $mV \cdot s^{-1}$ at IR compensations of 80%. The resultant capacitive CV traces (**Figure A-11**) were used to calculate the total capacitive current i, as the difference of the cathodic current i_c and the anodic current i_a taken at the midpoints (OCP) of the capacitive curve. These currents are related to the overall electrode capacitance C by the relation

$$C = \frac{1}{2}\frac{\partial(i_a - i_c)}{\partial(scanrate)}.$$

[7] Hall, A. S.; Yoon, Y.; Wuttig, A.; Surendranath, Y. *J. Am. Chem. Soc.* **2015**, *137* (47), 14834–14837.

[8] Yoon, Y.; Hall, A. S.; Surendranath, Y. *Angew. Chemie - Int. Ed.* **2016**, *55* (49), 15282–15286.

[9] Yoon, Y.; Yan, B.; Surendranath, Y. *J. Am. Chem. Soc.* **2018**, *140* (7), 2397–2400.

[10] Korzeniewski, C.; Conway, B. E. In *Proceedings of the Symposium on the Electrochemical Double Layer*; The Electrochemical Society, 1997; Vol. 97, pp 349–350.

Hence, the electrode capacitance (and hence ECSA) could be determined by plotting the capacitive currents as a function of scan rate and dividing the slope of the resulting linear fit, as demonstrated in **Figure A-12**.

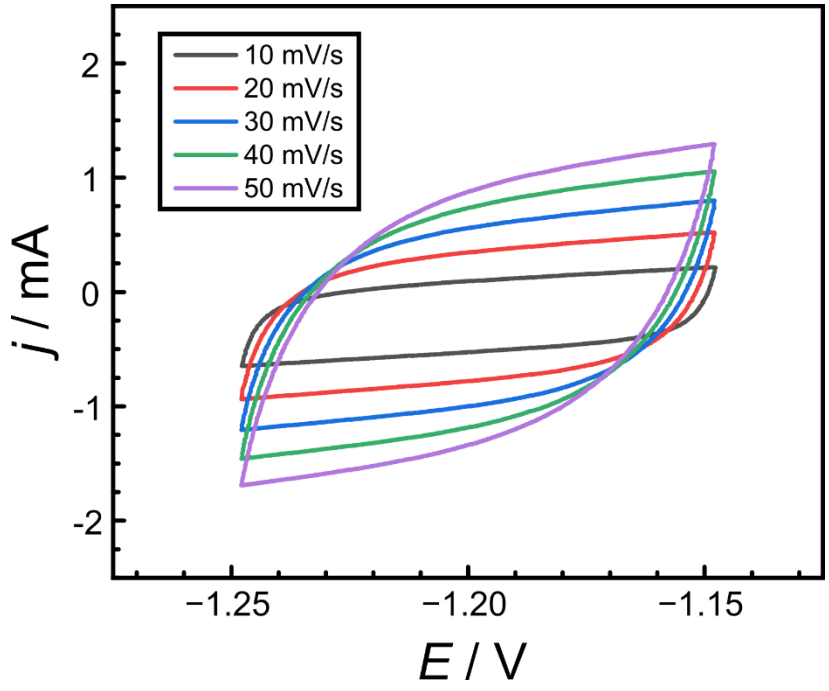

***Figure A-11**. Representative cyclic voltammograms of a graphite electrode scanning ±50 mV around OCP at scanrates of 10 mV·s^{-1}, 20 mV·s^{-1}, 30 mV·s^{-1}, 40 mV·s^{-1} and 50 mV·s^{-1}. Electrolyte is 0.1 M aqueous sodium perchlorate solution.*

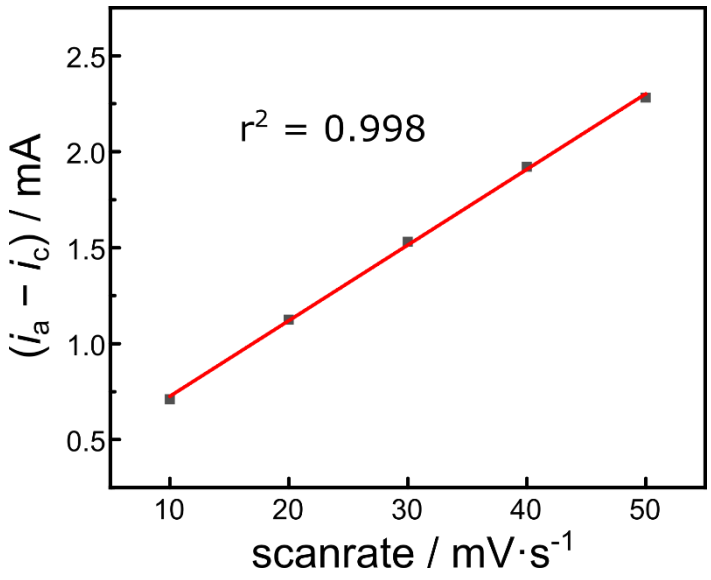

Figure A-12. *Representative linear fit for scan rate dependence of capacitive current at OCP in* ***Figure A1.13****. At an aqueous specific capacitance of 20 μF·cm^{-2}, this slope corresponds to an electrode surface area of 1.08 cm^2.*

A-1.4b – Collection of Cyclic Voltammetry Data

The collection of cyclic voltammetry data (**Figure 2-7** and **Figure 2-9**) entailed capacitive CV collection for ECSA determination followed by cyclic voltammetry scans beginning at the open-circuit potential and spanning ±350 mV around the solution OCP, with three scans each at scan rates of 10 $mV \cdot s^{-1}$, 25 $mV \cdot s^{-1}$, 50 $mV \cdot s^{-1}$, and 100 $mV \cdot s^{-1}$.

A-1.4c – Current-Overpotential Studies

The collection of current-overpotential data for Tafel studies (**Figure 2-9**) entailed capacitive CV collection for ECSA determination, followed by chronopotentiometric steady state electrolysis. ECSA experiments were performed pre- and post-experiment in both aqueous and molten-salt conditions and found not to substantially differ; however, due to the fixed galvanostatic currents, variation in the electrode surface areas between experiments (due to variable depth of immersion in the melt) is responsible for the slight variation in areal current density values in these plots.

A-1.4d – Collection of Galvanostatic Tafel Data

Electrolyses were performed galvanostatically with a fixed current series of 10 µA, 30 µA, 100 µA, 300 µA, 1 mA, 3 mA, 10 mA, 30 mA, 100 mA and 300 mA with 30 second traces and 30 second rest periods at open-circuit between electrolyses. Typically, chronopotentiometry traces reached steady state within 15 seconds. However, for traces in the transition region of the Tafel plots (**Figure 2-9**), the potential decayed to more negative values over the course of 30 seconds before reaching steady state. This slower approach to steady state is attributed to anhydride depletion local to the electrode. In all cases, the final potential at the conclusion of chronopotentiometry trace was taken as the steady-state value plotted in **Figure 2-9**. Voltage compensation for solution resistance was implemented manually during data processing. Each galvanostatic series was performed sequentially in triplicate in every experimental setup, and the experimental setups themselves were replicated between three and nine times each to account for random variations in reactor arrangement. Error bars were calculated from 95% confidence intervals as 1.95996 times the sample standard error.

A-1.5e – Methodology for Tafel Analysis

The relationship between the cathodic current density j and the overpotential η is defined by the Tafel equation:

$$\eta = -\frac{RT \ln 10}{\beta n F} \log_{10}\left[\frac{j}{j_0}\right],$$

where β is the symmetry factor for a single-step electrochemical reaction in which n electrons are transferred and j_0 is the exchange-current density. The symmetry factor is defined as a number between 0 and 1, corresponding to the relative position of the activated complex as a fraction of the reaction coordinate from reduced to oxidized species. Experimentally determined symmetry factors typically range

from 0.4 to 0.6, and hence β is typically assumed to be 0.5 in nearly all cases.[1111] Meanwhile, the exchange-current density is defined as the equilibrium current density at net zero overpotential, at which the magnitudes of anodic and cathodic current are equal, thereby evincing no net electrolysis.

Generalizing the Tafel equation to a multistep case, we have

$$\eta = -\frac{RT \ln 10}{\alpha F} \log_{10} \left[\frac{j}{j_0} \right],$$

in which the single-step symmetry factor-adapted electron transfer number $n\beta$ is replaced by the multi-step *transfer coefficient*

$$\alpha = \frac{\gamma}{\nu} + r\beta,$$

where γ is the number of electrons transferred prior to the rate-limiting step (RLS), ν is the stoichiometric number of the reaction, r is the number of electrons transferred in the RLS, and β is the symmetry factor of the RLS (*41*–*43*). At 800 °C, this corresponds to a Tafel slope

$$b_{800\ ^\circ\mathrm{C}} = \frac{\partial \eta}{\partial(\log j)} = \frac{212.9\,\mathrm{mV \cdot dec^{-1}}}{\alpha}.$$

Tafel slopes and errors were assessed by least-squares linear fitting (using OriginLab Origin2018's Linear Fit with Y Error algorithm to propagate errors) of the current-potential data in the 'macropolarization' regime, defined as current densities ≥1 mA·cm^{-2}. All Tafel slopes are reported in units of mV·dec^{-1}.

A-1.5 – Gas Chromatography of Gas Outflow Streams

For analysis of counter electrode outflow streams, GC analysis was performed by injection of the effluent gas into a Multi-Gas Analyzer (#3; SRI Instruments) equipped with a thermal conductivity detector, methanizer, and flame ionization detector in series after Molsieve 13x and Hayesep D Columns. With the counter compartment gas flowrate set to 60 sccm, baseline measurements were collected by injecting gas from the counter electrode outflow stream at rest, while experimental values were collected by injecting gas from the counter electrode outflow stream while passing a fixed cathodic current of 75 mA through the working electrode (and thereby an equivalent anodic current through the counter electrode).

The GC traces evince a significant increase in the gas fractions of CO and CO_2 while the counter electrode is under anodic polarization relative to a control experiment without electrolysis. Integrating the GC traces

[11] Bard, A. J.; Faulkner, L. R. *Electrochemical Methods: Fundamentals and Applications*, 2nd ed.; Wiley: New York, 2000.

reveals a gas outflow stream that is 96% CO_2 and 4% CO, equivalent to a net electron efficiency of 3.9 electrons per atom of carbon, out of a theoretical 4 electrons per carbon for the total conversion of C → CO_2. This compares favorably to the value of 2 electrons per carbon for the incomplete combustion C → CO used in the thermal process. The generation of CO may be attributable to either the partial oxidation of graphite and/or the Boudouard reaction, the comproportionation of CO_2 with carbon, $CO_2 + C \rightleftharpoons 2\ CO$.[12–14121314]

A-1.6 – Composition and Structure of Molten Condensed Phosphates

Condensed phosphates are defined as phosphate salts that are dehydrated relative to free orthophosphate, possessing at least one phosphoryl anhydride linkage between adjacent phosphorus atoms. Collectively, the condensed phosphates comprise the linear polyphosphates, the cyclic metaphosphates, and the branched ultraphosphates (**Figure A-13**). These phosphoryl anhydride linkages are crucial to describing the chemistry of the condensed phosphates, as their oxide-induced cleavage to terminal phosphates is fundamental to the 'oxide-accepting' character of condensed phosphate melts (**Figure A-14**).

This reactivity allows condensed phosphate melts to intrinsically fulfill the role performed in the thermal process by the conversion of silicon dioxide to metasilicate, which is associated with a majority of the slag formation (and associated energetic losses) of the thermal process.

Individual condensed phosphate species consist of a mixture of terminal, branching, and bridging moieties such that, by the relations detailed in **Table A-1**, all condensed phosphate ions will satisfy the relation $[(PO_{2.5})_u(PO_3)_m(PO_{3.5})_p]^{(m+2p)-}$, where u is the number of branching (ultraphosphate) moieties, m is the number of bridging (metaphosphate) moieties, and p is the number of terminal (paraphosphate) moieties. While the presence of fractional oxygen atoms for bridging and terminal phosphate groups may seem problematic at first, the nature of terminal and branching groups in a phosphate oligomer is such that the total number of bridging and terminal phosphates must always be an even number, so this is not an issue. For obvious reasons, free orthophosphate ions cannot be part of a condensed phosphate oligomer, as they have no phosphoryl anhydride linkages and hence are not condensed phosphates. The interconversion of phosphate oligomers – for example, of two paraphosphates into an orthophosphate and a metaphosphate, two metaphosphates into a paraphosphates and an ultraphosphate, or the reverse of these reactions – is expected to occur rapidly at the high temperature of the melt and, thus, we consider all molten phosphate species to be in equilibrium under the conditions of electrolysis.[1515] As the precise distribution of condensed phosphate chains is a function of temperature, precise characterization of a melt cannot be performed by analysis of the solidified electrolyte, although such post-solidification analysis vindicates our conflation of mixed orthophosphate-metaphosphate solutions with their equivalent pure polyphosphate melts (see below). Future studies on the in situ character of the melt (perhaps by high-temperature NMR) may permit quantification of the phosphate speciation in the reaction media.

[12] Chen, P.; Zhang, H.-B.; Lin, G.-D.; Hong, Q.; Tsai, K. R. *Carbon N. Y.* **1997**, *35* (10–11), 1495–1501.

[13] Wiberg, E.; Holleman, A. F.; Wiberg, N. In *Inorganic Chemistry*; San Diego, 2001; pp 810–811.

[14] Basu, P. In *Biomass Gasification, Pyrolysis and Torrefaction*; Basu, P., Ed.; Academic Press, 2018; pp 211–262.

[15] Greenfield, S.; Clift, M. *Analytical Chemistry of the Condensed Phosphates*; Pergamon: Oxford, 1975.

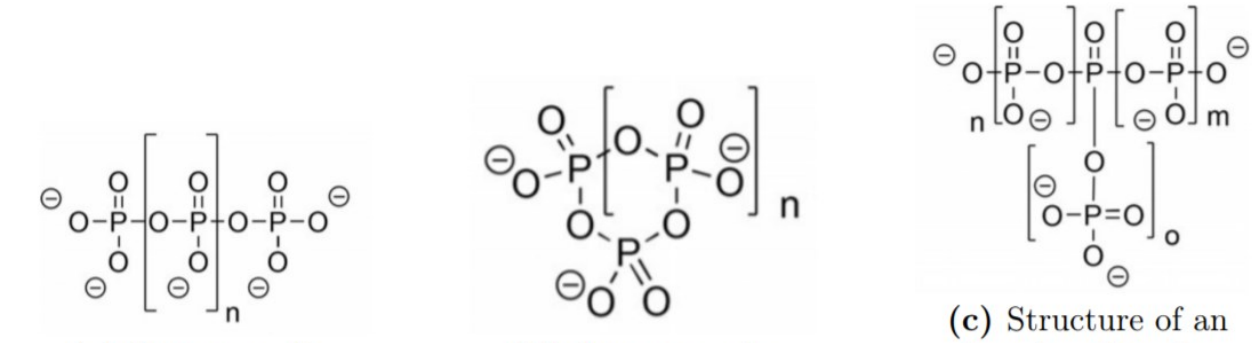

(a) Structure of a polyphosphate ion, $n \geq 0$.

(b) Structure of a metaphosphate ion, $n \geq 1$.

(c) Structure of an ultraphosphate ion, $m, n, o \geq 1$.

Figure A-13. *Classifications of condensed phosphate species.*

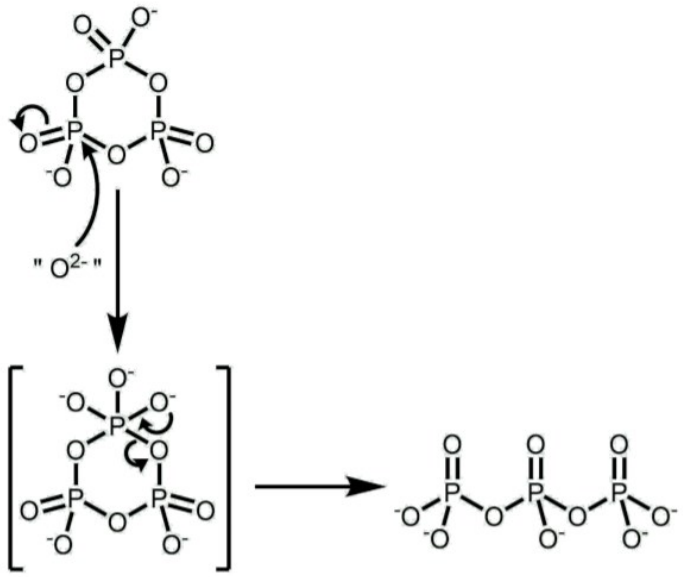

Figure A-14. *Representative mechanism for cleavage of a phosphoryl anhydride linkage by an oxide equivalent, here showing the formation of tripolyphosphate ($P_3O_{10}^{5-}$) from trimetaphosphate ($P_3O_9^{3-}$). Note that oxide equivalents rarely exist as free O^{2-} ions, and in practice are more likely to be represented as nucleophilic polyphosphate chains.*

Prefix	Structure	Anhydrides	Oxides	Formula Unit
ortho-	free	0	1½	PO_4^{3-}
para-	terminal	1	1	$PO_{3.5}^{2-}$
meta-	bridging	2	½	PO_3^-
ultra-	branching	3	0	$PO_{2.5}$

Table A-1. *Phosphate species by the number of phosphoryl anhydride linkages per phosphorus atom and their equivalent oxide content relative to phosphoric anhydride, P_4O_{10}.*

A-1.6a – Preparation of Selected Condensed Phosphate Mixtures

As seen in **Table A-2**, four selected condensed phosphate melts of varying degrees of oxide content were selected for analysis in this work, spanning a range of phosphoryl anhydride molalities from 5.4 mol·kg^{-1} to 9.8 mol·kg^{-1}. While the first of these melts was equivalent to a pure metaphosphate melt, the remainder were synthesized by mixing targeted mole fractions of sodium trimetaphosphate (S3MP) and sodium orthophosphate (SOP) to produce a homogenous electrolyte upon fusion. A 75:25 mol:mol mixture of S3MP:SOP (85:15 by mass) is 8.3 mol·kg^{-1} in phosphoryl anhydride linkages, equivalent to that of sodium decapolyphosphate (S10PP); a 50:50 mol:mol mixture (65:35 by mass) is 6.4 mol·kg^{-1}, equivalent to sodium tetrapolyphosphate (S4PP); finally, a 40:60 mol:mol mixture (55:45 by mass) is 5.4 mol·kg^{-1}, equivalent to sodium tripolyphosphate (S3PP). Lower concentrations of phosphoryl anhydride linkages are largely inaccessible as melts at the reaction temperature of 800 °C; the next lowest polyphosphate, sodium pyrophosphate (3.8 mol·kg^{-1} in phosphoryl anhydride linkages) has a melting point of 988 °C, and pure sodium orthophosphate (0 mol·kg^{-1} in phosphoryl anhydride linkages) has a melting point of 1583 °C. For each of these selected melts, a total mass of 60 g was measured out in the prescribed ratio of S3MP (99.9999%, anhydrous, #AA89063A1 from Alfa Aesar™) to SOP (99.9999%, anhydrous, #AC389810010 from Acros Organics™) and ground together in a mortar & pestle to ensure homogeneity. This mixture was then poured into a glassy carbon crucible for electroanalysis as described above.

Melt Equivalent	[anhydride]	$Na_3P_3O_9$ mol%	Na_3PO_4 mol%
S3MP ($Na_3P_3O_9$)	9.8076	100%	0%
S10PP ($Na_{12}P_{10}O_{31}$)	8.3210	75%	25%
S4PP ($Na_6P_4O_{13}$)	6.3883	50%	50%
S3PP ($Na_5P_3O_{10}$)	5.4368	40%	60%

Table A-2. *Condensed phosphate melts selected for study, their net anhydride content (in mol·kg^{-1}), their homogeneous equivalent species (in terms of melt oxide/anhydride content), and the molar ratios of sodium trimetaphosphate (S3MP) and sodium orthophosphate (SOP) required for synthesis.*

A-2: SUPPLEMENTAL EXPERIMENTS

A-2.1 – Replenishment of Anhydride-Depleted Melt with Phosphoric Acid

A-2.1a – Electrochemical Characterization of Anhydride-Depleted Polyphosphate Melt

In order to simulate a melt with a depleted concentration of anhydride bonds after extended electrolysis, 18.1420 g (0.110 mol) of Na_3PO_4 was combined with 33.8582 g (0.110 mol) of $Na_3(PO_3)_3$ to produce 52 g of a 50 mol % Na_3PO_4 / 50 mol% $Na_3(PO_3)_3$ mixture, with an expected anhydride molality of 6.4 mol·kg^{-1}. This mixture was heated and melted in the molten salt electrochemical reactor, and the melt was subsequently characterized via cyclic voltammetry at 800 °C (**Figure A-15,** "Anhydride-Depleted Electrolyte") with a sharpened graphite working electrode whose surface area was previously measured via capacitance.

A-2.1b – Phosphoric Acid Addition and Dehydration

After characterization and cooling, the phosphate salt compact was removed from the crucible and ground into a fine powder with a mortar and pestle. 0.086 g of this powder was saved for NMR analysis (see below), and 39.94 g (0.085 mol tetrapolyphosphate on average) of the powdered mixture was mixed with 19.60 g (0.17 mol) of 85 wt % phosphoric acid, the stoichiometric amount to permit complete conversion of the melt composition into $Na_3(PO_3)_3$ after dehydration. This mixture was placed in the glassy carbon crucible, left to set under a flow of nitrogen overnight, and then reheated via a slow manual ramp from room temperature up to 800 °C, where it was held at temperature overnight and then cooled. This melt is referred to as the phosphoric acid treated melt.

A-2.1c – Electrochemical Characterization Following Addition of Phosphoric Acid

After cooling, the melt compact was again ground into a powder via mortar-and-pestle. While the 50%/50% mixture had been a semi-crystalline solid that was difficult to pulverize, the new melt compact was a soft, crumbly solid that readily broke apart, indicating compositional changes. Roughly 0.1 g of the phosphoric acid-treated melt was saved for NMR analysis (see below) and the remainder was re-melted in the molten salt electrochemical reactor. The melt was subsequently characterized via cyclic voltammetry at 800 °C on the same sharpened graphite working electrode (**Figure A-15**, "Replenished Electrolyte"), whose surface area was previously evaluated via capacitance measurements to have a value of 13.6 cm^2. The current densities reported were corrected from raw current using this value, in the manner of Section A-1.4a – Calculation of Electrochemical Surface Area.

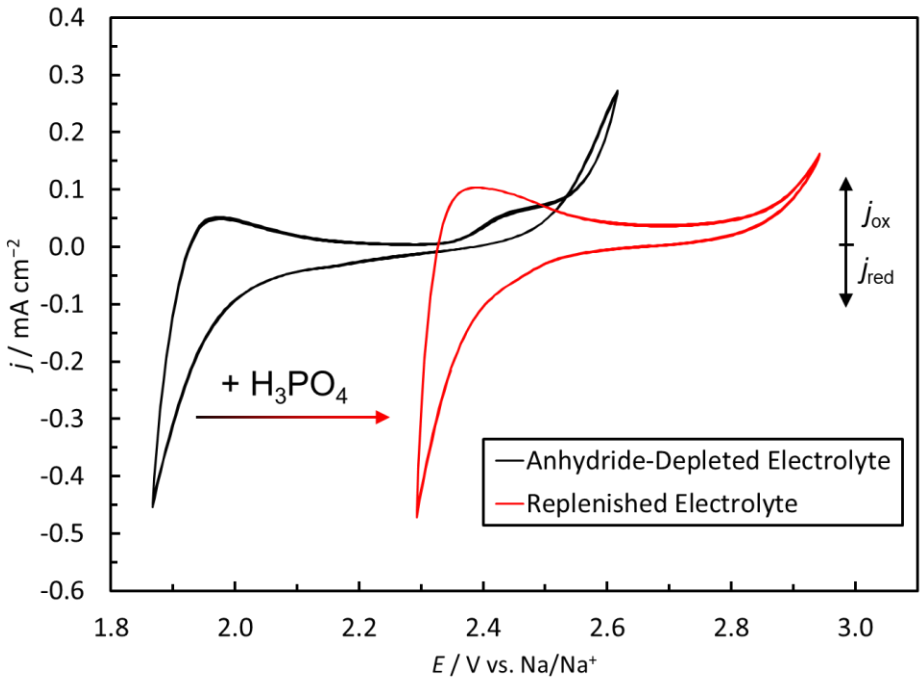

Figure A-15. *Cyclic voltammetry (black) of a sodium polyphosphate melt containing an anhydride molality of 6.4 mol·kg^{-1}. This low anhydride molality simulates the electrolyte composition following extensive electrolysis. Cyclic voltammetry (red) following addition of phosphoric acid to the low anhydride melt to generate an anhydride molality of 9.2 mol·kg^{-1}. Data were recorded at 100 mV·s^{-1} scan rate at 800 °C on a sharpened graphite rod working electrode. Potentials are reported vs. the Na/Na^{+} redox couple.*

A-2.1d – ^{31}P NMR Characterization Prior to and Following Phosphoric Acid Addition

The powder samples of the anhydride-depleted and phosphoric acid-treated melts were dissolved in 0.6 mL of deuterated water and characterized by ^{31}P NMR (**Figure A-16)**. ^{31}P NMR spectra for the anhydride-depleted melt display resonances at −5 and −20-21 ppm corresponding to polyphosphate 'end' groups (-O-PO_3^{2-}) and polyphosphate 'middle' groups (-O-PO_2^--O-), respectively. Relative integrations of these peak families indicate an 'end' to 'middle' ratio of approximately 1:1, which would be consistent with an average composition corresponding to sodium tetrapolyphosphate. In contrast, the phosphoric-acid treated melt displays a single resonance at −21 ppm corresponding to pure sodium trimetaphosphate. This indicates that phosphoric acid treatment and dehydration is sufficient to regenerate the anhydride bonds in the native melt and allow for continued replenishment of the electrolyte.

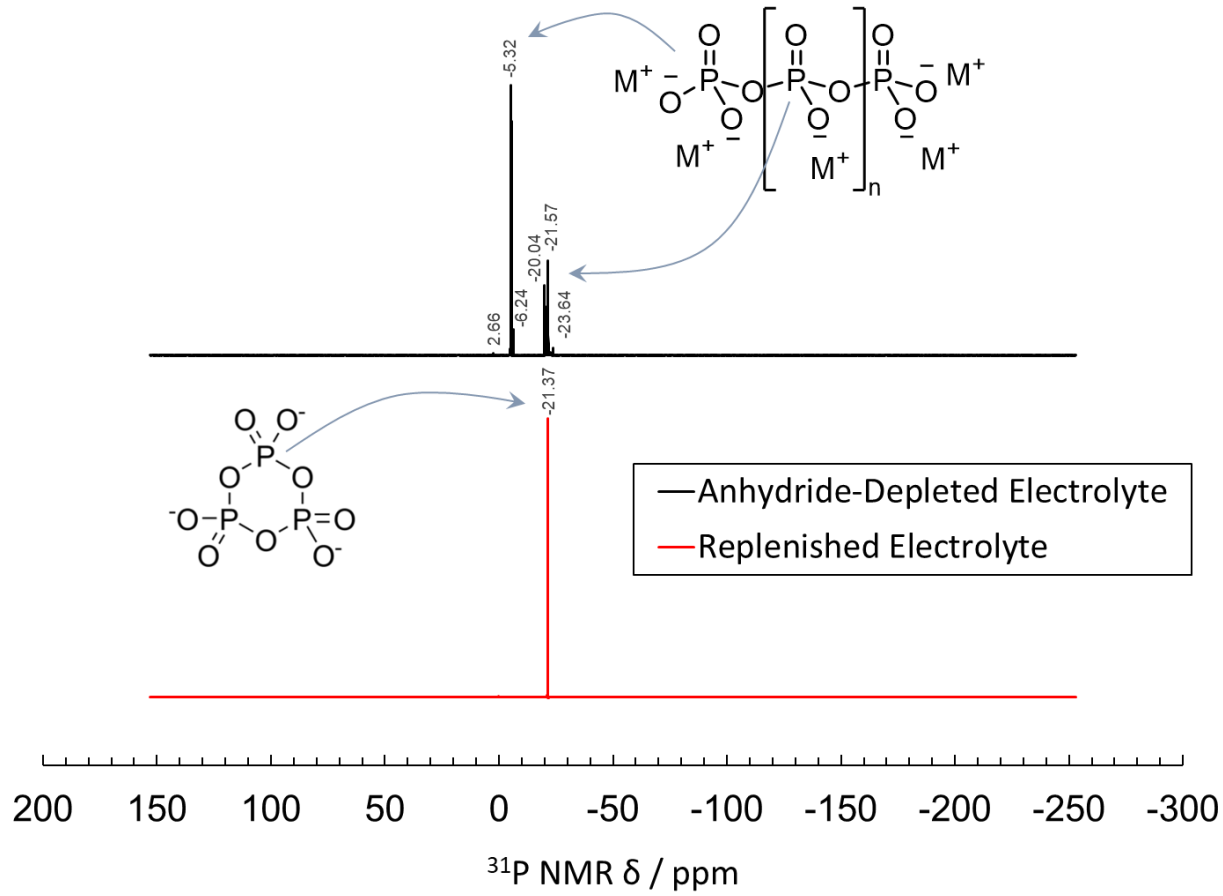

Figure A-16. *^{31}P NMR of the anhydride-depleted (black) and phosphoric acid-replenished (red) samples in D_2O. Arrows indicate assignments of the peak families to phosphorus atoms in the respective polyphosphate structures.*

A-2.2 – Electrolysis of "Impure" Phosphoric Acid

Wet-process phosphoric acid contains an array of impurities. Thus, we investigated the electrochemical behavior of a melt generated from impure phosphoric acid. To simulate an impure polyphosphate melt, we combined the following listed compounds (**Table A-3**), in their respective proportions known to exist in wet-process phosphoric acid.[1616] This mixture was added to a glassy carbon crucible and heated to 800 °C in the electrochemical furnace. This heating served to both dehydrate and melt the impure polyphosphate mixture. Electrochemical measurements were then performed with graphite rod electrodes using the procedures described above. Despite the large population of impurity ions, the voltammetric signatures resemble those of a pure polyphosphate melt with a phosphoryl anhydride molality of 6.4 $mol \cdot kg^{-1}$ (**Figure A-17**). This data suggests that the presence of impurities does not dramatically impede the native electrochemical processes for P_4 synthesis.

Following prolonged electrolysis for 2 hrs at a current density of 12.8 $mA \cdot cm^{-2}$ on a graphite cone electrode (corrected by the submerged surface area of 7.84 cm^2, measured via capacitance), the cell was allowed to cool to room temperature and was subsequently disassembled. The graphite cathode was coated around the tip with a black powdery deposit which we attribute to the reduction of impurity metals in the melt and/or to the reaction of the produced P_4 with metal impurities to form metal-phosphide phases. Given the voltammetric similarity between the pure and impure melts, we favor the latter explanation. Irrespective of the mechanism, these findings suggest that impurity induced the formation of insoluble deposits on the electrode, facilitating their periodic removal.

[16] Feki, M.; Ayedi, H. F. *Sep. Sci. Technol* **2008**, *33*, 2609–2622.

	Wt% in wet-process phosphoric acid	**Analog Species**	**Amount Used**
H_3PO_4	75.3	**H_3PO_4 85 wt %**	9.3921 g
		$Na_3(PO_3)_3$	43.6935 g
P_2O_5	54.6		
CaO	0.15	**$CaSO_4*2H_2O$**	0.3062 g
MgO	1.09	**$Mg_5(CO_3)_4(OH)_2*3H_2O$**	1.6136 g
Al_2O_3	0.86	**Al_2O_3**	0.5707 g
Fe_2O_3	0.48	**$FePO_4*H_2O$**	0.6740 g
SO_4^{2-}	1.03	**Na_2SO_4**	0.7598 g
F^-	0.048	**F-**	-
C	0.03	**C (carbon black)**	0.0200 g

Table A-3. *Chemical constituents for a melt simulating sodium metaphosphate derived from 'dirty' phosphoric acid at industrial wet process concentrations.*

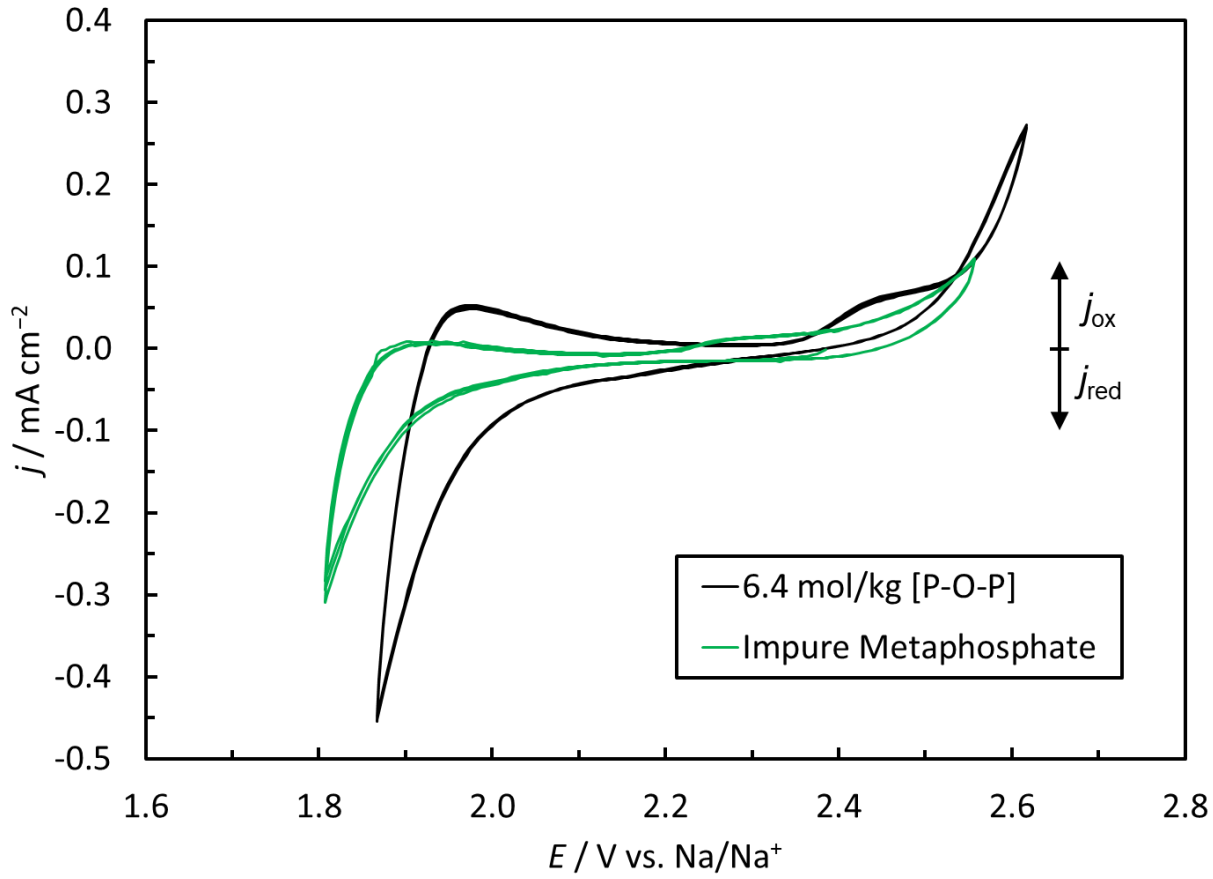

Figure A-17. *Cyclic voltammetry of a metaphosphate solution prepared from the impurities in dirty phosphoric acid (green), overlaid with cyclic voltammetry of a typical 6.4 mol·kg^{-1} melt of sodium polyphosphate (black). Data were recorded on a sharpened graphite rod work electrode. Potentials are reported vs the Na/Na^{+} redox couple.*

A-2.3 – Solubility of Calcium in Condensed Phosphate Melts

Tuning the anhydride population provides an additional handle for controlling the solubility and managing the build-up of impurity ions.

Prior studies establish that pure metaphosphate metals are able to solubilize substantial quantities of Ca^{2+} ions. Indeed, Na^{+} and Ca^{2+} metaphosphate binary melts remains liquid at the 800 °C operating temperature of our system up to a 49 mass % of calcium metaphosphate in sodium metaphosphate (0.33 mole fraction of Ca^{2+}).[1717] The solid phase in equilibrium with the melt is reported to be enriched in, if not entirely comprised of, calcium metaphosphates. This data suggests that Ca^{2+} impurities would remain quite soluble in pure metaphosphate melts.

To best of our knowledge, no studies have examined Ca^{2+} solubility as a function of anhydride concentration in polyphosphate melts. As a qualitative assessment, we examined whether various ratios of calcium orthophosphate ($Ca_3(PO_4)_2$) and sodium trimetaphosphate would form precipitates at the operation temperature of 800 °C. Powders **of $Na_3(PO_3)_3$ and** ($Ca_3(PO_4)_2$) were mixed in the ratios shown in **Table A-4**. Each sample was transferred to a quartz crucible and heated to 800 °C. They were held at this temperature overnight to provide adequate time to equilibrate, and then visually inspected.

At the high anhydride molality of 8.9 mol·kg^{-1}, the presence of 6.7% Ca^{2+} still leads to a transparent melt (**Figure A-18a**). In contrast, a cloudy melt containing visible precipitates is observed for a 14% Ca^{2+} fraction at a slightly lower anhydride molality of 7.7 mol·kg^{-1} (**Figure A-18b**). Higher Ca^{2+} percentages and lower anhydride molalities lead to solid compacts or powders at 800 °C (**Table A-4**). This qualitative behavior contrasts with the ability of metaphosphate melts (anhydride molality ~9.8 mol·kg^{-1}) to support 33% Ca^{2+} and highlights that anhydride molality can be used to tune the soluble of divalent ions in the melt.

[17] Morey, G. W. *J. Am. Chem. Soc.* **1952**, *74* (22), 5783–5784.

Calcium Phosphate (g)	Sodium Trimetaphosphate (g)	Mole % Ca^{2+} (in Na^{+})	Theoretical anhydride molality ($mol \cdot kg^{-1}$)	State at 800 °C
1.04	8.95	6.7%	8.9	Uniform liquid
2.15	7.85	14%	7.7	Liquid with white precipitate
5.51	4.48	33%	4.4	Solid compact
7.00	3.00	59%	2.9	Crumbly cake of powders

Table A-4. *Prepared mixtures of calcium orthophosphate and sodium trimetaphosphate and their physical states after being held overnight at 800 °C. Melt compositions represented both by mole percentage of calcium ions relative to sodium ions in the melt, as well as theoretical anhydride bond molality in the melt, in $mol \cdot kg^{-1}$.*

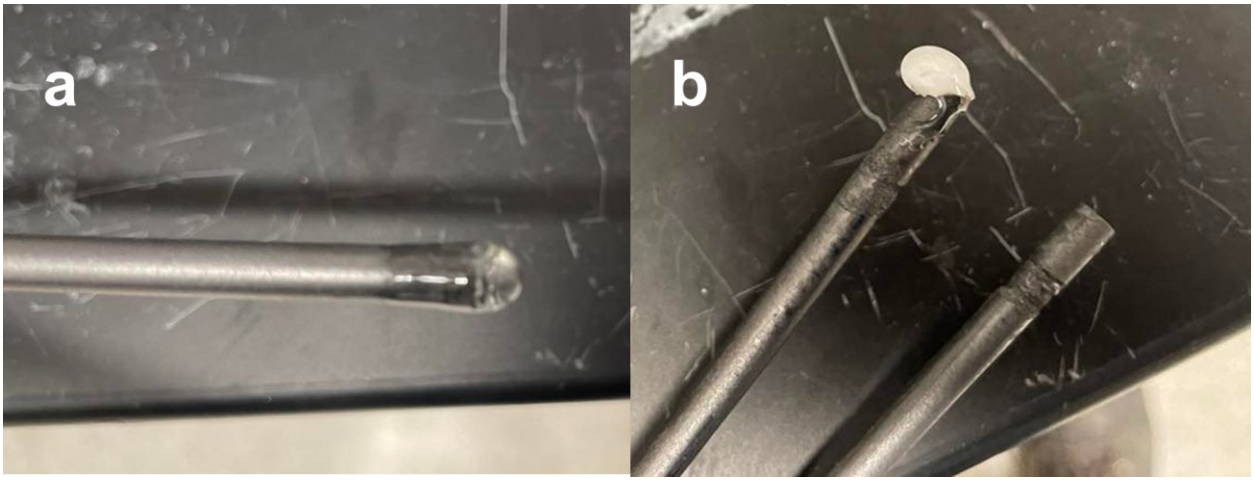

Figure A-18. *Photographs of select melts tested for precipitation of a calcium ion-based solute. a) Aliquot of a melt containing 6.7% Ca^{2+} and an anhydride molality of 8.9 mol·kg^{-1} showing a clear glassy appearance with no precipitate. b) Aliquot of a melt containing 14% Ca^{2+} and an anhydride molality of 7.7 mol·kg^{-1} showing a cloudy appearance with visible precipitates. Photographs were taken immediately upon removal of the aliquot from the 800 °C melt.*

A-2.4 – Longer-Term Electrolysis

Typically, electrolyses were manually terminated after 30 min to 3 hours so as not to generate excessive amounts of white phosphorus. However, we have conducted several long-term electrolyses, and representative 17-hour electrolysis trace at a −30.4 $mA \cdot cm^{-2}$ current density (corrected via capacitive area of 9.87 cm^2) is shown in **Figure A-19**. Running the reaction beyond this point is a challenge given the limits of our experimental design for several engineering reasons, including:

a) the neck leading to our collection flask is narrow and eventually clogs with condensed red phosphorus, preventing further nitrogen flow,

b) our research-grade graphite electrodes are thin and fragment over time due to anodic corrosion; we have no means to add more graphite *in situ* as the reaction progresses.

c) we employ no liquid-phase separator or membrane in our small-scale system and, thus, crossover of loose graphite particles released from aggressive anode oxidation can short the electrochemical cell. The potential spike in **Figure A-19** is attributed to this phenomenon.

d) because we are operating with a fixed electrolyte volume, and do no replenish it *in situ* via the methods we discuss earlier (see "Replenishment of Anhydride-Depleted Melt with Phosphoric Acid" and **Figure A-17**), the Lux acidity of the system is depleted over time and this can a progressive drift in the working electrode potential.

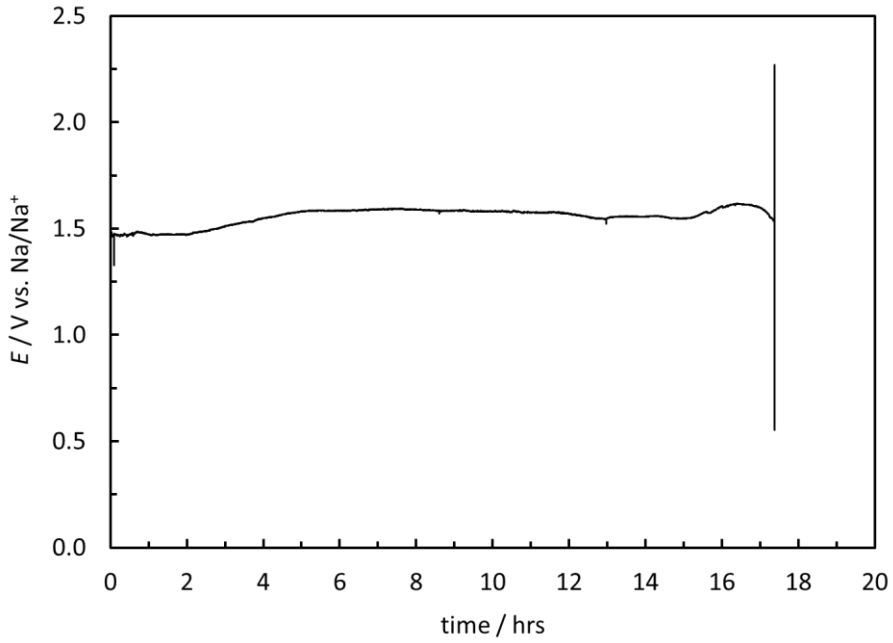

Figure A-19. *Long-term chronopotentiometry data at 30.4 mA·cm^{-2} on a sharpened graphite working electrodes in a molten sodium metaphosphate melt at 800 °C. The abrupt spike in potential at ~17 hrs is attributed to the progressive corrosion of the graphite anode and the formation of graphite particle in the melt that eventually short the electrochemical cell.*

A-2.5 – Steady-State Kinetics of Graphite Rod Oxidation

In order to examine whether the kinetic benefits of high Lux acidity for PRR are mitigated by attenuation kinetics at the carbon anode, we collected steady-state chronopotentiometry of the graphite oxidation reaction at the endpoint of high and low Lux acidity examined in this study. Specifically, the anhydride concentrations were 9.8 mol kg^{-1} (pure metaphosphate) and 5.4 mol kg^{-1} (produced from 23.1743 g Na_3PO_4 and 28.8263 g $Na_3(PO_3)_3$). Constant current electrolyses were performed at 800 °C and the steady-state potentials were measured relative to a graphite pseudoreference and Na/Na+ primary reference as detailed above. Electrode surface areas was evaluated via capacitance of the submerged graphite tip in the melts using the 100 µF cm^{-2} specific capacitance value determined in Section S1.5a. Steady-state voltage values were measured at for electrolyses conducted over a range of currents spanning 10 µA to 200 mA and the resulting Tafel data is plotted in **Figure A-20**. Before collection of each chronopotentiometry data point, the solution resistance was measured and used to correct the observed steady state potential for ohmic losses.

The top plot in **Figure A-20** shows the polarization data referenced a Lux-acidity independent Na/Na^+ reference and shows the offset between the two curves caused by shifts in the thermodynamic potential for carbon oxidation. The bottom plot **Figure A-20** references the data to a graphite pseudoreference which we found to closely pin to the phosphate/P_4 equilibrium potential. Thus, the bottom plot accounts for shifts in the equilibrium potential with changing Lux acidity and captures differences in overpotential between the two melts. While a greater overpotential penalty is observed for the high Lux acidity melt (**Figure A-20** black), the sensitivity to Lux acidity is less pronounced than for PRR. At 30 mA cm^{-2} current density, we observe ~0.6 V increase in overpotential upon going from low to high Lux acidity. In contrast, at the same current density, we observed a ~1.1 V reduction in overpotential for P_4 production in the high Lux acidity melt (**Figure 2-9**). Thus, this data suggests a ~0.5 V reduction in overall cell voltage at this current density for the high Lux acidity melt.

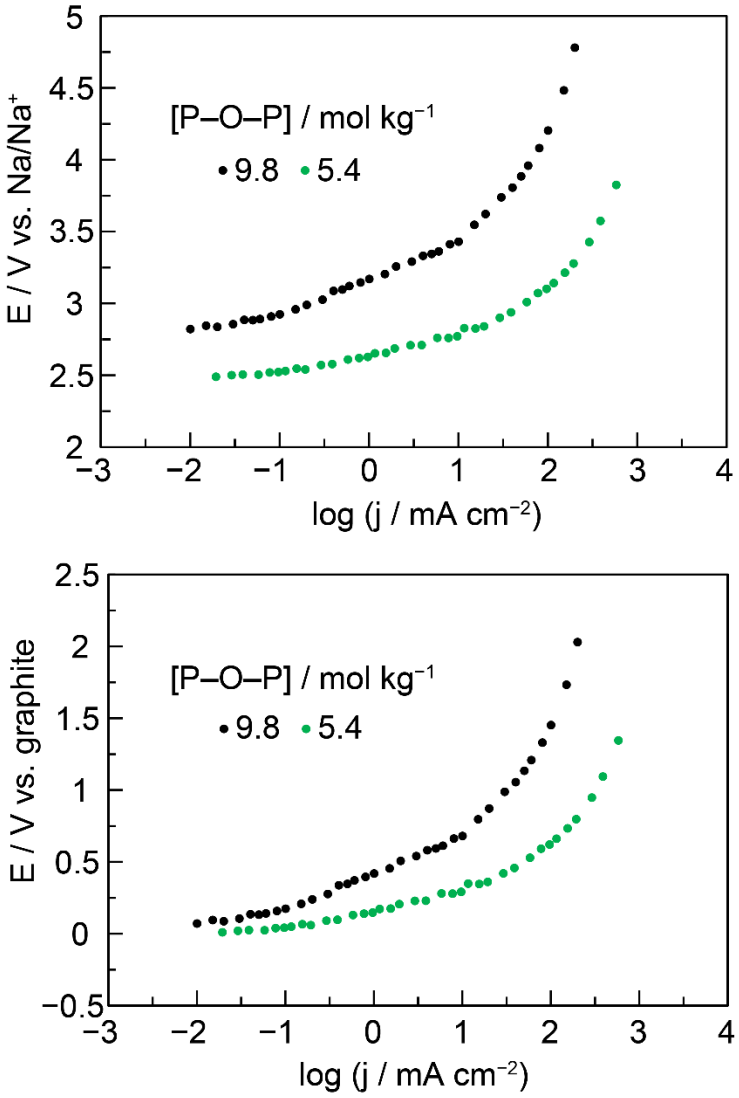

Figure A-20. *(Top) Steady-state voltage for oxidation of graphite vs. a Na/Na^+ reference electrode with respect to chronopotentiometric current density in both sodium trimetaphosphate (black) and sodium tripolyphosphate (green) electrolyte melts. (Bottom) Same data as top, with voltages expressed relative to the graphite pseudoreference potential which accounts for shifts in the equilibrium potential with changing Lux acidity.*

A-2.6 – XPS of Graphite Cathode Tips

In order to investigate local species generated at the graphite cathode, X-ray photoelectron spectra (XPS) were collected on the tips of three graphite cathodes. Two cathodes were prepared using the methods described in section S1.1c, while the third was additionally oxidized with aqua regia before use as a cathode in order to interrogate whether the oxidation state of the surface affected its electrochemical properties. After preparation, each of these graphite rods were individually utilized in the melt as cathodes for the steady-state analysis of phosphorus evolution kinetics, with current densities ranging from 10 μA cm^{-2} to 100 mA cm^{-2}. After use, these electrodes were subsequently removed from the melt, cooled and their tips severed from the graphite rod and examined under XPS.

X-ray photoelectron spectra of these graphite electrode tips (**Figure A-21**) were recorded using a Physical Electronics PHI Versaprobe II with a monochromatic aluminum Kα X-ray source (1486.6 eV) and a hemispherical energy analyzer. Spectra were collected by fixing the graphite rod tips to the support platen with conductive carbon tape. Data were collected at a base pressure of 5×10^{-9} torr using a 200 μm, 50 W focused beam at a take-off angle of 45°. Survey spectra (**Figure A-21a**) were collected using a pass energy of 187.85 eV and a step size of 0.8 eV. High energy resolution scans that were used for peak fitting (**Figure A-21b-d**) were collected with a pass energy of 23.50 eV and a step size of 0.1 eV. Element identification was performed using MultiPak software (version 9.6.3.B).

The only elements consistently observed in all three samples (**Figure A-21a**) were carbon, sodium, oxygen, and phosphorus, as was anticipated for a graphite electrode in contact with a sodium metaphosphate melt. In one of the two electrodes prepared without aqua regia, a small silicon peak was also observed, which was attributed to accidental contact of that particular sample with the crucible furnace's ceramic foam cap. Peak splitting in the phosphorus and oxygen regions (**Figure A-21c-d**) were observed for all samples, which was attributed to differential charging during spectroscopic analysis due to the nonconductive nature of the salt films. When an argon neutralizer gun was employed, the splitting behavior vanished.

In all samples, the carbon 1s profile (**Figure A-21b**) showed a single peak at 284.5 eV consistent with graphite, indicating that the surface had not significantly changed as a result of the electrochemistry or, in the case of the aqua regia-treated sample, the oxidative pretreatment. Under the neutralizer gun, the oxygen 1s region (**Figure A-21c**) displayed a single peak at 532.5 eV consistent with a phosphate-bound oxide, while the phosphorus spectrum (**Figure A-21d**) showed a single peak at 135.5 eV consistent with P(V) phosphate species. In contrast, reduced phosphorus species are expected to display peaks in the 133-131 eV binding energy range. No peaks were observed in that range either with or without the use of the argon neutralizer gun.

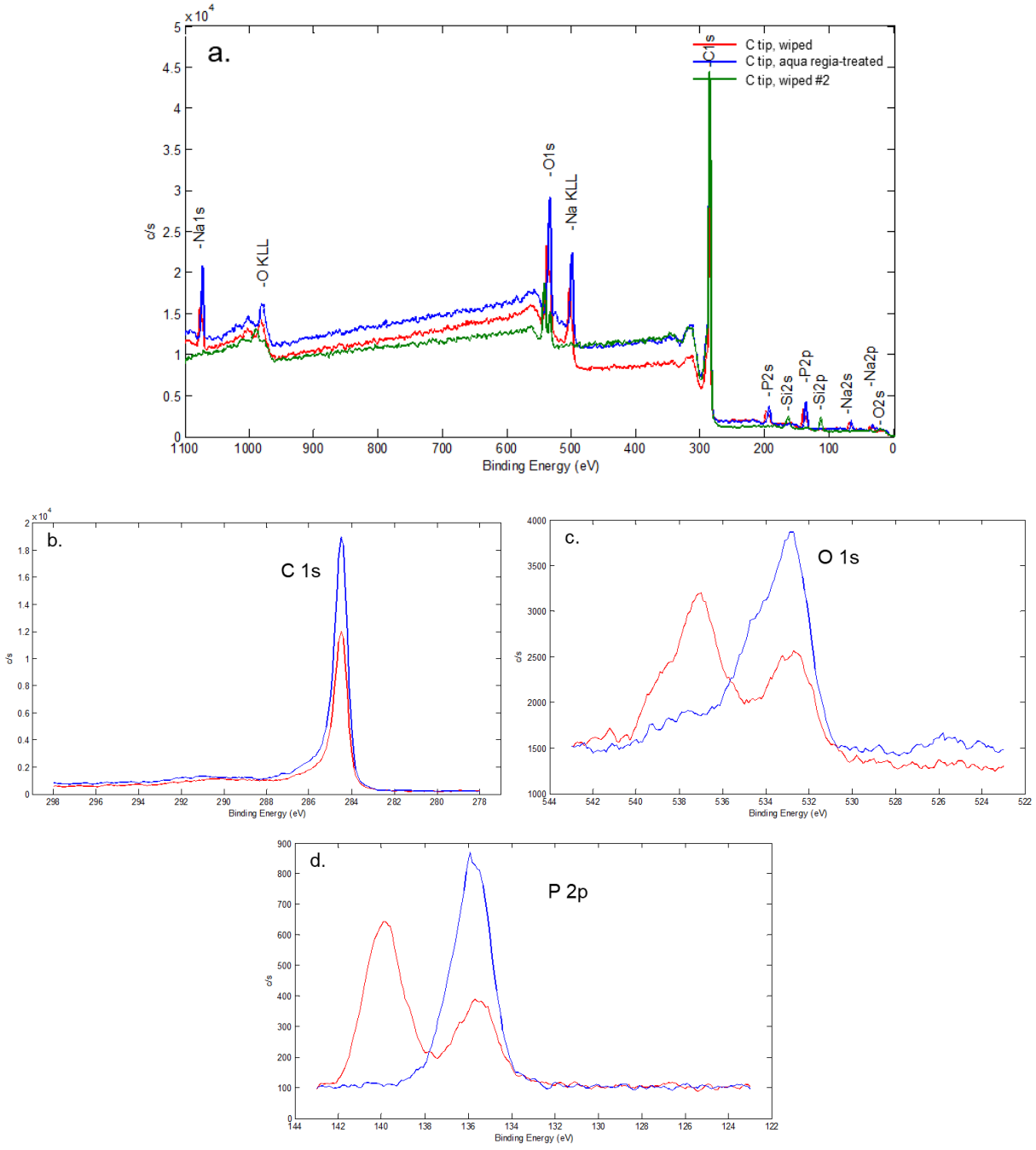

Figure A-21. *(a) Survey XPS spectrum of three graphite cathode tips following steady-state phosphorus evolution. (b) C 1s XPS spectrum of a graphite cathode tip. Red: no charge neutralization; blue: neutralization with argon beam. (c) O 1s XPS spectrum of a graphite cathode tip. Red: no charge neutralization; blue: neutralization with argon beam. (d) P 2p XPS spectrum of a graphite cathode tip. Red: no charge neutralization; blue: neutralization with argon beam.*

A-2.7 – Estimation of Power Efficiency

A-2.7a – Estimation of Electrochemical Phosphate Reduction Power

This portion of the calculation was performed by Jonathan F Melville. Assuming 100% Faradaic efficiency for phosphate reduction at a fixed current of 0.300 A and an overall cell voltage of 1.00 V (a reasonable voltage estimate for an electrochemical system with a pure metaphosphate melt and a graphite anode, as observed in the voltammetric separation of cathodic and anodic processes in **Figure 2-9** bottom):

$$\frac{(0.3\ \mathrm{A} \times 1\ \mathrm{V}) \times \frac{1\ \mathrm{W}}{1\ \mathrm{A{\cdot}V}} \times 1\ \mathrm{h} \times \frac{1\ \mathrm{kW{\cdot}h}}{1000\ \mathrm{W{\cdot}h}}}{0.3\ \mathrm{A} \times \frac{1\ \frac{\mathrm{C}}{\mathrm{s}}}{1\ \mathrm{A}} \times \frac{1\ \mathrm{mol}\ e^-}{96485\ \mathrm{C}} \times \frac{1\ \mathrm{mol}\ \mathrm{P_4}}{20\ \mathrm{mol}\ e^-} \times \frac{0.124\ \mathrm{kg}}{1\ \mathrm{mol}\ \mathrm{P_4}} \times 1\ \mathrm{h} \times \frac{3600\ \mathrm{s}}{1\ \mathrm{h}}}$$

$$= \frac{3.00 \times 10^{-4}\ \mathrm{kW \cdot h}}{6.94 \times 10^{-5}\ \mathrm{kg\ P_4}}$$

$$= 4.32\ \frac{\mathrm{kW \cdot h}}{\mathrm{kg\ P_4}}$$

A-2.7b – Estimation of Thermal Phosphoric Acid Dehydration Power

Because the proposed electrolysis process would remove phosphorus and oxygen ions from the melt while keeping the sodium ion content constant, the system will need to be replenished with a form of phosphorus oxide, i.e. phosphorus pentoxide (P_2O_5). While the actual process could input phosphoric acid directly with in-situ dehydration, the minimum work calculation is most easily performed by considering the following three stages:

1) $2\ H_3PO_4 \rightarrow P_2O_5 + 3\ H_2O$ (dehydration of phosphoric acid to phosphorus pentoxide)
2) $P_2O_5 + Na_3PO_4 \rightarrow Na_3(PO_3)_3$ (absorption of phosphorus pentoxide by orthophosphate equivalents in the melt, replenishing anhydride bonds)
3) $2\ Na_3(PO_3)_3 + 5\ C \rightarrow P_4 + 2\ Na_3PO_4 + 5\ CO_2$ (electrolysis of metaphosphate)

Since metaphosphate is generated in step 2 and then immediately consumed in step 3, it is appropriate for the purposes of this analysis to treat orthophosphate-enriched metaphosphate as a temporary solvent for the reagent P_2O_5 (analogously to cryolite acting as a solvent for electrolysis of Al_2O_3 in the Hall-Héroult process).[1–3] As a result, we can combine steps 2 and 3 as follows:

$$2\ P_2O_5 + 5\ C \rightarrow P_4 + 5\ CO_2$$

However, this reaction cannot be combined with step 1 without double-counting the electrical work, which we calculate experimentally in this paper, as part of the required enthalpy. As a result, the simplest thermodynamic cycle to calculate the additional heating costs would be as follows:

a) $4\ H_3PO_4 \rightarrow 2\ P_2O_5 + 6\ H_2O$, at room temperature.
b) $2\ P_2O_5$ and $6\ H_2O$ are both heated and vaporized at the reaction temperature of 800 °C.
c) Following electrochemical reaction, the product gases P_4 and $5\ CO_2$, as well as the $6\ H_2O$ released from the phosphoric acid, are cooled to room temperature.

For simplicity, we will assume that all reactions and gas flows take place under 1 atm of pressure. Among these, only the first two steps and the heating of the stoichiometrically-consumed graphite electrode incur thermal costs, as calculated below:

Reaction / Process	**Calculations**	**Heat Input Requirements (per mol P_4)**
$4\ H_3PO_{4(l,\ R.T.)} \rightarrow 2\ P_2O_{5(s,\ R.T.)} + 6\ H_2O_{(l,\ R.T.)}$	$\Delta H°_f\ (H_3PO_{4(l)}) = -1271.7$ kJ/mol[18][18] $\Delta H°_f\ (P_2O_{5(s)}) = -365.83$ kcal/mol × 4.184 kJ/kcal = −1,530.63 kJ/mol[19][19] $\Delta H°_f\ (H_2O) = -285.82$ kJ/mol[18] $\Delta H_{rxn} = 2 \times (-1.530.63\ \text{kJ/mol}) + 6 \times (-285.82\ \text{kJ/mol}) - 4 \times (-1271.7\ \text{kJ/mol})$	310.6 kJ/mol
$2\ P_2O_{5(s,\ R.T.)} \rightarrow 2\ P_2O_{5(s,\ 633\ K)}$	Molar heat capacity of condensed P_4O_{10} (i.e. 2 moles P_2O_5) = $C_p°$ = A + Bt + Ct^2 + Dt^3 + E/t^2 (J/mol) where t = temperature (K) / 1000 and A = 67.70925, B = 576.4548, C = −219.7520, D = 18.93072 and E = −0.774806.[20][20] Integration of $C_p°$ from 298.15 K to 633.15 K	95.3 kJ/mol

[18] Engel, T.; Reid, P. In *Thermodynamics, Statistical Thermodynamics, & Kinetics: Pearson New International Edition*; Pearson: Harlow, 2013; p 546.
[19] Williams, M. In *The Merck Index: An Encyclopedia of Chemicals, Drugs, and Biologicals*; Neil, M. J., Ed.; Royal Society of Chemistry: Cambridge, UK, 2013; Vol. 74, p 1266.
[20] Chase, M. *J. Phys. Chem. Ref. Data Monogr.* **1998**, 1948–1951.

$2\ P_2O_{5(s,\ 633\ K)} \rightarrow 2\ P_2O_{5(g,\ 633\ K)}$	P_2O_5's 'low temperature form' $\Delta H_{vap(633\ K)}$ = 22,800 cal/mol.[21][21] Multiply by 4.184 J/cal and then by 2 for 2 moles	191 kJ/mol
$2\ P_2O_{5(g,\ 633\ K)} \rightarrow 2\ P_2O_{5(g,\ 1073\ K)}$	Molar heat capacity of gaseous P_4O_{10} = $C_p° = A + Bt + Ct^2 + Dt^3 + E/t^2$ (J/mol) where t = temperature (K) / 1000 and A = 318.4915, B = 9.572616, C = −2.238758, D = 0.172783 and E = −18.83829. [20] Integration of $C_p°$ from 633.15 K to 1,073.15 K.	131 kJ/mol
$6\ H_2O_{(l,\ R.T.)} \rightarrow 6\ H_2O_{(l,\ 373\ K)}$	Molar heat capacity of liquid H_2O = $C_p° = A + Bt + Ct^2 + Dt^3 + E/t^2$ (J/mol) where t = temperature (K) / 1000 and A = −203.6060, B = 1523.290, C = −3196.413, D = 2474.455 and E = 3.855326.[20] Integration of $C_p°$ from 298.15 K to 373.15 K, then ×6 moles.	34.0 kJ/mol
$6\ H_2O_{(l,\ 373\ K)} \rightarrow 6\ H_2O_{(g,\ 373\ K)}$	ΔH_{vap} of water = 40.65 kJ/mol at 373 K,[18] ×6 moles.	244 kJ/mol
$6\ H_2O_{(g,\ 373\ K)} \rightarrow 6\ H_2O_{(g,\ 1073\ K)}$	Molar heat capacity of gaseous H_2O = $C_p° = A + Bt + Ct^2 + Dt^3 + E/t^2$ (J/mol) where t = temperature (K) / 1000 and A = 30.09200, B = 6.832514, C = 6.793435, D = −2.534480 and E = 0.082139.[20] Integration of $C_p°$ from 373.15 K to 1,073.15 K, then ×6 moles.	159 kJ/mol
$5\ C_{(s,\ R.T.)} \rightarrow 5\ C_{(s,\ 1073\ K)}$	Heat capacity of graphite by mass (cal $g^{-1}\ K^{-1}$) = $C_p = 0.630375 - 1.60535\times10^{-5}\ T - 225.861\ T^{-1} + 3100.10\ T^{-2} - 910737.0\ T^{-3} - 9.64607\times10^{7}\ T^{-4}$.[22][22] Integration from 298 to 1073 K yields 192 cal/g, then convert to kJ and multiply by 5 moles C.	48.3 kJ/mol
Total reaction / reactant heating inputs	**Partial Totals:** **310.6 kJ/mol (*dehydration reaction*)** **+ 417 kJ/mol (*heating of P_2O_5 and phase transitions*)** **+ 437 kJ/mol (*heating of H_2O and phase transitions*)** **+ 48.3 kJ/mol (*heating of C*)**	**1,210 kJ/mol,** **-or-** **2.7 kWh/kg P_4**

[21] Southard, J. C.; Nelson, R. A. *J. Am. Chem. Soc.* **1937**, *59*, 911–916.

[22] Butland, A. T. D.; Maddison, R. J. *J. Nucl. Mater.* **1973**, *49*, 45–56.

Heating costs for lower-concentration industrial H_3PO_4	**Adjustments (*derived in text*):** **Negative enthalpy of diluting H_3PO_4 into 37 wt. % H_2O to make an industrial 63 wt. % solution = 14 kJ/mol, ×4 moles = 58 kJ/mol P_4** 437 kJ/mol (*old heating of H_2O from pure H_3PO_4)* **+ 2,950 kJ/mol (*heating of excess H_2O from industrial 63 wt % H_3PO_4*)** **= 3390 kJ/mol total H_2O heating**	**4,220 kJ/mol,** **-or-** **9.4 kWh/kg P_4**

Table A-5 (this page and previous). *Estimated molar heating input calculations for a putative P_4 production process, assuming pure liquid H_3PO_4 and no heat of mixing.*

Practically speaking, phosphoric acid produced by the industrial wet process is only 26-30% P_2O_5:H_2O by weight[2323] which, when the average of 28 wt% is converted into a molar ratio, is roughly 4.7 mol% or 1 mole of P_2O_5 per 20.3 moles of water. This would add an extra 20.3 moles to the water being heated per mole of P_2O_5, for a rough total of 46.6 total units of water per unit of P_4 (including waters of dehydration) – so the existing water heating costs must be adjusted by a scaling factor of (46.6 mol / 6 mol) × 437 kJ/mol = 3390 kJ/mol. Relatively to the calculation in **Table S7**, this introduces an additional water heating requirement of **2,950 kJ/mol**.

This introduces another consideration; as a non-ideal mixture, the dissolution of pure phosphoric acid into water will be exothermic – meaning that in this theoretical thermodynamic cycle, additional heat will be needed to concentrate the industrial-grade phosphoric acid (with a weight percent of ~28 wt% P_2O_5 and thus ~63 wt% of H_3PO_4) into the pure liquid used in the thermochemical reaction calculation. The relative apparent molal heat content ϕ_L of H_3PO_4 (which corresponds to the enthalpy released by dissolving H_3PO_4 of a given concentration into water until infinite dilution is reached), has been determined experimentally to follow the equation ϕ_L (cal/mole H_3PO_4) = $292.06 + 923.79w + 3374.87w^2 - 2478.92w^3 + 3473.99w^4$, where w = the weight fraction.[2424] This formula yields values of 5600 cal/mol and 2100 cal/mol when w = 1 and 0.63, respectively, and, therefore, the theoretical heat energy required to reverse the exothermic dilution from pure H_3PO_4 to the industrial 63 wt% H_3PO_4 is 3400 cal/mol or 14 kJ/mol. Because four moles of phosphoric acid are required per mole of P_4, this raises the total heating costs by an additional **58 kJ/mol P_4**.

[23] Speight, J. G. *Environmental Organic Chemistry for Engineers*; Butterworth-Heinemann, 2016.

[24] Egan, E. P.; Luff, B. B. *J. Phys. Chem.* **1961**, *65*, 523–526.

Adjusting for the additional water heating costs in the final total of **Table A-5** and adding the heat energy lost from working against the exothermic dissolution of H_3PO_4 into water results in a newly adjusted heat energy total, when starting from industrial-grade wet process phosphoric acid, of 4220 kJ/mol or **9.4 kWh/kg P_4**.

Given the electrical costs of our electrolysis are calculated to be ~4.3 kWh/kg, this worst-case-scenario total of **13.7 kWh/kg** corresponding to no thermal recovery already falls comfortably within the 12.5-14 kWh/kg requirements of the industrial thermal process[25,262526] while cutting the CO_2 emissions in half. However, much of the thermal energy input to heat the reagents can be reclaimed via heat exchange with the cooling product gases (P_4 and CO_2) as well as the steam released in the dehydration process.

The theoretical heat released by cooling the steam back to room temperature should be the same as the cost of its original heating, i.e. 3390 kJ/mol. However, we must also calculate the heat that would be released by the P_4 and CO_2 as they cool to 75 ºC / 348 K (a reasonable storage temperature for P_4 at which it is liquid) and room temperature, respectively (**Table A-6**). (The cooling of the products theoretically releases slightly more thermal energy than the heating of the reagents requires, but this is thermodynamically expected because the electrolysis which separates the two steps involves a large external input of energy.)

Reaction / Process	Calculations	Heat Recovery (per mole P_4)
46.6 $H_2O_{(g,\ 1073\ K)}$ → 46.6 $H_2O_{(l,\ R.T.)}$	−(437 kJ/mol (from $H_3PO_{4(l)}$) + 2953 kJ/mol (additional H_2O of dilution))	**−3,390 kJ/mol**
$P_{4(g,\ 1073\ K)}$ → $P_{4(g,\ 553\ K)}$	Molar heat capacity of gaseous P_4 = $C_p° = A + Bt + Ct^2 + Dt^3 + E/t^2$ (J/mol) where t = temperature (K) / 1000 and A = 81.38466, B = 1.498484, C = −0.405575, D = 0.034585 and E = −1.327329.[20] Integration of $C_p°$ from 1,073.15 K to 553.15 K.	**−44.5 kJ/mol**
$P_{4(g,\ 553\ K)}$ → $P_{4(l,\ 553\ K)}$	The ΔH_{vap} of P_4 is 545 J/g at 560 K,[2727] which will be close to that at 553 K.	**−67.5 kJ/mol**
$P_{4(l,\ 553\ K)}$ → $P_{4(l,\ 348\ K)}$	Molar heat capacity of molten P = $C_p° = A + Bt + Ct^2 + Dt^3 + E/t^2$ (J/mol) where t = temperature (K) /	**−21.6 kJ/mol**

[25] Diskowski, H.; Hofmann, T. *Ullmann's Encyclopedia of Industrial Chemistry*; Wiley-VCH: Weinheim, Germany, 2012; Vol. 26, pp 725–746.

[26] Jupp, A. R.; Beijer, S.; Narain, G. C.; Schipper, W.; Slootweg, J. C. *Chem. Soc. Rev.* **2021**, *50* (1), 87–101.

[27] Walsh, M. E.; Collins, C. M.; Racine, C. H. *Environ. Toxicol. Chem.* **1996**, *15*, 846–855.

	1000 and A = 26.3260, B = 1.041373×10^{-10}, C = -6.121360×10^{-11}, D = 1.094033×10^{-11} and E = 2.995196×10^{-12}.[20] Essentially constant $C_p°$, so heat released = (26.32602 J/mol mK) ((348 − 553 K) / 1000), then ×4 moles	
$CO_{2(g,\ 1073\ K)} \rightarrow CO_{2(g,\ R.T.)}$	Molar heat capacity of gaseous CO_2 = $C_p° = A + Bt + Ct^2 + Dt^3 + E/t^2$ (J/mol) where t = temperature (K) / 1000 and A = 24.99735, B = 55.18696, C = −33.69137, D = 7.948387 and E = −0.136638.[20] Integration of $C_p°$ from 1,073.15 K to 298.15 K, then ×5 moles.	**−935 kJ/mol**
Total product cooling gains (assuming 100% efficiency)	**Partial Totals:** **−3390 kJ/mol (*cooling of H_2O and phase transitions*)** **− 133.6 kJ/mol (*cooling of P_4 and phase transitions*)** **− 935 kJ/mol (*cooling of CO_2*)**	**−4,460 kJ/mol**

Table A-6. *Calculation of total reclaimable heat energy of the products for an H_3PO_4-fueled P_4 production cell.*

However, not all of this heat energy can be directly reclaimed at 100% efficiency. In order to calculate the true efficiency of heat energy transfer for a counterflow heat exchanger for this process, one must calculate R, the ratio of the product of molar heat capacity and molar flow rate for the hot and cold streams.[2828] This value is different for each input and output stream, and is further complicated by the presence of phase transitions which cause the R value to vary along different regions of the exchange contact area. However, even as R changes from its minimum of 0 to its maximum of 1, the efficiency of thermal transfer only varies from 100% to 85% at its asymptote. Since a detailed plant design is beyond the scope of this research, we will (for simplicity) conservatively assume a blanket thermal energy transfer efficiency of 80% for all chemical streams; this value assumes the worst possible transfer efficiency from R = 1 in conjunction with minor losses due to thermal leaks.

Based on this, we take 4220 kJ/mol heating total derived above and deduct 80% of the theoretical heat energy of the products (**Table A-6**) of 4460 kJ/mol to arrive at total system heat input estimate of 652 kJ/mol = **1.5 kWh/kg P_4**:

[28] McCabe, W.; Smith, J.; Harriott, P. In *Unit Operations of Chemical Engineering*; McGraw-Hill Education: Boston, 2004; p 454.

By these methods, we estimate that **the combined energy costs incurred by electrolysis and heating total to ~5.8 kWh/kg, which is ~46% of the total energy costs of the modern industrial thermal process**.

A-3: SUPPLEMENTAL REFERENCES

(1) Frank, W. B.; Haupin, W. E.; Vogt, H.; Bruno, M.; Thonstad, J.; Dawless, R. K.; Kvande, H.; Taiwo, O. A. *Ullmann's Encyclopedia of Industrial Chemistry*; Wiley-VCH: Weinheim, Germany, 2012; Vol. 2, pp 483–520.

(2) Prasad, S. *J. Braz. Chem. Soc.* **2000**, *11* (3), 245–251.

(3) Tabereaux, A. T.; Peterson, R. D. In *Treatise on Process Metallurgy*; Elsevier: Oxford, 2014; Vol. 3, pp 839–917.

(4) Campbell, F. H. *Trans. Faraday Soc.* **1907**, *3*, 103–113.

(5) Cherevko, S.; Topalov, A. A.; Zeradjanin, A. R.; Katsounaros, I.; Mayrhofer, K. J. J. *RSC Adv.* **2013**, *3* (37), 16516–16527.

(6) Inzelt, G. In *Handbook of Reference Electrodes*; Inzelt, G., Lewenstam, A., Scholz, F., Eds.; Springer: Berlin, 2013; pp 331–332.

(7) Hall, A. S.; Yoon, Y.; Wuttig, A.; Surendranath, Y. *J. Am. Chem. Soc.* **2015**, *137* (47), 14834–14837.

(8) Yoon, Y.; Hall, A. S.; Surendranath, Y. *Angew. Chemie - Int. Ed.* **2016**, *55* (49), 15282–15286.

(9) Yoon, Y.; Yan, B.; Surendranath, Y. *J. Am. Chem. Soc.* **2018**, *140* (7), 2397–2400.

(10) Korzeniewski, C.; Conway, B. E. In *Proceedings of the Symposium on the Electrochemical Double Layer*; The Electrochemical Society, 1997; Vol. 97, pp 349–350.

(11) Bard, A. J.; Faulkner, L. R. *Electrochemical Methods: Fundamentals and Applications*, 2nd ed.; Wiley: New York, 2000.

(12) Chen, P.; Zhang, H.-B.; Lin, G.-D.; Hong, Q.; Tsai, K. R. *Carbon N. Y.* **1997**, *35* (10–11), 1495–1501.

(13) Wiberg, E.; Holleman, A. F.; Wiberg, N. In *Inorganic Chemistry*; San Diego, 2001; pp 810–811.

(14) Basu, P. In *Biomass Gasification, Pyrolysis and Torrefaction*; Basu, P., Ed.; Academic Press, 2018; pp 211–262.

(15) Greenfield, S.; Clift, M. *Analytical Chemistry of the Condensed Phosphates*; Pergamon: Oxford, 1975.

(16) Feki, M.; Ayedi, H. F. *Sep. Sci. Technol* **2008**, *33*, 2609–2622.

(17) Morey, G. W. *J. Am. Chem. Soc.* **1952**, *74* (22), 5783–5784.

(18) Engel, T.; Reid, P. In *Thermodynamics, Statistical Thermodynamics, & Kinetics: Pearson New International Edition*; Pearson: Harlow, 2013; p 546.

(19) Williams, M. In *The Merck Index: An Encyclopedia of Chemicals, Drugs, and Biologicals*; Neil, M. J., Ed.; Royal Society of Chemistry: Cambridge, UK, 2013; Vol. 74, p 1266.

(20) Chase, M. *J. Phys. Chem. Ref. Data Monogr.* **1998**, 1948–1951.

(21) Southard, J. C.; Nelson, R. A. *J. Am. Chem. Soc.* **1937**, *59*, 911–916.

(22) Butland, A. T. D.; Maddison, R. J. *J. Nucl. Mater.* **1973**, *49*, 45–56.

(23) Speight, J. G. *Environmental Organic Chemistry for Engineers*; Butterworth-Heinemann, 2016.

(24) Egan, E. P.; Luff, B. B. *J. Phys. Chem.* **1961**, *65*, 523–526.

(25) Diskowski, H.; Hofmann, T. *Ullmann's Encyclopedia of Industrial Chemistry*; Wiley-VCH: Weinheim, Germany, 2012; Vol. 26, pp 725–746.

(26) Jupp, A. R.; Beijer, S.; Narain, G. C.; Schipper, W.; Slootweg, J. C. *Chem. Soc. Rev.* **2021**, *50* (1), 87–101.

(27) Walsh, M. E.; Collins, C. M.; Racine, C. H. *Environ. Toxicol. Chem.* **1996**, *15*, 846–855.

(28) McCabe, W.; Smith, J.; Harriott, P. In *Unit Operations of Chemical Engineering*; McGraw-Hill Education: Boston, 2004; p 454.

Appendix B – Supplemental Information for Chapter 3

B-1: MATERIALS AND METHODS

B-1.1 – Molten Salt Electroanalytical Reactor

B-1.1a – Reactor Body

An electrochemical reactor (**Figure B-1**) was previously designed from the ground up to accommodate the electroanalysis of a molten-salt system while maintaining separation of cathodic and anodic gas flow streams. The main reactor body consisted of a custom closed-end alumina tube (designated "Alumina tube, one-end-closed, OD60.33mm*ID52mm*L279.4mm (OD+/-4%, ID+3/-0)" by AdValue Technologies), to which a custom-machined stainless-steel cap with four Swagelok™ Ultra-Torr® fittings could be attached. These fittings, as well as the junction between the reactor head and body, were sealed with DuPont™ Kalrez® perfluoroelastomer O-rings (temperature rated to 325 °C). Of the four fittings, three (of 1/4" diameter) held alumina-sheathed electrodes, while the fourth (of 3/4" diameter) held the isolated counter compartment and electrode. The top of the cell has the capacity to be heated for collection of white phosphorus by careful temperature control, but because the analytical focus of this study was the oxygen-evolving anode, the top of the cell was not heated for these particular experiments. The furnace itself was designed to fit a CF56622C Lindberg/Blue M™ top-loading Crucible Furnace (now discontinued) as controlled by a CC58114C-1 Lindberg/Blue M™ Furnace Controller.

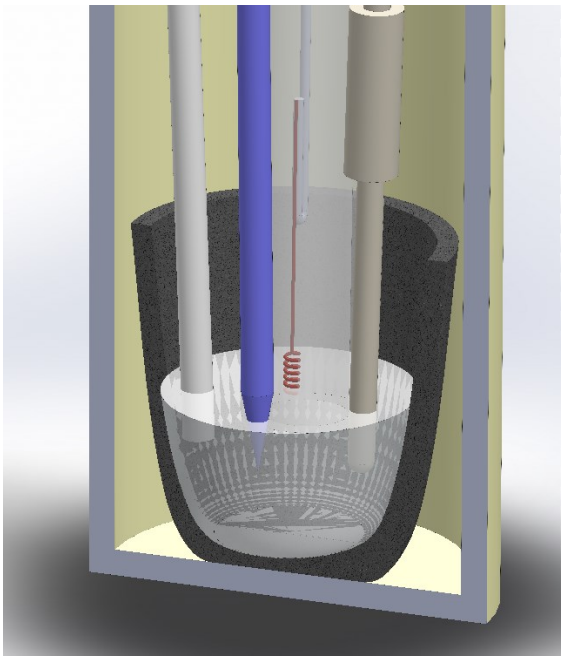

***Figure B-1**. Molten salt reactor from Appendix 1, adapted to new configuration in melt for oxygen evolution experiments.*

B-1.1b – Molten Salt Crucible

The bottom of the electrochemical reactor contained a conical glassy carbon crucible (60 mL, 52 mm outer diameter (OD), part #39006KT from Alfa Aesar), which had previously been found to be relatively inert to the molten polyphosphate electrolyte at temperature under nitrogen. Between experiments, the interior of the crucible was polished by hand via scrubbing with a polishing pad (Buehler MicroCloth,

PSA backing, 2.875 in) adhered onto a parafilm backing (Bemis Parafilm M Laboratory Wrapping Film) and an alumina slurry solution (1 micron deagglomerated hexagonal alumina powder, part #PSI-5601-5 by Precision Surfaces International, Inc.) in reagent grade water (purified to a resistivity of 18.2 MΩ cm by a Millipore Milli-Q Advantage A10 Q-pod and filtered by a secondary 0.22 µM Millipak Express 40 filter). This polishing procedure was necessary to ensure that the fused melts could be easily separated from the crucible upon cooling following a reaction run. The polishing also served to prevent contamination of the melt from metal residue or ions released from prior experiments.

B-1.1c – Working Electrode Compartment

For all experiments conducted in this study, the counter compartment consisted of a single-bore clear fused quartz tube (19 mm OD, 15 mm ID, 1219 mm length, part #FQ-T-19-15-4 by AdValue Technologies, subsequently cut into 16"-long segments). Quartz displayed enhanced resistance to corrosion in the presence of the molten metaphosphate electrolyte relative to the former separator material (alumina) and its transparency allowed for visual inspection of the electrical contact made to the counter electrode.

B-1.2 – Electrode Materials

B-1.2a –Metal Anode Working Electrode Design

Because the study of metal electrodes was the focus of our study, particular care was taken towards surface area control while minimizing sources of error. As found in previous studies, sheathing of electrodes was difficult due to the corrosion of most common nonconductive sheathing materials. Additionally, downward-facing electrodes of controlled area traps gas bubbles in molten metaphosphates in a way that broadens electrochemical features and increases resistances and overpotentials (a system of phenomena termed “anode effects,” particularly notable in the Hall-Héroult process for aluminum production).[1–3] Unlike on graphite, the presence of faradaic features under cyclic voltammetry at or around the open circuit of the examined metals were also found to render *in situ* capacitive surface area measurement unreliable for determining surface area, and could not be used to estimate the surface area of graphite electrodes as was done in our cathodic work.

To work around these constraints, we decided to deploy metal anodes in the form of coiled wires. This design choice served several purposes simultaneously. Firstly, unlike bare discs or cones, precious metal wires are commercially available for purchase and relatively inexpensive. Secondly, the thin profile of a coil provides few horizontal surfaces to which gas bubbles could cling, optimizing mass transport and minimizing non-uniform voltage fields across the wire surface.[4] Thirdly, the structure of a coil increases exposed surface area, which magnifies the range of weight change of an electrode due to corrosion. Finally, provided the electrode is submerged beyond the level of the coil, the bottom-weighted design minimizes variability in total submerged surface area. This principle is best illustrated in **Figure B-2**. While this configuration precluded traditional steady-state analytical methodology at high current densities, the use of coiling allowed for minimization of the differential impact dA/dx where A is area and x is the submersion depth of the electrode (a variable which could only be controlled by hand to

[1] Tabereaux, A. T.; Peterson, R. D. In *Treatise on Process Metallurgy*; Elsevier: Oxford, 2014; Vol. 3, pp 839–917.
[2] Frank, W. B.; Haupin, W. E.; Vogt, H.; Bruno, M.; Thonstad, J.; Dawless, R. K.; Kvande, H.; Taiwo, O. A. *Ullmann’s Encyclopedia of Industrial Chemistry*; Wiley-VCH: Weinheim, Germany, 2012; Vol. 2, pp 483–520.
[3] Prasad, S. *J. Braz. Chem. Soc.* **2000**, *11* (3), 245–251.
[4] Wilson, S. D. R.; Hulme, A. *Proc. R. Soc. London, Ser. A Math. Phys. Sci.* **1983**, *387* (1792), 133–146.

around 1-2 mm of accuracy). d*A*/d*x* drastically decreases when the submersion depth of the electrode goes above the coil, causing a large change in x to have a minimal impact on the total surface area A.

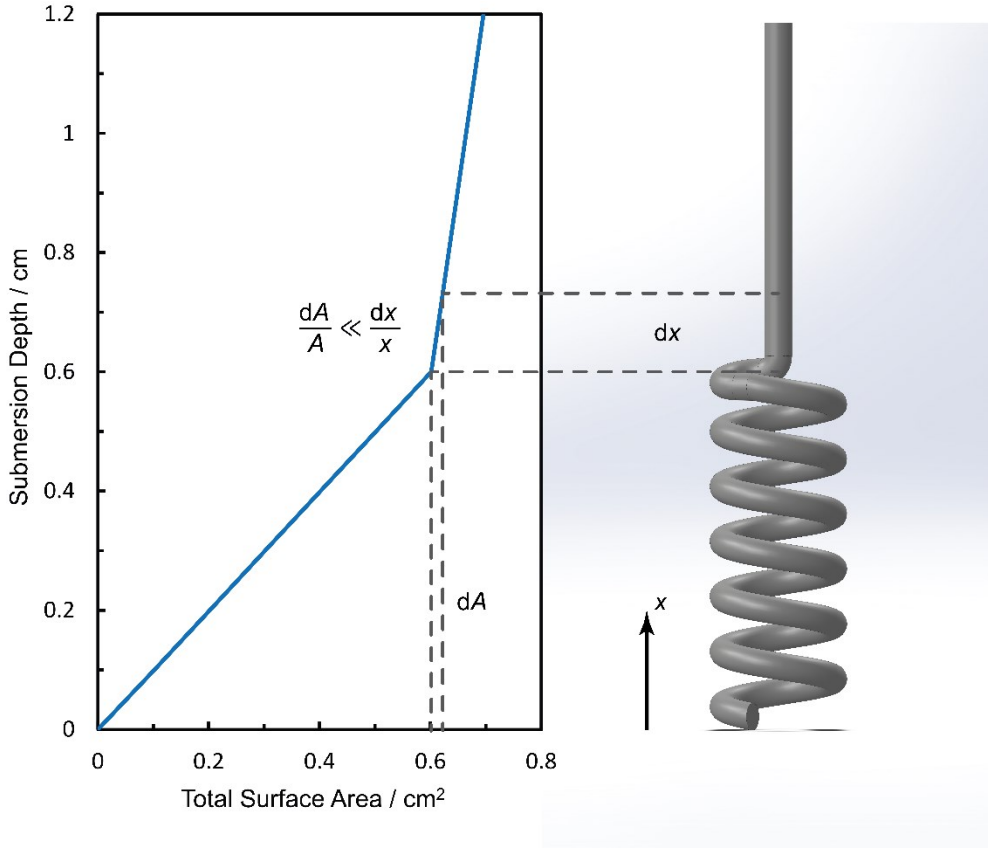

***Figure B-2**. Dependence of surface area A (horizontal axis) in cm² as a function of submersion depth x (vertical axis), with dashed lines as visual indicators correlating submersion depth to position on a model coil.*

This design came with drawbacks, since the diffusion rates of active species may be nonuniform at high current densities, since the diffusion layers will begin to overlap at high current densities. This prevented us from performing traditional steady-state analysis to interrogate the oxygen evolution mechanism through current-voltage profiles.[5] We also acknowledge that these overlapping diffusion gradients are likely to render the reagent concentration profiles nonuniform along our coil electrode surfaces, so certain areas of the electrode may corrode at different rates. However, we also note that this effect will cause the depletion of active species in nonuniform regions to be greater than standard diffusion equations would anticipate. Thus, deviations in the expected impact of current density are expected to overestimate corrosion-based effects and underestimate faradaic efficiencies, rather than inflating F.E. and minimizing corrosion. Thus, our electrode configuration provides a conservative lower bound, rather than an upper bound, on the performance of the examined electrode materials.

[5] Bard, A. J.; Faulkner, L. R. *Electrochemical Methods: Fundamentals and Applications*, 2nd ed.; Wiley: New York, 2000.

B-1.2b –Metal Coil Working Electrode Preparation

All our anodes were made from commercially available Pt (Sigma Aldrich 99.99% trace metal basis), Au (Sigma Aldrich 99.99% trace metal basis) and Ir (Sigma Aldrich 99.9% trace metal basis) wires. Several different wire thicknesses were used in initial surveys. All final data, however (aside from one iridium experiment in pure metaphosphate which used a 0.15 mm wire) was collected using wires that were either 0.25 to 0.5 mm in diameter, depending on price and availability. These wires were subsequently coiled 3-7 times, depending on the stiffness of the wire, around the tip of a glass disposable pipette. The result was a coil around 3-5 mm in diameter and 5-8 mm in length, suspended by the rest of the wire length. After coiling, the samples were sonicated in Milli-Q water for at least 20 minutes to remove any particulates or films on the coil. After this process, the capacitance of the coils were measured to estimate their electrochemical surface area (see section B-1.5b – Calculation of Electrochemical Surface Area), rinsed in Milli-Q water, and left to dry in a vial in a drying oven (120 °C). Once dry, the electrodes were cooled and massed (see section B-1.7a – Mass-Based Quantification of Metal Anode Corrosion), then connected to a premade 1 mm-diameter titanium wire hook at was used as a thermally resilient lead between the working electrode and potentiostat clip. This connection was made by lashing the precious metal coil to the titanium lead with a 0.25 mm-diameter titanium wire (Millipore-Sigma, 99.7% trace metal basis). This smaller wire embrittled over the course of the experiment due to a combination of the intense heat and the oxidizing effect of the oxygen evolving from the working electrode. As a result, it consistently broke during the removal process, was disposed of and replaced with a fresh wire for the next experiment.

The titanium lead wire itself consisted of a straight portion of wire roughly 19 inches in length which were stabilized by two titanium wire rings designed to fit snugly on the inside of the quartz tube. The purpose of these stabilizing rings was to hold the end of the rigging stably in the center of the quartz tube, such that the working electrode coil would never touch the sides of the quart tube separator. This design was found to be critical because of the melt's tendency to creep up above the submersion depth to form a meniscus. Because resistance was used to evaluate the depth at which the coil touched the electrode, contact with the molten salt meniscus along the walls was found to invalidate the submersion process and drastically underestimate the submersion depth of the electrode. The other end of the titanium lead wire was fed through a ¼" outer diameter fragment of alumina tubing and sealed inside it using a blowtorch and a bead of molten metaphosphate salt to make an airtight seal. This allowed the long wire rigging to fit through the ¼" Ultra-Torr port at the top of the quart tube's cap.

B-1.2c – Graphite Psuedoreference Electrode Preparation

Graphite rods (Spectro-Grade, 3/16 in. diameter, 12 in. length from Electron Microscopy Sciences) were scored at one end with a pair of pliers to increase their surface area, and, using a blowtorch, a drop of molten polyphosphate salt was adhered to that scored surface and twisted inside an alumina sheath to make an airtight glass seal. After cooling, the electrochemically active end was polished by rubbing against a Kimwipe™ until reflective to exfoliate potential impurities by hand, then rinsed with Milli-Q water and allowed to air-dry. A wax paper sheath was used to protect the tip during cell assembly to prevent the graphite from touching the O-rings, Ultra-Torr bearing or the steel wall of the electrode port.

B-1.2d – Graphite Counter Electrode Preparation

Graphite counter electrodes were prepared analogously to the graphite psuedoreferences (see Section B-1.2c – Graphite Psuedoreference Electrode Preparation). However, before polishing, the end of the graphite rod was sharpened to a point in a pencil sharpener. This shaped the electrode tip into a cone to minimize the amount of horizontal surface area, which had been found to trap bubbles and reduce current density.

B-1.2e – Liquid Sodium Reference Electrode

The graphite pseudoreference maintains a stable potential in a quiescent melt over long timescales, but the precise value of its potential was found to vary both within an experiment (due to local variations in melt composition induced by electrochemical action) and between experiments (due to alterations in the bulk composition of the melt). Thus, the graphite pseudoreference electrode was calibrated before and after each experiment against a liquid-sodium Na/Na^+ absolute reference electrode (S4 Na/Al by Ionotec Ltd.). The potential pinned by the reference is the equilibrium between the sodium metal and the sodium ions within the membrane, as depicted by **Figure B-3**. The solid-electrolyte junction of the sodium reference electrode was subject to slow corrosion in the metaphosphate electrolyte precluding its direct use as a full-time reference electrode. This calibration procedure minimized exposure of the Na/Na^+ reference to the corrosive medium, but still allowed for comparison of the potentials across a variety of melt compositions. The specific batch of reference electrodes ordered for these experiments did vary more widely in potential distribution, however, than those previously used, with several measuring a potential as large as 0.3-0.4 V more positive than those commonly observed in prior experiments. For maximum consistency, therefore, the calibration of graphite on an absolute scale was performed using the known voltage dependence of graphite open-circuit potential on the Na/Na^+ couple previously characterized in studies on the reduction of phosphates,[6] while monitoring pseudoreference drift relative to the second-generation Na/Na+ electrodes. When not in use, the sodium references were wrapped in parafilm and kept in a tube to prevent damage to the beta alumina ceramic from humidity.

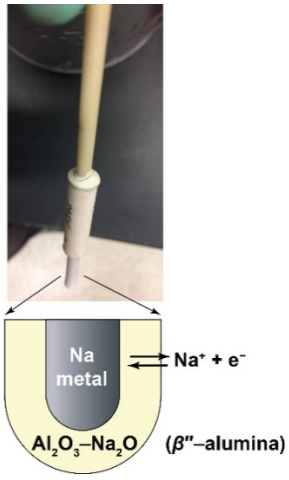

Figure B-3. *Photograph of Na/Na^+ reference electrode, with blowup indicating the structure of the electrochemically active sodium metal tip encased in a sodium ion-selective β"-alumina ceramic membrane.*

[6] Melville, J. F.; Licini, A. J.; Surendranath, Y. *ACS Cent. Sci.* **2023**, *9* (3), 373-380.

B-1.3 – Cell Assembly and High-Temperature Operation

After assembling the electrodes and quart tube at the top of the cell, the crucible was filled with the appropriate melt mixture (see Section B-1.4 – Preparation of Selected Condensed Phosphate Mixtures) and inserted into the alumina cell body. The top was screwed on, and the leads of both the working and main chambers were connected to house nitrogen and purged. Because isolated reports in the literature raise concerns about moisture contributing to metal corrosion,[7,8] the temperature of the cell was brought to 575 °C and held overnight under nitrogen, with the goal of removing atmospheric moisture from the powder sample and dehydrating it as much as possible. This temperature was chosen so that the metaphosphate on the sodium reference electrode would not melt and cause the beta alumina to corrode. After this dry heat purge under nitrogen, the temperature was raised to the experimental temperature of 800 °C.

Because the quartz working electrode chamber required relatively high gas flow rates (30-40 mL min^{-1}) to produce accurate and responsive binary gas analyzer readings, a great deal of care was required to minimize pressure differentials in the system. Such differentials were especially problematic because of how important submersion depth was for the accurate evaluation of corrosion rates and electrochemical current densities. In the worst case scenario, bubbling could occur, rendering surface area impossible to control and potentially contaminating the measurement by exposing the titanium wire to the melt. This issue, alongside electrode disintegration, was the primary factor behind the large failure rate of these experiments to collect meaningful data. As a result, house nitrogen pressure was found to be too unreliable for consistent use. Thus, immediately before immersion of electrodes in the melt, the cell's gas feed was switched over to a dedicated nitrogen tank (Airgas, Ultra High Purity). Rigorous flow rate calibrations were performed in advance of cell use where the quartz tube was immersed in an airtight flask of water, the nitrogen leads of the cell were connected to flask ports and the flow rates were adjusted until the two solution levels were constant and maintained their height over several hours. These flow rates tended to be around 35 mL min^{-1} of nitrogen through the working chamber and 160 mL min^{-1} of nitrogen through the counter chamber, the main body of the cell. Real-time adjustments to these flow rates also occasionally had to be performed, which were aided by the fact that bubbling was easily diagnosed by periodic fluctuations in the flow rate observed in the bead rotameter from the working electrode chamber. After calibration, the solution level of the molten salt in the quartz tube could be maintained practically indefinitely. Because white phosphorus collection was not a focus of these studies, the main chamber nitrogen exhaust was allowed to feed into a bleach bath to neutralize the toxic gas, and the cell itself was cleaned with bleach to remove condensed red phosphorus after experiments.

After immersing the quartz tube and stabilizing the nitrogen flows through the cell, the graphite counter and reference were immersed in the melt. At this point, the working electrode lead was slowly lowered into the cell, and the resistance between the working and reference electrodes was constantly measured. The point at which the resistance plummeted from an undefined value (due to lack of

[7] Casey, E. J.; Dubois, A. R. *Can. J. Chem.* **1971**, *49*, 2733–2745.
[8] Casey, E. J.; Dubois, A. R.; Gorman, R. W. In *Corrosion*; 1975; Vol. 31, pp 358–363.

electrical contact) to a value of roughly 300-100 Ω was deemed to be the point where the coil tip made contact with the melt. From there, the electrode was lowered further by the known length of the electrode coil, at which point the resistance stabilized around 3-7 Ω. At this point, the cell was allowed to purge for roughly 20-30 minutes to remove residual oxygen introduced by the loosening of the Ultra-Torr seal and lowering of the working electrode. From there, electrochemical measurements could proceed normally, and this electrode-lowering process was reversed after measurements to prevent the working electrode from freezing inside the melt.

B-1.4 – Preparation of Selected Condensed Phosphate Mixtures

The two condensed phosphate melts chosen as the focus for these experiments were a basic melt with a phosphoryl anhydride molalities of 6.4 $mol \cdot kg^{-1}$ and an acidic melt with a phosphoryl anhydride molality of 9.8 $mol \cdot kg^{-1}$. While the latter of these melts was equivalent to a pure metaphosphate melt, the former was synthesized by mixing equimolar (50:50) fractions of sodium trimetaphosphate (S3MP) and sodium orthophosphate (SOP) to produce a homogenous electrolyte upon fusion. Because bonds in the metaphosphate reequilibrate quickly at temperature, this method was functionally identical to the use of shorter-chain polyphosphates.[9,10] This composition of 6.4 $mol \cdot kg^{-1}$ is equivalent to sodium tetrapolyphosphate (S4PP). For a few survey studies, compositions of 8.3 (25% SOP in S3MP) and 5.4 (60% SOP in S3MP) were also used. For all electrolyte preparations, a total mass of 52 g was measured out in the prescribed ratio of S3MP (Sigma Aldrich, trisodium trimetaphosphate, ≥95%) to SOP (Sigma Aldrich, 96%) and thoroughly mixed by hand to ensure homogeneity. This mixture was then poured into a glassy carbon crucible for electroanalysis as described above.

[9] Van Wazer, J. R. In *Phosphorus and its Compounds, Vol. I*; Interscience: New York, 1958; pp 717–800.
[10] Greenfield, S.; Clift, M. *Analytical Chemistry of the Condensed Phosphates*; Pergamon: Oxford, 1975.

B-1.5 – Experimental Electrochemical Studies

B-1.5a – Potentiostat and Settings

Unless otherwise specified, all electrochemical measurements were conducted in the molten salt electrochemical cell (see section B-1.1 – Molten Salt Electroanalytical Reactor) at 800 °C, which we found to correlate well to the internal equilibrated reactor temperature as measured by an internal thermocouple. Electrochemical data were collected using a Biologic VSP potentiostat without IR compensation for noncapacitive voltammetric studies for measurements where current did not exceed roughly 5 mA. Above this value, iR compensation was applied at the default value of 80%. Except where specified otherwise, a graphite electrode was employed as a pseudoreference electrode for all experiments, the potential of which was retroactively corrected for against a Na/Na^+ reference that was briefly (15 seconds – 2 minutes) dipped into the melt before and after each experiment (see section B-1.2e – Liquid Sodium Reference Electrode). Uncompensated resistance (R_u) values were measured by the current-interrupt (CI) method; typical R_u values on the working electrode coils for the melt ranged from 2-7 Ω for all electrolyte conditions, with higher-melting salts displaying greater solution resistances.

B-1.5b – Calculation of Electrochemical Surface Area

Observed currents i were normalized to areal current densities j using electrochemical surface areas (ECSAs) assessed following adapted literature methodologies.[11–13] Because the open-circuit potential of platinum, gold and iridium wires all pinned to redox features, their capacitance in the melt could not be directly determined. As a result, the capacitance of the coils were instead measured in aqueous 0.1 M $NaClO_4$, made by dissolving 7.0126 g of $NaClO_4 \cdot xH_2O$ (Sigma-Aldrich, 99.99% trace metal basis) in 500 mL of H_2O (purified to a resistivity of 18.2 MΩ cm by a Millipore Milli-Q Advantage A10 Q-pod and filtered by a secondary 0.22 µM Millipak Express 40 filter). The working electrode was suspended by an alligator clip in a five-necked glass electrochemical cell and lowered down into the solution on the benchtop. The reference electrode used in these studies was a Ag/AgCl reference electrode (BASi RE-5B) in 3.0 M KCl solution (5.5915 g KCl in 25 mL of Milli-Q water), although a 1.0 M KCl Ag/AgCl reference electrode was occasionally used for some initial experiments. A ¼ inch-thick graphite rod electrode was used as the counter electrode. Using this setup, 3-electrode cyclic voltammetry was performed on the metal coil. For consistency, the submersion depth of the coil was always made to be roughly 1 mm above the last coil of the electrode. DLC values were assessed by CV scans spanning ±75 mV around the measured OCP, using the last of three identical cycles collected at scan rates of 5 $mV \cdot s^{-1}$, 10 $mV \cdot s^{-1}$, 25 $mV \cdot s^{-1}$, 36 $mV \cdot s^{-1}$, 50 $mV \cdot s^{-1}$, 63 $mV \cdot s^{-1}$, 75 $mV \cdot s^{-1}$, 87 $mV \cdot s^{-1}$, and 100 $mV \cdot s^{-1}$ without IR compensation. To avoid convolution of scan rate with any time-based surface changes, the order of these scans was always collected in the following order: 100 mV s^{-1}, 10 mV s^{-1}, 50 mV s^{-1}, 25 mV s^{-1}, 75 mV s^{-1}, 36 mV s^{-1}, 63 mV s^{-1}, 5 mV s^{-1}, 87 mV s^{-1}. The resultant capacitive CV traces (**Figure B-4.** – Example cyclic voltammograms (CVs) collected under scan rates from 5 to 100 mV s^{-1} for electrochemical surface area (ECSA) estimation. This specific set of CVs was collected on an iridium coil wire in aqueous 0.1 M $NaClO_4$) were used to calculate the total capacitive current i, as the difference of the cathodic current i_c and the anodic current i_a taken at the

[11] Hall, A. S.; Yoon, Y.; Wuttig, A.; Surendranath, Y. *J. Am. Chem. Soc.* **2015**, *137* (47), 14834–14837.
[12] Yoon, Y.; Hall, A. S.; Surendranath, Y. *Angew. Chemie - Int. Ed.* **2016**, *55* (49), 15282–15286.
[13] Yoon, Y.; Yan, B.; Surendranath, Y. *J. Am. Chem. Soc.* **2018**, *140* (7), 2397–2400.

midpoints (OCP) of the capacitive curve. These currents are related to the overall electrode capacitance C by the relation

$$C = \frac{1}{2}\frac{\partial(i_a - i_c)}{\partial(scanrate)}. \quad \text{(XX)}$$

Under these conditions, a plot of capacitive current as a function of scan rate resulted in a linear relation, as exemplified by **Figure B-5.** – Example fitting of cyclic voltammetry (CV) capacitive currents for a capacitance value to estimate electrochemical surface area (ECSA). , and the slope was taken to be the electrode capacitance. This capacitance value was then converted into an approximate ECSA via a value of 25 μF·cm^{-2}, the average value observed for electrodes in aqueous 0.1 M $NaClO_4$.[13] This approach was used for consistency because of the practical difficulty associated with acquiring an iridium electrode of well-defined area. However, later investigation revealed that the open circuit potential for platinum pinned close to a redox feature in many cases, which may mean that the ECSAs of platinum electrodes used in these studies may have been lower than the value of 25 μF·cm^{-2} would predict. Platinum capacitances measure closer to 40 μF·cm^{-2} in this region according to literature,[13] so one might expect the ECSA of platinum to be smaller than the ECSAs of gold and iridum by a factor of 37%. Gold, as well, has a lower-than-average aqueous capacitance under these conditions.[13] These values, however, does not seem sufficient to explain the observed magnitude difference of corrosive instability of platinum relative to other metals, which likely results in part from the formation of phosphides along grain boundaries, leading to internal weakening.[14]

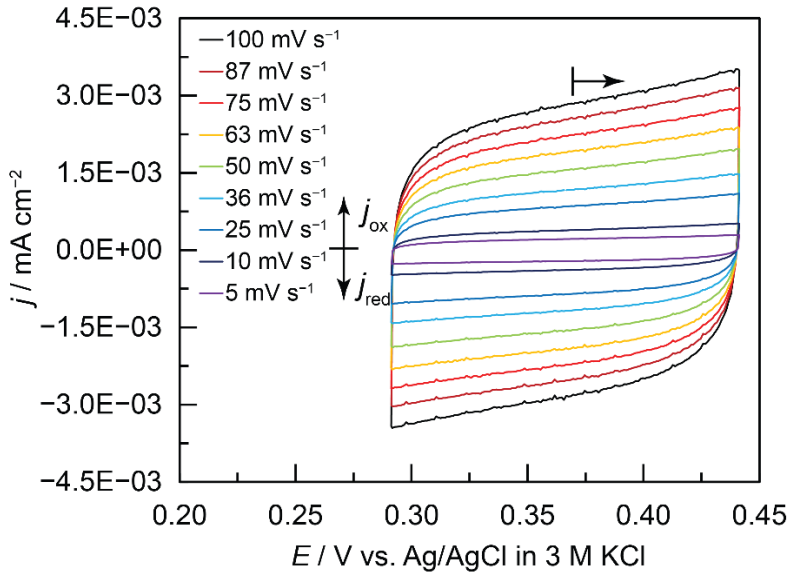

Figure B-4. *– Example cyclic voltammograms (CVs) collected under scan rates from 5 to 100 mV s^{-1} for electrochemical surface area (ECSA) estimation. This specific set of CVs was collected on an iridium coil wire in aqueous 0.1 M $NaClO_4$. Potentials reported vs. an Ag/AgCl reference electrode in aqueous 3 M KCl. Arrow indicates scan starting point and direction.*

[14] Fischer, B. *Platin. Met. Rev.* **1992**, *36* (1), 14–25.

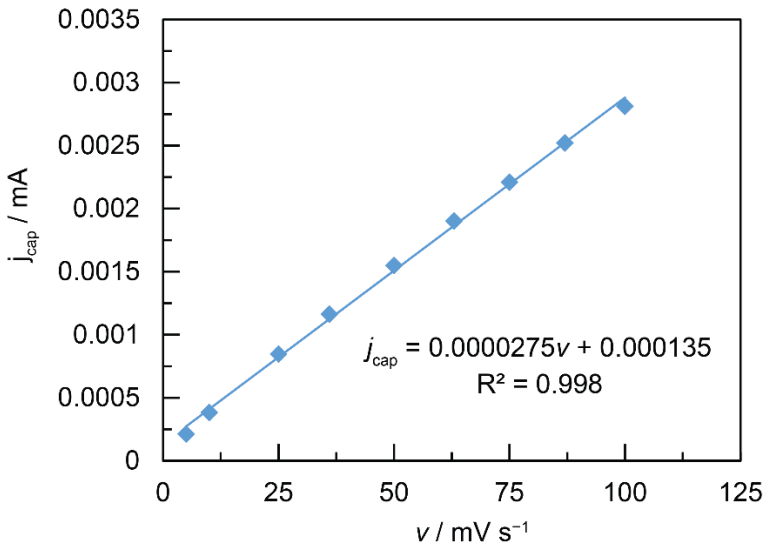

Figure B-5. *– Example fitting of cyclic voltammetry (CV) capacitive currents for a capacitance value to estimate electrochemical surface area (ECSA). This specific set of CVs was collected on an iridium coil wire in aqueous 0.1 M $NaClO_4$, with corresponding CV traces shown in* ***Figure B-4****. Slope, intercept and R^2 values reported in label.*

B-1.5c – Collection of Cyclic Voltammetry in Molten Polyphosphates

The collection of cyclic voltammetry data (**Figure 3-1** and **Figure 3-3**) entailed cyclic voltammetry scans beginning at the open-circuit potential and spanning anywhere from roughly ±250 mV to around ±1000 mV around the solution OCP depending on the current densities required. These scans were typically collected 100 mV·s^{-1}, but occasionally 10 mV·s^{-1} or 50 mV·s^{-1} were used. When performing scan rate analysis on specific peaks, scan rates were varied from 10 to 1000 mV·s^{-1}.

B-1.5d – Collection of Galvanostatic Polarization Data

For **Figure 3-2**, **Figure 3-4**, **Figure 3-5** and **Figure 3-6**, electrolyses were performed galvanostatically with a fixed current density of 100 mA cm^{-2} relative to the measured ECSA. Voltage compensation for solution resistance was primarily done with automatic 80% iR compensation, but was occasionally implemented manually during data processing. Experiments were typically performed in duplicate due to the expense of the materials, although some were performed once (in cases where coils broke in the melt) or multiple times as indicated below:

Figure 3-2 OER: 1 trial for Pt in 9.8 mol kg^{-1} [P–O–P], 1 trial for Pt in 6.4 mol kg^{-1} [P–O–P], 3 trials for Au in 9.8 mol kg^{-1} [P–O–P], 1 trial for Au in 6.4 mol kg^{-1} [P–O–P], 2 trials for Ir in 9.8 mol kg^{-1} [P–O–P], 2 trials for Ir in 6.4 mol kg^{-1} [P–O–P].

Figure 3-4 Pt corrosion at 100 mA cm^{-2}: 1 trial in 9.8 mol kg^{-1} [P–O–P] (other two attempts had electrode break apart), 2 trials in 6.4 mol kg^{-1} [P–O–P]

Figure 3-5 Au corrosion at 100 mA cm^{-2}: 2 trials in 9.8 mol kg^{-1} [P–O–P], 2 trials in 6.4 mol kg^{-1} [P–O–P]

Figure 3-6 Ir corrosion at 100 mA cm^{-2}: 2 trials in 9.8 mol kg^{-1} [P–O–P], 2 trials in 6.4 mol kg^{-1} [P–O–P]

Error bars were calculated from 95% confidence intervals as 1.95996 times the sample standard error (standard population deviation divided by the square root of sample size).

B-1.6 – Binary Gas Analysis of Gas Outflow Streams

For quantification of evolved oxygen from the working chamber (**Figure 3-2**), the nitrogen stream from the working chamber's outlet port was flowed through hosing through a bead rotameter (Omega FT-032-ST-VN, 50 mL min^{-1} maximum) and fed into a Stanford Research Systems, Inc. (SRS) Model BGA2 binary gas analyzer (chamber volume 130 mL, max pressure 150 psi, max gas flow 5000 mL min^{-1}). The percentage of oxygen in nitrogen was analyzed using the Stanford Research Systems, Inc. (SRS) BGA Monitor software (version 1.0.6.0, June 2019). Before evolution of gas, the level of oxygen in nitrogen was allowed to stabilize, and this value was set using the software to the baseline of 0% oxygen and nitrogen. This baseline varied between experiments and was generally around 5000-7000 ppm oxygen, which represented the lowest detection limit of the system. At steady-state applying oxidative current densities of 100 mA cm^{-2}, the measured oxygen levels relative to the baseline generally ranged from 0.4% to 5% O_2 in N_2. Oxygen levels only increased during the passage of charge, and tailed off when the current was halted (**Figure B-6**).

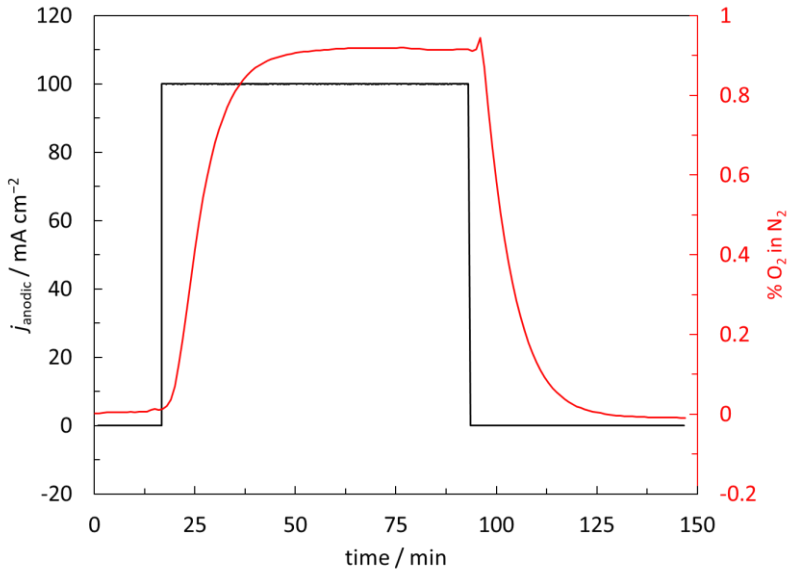

Figure B-6. – Example overlay of steady-state current and binary gas analysis data. (black) Applied steady-state current density on a gold coil electrode, set to 100 mA cm^{-2} during the active electrolysis window. (red) Binary gas analysis data, measured as a percentage of oxygen gas in the inert nitrogen gas exhaust stream of the working electrode chamber.

In most cases, oxygen levels stabilized within 1-2 hours, and, thus, the faradaic efficiency of oxygen evolution was calculated by comparing this steady-state value to the steady-state anodic current. The moles of O_2 calculated by BGA were scaled by the flow rate of nitrogen into the cell (measured using a second bead rotameter (Omega FT-032-ST-VN, 50 mL min^{-1} maximum), making the assumption that all

nitrogen in the product stream originated from the stream of nitrogen feeding into the headspace. Thus, the faradic efficiency of OER was calculated using the following method:

$$\text{moles } O_2\ s^{-1} \text{ via BGA} = \text{ } N_2 \text{ inflow rate } (\text{mL min}^{-1}) * \frac{\%\ O_2 \text{ in } N_2}{100\% - \%\ O_2 \text{ in } N_2} * \frac{1 \text{ mole } O_2}{22400 \text{ mL}} * \frac{1 \text{ min}}{60 \text{ s}}$$

$$\text{moles } O_2\ s^{-1} \text{ via echem} = \text{ anodic current (A)} * \frac{1 \text{ mole } e^-}{96485 \text{ C}} * \frac{1 \text{ mole } O_2}{4 \text{ moles } e^-}$$

$$\text{OER FE } (\%) = \frac{\text{moles } O_2\ s^{-1} \text{ via BGA}}{\text{moles } O_2\ s^{-1} \text{ via echem}} * 100\%$$

In some trials, however, the % of oxygen in nitrogen was found to rise linearly over time without ever stabilizing to a plateau value over the course of 1-3 hours. This phenomenon was especially true for cases in which the metal was heavily corroded by the melt, and we attributed this to an effective increase in the rate of oxygen evolution resulting from metal ions back-reducing to neutral metal. In such cases, the OER efficiency was instead calculated via integration. To do so, an instantaneous collection rate of oxygen (in moles s^{-1}) was calculated analogously to the steady-state method above, but these values were then multiplied by the time interval between each data point and summed. This resulted in a total observed number of moles of O_2, and this value was then divided by the total theoretical moles of O_2 generated by the anodic charge, rather than the instantaneous rate, to get the faradaic efficiency value.

B-1.7 – Corrosion Quantification and Analysis

B-1.7a – Mass-Based Quantification of Metal Anode Corrosion

Because the metal coils were relatively light and had relatively high surface contact in the melt, mass losses collectively represented a sensitive and easily observable means of measuring corrosion. Masses for initial surveys were collected before and after electrochemical measurements on a Mettler Toledo ML104 NewClassic MF balance (max mass 120 g, d = 0.1 mg), but for final data, the electrodes were massed on a more sensitive Mettler Toledo XSR105 DualRange microbalance (Max mass 41 g / 120 g, d = 0.01 mg / 0.1 mg). Because the mass losses were small in many cases, masses were collected nine times and then averaged to minimize noise. The high number of replicates became less necessary in the final data due to the more accurate balance, but the practice was preserved for the sake of consistency. After averaging, corrosion rates were evaluated as follows:

$$\text{Corrosion rate } (\text{mm yr}^{-1}) = \frac{\frac{(m_{initial} - m_{final})}{\rho_{\text{Pt/ Au/Ir}}} \times \frac{1000 \text{ mm}^3}{\text{cm}^3}}{(t_{electrolysis} * 3.171 \times 10^{-8} \text{yr s}^{-1}) \times (\text{ECSA})}$$

where m_{initial} is the initial mass in g, m_{final} is the final mass in g, $\rho_{\text{Pt/Au/Ir}}$ is the density of Pt, Au or Ir metal at 25 °C in g cm^{-3}, $t_{\text{electrolysis}}$ is the duration of the electrolysis in s, and ECSA is the electrochemical surface area in cm^2 as estimated by electrochemical capacitance in 0.1 M $NaClO_4$ (see section B-1.5b – Calculation of Electrochemical Surface Area). Occasionally, a "faradaic efficiency" of corrosion was also calculated, in order to estimate what fraction of the applied current was responsible for the mass loss relative to that of oxygen evolution. This value was calculated as follows:

$$Corrosion\ F.E.(\%) = \frac{\frac{(m_{initial} - m_{final})}{M_{Pt/Au/Ir}}}{\frac{it_{electrolysis}}{nF}} \times 100\%$$

where $m_{initial}$ is the initial mass in g, m_{final} is the final mass in g, $M_{Pt/Au/Ir}$ is the molar mass of Pt, Au or Ir metal at 25 °C, i is the steady-state current in A passed during the electrolysis, $t_{electrolysis}$ is the duration of the electrolysis in s, n is the number of electrons removed in the oxidation of a single metal atom, and F is Faraday's constant (96,485 C mol^{-1} e^{-}). In practice, the charge state of corroded ions in the melt could not be reliably determined due to the ions' short-lived nature and the uncertainty of diffusion coefficients for said species in the melt. Thus, for the value of n, the highest common charge of each metal was selected to err on the side of overestimating corrosion faradaic efficiency (a negative trait) rather than underestimating it. n was chosen to be 2 for Pt (Pt^{2+}), 3 for Au (Au^{3+}) and 4 for Ir (Ir^{4+}).

B-1.7b – SEM Imaging of Metal Coils

Post-electrolysis SEM images of the metal coil working electrodes were recorded using a Zeiss Gemini 450 SEM with an acceleration voltage of 1-2 keV. The full details of each image used in the main text are provided graphically below (**Figure B-7** to **Figure B-9**).

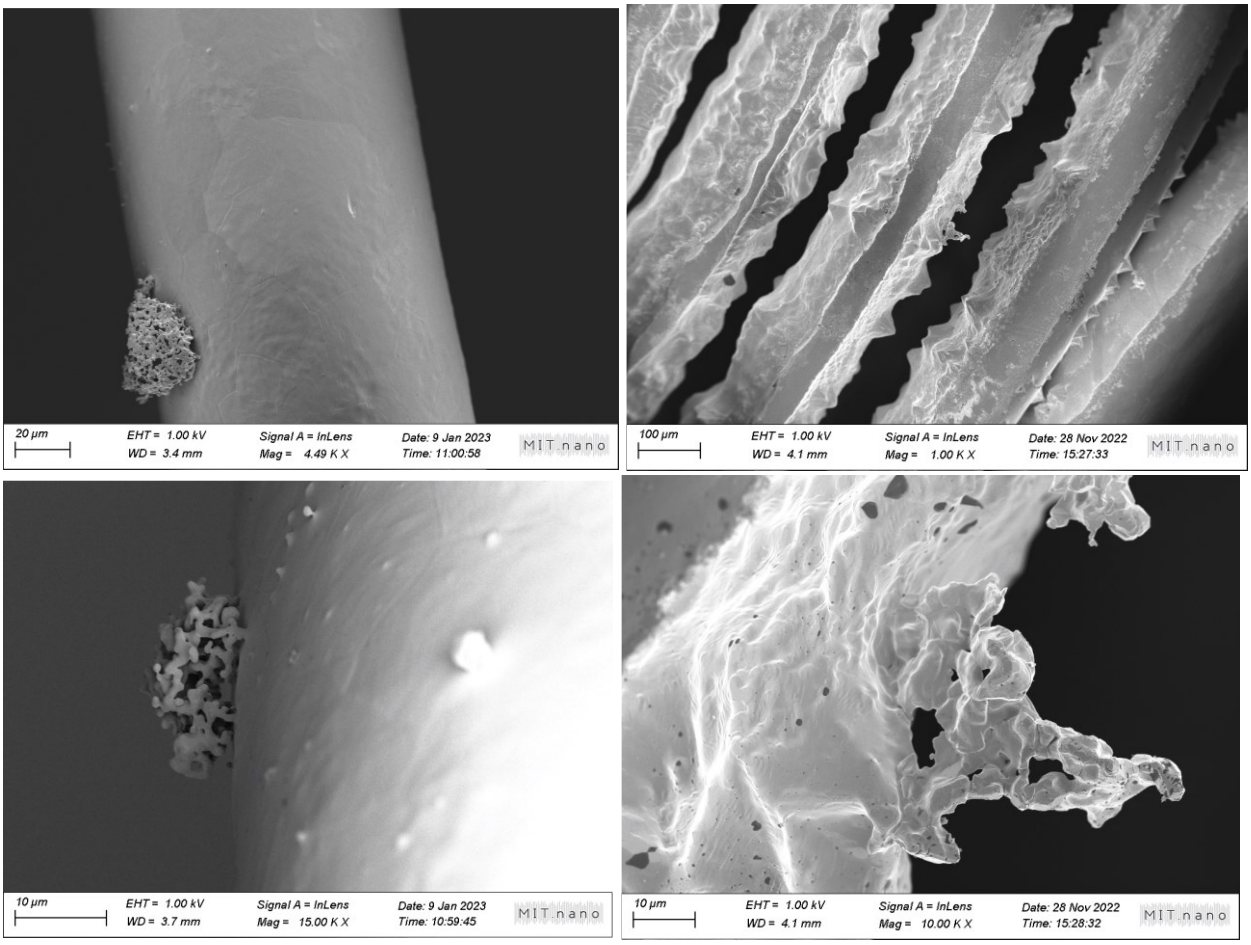

Figure B-7. *SEM images of Pt coils provided in* ***Figure 3-4****, reproduced here with magnification, WD and beam acceleration below each image.*

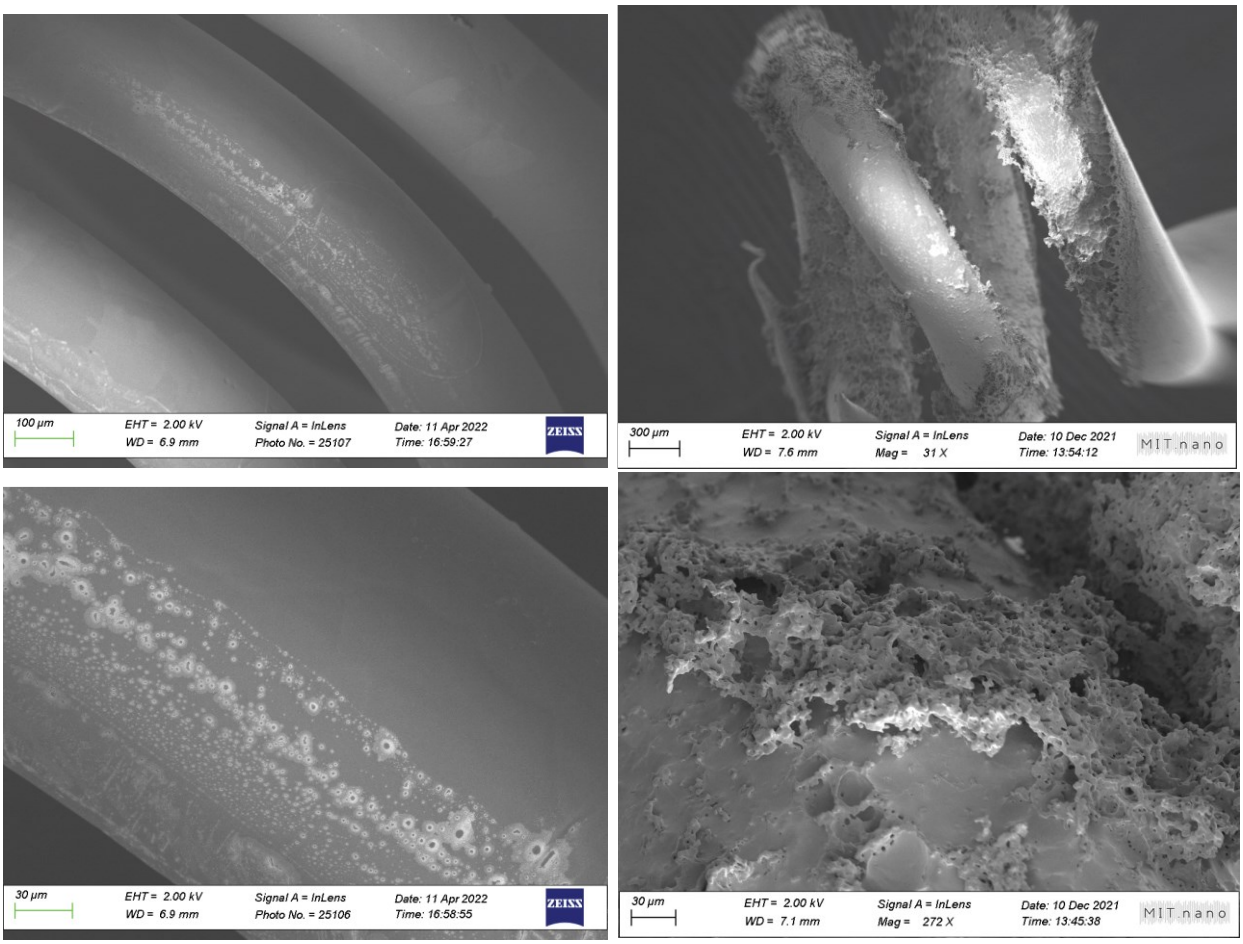

Figure B-8. *SEM images of Au coils provided in* ***Figure 3-5****, reproduced here with magnification, WD and beam acceleration below each image.*

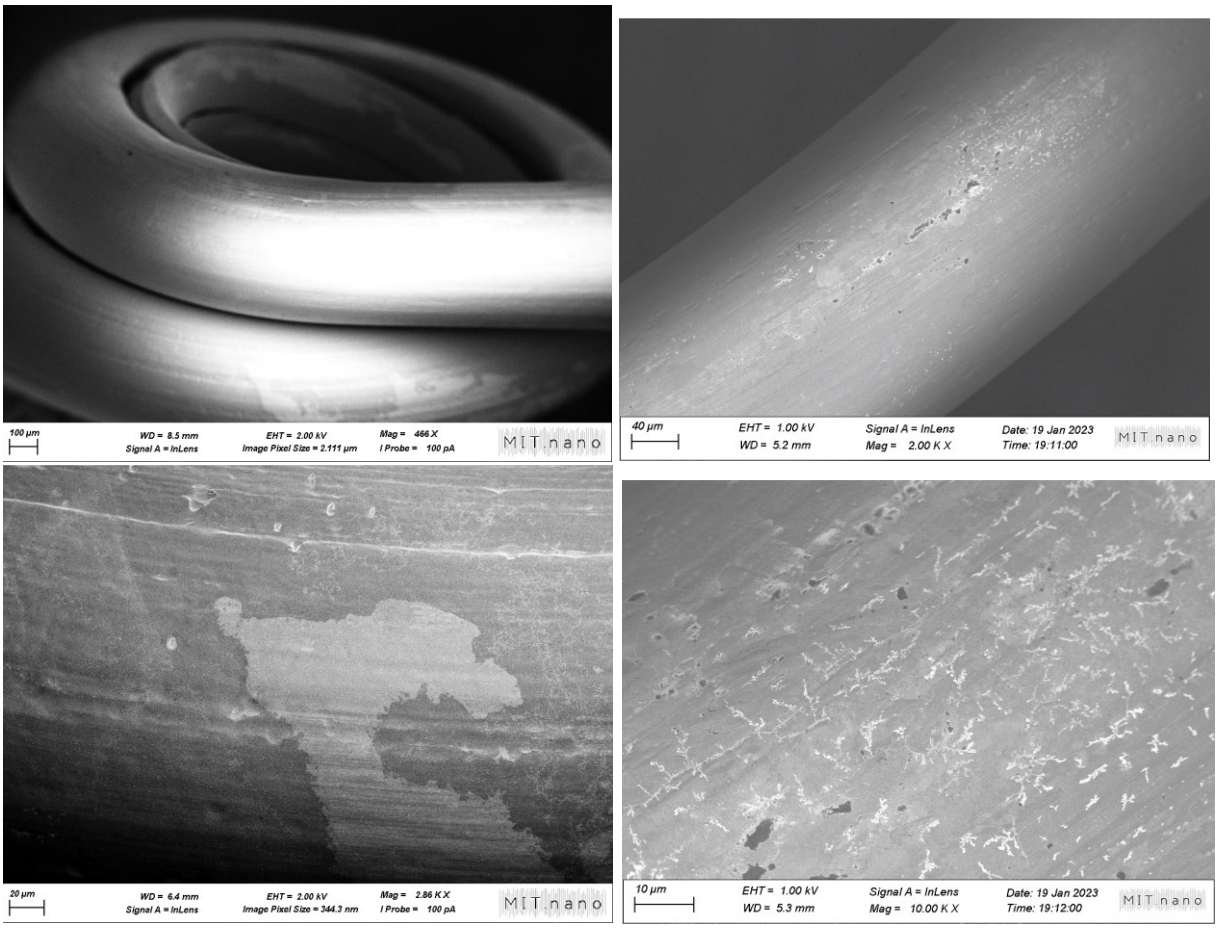

Figure B-9. *SEM images of Ir coils provided in* ***Figure 3-6****, reproduced here with magnification, WD and beam acceleration below each image.*

B-2: SUPPLEMENTAL EXPERIMENTS

B-2.1 - Cyclic Voltammetry: Scan Rate Analysis of Iridium Anodic Features

To evaluate the properties of the cyclic voltammetry peak features found on iridium wire in molten metaphosphates (**Figure 3-1**), we performed a study of the scan rate dependence of these peaks under cyclic voltammetry. The surface area of this coil of 0.25 mm-diameter iridium wire was estimated in advance to be 1.14 cm^2 via aqueous capacitance (see section B-1.5b – Calculation of Electrochemical Surface Area). The scan window of this study was 2.2 to 3.5 V vs. Na/Na^+, scanning to positive voltages first and reversing to negative potentials in three identical, sequential sweeps. The third scan in each series was then used for peak analysis. Three peaks of interest were selected and labelled oxidative feature 1 (O1), oxidative feature 2 (O2) and reductive feature 1 (R1), respectively (see **Figure B-10a**). Feature R1 only manifested in the reverse sweep when the positive potential window was increased to a range including Feature O1.

Cyclic voltammetry peak analysis and integration was performed using EC-Lab® software V10.39 (September 5, 2014) from Bio-Logic Science Instruments. Because the O2 feature was convolved with the onset of a separate catalytic current feature, its peak height was estimated visually by inspection, and was found to be roughly half the height of O1 in all cases. The 100 mV s^{-1} scan was the first scan collected, which may explain why its properties differ from the trend observed at all other scan rates.

As shown in **Figure B-10b**, the peak potential of O2 drifted significantly more as a function of scan rate than O1 or R1. This suggests that relative to O1 and R1, the O2 feature encounters a higher kinetic resistance to electron transfer. In contrast, O1's peak position drifts outward by a much lower rate, and R1's peak position remains fairly constant regardless of scan rate. Interestingly, the features O1 and O2 seem to converge to the same potential at slow scan rates, which would suggest that the two processes have the same thermodynamic onset value. The iridium used in this experiment is polycrystalline, so the formation of IrO_x may occur with a kinetic preference on one iridium face vs. others under these conditions, resulting in the separation of features as scan rate increases.

As shown in **Figure B-10c**, the integration of the sum of overlapping peaks O1 and O2 falls asymptotically with respect to increasing scan rate, as does the integration of peak R1. This finding contrasts somewhat with the expected behavior of a surface-limited process, since if the overall reaction is simply the self-limiting oxidation and re-reduction of the iridium surface, one would expect roughly the same charge to pass at all scan rates.[5] The increase in charge integration at slower scan rates would suggest that the reaction involves the continual generation / migration of some species, and, thus, at slower scan rates, the system is held at the active voltage for longer and more product can form. One possible interpretation could be that iridium forms multiple layers of IrO_x that penetrate deeper into the surface over time, and both the growth and re-reduction of this layer require migration of oxides. IrOx is a potent oxygen evolution catalyst which forms in, and is reasonably conductive in, layers of variable thickness,[15–18] so this hypothesis would be supported by current understanding of the catalyst at room temperature. Alternatively, this diffusion process could involve the evolution of trace amounts of

[15] Nunes, D. In *Metal Oxide Nanostructures: Synthesis, Properties and Applications*; Elsevier: Amsterdam, 2019; pp 103–147.
[16] Scarpelli, F.; Godbert, N.; Crispini, A.; Aiello, I. *Inorganics* **2022**, *10* (8).
[17] Altowyan, A. S.; Shaban, M.; Abdelkarem, K.; El Sayed, A. M. *Nanomaterials* **2022**, *12* (19), 1–13.
[18] Shchetkovskiy, A.; McKechnie, Timothy Sadoway, Donald R. Paramore, J.; Melendez, O.; Curreri, P. A. In *Earth and Space 2010: Engineering, Science, Construction, and Operations in Challenging Environments*; American Society of Civil Engineers: Honolulu, 2010.

oxygen. However, rigorous lower-voltage polarization would be required to investigate these hypotheses, and quantification of oxygen levels at such current densities would require a method more precise than binary gas analysis. Regardless, the fact that O1 + O2 and R1's peak integrations follow a similar scan rate dependence suggests that the two features are, in fact, electrochemically related, and as scan rate increases, the charge integrations approach each other. (Because of the curvature of the baseline, the integration of O1 + O2 at high scan rates is likely underestimated by a fraction that is comparable to the gap between O1 + O2 and the higher nominal integration of R1.) Thus, it seems that R1 is, indeed, assignable to the back-reduction of the oxidized species generated under the conditions of O1 and O2. Since the potentials of this feature are close to the kinetic onset of OER, it seems reasonable to assign this relationship to the formation and re-reduction of a combination of IrO_2 and/or potentially O_2 gas.

By peak height analysis, peak current density for R1 and O1 seems to scale more directly with the square root of scan rate (**Figure B-10e**) relative to linear scan rate (**Figure B-10d**). This principle is illustrated by the considerably higher R^2 values of the best-fit lines for *j* vs. SQRT(*v*) (R^2 = 0.998 for R1, R^2 = 0.959 for O1) relative to those for the direct plot of *j* vs. *v* (R^2 = 0.949 for R1, R^2 = 0.870 for O1). This suggests that the processes occurring at O1 and R1 both involve a diffusion-limited component.[5] Unfortunately, because the O2 peak was convolved with that of O1, estimating its peak height was fraught with error and likely results in the low fit values in both the plot vs. *v* and the plot vs. SQRT(*v*). As discussed above, this diffusion behavior could be rooted in the formation and re-reduction of a multilayered IrO_2 surface oxide based around the transport of oxides in and out of the bulk of the iridium. This hypothesis is supported by the positive shift these peaks experience as the anhydride concentration is increased from 6.4 mol kg to 9.8 mol kg, depleting the concentration of "end groups" in the melt (**Figure 3-3c**). If the feature observed for peak O2 is indeed the same reaction as that of O1 but occurring on a less kinetically favored surface facet, this could also provide an explanation for the increase in peak separation observed between O1 and O2 as the anhydride concentration increases, since additional transport issues would be compounded on top of the sluggishness in electron transfer dynamics that the second peak already experiences.

Overall, the takeaway of these peak analysis data is that the integration of R1 corresponds nicely to the back-reduction of the process occurring in O1 and O2, these peaks appear to have a diffusion dependence that could explain the higher charge passage at slower scan rates, and O2 appears to have higher kinetic barriers than those of O1 for electron transfer, possibly corresponding to a thermodynamically adjacent process occurring under less favorable conditions or a less favorable surface structure.

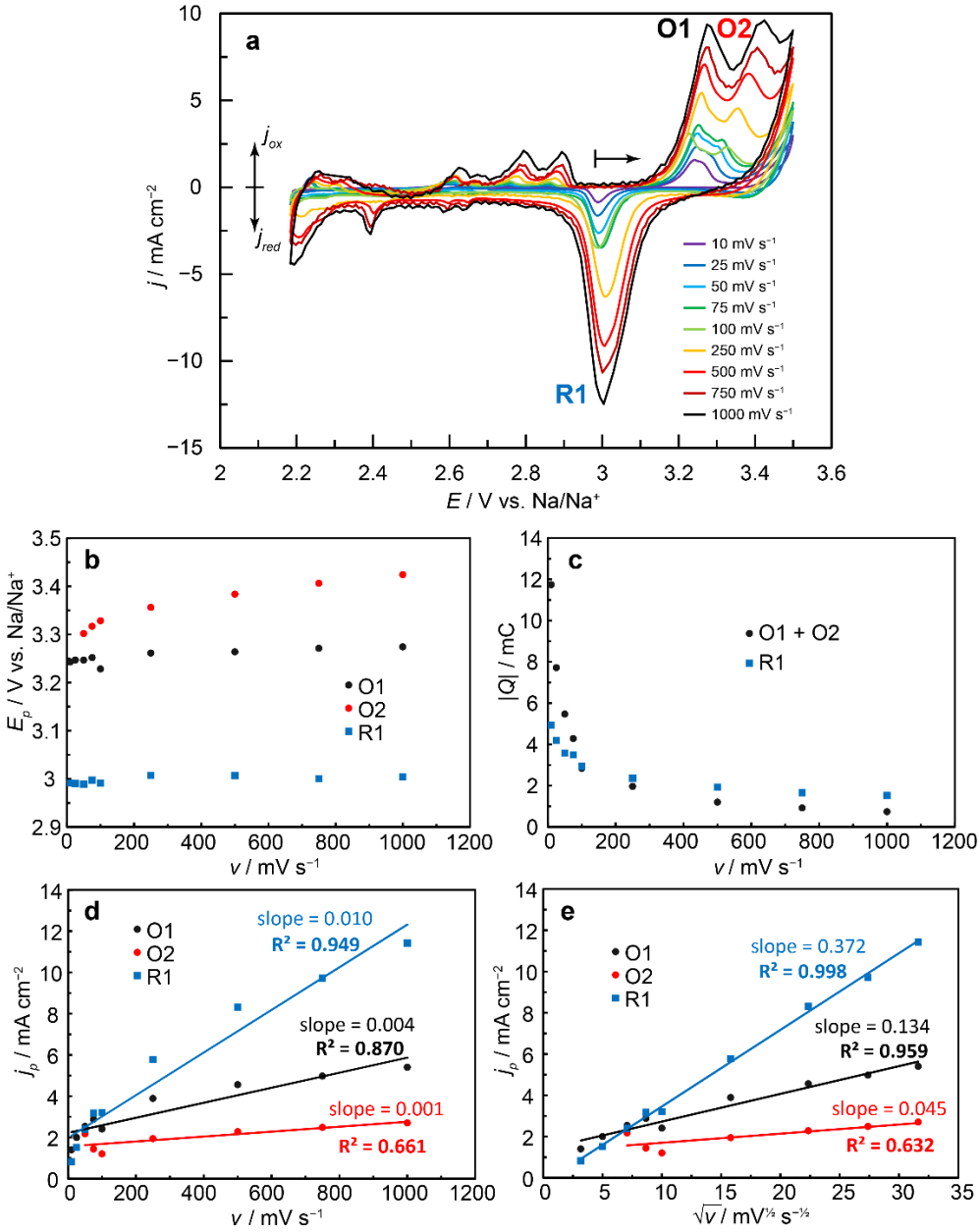

Figure B-10. *a) Cyclic voltammograms of an iridium coil in a condensed sodium phosphate melt ([P–O–P] = 6.4 mol kg^{-1}) at 800 °C. Arrow indicates point of initiation and direction of scan. Oxidative features of interest labelled as O1 and O2. Reductive feature of interest labelled as R1. b) Peak voltage of oxidative features O1 and O2 and reductive feature R1 as a function of scan rate. c) Magnitude of charge integration for combined oxidative feature O1 + O2 and reductive feature R1 as a function of scan rate. d) Magnitude of peak current density for oxidative features O1 and O2 and reductive feature R1 as a function of scan rate. Best-fit lines for each data set displayed with slope and R^2 values. e) Magnitude of peak current density for oxidative features O1 and O2 and reductive feature R1 as a function of the square root of scan rate. Best-fit lines for each data set displayed with slope and R^2 values.*

B-2.2 – Survey of Gold Corrosion Varying Current Density and Melt Acidity

To canvas the current-acidity space and determine optimal operation conditions for the corrosion experiment replicates to be taken, gold wires were used as oxygen evolution anodes under a variety of current densities and melt acidities in a broad survey over the course of several months. These data were then compiled and analyzed to search for correlations (**Figure B-11**). These data tended to fall into two categories; current densities of 100 mA cm^{-2} and those of 5-10 mA cm^{-2}. Corrosion rate of gold was found to scale with both a) current density, suggesting an electrochemical corrosion, and b) melt acidity ([P–O–P] concentration), suggesting an acid-promoted corrosion mechanism. Notably, the dependence of corrosion on the melt acidity (i.e. the slope of the plot of rate vs. anhydride concentration) seems to increase in magnitude as the current density is increased. Thus, the corrosion process seems to couple electrochemical oxidation together with reaction with acid, rather than the acid-based corrosion and electrochemical-based oxidation being entirely orthogonal factors.

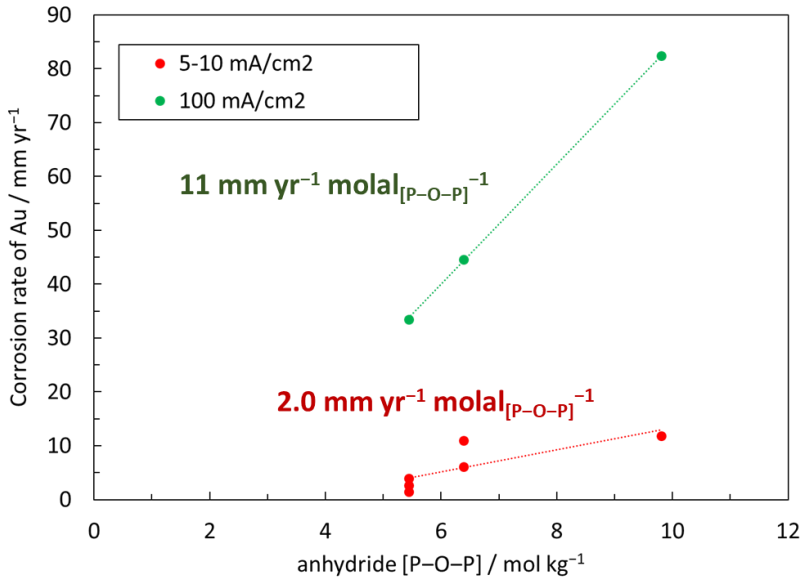

Figure B-11. *Survey data of corrosion rate of gold coils as a function of melt phosphoryl anhydride concentration in mol kg^{-1}. (green) Data collected at an oxidative current density of 100 mA cm^{-2}. (red) Data collected at an oxidative current density ranging from 5-10 mA cm^{-2}.*

B-3: SUPPLEMENTAL REFERENCES

(1) Tabereaux, A. T.; Peterson, R. D. In *Treatise on Process Metallurgy*; Elsevier: Oxford, 2014; Vol. 3, pp 839–917.

(2) Frank, W. B.; Haupin, W. E.; Vogt, H.; Bruno, M.; Thonstad, J.; Dawless, R. K.; Kvande, H.; Taiwo, O. A. *Ullmann's Encyclopedia of Industrial Chemistry*; Wiley-VCH: Weinheim, Germany, 2012; Vol. 2, pp 483–520.

(3) Prasad, S. *J. Braz. Chem. Soc.* **2000**, *11* (3), 245–251.

(4) Wilson, S. D. R.; Hulme, A. *Proc. R. Soc. London, Ser. A Math. Phys. Sci.* **1983**, *387* (1792), 133–146.

(5) Bard, A. J.; Faulkner, L. R. *Electrochemical Methods: Fundamentals and Applications*, 2nd ed.; Wiley: New York, 2000.

(6) Melville, J. F.; Licini, A. J.; Surendranath, Y. *ACS Cent. Sci.* **2023**, *9* (3), 373-380.

(7) Casey, E. J.; Dubois, A. R. *Can. J. Chem.* **1971**, *49*, 2733–2745.

(8) Casey, E. J.; Dubois, A. R.; Gorman, R. W. In *Corrosion*; 1975; Vol. 31, pp 358–363.

(9) Van Wazer, J. R. In *Phosphorus and its Compounds, Vol. I*; Interscience: New York, 1958; pp 717–800.

(10) Greenfield, S.; Clift, M. *Analytical Chemistry of the Condensed Phosphates*; Pergamon: Oxford, 1975.

(11) Hall, A. S.; Yoon, Y.; Wuttig, A.; Surendranath, Y. *J. Am. Chem. Soc.* **2015**, *137* (47), 14834–14837.

(12) Yoon, Y.; Hall, A. S.; Surendranath, Y. *Angew. Chemie - Int. Ed.* **2016**, *55* (49), 15282–15286.

(13) Yoon, Y.; Yan, B.; Surendranath, Y. *J. Am. Chem. Soc.* **2018**, *140* (7), 2397–2400.

(14) Fischer, B. *Platin. Met. Rev.* **1992**, *36* (1), 14–25.

(15) Nunes, D. In *Metal Oxide Nanostructures: Synthesis, Properties and Applications*; Elsevier: Amsterdam, 2019; pp 103–147.

(16) Scarpelli, F.; Godbert, N.; Crispini, A.; Aiello, I. *Inorganics* **2022**, *10* (8).

(17) Altowyan, A. S.; Shaban, M.; Abdelkarem, K.; El Sayed, A. M. *Nanomaterials* **2022**, *12* (19), 1–13.

(18) Shchetkovskiy, A.; McKechnie, Timothy Sadoway, Donald R. Paramore, J.; Melendez, O.; Curreri, P. A. In *Earth and Space 2010: Engineering, Science, Construction, and Operations in Challenging Environments*; American Society of Civil Engineers: Honolulu, 2010.